

Aus der Klinik für Rheumatologie und Klinische Immunologie
der Medizinischen Fakultät Charité – Universitätsmedizin Berlin &
Deutsches Rheuma-Forschungszentrum, ein Leibniz-Institut

DISSERTATION

Elucidating the mechanisms of bone regeneration using longitudinal intravital
multiphoton endomicroscopy in the murine bone marrow

zur Erlangung des akademischen Grades
Doctor of Philosophy (PhD)

vorgelegt der Medizinischen Fakultät
Charité – Universitätsmedizin Berlin

von

Jonathan Stefanowski
aus Lüdenscheid

Datum der Promotion: 17. September 2021

Contents

Zusammenfassung	1
Abstract.....	2
1 Introduction	3
1.1 Motivation for This Dissertation	3
1.2 Bone Physiology	5
1.2.1 Osteogenesis and Bone Homeostasis	5
1.2.2 The Role of Vasculature in Bone Homeostasis	6
1.3 The Immune System and the Bone	7
1.3.1 Hematopoiesis	7
1.3.2 Monocytes	7
1.3.3 Macrophages of the Bone Marrow	9
1.3.4 The CX ₃ CR1/CX ₃ CL1 Axis.....	10
1.4 Bone Regeneration	11
1.4.1 Organization of Bone Regeneration.....	11
1.4.2 Initial Fracture Hematoma and Vascularization	11
1.4.3 Macrophages in Bone Regeneration.....	12
1.4.4 The Role of Macrophages in Regenerative Angiogenesis	13
1.5 Multiphoton Intravital Microscopy of the Bone	13
2 Material and Methods	14
2.1 Mice	14
2.2 LIMB and Limbostomy System Implantation	14
2.3 Longitudinal Intravital 2-Photon Microscopy	15
2.4 Immunofluorescence Histology	15
3 Results.....	16
3.1 Internal Fixation of a Microendoscope Is Suitable for Longitudinal Intravital Microscopy under Homeostatic Conditions.....	16
3.2 Longitudinal Multiphoton Microendoscopy of the Bone Marrow Allows Visualization of Bone Regeneration after Osteotomy.....	17
3.3 The Vascular Network in the Bone Marrow Dynamically Reshapes during Homeostasis.....	18
3.4 Vascularization from Existing Vessels during Intramedullary Bone Regeneration Occurs in Two Distinct Phases in Cdh5 ^{GFP/tdT} Mice	18

3.5	Bone Marrow Endothelial Cells at Sites of Bone and Bone Marrow Regeneration Exhibit a Type H Immunophenotype.....	19
3.6	Macrophages Localize towards the Type H Endothelium during Regeneration	19
3.7	VEGF is Provided by CD80 ⁺ Cells in the Early Phase of Healing	20
3.8	CX ₃ CR1 ⁺ F4/80 ⁺ Macrophages Are the Major Subset of Cells in the Osteotomy Gap and Precede Vascularization.....	20
4	Discussion.....	21
4.1	Applications of LIMB and Limbostomy	21
4.2	The Impact of Vessel Plasticity on the Bone Marrow Microenvironment during Homeostasis.....	22
4.3	Vascularization and Endothelial Proliferation after Injury.....	24
4.4	The Role of CX ₃ CR1 ^{hi} Gr1 ^{lo} Mononuclear Phagocytes.....	25
5	References	28
6	Statutory Declaration.....	34
7	Declaration of Contribution	35
8	Selected Publications	37
8.1	Reismann et al., 2017 – Longitudinal Intravital imaging of the Femoral Bone Marrow Reveals Plasticity within Marrow Vasculature	37
8.2	Reismann et al., 2017 – Supporting Material	53
8.3	Stefanowski et al., 2019 – Spatial Distribution of Macrophages During Callus Formation and Maturation Reveals Close Crosstalk Between Macrophages and Newly Forming Vessels	64
8.4	Stefanowski et al., 2019 – Supporting Material.....	82
8.5	Stefanowski et al., 2020 – Limbostomy: Longitudinal Intravital Microendoscopy in Murine Osteotomies.....	91
8.6	Stefanowski et al., 2020 – Supporting Material.....	105
9	Curriculum Vitae	117
10	Complete List of Publications.....	118
11	Acknowledgements.....	119

Zusammenfassung

Die Knochenregeneration ist ein komplexer Prozess mit enger Interaktion von Zellen des Gefäßnetzes, des Immunsystems und mesenchymaler Zellen. Die dem Prozess zugrundeliegenden Mechanismen und die Dynamiken sind noch nicht vollständig verstanden. Methoden, die die Analyse dieser Mechanismen während der Heilung und über die Zeit visualisieren, sind nicht verfügbar. Daher wird ein System für longitudinale intravitale Multi-Photonen-Mikroendoskopie des murinen Knochens (longitudinal intravital multiphoton endomicroscopy in the murine bone marrow, LIMB) entwickelt. Diese Arbeit zielt darauf ab, 1) die immunologische Reaktion auf das LIMB-System zu beschreiben, 2) das System für die longitudinale Mikroendoskopie bei Osteotomien (Limbostomy) anzupassen und 3) die Rolle mononukleärer Phagozyten im Prozess der Angiogenese während der Heilung aufzuklären.

Die Implantation des LIMB-Systems führte zu einer transienten immunphysiologischen Reaktion, die von der Expression des extrazellulären Matrixmarkers Laminin, einer Akkumulation von CD45⁺ Lymphozyten und der Anwesenheit von CD31^{hi}Emcn^{hi} (Typ H) Endothel am Ort der Knochenverletzung begleitet wurde. Alle Reaktionen verschwanden nach 28 Tagen, ohne bleibende Beeinträchtigung der Knochengefäßperfusion oder Hämatopoese. Die Analyse des Gefäßsystems mit Hilfe eines vaskulären Fluoreszenzfarbstoffs zeigte vaskuläre Plastizität im Knochenmark während der Homöostase über die Zeit.

Ein adaptiertes LIMB-System mit modularem Design, Limbostomie benannt, wurde mit verbessertem Sichtfeld und Bildqualität, sowie Anpassungsfähigkeit in der Eindringtiefe des Endoskops entwickelt. Mit transgenen Fluoreszenz-Reportermäusen unter dem Endothelzellpromotor Cadherin wurden nach der Osteotomie zwei Phasen der Vaskularisierung beobachtet. Eine initiale Neovaskularisierung, die zwischen Tag 3 und 4 nach der Osteotomie einsetzt und innerhalb von 24 h abgeschlossen war. Aktivierte Endothelzellen, die in das initiale Frakturhämatom eindringen, stammten aus dem bestehenden Gefäßnetz. Das Endothelnetzwerk wurde in einer zweiten Phase kontinuierlich umgestaltet, während Knochenkallus auf- und umgebaut wurde.

Mit Hilfe der Immunfluoreszenz-Histologie wurde festgestellt, dass das vorherrschende Gefäßsystem einen Typ-H Endothelphänotyp aufweist und während der Heilung mit F4/80^{hi} Makrophagen kolokalisierte. Am siebten Tag nach der Osteotomie waren die meisten Zellen in dem Osteotomiespalt CX₃CR1⁺Gr1⁻F4/80⁺ Makrophagen. Mit der Limbostomie-Methode wurde beobachtet, dass die Zunahme der CX₃CR1⁺ Zellen 2 – 3 Tage nach der Osteotomie einsetzte. CX₃CR1⁺ Zellen gingen der Vaskularisierung voraus und waren während des gesamten Regenerationsprozesses vorhanden.

Zusammenfassend lässt sich sagen, dass die LIMB-Methode vaskuläre Plastizität während der Homöostase offenbart. Außerdem wurde hier der neue, technische Ansatz der LIMB-Methode erweitert, um die Visualisierung der räumlichen und zeitlichen Organisation während der Knochenregeneration zu ermöglichen. Die Ergebnisse implizieren, dass Nischen im Knochenmark kontinuierlichen Gewebeveränderungen unterworfen sind und dass mononukleäre CX₃CR1⁺ Phagozyten an der Vaskularisierung und dem Umbau des Gefäßnetzwerks beteiligt sind.

Abstract

Bone regeneration is a complex process that involves the interaction between cells of the vascular network, the immune system, and mesenchymal cells. The underlying mechanisms and dynamics are not fully understood. To allow a visual analysis of these mechanisms during regeneration and over time, a system for longitudinal intravital multiphoton microendoscopy of the murine bone (LIMB) was developed. This dissertation aims to 1) describe the immunophysiological reaction to the LIMB system, 2) to adapt the system for longitudinal microendoscopy in osteotomies (Limbostomy), and 3) to elucidate the role of mononuclear phagocytes in the process of angiogenesis during healing.

The implantation of the LIMB system resulted in a transient immunophysiological reaction accompanied by the expression of the extracellular matrix marker Laminin, an accumulation of CD45⁺ lymphocytes, and the presence of CD31^{hi}Emcn^{hi} (type H) endothelium at the site of injury. All reactions cleared after 28 days without impairment of bone vessel perfusion or hematopoiesis. Longitudinal analysis of vasculature using vascular fluorescent dye revealed vascular plasticity in the bone marrow during homeostasis.

A modular design of the LIMB system for longitudinal intravital microendoscopy of murine osteotomies, termed Limbostomy, was developed. It is specified by an improved field of view and image quality, as well as adaptability of the endoscope tissue penetration depth. Using transgenic fluorescent reporter mice for the endothelial cell promoter Cadherin, two phases of vascularization were observed after osteotomy. In the first phase, neovascularization started between day 3 and 4 post-osteotomy and was completed within 24 hours. Activated endothelial cells that penetrated the initial fracture hematoma were derived from an existing vascular network. In the second phase, the endothelial network continuously remodeled, while the bony callus was built and restructured.

Using immunofluorescent histology, type H endothelium was found to be the predominant vasculature and co-localized with F4/80^{hi} macrophages during healing. In the osteotomy gap, the majority of cells seven days post-osteotomy were CX₃CR1⁺Gr1⁻F4/80⁺ macrophages. Using Limbostomy, the increase of CX₃CR1⁺ cells was observed to be initiated 2–3 days post-osteotomy. CX₃CR1⁺ cells preceded vascularization and were present throughout the regeneration process.

In summary, LIMB reveals vascular dynamics during homeostasis. In addition, the new LIMB approach was further developed to visualize spatiotemporal organization during bone regeneration. The findings imply that niches in the bone marrow are subject to continued tissue changes and that CX₃CR1⁺ mononuclear phagocytes play a role in promoting vascularization and endothelial remodeling.

1 Introduction

1.1 Motivation for This Dissertation

Broken bone initiates a regeneration process that secures complete healing. Basic research on bone regeneration is driven by three major motivations: First, depending on injury location, age, and risk factors, bone healing results in nonunion in 5 – 10 % of all cases (Praemer et al., 1999). Due to a strong link between severity and age, this incidence displays a heavy socio-economic burden to an aging society (Watkins-Castillo and Andersson, 2014). Second, bone healing develops distinct phases of its regeneration cascade that eventually result in scar free healing (Schmidt-Bleek et al., 2014a). Studying bone regeneration can refine our understanding of the basic principles in regeneration cascades and the impact of its sequential phases on the healing outcome. As these principles might be transferable to the regeneration of other tissues, this knowledge will allow the development of well-timed and adequate clinical intervention strategies in both bone and other tissue regeneration settings (Schmidt-Bleek et al., 2014). Third, deciphering cellular regulatory functions between bone compartments and the immune system, also called osteoimmunological functions, will contribute to develop pharmaceuticals for bone development, homeostasis, and healing, by specifically targeting immune cell functions (Tsukasaki and Takayanagi, 2019). Importantly, some phases of bone regeneration, such as callus formation, resemble processes of developmental bone formation (Marsell and Einhorn, 2011). In addition, key functions of bone regeneration reflect musculoskeletal disease mechanisms such as vascularization of cartilage and its subsequent degradation in rheumatoid arthritis (Elshabrawy et al., 2015). Consequently, understanding bone regeneration can contribute to basic insights into a wide range of mechanisms in bone formation, homeostasis, and pathology.

The highly complex process of bone regeneration involves signaling between cells of the vascular network, the immune system, and mesenchymal cells. It includes the differentiation of bone cells from distinct cellular progenitors, the growth of vasculature to secure oxygen and nutrient supply, and inflammatory processes orchestrated by immune cells. These mechanisms occur simultaneously and are highly dependent on signals in their immediate proximity, their microenvironment. Furthermore, reorganization and migration of the cells involved occurs in space and over time. This spatiotemporal organization of cells is important, e.g. for the effectiveness of receptor-bound factors such as receptor activator of NF- κ B (nuclear factor ‘kappa-light-chain-enhancer’ of activated B cells) (RANK) ligand (RANKL)

when compared to soluble factors (Nakashima et al., 2000), as well as the simultaneous contribution of multiple cell types, e.g of the hematopoietic stem cell microenvironment (HSC niche) (Birbrair and Frenette, 2016), or plasma cell niche (Zehentmeier et al., 2014).

However, the spatiotemporal organization is not preserved when using state of the art methods such as fluorescence-activated cell sorting (FACS) analysis or histological approaches. Here, intravital microscopy – the microscopic imaging of living organisms – allows us to improve the understanding of biological functions within tissue context. By maintaining the spatiotemporal cellular context of the tissue, a better understanding of mechanisms such as hematopoietic stem and progenitor cell (HSPC) homing can be achieved (Bixel et al., 2017; Itkin et al., 2016).

To visualize the spatial organization and cellular dynamics in bone under homeostatic conditions over time, an intravital microendoscopic imaging approach called longitudinal intravital multiphoton microendoscopy of the murine bone (LIMB) has been developed by the working groups of Prof. Anja Hauser and Prof. Raluca Niesner. Application and functionality of LIMB were not yet established.

The work of this dissertation aimed

- to analyze the immunophysiological reaction to the LIMB endoscope, including the immune cell reaction to the implant, the response of the endothelial network, and the cellular composition of the bone marrow tissue over the course of post-surgical healing.
- to develop an intravital microendoscopic imaging approach that allows visualization of the spatiotemporal organization of bone and bone marrow longitudinally under regenerative conditions. This approach was termed longitudinal intravital microendoscopy in murine osteotomies (Limbostomy).
- to elucidate the role of mononuclear phagocytes in the process of angiogenesis during bone regeneration using Limbostomy.

Lux et veritas!

1.2 Bone Physiology

In mammals, bones are highly vascularized and composed of osseous tissue and bone marrow. The osseous tissue is primarily type I collagen fiber-based extracellular matrix (ECM), deposited calcium and phosphate, bone cells, and vessels. The bone marrow contains cells of the hematopoietic system, mesenchymal stromal cells (MSC), and vessels. Composition and quality of both osseous tissue and the bone marrow are influenced by age, nutrition, and exercise, regulated by the endocrine and immune system. Pathological conditions such as cancer and autoimmune diseases including rheumatoid arthritis can deregulate the maintenance of the bone tissue - the bone homeostasis (Al-Sebaei et al., 2014; Einhorn and Gerstenfeld, 2015).

1.2.1 Osteogenesis and Bone Homeostasis

Bone is a highly dynamic tissue. Over a mammal's lifetime bone is produced, reorganized, and maintained by cells of mesenchymal origin such as bone-producing osteoblasts and their progeny, bone matrix-embedded osteocytes. In osteogenesis, growth, and regeneration, chondrocytes produce and maintain a cartilaginous template, which is converted into osseous tissue. During constant reorganization of the tissue, the remodeling process, bone-degrading osteoclasts of myeloid hematopoietic origin are essential. Bone mass quality is determined by an equilibrium of osteoblasts and osteoclasts. Osteoclasts differentiate from myeloid cells after stimulation with macrophage-colony stimulating factor (M-CSF) and RANKL. M-CSF binds to cluster of differentiation (CD) 115 (C-FMS; CSF1R). Differentiation and proliferation of osteoclasts is indicated by high expression of tartrate-resistant acid phosphatase (TRAP).

Bone cells are of different developmental origin. MSCs can differentiate into osteoprogenitor cells under the expression of runt-related transcription factor 2 (Runx2) (Komori, 2006), while maturation of osteoblasts is marked by the expression of osterix (Osx). Chondrocytes, however, require the expression of sex-determining region Y (SRY)-box transcription factor 9 (Sox9). To initiate conversion of cartilage into bone, chondrocytes turn into hypertrophic chondrocytes. Osteoblasts, once differentiated, produce the main organic bone ECM component osteoid, which primarily contains type I collagen fibers built by one alpha-2 chain and two alpha-1 chains, within which calcium is deposited in the form of crystalline hydroxyapatite (Lian et al., 2011). In this process, some osteoblasts are actively embedded into the ECM and differentiate into osteocytes.

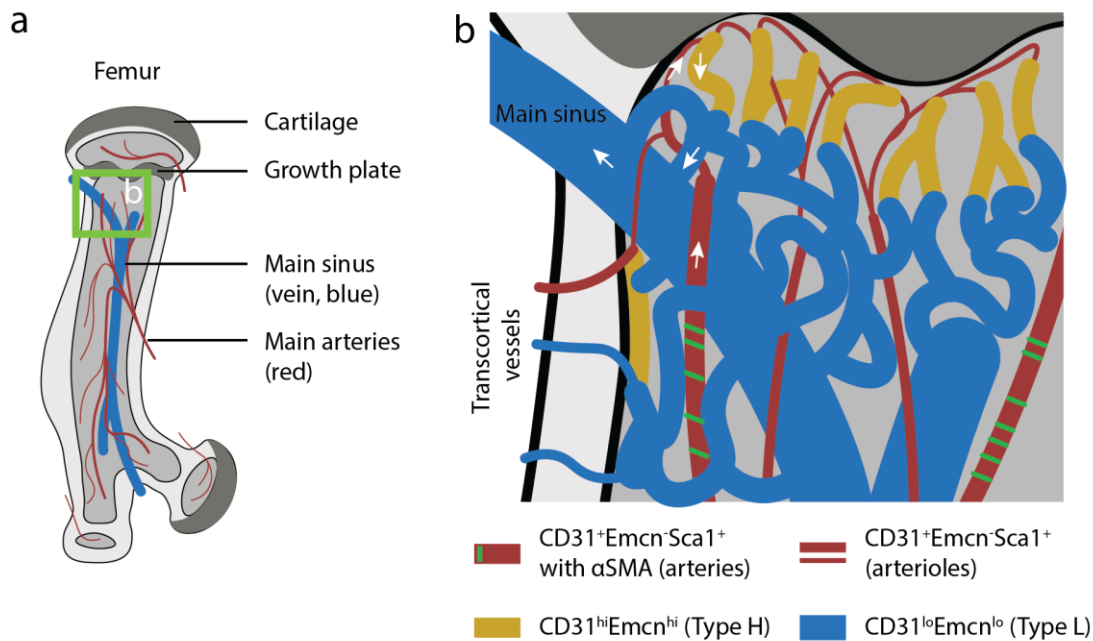


Figure 1: Overview of vasculature in the femoral long bone.

Bones are formed via two pathways of ossification during embryogenesis. Intramembranous ossification is a process in which osteoblast cells differentiate from MSCs within vascularized tissue to produce bone. In endochondral ossification MSCs differentiate into chondrocytes in non-vascularized connective tissue.

1.2.2 The Role of Vasculature in Bone Homeostasis

The highly vascularized bones contain various types of endothelium (Figure 1). In long bones hypertrophic cartilage is vascularized during endochondral ossification. This process results in a small number of main arteries that supply bones, such as the femur, at the center and the terminal ends. $CD31^+Emcn^+Sca1^+$ ($CD31^+Endomucin^+Stem\ cell\ antigen-1^+$) arteries, which are surrounded by α smooth muscle actin (αSMA)⁺ pericytes, split at bone surfaces and particularly below the growth plate in the metaphysis into $CD31^+Emcn^+Sca1^+$ arterioles, that are smaller in diameter compared to arteries ($\sim 5\ \mu m$) (Itkin et al., 2016). In regions of bone growth, they feed into columnar $CD31^{hi}Emcn^{hi}$ (type H) vascular endothelium (Kusumbe et al., 2014). Following the blood flow away from bone surfaces, vessel diameter increases, blood flow decreases and enters the $CD31^{lo}Emcn^{lo}$ sinusoid system of larger diameter ($\sim 25\ \mu m$), that subsequently empties in the main, central sinus of the bone marrow (Itkin et al., 2016). The central sinus eventually exits the femur at the tips in few major locations (Grüneboom et al., 2019). Additionally, recently transcortical vessels have been shown to supply a major portion of blood in and out of the bone marrow (Grüneboom et al., 2019). This relatively new and detailed understanding of the bone vasculature network is the result of research using microscope techniques, including light-sheet microscopy, intravital microscopy, and confocal microscopy combined with advanced immunofluorescence histology.

1.3 The Immune System and the Bone

Immune cells are mostly generated via definitive hematopoiesis, primarily in the bone marrow. The immune system consists of the innate immune system, the general defense apparatus, and the adaptive immune system. The latter has evolved to detect pathological cells or particles via antigen-specific recognition and store this information in memory cells.

1.3.1 Hematopoiesis

Hematopoiesis describes the production of blood cells. These cells include the cells of the adaptive immune system, T and B lymphocytes, cells of innate immunity, among them myeloid cells, megakaryocytes, erythrocytes, and innate lymphoid cells (ILCs), including natural killer cells. Some immune cells such as a population of myeloid cells - the tissue resident macrophages - develop during embryogenesis. Through intermediate steps, embryonic progenitors of HSCs gain full and definite hematopoietic potential. Postnatal, self-renewing long-term HSCs hierarchically differentiate into distinct intermediate progenitors of increasing commitment, which are classified into short-term HSCs, multipotent progenitor (MPP), common lymphoid progenitor (CLP), common myeloid progenitor (CMP) cells, which can turn in to megakaryocyte-erythrocyte progenitor (MEP) or granulocyte-monocyte progenitor (GMP) cells. HSPCs reside in microenvironments called niches, which provide specific signals such as oxygen tension and signals from mesenchymal stromal cells for survival, proliferation, and mobilization (Wei and Frenette, 2018). Understanding these niches enables us to influence hematopoietic cell differentiation in health and disease.

1.3.2 Monocytes

Monocytes are mononuclear phagocytes along with dendritic cells, and macrophages. They belong to the myeloid cell population that includes granulocytes, polymorphonuclear leukocytes such as neutrophils, eosinophils, basophils, and mast cells. Monocytes represent accessory cells that link the innate and adaptive immune system via antigen presentation. Once definitive hematopoiesis is established, monocytes develop from the CMP cell descendant macrophage dendritic progenitor (MDP) cells via common monocyte progenitor (cMoP) cells in the bone marrow (Hettinger et al., 2013). Monocytes were long considered to be the sole progenitor of all macrophages, which is formulated in the mononuclear phagocyte system (MPS) model. Monocytes are short-lived mononuclear phagocytes of the blood. They are recruited during early inflammation via pathogen-associated molecular patterns and damage-associated molecular patterns along with granulocytes. They fulfil phagocytic functions and can differentiate into macrophages and dendritic cells.

The generation of monocytes is largely dependent on M-CSF, since upon the deletion of both (*csf1*^{-/-}) or its receptor CD115 (*csf1r*^{-/-}), a dramatic reduction of blood monocytes is observed (Auffray et al., 2009).

Monocytes are released into the blood from the bone marrow upon inflammatory stimuli such as type 1 interferons (IFN) and toll-like receptor ligands (Shi and Pamer, 2011). They are continuously released under homeostatic conditions depending on C-C chemokine receptor type 2 (CCR2) and its ligand, which is secreted by pericytes and MSCs (Shi and Pamer, 2011).

The immunophenotype of monocytes consists of various markers. Monocytes are positive for integrin CD11b, which is, together with CD18, one of two subunits of the complement receptor 3. CD11b is involved in adhesion and spreading of cells and expressed on myeloid cells such as macrophages, granulocytes but also natural killer cells. Monocytes are positive for F4/80, an adhesion G protein-coupled receptor glycoprotein, which is required for peripheral tolerance in mice (Lin et al., 2005). Most blood monocytes carry lymphocyte antigen 6 complex, locus C1 (Ly6C) on their surface. It is the co-receptor of Ly6G, which in combination with Ly6C constitute the granulocytic marker 1 (Gr1) receptor.

In the blood, among CD11b⁺F4/80⁺ myeloid cells, two monocyte populations are distinguished (Table 1). These are split into CX₃CR1^{lo}CCR2⁺Gr1⁻ classical monocytes and CX₃CR1^{hi}CCR2⁻Gr1⁻ non-classical monocytes (Geissmann et al., 2003). Classical monocytes are characterized by a Ly6C^{hi/+}(Gr1⁺)CD62L⁺ immunophenotype and fulfill pro-inflammatory functions in an immune response. There is evidence that CX₃CR1^{lo}Ly6C^{hi} monocytes are the precursors of CX₃CR1^{hi}Ly6C⁻ monocytes, although research suggests that an undiscovered pathway for differentiation under non-homeostatic conditions exists (Mildner et al., 2017). Non-classical blood monocytes are Ly6C^{lo/-}(Gr1⁻)CD62L⁻ and are described as CX₃CR1^{hi}Ly6C^{lo/-} non-classical monocytes. They patrol endothelial cells (Auffray et al., 2007) and control their disposal in an

Table 1: Immunophenotype and function of classical and non-classical monocytes.

Immunophenotype	Subset	Function
CX ₃ CR1 ^{lo} CCR2 ⁺ Gr1 ⁻ CX ₃ CR1 ^{lo} Ly6C ^{hi} Ly6C ^{hi/+} (Gr1 ⁺)CD62L ⁺ Nr4a1 (Nur77) ⁻	Classical monocytes	Pro-inflammatory functions in immune response
CX ₃ CR1 ^{hi} CCR2 ⁻ Gr1 ⁻ CX ₃ CR1 ^{hi} Ly6C ^{lo/-} Ly6C ^{lo/-} (Gr1 ⁻)CD62L ⁻ Nr4a1 (Nur77) ⁺	Non-classical monocytes	Patrol endothelial cells and control their disposal

Nr4a1 (Nur77)-dependent manner (Carlin et al., 2013). They can be identified by using Nur77 in a transgenic Nur77^{GFP} mouse model (Buscher et al., 2017). Under inflammatory conditions, non-classical monocytes seem to be biased to differentiate into anti-inflammatory macrophages that support vascularization during regeneration (Olingy et al., 2017). The mouse immunophenotypes of the distinct monocyte subsets is reflected with similar functions in human CX₃CR1^{lo}CD14^{hi}CD16^{lo} and CX₃CR1^{hi}CD14^{lo}CD16^{hi} (Geissmann et al., 2003). It is yet unknown how these monocyte populations contribute to the process of bone regeneration.

1.3.3 Macrophages of the Bone Marrow

Macrophages are often referred to as the most plastic cells of the hematopoietic system (Wynn et al., 2013). They can be found in all tissues of vertebrates and are involved in development, homeostasis, tissue repair, and immunity (Udalova et al., 2016; Wynn et al., 2013). In general, macrophages express F4/80, CD11b, and Fcγ-receptors. For their functional classification, a dichotomous model of M1 (pro-inflammatory, classically activated macrophages) and M2 (anti-inflammatory, alternatively activated macrophages) was proposed (Gordon, 2003; Sica and Mantovani, 2012). Although the M1/M2 classification has been rejected from the field of macrophage research (Murray et al., 2014), for simplicity reasons, these macrophages are referred to as M1-*like* or M2-*like*, if they fulfill certain criteria. Typical markers are CD206 for M2-like macrophages and CD80/86 for M1-like macrophages (Schlundt et al., 2018).

The developmental origin of macrophages in the bone marrow remains elusive. During development, vascularization of the murine femur by embryonic CD31^{hi}Emcn^{hi} (type E) endothelium occurs on embryonic day (E)15.0 (Langen et al., 2017). Around the same time osteoclasts develop from erythrocyte myeloid progenitors (EMPs) and not HSCs (Jacome-Galarza et al., 2019). From there, the bone marrow cavity is formed and adult, repopulating HSCs seed from the fetal liver to the bone marrow around E15.5 – E16.5 (Coşkun et al., 2014; Jacome-Galarza et al., 2019). Considering that tissues become populated by yolk-sac derived macrophages much earlier in development, it is unclear whether bone marrow macrophages derive from proliferating embryo-derived macrophages of surrounding tissues or *de novo* from monocytes of the bone marrow. Similarly, the immunophenotype of macrophages is described in detail for most tissues (Kierdorf et al., 2015), but barely considered for macrophages in the bone marrow. It is also unclear to what extent macrophages of the bone marrow are resident.

Macrophages of the bone marrow support hematopoiesis. Using the macrophage FAS-induced apoptosis (MaFIA) mouse model, which allows depletion of macrophages under the *Csf1r* promoter in mature animals, showed depletion of F4/80⁺CD11b⁺Ly6G⁺ macrophages and mobilization of HSCs from their niches (Winkler et al., 2010). This observation has been confirmed by Chow et al. using clodronate

phagocyte depletion (Chow et al., 2011). Using diphtheria toxin-inducible depletion of CD169⁺ cells in the CD169^{DTR/+} mouse model, these macrophages have been shown to contribute to the maintenance of erythroid islands and the retention of hematopoietic stem and progenitor cells (HSPCs) in their niche (Chow et al., 2013, 2011; Jacobsen et al., 2014). CD169⁺ macrophages were further described as F4/80⁺VCAM-1⁺ERHR3⁺Ly6G⁺ in a flow cytometric approach (Jacobsen et al., 2014). The macrophage population of the bone marrow is a heterogeneous population, which becomes evident from the example of erythroid island macrophages which are negative for the pan-phagocyte marker CD11b (Birbrair and Frenette, 2016). Furthermore, Ludin et al. identified a rare subset of CX₃CR1⁺ radiation-resistant αSMA⁺ monocyte-macrophages as a component for HSPC retention under stress in the bone marrow niche (Ludin et al., 2012).

In the bone, mononuclear phagocytes represent precursors of osteoclasts. Osteoclast differentiation is potently enhanced by the pro-inflammatory cytokine interleukin (IL)-17 and inhibited by IFNγ (Sato et al., 2006; Takayanagi et al., 2002). Osteoclast progenitor cells express CD80/86 which interacts with CD28 on T cells to support osteoclastogenesis. New data show that osteoclasts are long-lived cells, which derive from EMPs during embryogenesis and grow by fusion with monocytes (Jacome-Galarza et al., 2019). Macrophages at osteal sites, sometimes named osteomacs, have also been shown to support osteoblastic differentiation and support their survival (Chang et al., 2008; Vi et al., 2015). In regeneration, however, the differentiation of osteoclasts and origin of their precursors is not well described.

1.3.4 The CX₃CR1/CX₃CL1 Axis

The CX₃CR1^{GFP} reporter mouse marks all monocytes (Jung et al., 2000; Palframan et al., 2001). CX₃CR1 is the only member of the CX₃C chemokine receptor family that binds the chemokine CX₃CL1, also known as neurotactin (Bazan et al., 1997; Pan et al., 1997). CX₃CL1 is expressed in a membrane bound version that is presented on a mucin-like stalk and additionally as a soluble splice-variant. CX₃CL1 is expressed on activated endothelial cells (Bazan et al., 1997; Pan et al., 1997) dendritic cells and neurons (Jung et al., 2000).

In the bone marrow, CD11c⁺MHCII⁺ (major histocompatibility complex molecule class II) dendritic cells are marked by a high expression of CX₃CR1 (Evrard et al., 2015). Dendritic cells were shown to cluster perivascular in the bone marrow and stimulate CD4⁺ T cells (Sapoznikov et al., 2008). This subset and the expression of the survival factor macrophage migration inhibitory factor is required for recirculating mature B cells in this niche in the bone marrow (Sapoznikov et al., 2008).

1.4 Bone Regeneration

1.4.1 Organization of Bone Regeneration

After bone injury, regeneration can be divided into three major phases: 1) inflammatory, 2) anabolic, and 3) catabolic (Einhorn and Gerstenfeld, 2015). Phase 1 can be subdivided into an initial, pro-inflammatory phase followed by an anti-inflammatory phase during which vascularization occurs and osteogenic signaling progressively allows callus formation and hardening in phase 2 (Schmidt-Bleek et al., 2014b, 2014a). The formed callus is then degraded in phase 3, the remodeling phase (Einhorn and Gerstenfeld, 2015). During these phases, the origin and differentiation of MSCs into bone cells, immune cell invasion such as macrophage invasion, and callus formation is highly dependent on microenvironmental cues and the cells' developmental stage in time (Gerstenfeld et al., 2003). Although various phase-models have been proposed for bone regeneration, it should be stressed that a clear differentiation of distinct phases in general is challenging due to significant overlaps across phases of characteristics such as the vascularization and spatial dependencies. To exclude effects of variations between individuals during the process of regeneration, a visualization of its phases in space in one and the same individual is needed.

1.4.2 Initial Fracture Hematoma and Vascularization

The initial fracture hematoma in phase 1 is an important and potent stimulator for recruitment of immune cells. It also acts as an initial stimulator of vascularization through vascular endothelial growth factor (VEGF), platelet-derived growth factor (PDGF), and transforming growth factor beta 1 (TGF- β 1) (Kolar et al., 2011, 2010; Shiu et al., 2018). Innate immune cells such as granulocytes and activated macrophages are recruited by damage-associated molecular patterns and the platelet-derived complement system. Since the bone marrow produces those cells, recruitment is likely to occur immediately.

Whether the immense tissue damage, which occurs in the bone marrow after fracture, also leads to significant changes in the bone marrow microanatomy and possibly its function is unclear. Innate immune cells produce pro-inflammatory cytokines such as IL-1, IL-6, and tumor necrosis factor (TNF) which recruit MSCs to the site of injury (Schmidt-Bleek et al., 2014a; Shiu et al., 2018). Due to disruption of vasculature and clotting of extravascular thrombin, the hematoma is hypoxic (Shiu et al., 2018). Hypoxia is a strong stimulator of VEGF expression via hypoxia-inducible factor (HIF) signaling, which is highest in the first 24 – 36 h after injury (Schmidt-Bleek et al., 2014b).

The pro-inflammatory milieu switches to an anti-inflammatory milieu as early as one day after injury, marked by a high expression of IL-10 (Schmidt-Bleek et al., 2014b). It has been shown that IL-10 strongly enhances neovascularization and endothelial progenitor recruitment (Balaji et al., 2020). Throughout this process, platelets, granulocytes, macrophages, and MSCs produce VEGF (Shiu et al., 2018). Endothelial cells progressively sprout into the hematoma, possibly on routes previously cleared by phagocytic activity

(Schmidt-Bleek et al., 2014a). The availability of endothelial progenitors also impacts regeneration as the migration of CD31⁺ endothelial progenitors from the bloodstream into the hematoma improves the fracture healing outcome (Sass et al., 2017). In phase 2, ECM is produced by osteoblasts, chondrocytes, MSCs, and to some extent endothelial cells, which allows callus and cartilage formation.

Vascularization of cartilage is an essential step in bone development (Langen et al., 2017), long bone growth (Kusumbe et al., 2014), and endochondral bone regeneration (Schmidt-Bleek et al., 2014a). This process involves specialized endothelial cells with high expression of CD31 and endomucin (Kusumbe et al., 2014; Lang et al., 2016; Langen et al., 2017). These type H and type E endothelial cells are functionally linked to osteogenesis and their growth is controlled by the blood flow (Kusumbe et al., 2014; Langen et al., 2017; Ramasamy et al., 2016). The survival and differentiation of type H endothelium is stabilized by HIF-1 α (Kusumbe et al., 2016). Recently, Romeo et al. showed that a specific subset of non-resorbing osteoclasts is involved in the vascularization of growth plate cartilage (Romeo et al., 2019). In this context it is important to highlight that vascularization of cartilage is mainly driven by factors released by chondrocytes under normal growth conditions, in contrast to the inflammation-driven vascularization of the fracture hematoma. It is unknown, how and when vascularization of regenerating bone tissue occurs on a cellular level and which underlying mechanisms initiate or drive angiogenesis in this context.

1.4.3 Macrophages in Bone Regeneration

Macrophages are important for the process of bone regeneration and homeostasis. They are known to be essential for the maintenance and differentiation of osteoblasts and bone lining cells (Chang et al., 2008). In a digit tip amputation model in mice, macrophages were essential for the epimorphic regeneration (Simkin et al., 2017). Similarly, macrophages were shown to be essential for regeneration after clodronate depletion and using the MaFIA mouse model (Alexander et al., 2011; Raggatt et al., 2014; Schlundt et al., 2018). Transferring F4/80⁺ macrophages from young into old mice during fracture healing completely rescued the healing outcome, suggesting a strong contribution to bone regeneration in general (Vi et al., 2018). In 2020, Clark et al. identified F4/80⁺Ly6C⁻ macrophage numbers to be decreased dramatically in young mice, when compared to older controls, while total macrophage numbers in the callus were similar in early regeneration (Clark et al., 2020). This underlines the importance of macrophages, especially in early fracture healing events, for the overall regeneration outcome. Some attempts have been made to further characterize the responsible subset of macrophages. For example, Li et al. identified M2-like polarized macrophages to promote bone healing (Li et al., 2019), while CCR2 seems not to be essential for the healing outcome in the craniofacial region (Bigueti et al., 2018). Additionally, pro-angiogenic, pro-inflammatory cytokines IL-1, IL-6, and TNF are secreted by activated, M1-like macrophages and neutrophils, which might support regeneration in the pro-inflammatory phase, especially during vascularization (Kolar et al., 2010; Schmidt-Bleek et al., 2014a).

1.4.4 The Role of Macrophages in Regenerative Angiogenesis

The role of macrophages during regenerative angiogenesis is not fully understood. Macrophages act as chaperones in the process of anastomosis during development in the brain of mice (Fantin et al., 2010; Geudens and Gerhardt, 2011) and soft tissue regeneration in the zebrafish (Gurevich et al., 2018). Interaction of macrophages and endothelial cells during angiogenesis is mediated by HIF-1 α (Gerri et al., 2017). Most recently, Balaji et al. showed that IL-10 supports wound healing by promoting neovascularization through endothelial progenitor cells in mice.

A potent factor for vascularization is VEGF, which is produced by osteoblasts and chondrocytes during bone regeneration. VEGF recruitment and on-site education of monocytes in liver regeneration improves their role as angiogenic accessory cells (Avraham-Davidi et al., 2013). In bone regeneration, deletion of VEGFA from osteoblasts slows bone regeneration in some cases (Buettmann et al., 2019). Another powerful, paracrine signal from macrophages to support angiogenesis is the pro-inflammatory cytokine IL-1 (Carmi et al., 2009). Furthermore, juxtacrine signals of macrophages for vascularization, such as accessory functions for anastomosis have been proposed, but remain largely elusive (Corliss et al., 2016).

1.5 Multiphoton Intravital Microscopy of the Bone

Multiphoton intravital imaging allows for the visualization of spatial organization and cellular dynamics in the tissue context of living organisms. The principle that a molecule can reach a higher energetic state by simultaneous absorption of two photons instead of one was initially predicted by Göppert-Mayer and is independent of the wavelength and photon flux, when the photon flux is high enough to allow for an optically non-linear process (Göppert-Mayer, 1931). With the invention of lasers, two-photon excitation has been experimentally demonstrated and later implemented to microscopy (2PM) of biological samples (Denk et al., 1990). Recently, three-photon excitation has been employed to generate microscopic images of the brain (Wang et al., 2018). Using wavelengths in the near infrared spectrum for fluorophore excitation allows deep sample imaging due to low scattering in this spectral range. Additionally, out-of-focus fluorescence is reduced, since the high photon flux density necessary for two-photon excitation is reached only within a small excitation volume around the focus of the objective lens. The sample is scanned in a raster pattern, while detection is performed using photomultiplier tubes. Sectioning in depth is limited by the resolution capacity of the microscope and depends not only on diffraction but also on sample scattering and wave front distortions, this is particularly relevant in tissue when *in vivo* imaging is performed. In bone and bone marrow, imaging depth using conventional 2-photon microscopy is limited to 150 μm in the bone (Io Celso et al., 2009). In recent years, the application of three-photon microscopy yielded improved imaging depths of up to 700 μm in the mouse brain including 100 – 150 μm of intact calvarium (Wang et al., 2018).

Multiphoton intravital microscopy of the bone is a challenging task due to the inaccessibility of the bone marrow tissue. In mice, intravital bone imaging has been established for the calvarial flat bone, subcutaneous ossicles metatarsal bones, femoral imaging through an external window, and the tibia through a thinned cortex¹. Amongst other limitations, none of the existing methods allows for the observation of regeneration in long bone fractures and all methods are limited to a total imaging depth of 150 μm . Therefore, the development of a method that enables deep bone imaging and the flexibility for microscopy of bone regeneration is needed.

2 Material and Methods

To avoid repetition and increase clarity of this summary, only the most relevant methods are listed here briefly. All additional material and methods such as FACS and bone sample preparation are described comprehensively in the selected publications.

2.1 Mice

All mice were female and kept under specific pathogen-free husbandry with water and food *ad libitum*. Transgenic mice were bred on C57/Bl6J background. CD19^{tdRFP} mice express tandem red fluorescent protein (tdRFP) after removal of the loxP-flanked STOP cassette by Cre-mediated recombination under a transgenic *cd19* promoter (Reismann et al., 2017). CX₃CR1^{GFP} were heterozygous mice expressing GFP under the endogenous *cx3cr1* locus (Reismann et al., 2017; Stefanowski et al., 2019). Wildtype mice were either C57/Bl6J or C57BL/6N (Reismann et al., 2017; Stefanowski et al., 2020, 2019). Cdh5^{GFP/tdTomato} mice express a membrane-tagged tandem tomato fluorescent protein (tdTomato) and histone 2B linked enhanced green fluorescent protein (GFP) under a transgenic VE-cadherin (*cdh5*) promoter (Stefanowski et al., 2020). Surgeries were performed at age of 10 – 14 weeks of age. All mice were bred in the animal facility of the DRFZ or Charité Universitätsklinikum and animal experiments were approved by Landesamt für Gesundheit und Soziales, Berlin, Germany, in accordance with institutional, state, and federal guidelines.

2.2 LIMB and Limbostomy System Implantation

LIMB is a microendoscopic method for longitudinal intravital imaging of the murine femoral bone marrow under homeostatic conditions. Limbostomy is a modular design of the LIMB system with a larger GRIN lens allowing for a larger FOV² that enables longitudinal intravital microendoscopy of murine osteotomies. Their main differences are listed in Table 2. In short, implantation under isoflurane was achieved by

¹ An overview of the existing intravital bone imaging techniques is listed in Reismann et al. (2017) and updated in Stefanowski et al. (2020) followed by a discussion of their advantages and limitations.

² The FOV of the two methods is compared in the Supp. Table 1 and Supp. Fig. 1 (Stefanowski et al., 2020).

Table 2: Functions of LIMB and Limbostomy.

Function	LIMB	Limbostomy
Reference	Reismann et al., 2017	Stefanowski et al., 2020
Field of view in lens diameter	~280 μm	~500 μm
Diameter of protrusion into bone/bone marrow	650 μm (interior metal ring)	600 μm (lens diameter)
Penetration depth	500 μm , 700 μm	Flexible, dependent on lens
Suitable for homeostasis?	Yes	Yes
Suitable for osteotomy?	No	Yes

removing the fur and cutting parallel to the right femur of the mouse. The LIMB system was inserted in a predrilled hole into the femur (Reismann et al., 2017) and the internal fixator plate (RISystem, Davos, Switzerland) was fixed using two bicortical screws. Using Limbostomy, the internal fixator plate was fixed using four screws and two cuts were made using a Gigli saw wire. The lens was inserted afterwards, and the wound sealed using an absorbable surgical thread (Reismann et al., 2017; Stefanowski et al., 2020). For lens protection and fixation, a reference plate was positioned on the tubing (Reismann et al., 2017; Stefanowski et al., 2020).

2.3 Longitudinal Intravital 2-Photon Microscopy

For intravital imaging (Reismann et al., 2017; Stefanowski et al., 2020, 2019), animals were anesthetized with isoflurane and positioned on a heating pad onto the intravital microscope table (LaVision BioTec GmbH, Bielefeld, Germany). Using a 20x objective lens (Olympus, Hamburg, Germany) the imaging plane was focused and recorded at specified settings in the InspectorPro software (LaVision BioTec GmbH, Bielefeld, Germany). Excitation of GFP was achieved using 940 – 980 nm, tdTomato with 980 nm, tdRFP at 1100 nm, and Qtracker 655 at 940 – 980 nm. Photomultiplier tubes were used to detect the emitted light in the ranges specified, respectively (Reismann et al., 2017; Stefanowski et al., 2020, 2019).

2.4 Immunofluorescence Histology

Sections of 7 μm were processed using blocking solution for 30 min, stained with respective antibodies for 1 – 2 h in staining solution and counterstained using DAPI at room temperature (Reismann et al., 2017;

Stefanowski et al., 2020, 2019). The microscopes used were a LSM710 (Carl Zeiss AG, Oberkochen, Germany) (Reismann et al., 2017), Biorevo (BZ-9000, Keyence GmbH, Neu Isenburg, Germany) (Reismann et al., 2017; Stefanowski et al., 2019), and LSM880 (Carl Zeiss AG, Oberkochen, Germany) (Stefanowski et al., 2020, 2019) with their respective software.

3 Results

This result section encompasses a description of the most relevant data from the selected publications, which is not a duplicate of the result sections in the publications. To allow an overarching discussion, individual paragraphs describe observations based on the data from multiple publications collectively.

3.1 Internal Fixation of a Microendoscope Is Suitable for Longitudinal Intravital Microscopy under Homeostatic Conditions

To visualize the spatial organization and longitudinal dynamics of the bone marrow of long bones, a longitudinal intravital multiphoton microendoscopy of the murine bone (LIMB) was developed. To access the deep bone marrow of a living animal for longitudinal multiphoton imaging, an internal fixator plate was combined with a customized gradient refractive index (GRIN) lens with a diameter of 350 μm (Fig. 1a, d) contained in an endoscope tubing, which protrudes 500 μm or 700 μm below the fixator plate (Fig. 1a, c) (Reismann et al., 2017)³. Stable fixation of the microendoscope system onto the murine femur was guaranteed by using two bicortical screws of four available screw threads (Fig. 1a, b). The combination of stable fixation and GRIN lens allowed deep bone marrow imaging of Qtracker 655 (here: Qdots) labeled vascular lumen down to 204 μm below the protruding lens surface (Fig. 1h) at weekly time points over the course of a month (Fig. 1i). The behavioral and immunological reaction of the animal to the implant was assessed during this period. All mice recovered within 14 days post-surgery based on clinical score (Fig. 2h), their overall motility (Fig. 2i), and gait (Supp. Movie 2⁴). In response to tissue damage, expression of the ECM marker laminin was increased at the site of injury (Fig. 3a, c), which coincided with accumulations of CD45⁺ cells (Fig. 3a, c) and an increase in Sca-1⁺ (Fig. 3a, c). The pan-leukocyte marker CD45 indicates immune cell accumulations and Sca-1 is a marker for mesenchymal stromal cells, immune cell subsets and endothelial cells. Some cells were round Sca-1⁺CD117(ckit)⁺ (Supp. Fig. 4a), others were elongated CD45⁺Sca-1⁺ (Supp. Fig. 4b), which indicates the possible presence of HSCs and endothelial progenitor cells, respectively. No immune cell accumulations were observed 28 days post-surgery (Fig. 3a-c). Similarly, HSPCs and differentiated hematopoietic cells of the bone marrow were

³ Data and figure references in this paragraph refer to Reismann et al. (2017).

⁴ Digital supporting information, such as movies are publicly available at the publishers' websites under the digital object identifiers of the selected publications.

unaltered in composition and absolute numbers between age-matched femora of control mice, the contralateral femur, and the LIMB-implanted bone (Fig. 3g; Supp. Fig. 5). Blood supply via periosteal vasculature (Fig. 3d) and the morphology of the main sinus (Fig. 3f) was not impaired and vessel morphology was comparable to contralateral femora (Fig. 7b) and unaffected endosteal areas (Fig. 7a) at 28 days post-surgery. Adoptively transferred CMTPIX-labeled (CellTracker, ThermoFisher, Frankfurt, Germany) splenocyte engraftment was unaffected in LIMB-implanted mice 28 days post-surgery (Fig. 3e). The only change in bone morphology was the gradual degradation of bone below the fixator plate as observed at 28 days post-surgery, possibly as a result of alterations of the force distribution within the bone due to the implanted fixator plate (Fig. 3a). A comparison between three bone marrow imaging techniques in the calvarium, the tibia, and the femur using LIMB in CD19^{tdRFP} mice showed no differences in velocity, volume, or displacement of tdRFP⁺ B lymphocytes (Fig. 4b-e). Positioning of the FOV was further shown to be stable over 36 h using ubiquitously expressing photoactivatable GFP (paGFP) mice (Fig. 5a).⁵

Taken together, bone marrow morphology and composition are comparable to homeostatic bone marrow one month after surgical implantation of the LIMB system. Consequently, LIMB allows visualization of the bone marrow cells in steady state, which is comparable to homeostasis.

3.2 Longitudinal Multiphoton Microendoscopy of the Bone Marrow Allows Visualization of Bone Regeneration after Osteotomy

The LIMB system has two major limitations: First, the FOV is limited by the GRIN lens' diameter of 350 μm , dictated by the inner diameter of the endoscope tubing, which cannot exceed the diameter of the bone marrow cavity. Second, the introduction of an osteotomy is spatially hindered by the protruding lens tubing inside the bone marrow. To improve FOV and suitability for an osteotomy model, a modular design was developed in which an endoscope-lens tubing of larger diameter was manufactured to be attachable via a tube thread to the plate (Fig. 1A) (Stefanowski et al., 2020)⁶. The protruding portion below the fixator plate is the GRIN lens, 600 μm in diameter; in total slightly smaller when compared to the lens tubing 650 μm in diameter of the LIMB system (Fig. 1B). This approach also allowed performance of an osteotomy (Fig. 3E-F) after fixation of the fixator plate (Fig. 3C-E) before the introduction of the lens tubing (Fig. 3G). The osteotomy gap size was therefore required to be larger than the lens diameter and was consistently 787 – 844 μm wide (Fig. 3J). Regeneration of the osteotomy results in vascularization and intramedullar callus formation (Fig. 3L). Using vascular label Qtracker 655, the blood stream was resolved at high resolution (Supp. Video 2) and using endothelial reporter mice (Cdh5^{GFP/tdTomato})

⁵ The observations in CD19^{tdRFP} and paGFP mice are discussed in Reismann et al. (2017).

⁶ Data and figure references in this paragraph refer to Stefanowski et al. (2020).

demonstrated longitudinal intravital multiphoton microendoscopy in murine osteotomies (Limbostomy) (Fig. 4A).

For the first time, Limbostomy enabled visualization of cellular dynamics during regeneration of osteotomies in mice. Furthermore, the FOV limitations of LIMB were overcome with Limbostomy due to its modular design and the possibility to use larger GRIN lenses.

3.3 The Vascular Network in the Bone Marrow Dynamically Reshapes during Homeostasis

Longitudinal intravital bone marrow microscopy in the femoral long bone using LIMB revealed continuous changes in the vessel structure one week after complete healing of the post-surgical tissue injuries (Fig. 6a-c) and the speed of those structural changes was negatively correlated with the diameter of blood vessels (Fig. 6d) (Reismann et al., 2017)⁷. Small vessels of 5 – 15 μm were more dynamic than intermediate (15 – 35 μm) and large (> 35 μm) vessels (Fig. 6d). Interestingly, vascular changes over a period of one week were also observed in the calvarial bone marrow (Fig. 6e).

This finding highlights that plasticity is an integral characteristic of the bone marrow vascular network and not restricted to regeneration.

3.4 Vascularization from Existing Vessels during Intramedullary Bone Regeneration Occurs in Two Distinct Phases in $\text{Cdh5}^{\text{GFP/tdTomato}}$ Mice

LIMB analysis of Qtracker 655 injected blood networks allows short term observation of the luminal blood before fluorescent labels are filtered from the bloodstream in the liver, taken up by phagocytic cells, or diffuse into the tissue. The latter especially occurred in the bone marrow via leaky sinusoids within 30 min under steady-state homeostasis (Supp. Video 2) (Stefanowski et al., 2020)⁸. To be able to identify endothelial cell number and their sprouting behavior, $\text{Cdh5}^{\text{GFP/tdTomato}}$ mice were used to study bone regeneration after osteotomy (Fig. 4A). Endothelial cells developed primarily from existing bone marrow vasculature as shown in histology using fluorophore labelled Emcn antibodies (Fig. 3L). Similarly, vessels grew in the x,y axis (Fig. 4A). The initial infiltration of the injury site by endothelial cells was observed intravitaly 3 – 4 days post-osteotomy (Fig. 4A, J) and was completed within 24 hours (Fig. 4A, J). In this time frame, endothelial sprouts with activated endothelial cell filopodia were observed (Supp. Video 4). These sprouts migrated into the osteotomy gap indicated by endothelial cell nuclei, which followed the direction of the sprouting tip (Supp. Video 4). After complete vascularization, endothelial cell density grew until day 5, changing the vascular network structure (Fig. 4A, I) without further increasing total vessel

⁷ Data and figure references in this paragraph refer to Reismann et al., (2017).

⁸ Data and figure references in this paragraph refer to Stefanowski et al., (2020), unless stated otherwise.

volume after day 4 (Fig. 4J). Soft callus formation was observed based on the presence of a second harmonic generation (SHG) signal, caused by collagen deposition on day 6 (Supp. Fig. 4C). Using three-dimensional segmentation of endothelial volume and endothelial cell nuclei based on tdTomato and GFP fluorescence signal, endothelial cell nuclei displacement, their migratory direction, and speed were determined, which showed no changes over 14 days of regeneration in the osteotomy gap (Fig. 4F-H). Surprisingly, although one cell division event was observed using LIMB (Supp. Video 3), no proliferation was detected within the observation time after osteotomy using Limbostomy.

In summary, two distinct phases of vascularization were observed. The first, initial infiltration of endothelial cells and active sprouting from existing endothelium into the damaged tissue was considered as the vascularization of the injury hematoma. The second, was the continuous adaptation of the vessel network within the intramedullary callus formation and remodeling phase.

3.5 Bone Marrow Endothelial Cells at Sites of Bone and Bone Marrow Regeneration Exhibit a Type H Immunophenotype

Bone and bone marrow tissue damage induced type H endothelium after drilling (Fig. 7a) (Reismann et al., 2017), introduction of an osteotomy with external fixation (Fig. 2B, C) (Stefanowski et al., 2019)⁹, internal fixation (Fig. 5A), and throughout the regeneration process (Fig. 2A-E). Using Limbostomy, intramedullary endothelial cell density was shown to be highest at 5 days post-osteotomy (Fig. 4I), coinciding with the highest number of *Osx*⁺ cells, which are considered late osteoprogenitor cells and osteoblasts (Fig. 1E). After drilling, based on pulse-chase experiments with the injected thymidine analogon 5-ethynyl-2'-deoxyuridine (EdU) no dividing endothelial cells were detected (Fig. 7b) (Reismann et al., 2017) and after osteotomy using Limbostomy, no cell division was observed.

Taken together, *Emcn*^{hi}*CD31*^{hi} endothelial cells that colocalized with *Osx*⁺ cells were found at sites of bone and bone marrow regeneration. Vascularization of type H endothelium, which functionally supports osteoblastic differentiation is an effective function of bone formation, also during bone regeneration. To support regeneration, the stimulation of vascularization emerges as a promising approach for pharmaceuticals that target bone regeneration.

3.6 Macrophages Localize towards the Type H Endothelium during Regeneration

Under homeostatic conditions, macrophages were evenly distributed throughout the bone marrow (Fig. 5C) (Stefanowski et al., 2019)¹⁰. After osteotomy, *F4/80*^{hi} macrophages accumulated intramedullary at the site of injury as early as day 2 post-injury (Fig. 4A, B) and were detected in increasing abundance

⁹ Data and figure references in this paragraph refer to Stefanowski et al. (2019), unless stated otherwise.

¹⁰ Data and figure references in this paragraph refer to Stefanowski et al. (2019).

extramedullary, periosteal from day 3 (Fig. 3A, B). F4/80⁺ macrophages remained present throughout the regeneration process (Fig. 3A, B) and decreased in abundance from day 7 (Fig. 3C). Throughout regeneration, all nuclei in the osteotomy gap localized close to type H endothelium (Emcn^{hi}) when compared to type L endothelium (Emcn^{lo}) (Fig. 3F) and F4/80⁺ cell number around type H endothelium decreased between day 3 and day 21 post-injury (Fig. 3E). Due to the spatial correlation of F4/80⁺ cells and Emcn^{hi} endothelium, the macrophage population at the osteotomy site was further characterized.

3.7 VEGF is Provided by CD80⁺ Cells in the Early Phase of Healing

During regeneration CD206⁺ M2-like macrophages resided primarily extramedullary throughout the regeneration process (Fig. 3A, B) and CD80⁺ M1-like macrophages were detected during the first two days of regeneration (Fig. 4A, B). Some CD80⁺ cells were F4/80⁺ (Fig. 4A) and some CD80⁺ cells produced VEGF (Fig. 4C). Macrophages accumulated intra- and extramedullary after injury, but only few were either CD206⁺ or CD80⁺, of which even less produced VEGF. This result might indicate a contribution of CD80⁺ cells to vascularization by VEGF production in the pro-inflammatory phase of the first 2-3 days and subsequent VEGF production performed by osteogenic cells (Fig. 4D). CD206⁺ macrophages were present primarily extramedullary in all phases of regeneration with no clear association to vascularization.

In summary, macrophages appear to contribute to vascularization via VEGF in the first two days of regeneration via CD80⁺ cells.

3.8 CX₃CR1⁺ F4/80⁺ Macrophages Are the Major Subset of Cells in the Osteotomy Gap and Precede Vascularization

Using CX₃CR1 reporter mice, immunofluorescence histology demonstrated the major subset in the osteotomy gap to be F4/80⁺Gr1⁻CX₃CR1⁺ within the first 2 weeks post-injury (Fig. 5F, G) (Stefanowski et al., 2019)¹¹. These cells densely accumulated at areas of bone formation (Fig. 5C) and CD31⁺ endothelial cells (Fig. 5D). Using Limbostomy, CX₃CR1⁺ cells were observed to infiltrate the osteotomy gap between 2 to 3 days post-injury, followed by perfused blood vasculature between day 3 and 4 post-injury. CX₃CR1⁺ cells populated the space between blood vessels and were divided into round and non-round cells (Fig. 5G). CX₃CR1⁺ cells in the osteotomy gap were primarily F4/80⁺ and the major subset of cells in the osteotomy gap were F4/80⁺Gr1⁻CX₃CR1⁺. The intravital observation that CX₃CR1⁺ cells preceded vascularization might indicate that CX₃CR1⁺ cells contribute to the first phase of vascularization.

¹¹ Data and figure references in this paragraph refer to Stefanowski et al. (2019).

4 Discussion

This section aims to provide an overarching discussion beyond the individual discussions of the selected publications. To extend the discussion, relevant parts of those discussions in the selected publications are referenced in footnotes for further reading.

4.1 Applications of LIMB and Limbostomy

Longitudinal intravital multiphoton microscopy has been established for numerous organs in the mouse including the central nervous system, retina, lymph nodes, brain, and calvarium (Reismann et al., 2017)¹². In the bone marrow, intravital multiphoton microscopy contributed to a better understanding of bone marrow niches for HSPCs in health and disease (Hawkins et al., 2016; Itkin et al., 2016) and the regulation of bone mass (Nevius et al., 2015). However, longitudinal observations over months in the bone marrow of long bones were not achieved¹³. Using the LIMB system, deep bone marrow imaging under steady-state homeostatic conditions revealed plasticity of the bone marrow vasculature (Reismann et al., 2017). LIMB and Limbostomy can be applied to further improve our understanding of niche plasticity of HSPCs and their progeny, the release of cells into the bloodstream, the differentiation of MSCs and hematopoiesis, and the impact of cells such as adipocytes in bone marrow niches. Using depths of 100 μm or 500 μm (Reismann et al., 2017) or a flexible depth of up to 700 μm (Stefanowski et al., 2020) allows investigation and better understanding of the heterogeneity of the bone marrow or the regenerating bone. The FOV of LIMB is big enough to visualize small cell subsets such as plasma cells (Reismann et al., 2017).

The large diameter of 600 μm of the GRIN lens using Limbostomy can be used to analyze rare subsets such as HSCs in their niche or differentiation events. Our data show changes in the vessel network of the bone marrow but it is unclear whether the microenvironments, the niches are also impacted and unstable with respect to cellular composition and localization. Very recently, Upadhaya et al. described HSC to be motile in both steady state and mobilization (Upadhaya et al., 2020), which indicates the niche environment to be less stable than previously known. Furthermore, to allow the tracking of cells such as motile HSCs, a large FOV is necessary. Similarly, long-lived plasma cells in the bone marrow, which are also considered to be sessile in their niches can be analyzed for motility patterns or for testing pharmaceuticals for their mobilization. A larger FOV using thicker stacks during image acquisition could be achieved by selecting a GRIN lens for 3-photon microscopy wavelengths.

¹² This publication contains further references for the examples mentioned.

¹³ An overview of the existing intravital bone imaging techniques is listed in Reismann et al. (2017) and updated in Stefanowski et al. (2020) followed by a short discussion of their advantages and limitations.

Models for murine bone regeneration such as drill hole injury or osteotomy can be combined with Limbostomy. While drill hole injury favors intramembranous ossification, endochondral ossification occurs in a full osteotomy. Since the two regeneration processes are functionally distinct (Buettmann et al., 2019), different observations such as osteogenic differentiation of MSCs could be compared using this standardized method.

The Limbostomy method greatly improved the FOV, image quality, and range of application compared to LIMB. However, the FOV is limited due to stable fixation of the implant. To allow visualization of trabecular bone an adaptation of the fixator plate is necessary. Furthermore, the internal fixator plate influenced bone remodeling due to a change in force distribution, although changes in bone marrow composition was not observed. Currently, no comparable, less invasive method is available that enables a comparison with Limbostomy to measure the impact of the implantation itself on bone homeostasis. A strong advantage of the LIMB and Limbostomy method is the longitudinal measurement at subcellular resolution. Progress of bone regeneration is strongly dependent on the individual organism and longitudinal data allow conclusion within, and not only between individuals. This contributes to refined data density, reduced usage of animals, and replacement of other techniques by intravital microscopy to actively implement the 3R principle and improve animal welfare.¹⁴

4.2 The Impact of Vessel Plasticity on the Bone Marrow Microenvironment during Homeostasis

A key finding of longitudinal intravital bone marrow microscopy is that the intramedullary vascular network undergoes change under homeostatic conditions. The impact on vascular remodeling might derive from the introduction of the internal fixator plate, which changes force distribution in the femur. However, due to the impressive velocity of changes within hours and days, it seems more likely to be dependent on proliferation, bone marrow cell motility, and blood pressure. EdU pulse-chase experiments in contralateral and implanted femora showed that bone marrow endothelial cells, especially type L sinusoids have limited proliferative capacity (Fig. 7b) (Reismann et al., 2017), supported by previous findings (Kusumbe et al., 2014). This indicates that under homeostatic conditions, vessel plasticity is not a consequence of endothelial cell proliferation. It can be assumed that the constant proliferation and release of hematopoietic cells, such as erythrocytes, monocytes, neutrophils, and naive B cells from the bone marrow, strongly impacts the volume balance of the bone marrow. Based on the observation that the release of HSC into the bloodstream and their homing to the bone marrow is regulated by cell adhesion molecules such as selectins, cell adhesion molecules and the stromal cell-derived factor 1 (CXCL12) (Méndez-Ferrer et al., 2008; Scheiermann et al., 2013) one can assume that the volume balance

¹⁴ A comparison of the two methods is included in the discussion of Stefanowski et al. (2020).

is subject to various phases because release and homing are controlled by cell and tissue-specific circadian rhythms and inflammation (Scheiermann et al., 2013). Changes in the volume balance due to cell trafficking requires the adaption of the endothelial network via expansion and contraction, while blood acts as a buffer volume. These changes in vasculature might add up to strong spatial shifts within the bone marrow requiring a high tissue flexibility and elasticity. Considering this highly dynamic context, it can be hypothesized that volume adaptability and vessel plasticity are necessary features of the bone marrow tissue to cope with volume changes due to cell proliferation, release, homing, and rapid release in the case of inflammation.

It can be observed that not all vessel types are subject to the same rate of change. The notion that small vessels of 5 – 15 μm , possibly arteriolar endothelial cells (Bixel et al., 2017; Itkin et al., 2016) undergo more rapid and obvious changes than larger vessels, allows the assumption that arteries are less adaptable to volumetric changes and are stiffer than sinusoids. In support of this, intercellular endothelial junctions of arteries, type H vasculature, and arterioles strongly express CD31 and Sca-1⁺ arteries further maintain αSMA^+ pericytes which add additional stability. On the other hand, type L endothelial sinusoids have only loose cell-cell-contacts and allow unhindered paracellular migration in combination with reduced blood flow velocity. In fact, Itkin et al. demonstrated that sinusoids, which express lower levels of adhesion molecules such as the vascular cell adhesion molecule 1 (VCAM-1), the intracellular adhesion molecule 1 (ICAM-1), P-selectin or the junctional adhesion molecule-A (JAM-A) compared to arterial bone marrow endothelial cells, are the exclusive site for cellular trafficking (Itkin et al., 2016).

Additionally, they showed that a low reactive oxygen species (ROS) state is maintained in the arterial bone marrow endothelial cell niche due to the reduced permeability, which consequently supports HSPC survival (Itkin et al., 2016). Of note, local oxygen availability (pO_2) in the bone marrow is considered hypoxic at $\text{pO}_2 < 32$ mmHg (Spencer et al., 2014). Peri-sinusoidal pO_2 in deep bone marrow is lowest and endothelial regions which contain arterioles are less hypoxic (Spencer et al., 2014). Assuming that continuous remodeling and adaption of the vascular bone marrow network influences cellular ROS and consequently hematopoietic niches, the question arises: Which cells are responsible for maintaining overall integrity of the bone marrow structure?

One candidate are MSCs, a cell population of heterogeneous functions which is evenly distributed throughout the bone marrow (Holzwarth et al., 2018). They are characterized by cell adhesion molecules such as VCAM-1 and maintain niche functions by the secretion of e.g. CXCL12 (Holzwarth et al., 2018). The dendrite-like cell phenotype creates a network-like structure and therefore, these MSCs might provide a cellular scaffold for other bone marrow cells to adhere to and additionally receive niche factors for differentiation and survival.

Macrophages of F4/80^{hi} and CD169⁺VCAM-1⁺ phenotype are another cellular subset that fulfills these requirements. To which extent macrophages contribute to the bone marrow architecture depends on their network stability. It is unclear if this network is stable over time, which can be answered by longitudinal intravital microscopy of the bone marrow in combination with macrophage reporter mice such as F4/80^{Cre}Rosa26^{stopfloxedTomato} reporter mice. Whether a bone marrow macrophage network exists permanently or is replaced continuously by the MPS is not known. Tracing the replacement rate of F4/80^{hi} macrophages in the network over time could be addressed by adoptively transferring fluorescent progenitors. Candidates are cMoPs or monocyte subsets such as CX₃CR1^{hi}Ly6C^{lo} or CX₃CR1^{lo}Ly6C^{hi}.

In summary, vascular plasticity discovered by LIMB is an important and previously unknown function to consider in the context of maintenance and stability in the bone marrow microenvironment.

4.3 Vascularization and Endothelial Proliferation after Injury

Bone marrow vasculature undergoes extensive remodeling after injury such as irradiation (Le et al., 2017), during cancer (Hawkins et al., 2016) and bone growth (Ramasamy et al., 2016). The underlying mechanisms are not fully understood. During bone growth, osteoblast function is linked to type H endothelium (Kusumbe et al., 2014). Type H endothelium has been described to promote osteoblast differentiation via growth factors such as TGF β , PDGF and the release of Noggin upon neurogenic locus notch homolog protein (Notch) signaling (Ramasamy et al., 2015, 2014). *Vice versa*, osteoblast progenitors provide signals for vascularization such as VEGF (Ramasamy et al., 2015). Here, spatial proximity was observed between Osx⁺¹⁵ osteoblasts and type H endothelium during regeneration (Stefanowski et al., 2019). A potential stimulus for neovascularization in the hypoxic environment of the damaged tissue is VEGFA release upon HIF1 α activation. In this context, Buettmann et al. showed that bone regeneration was delayed when VEGFA was deleted from Osx⁺ cells only in full osteotomies, but not drill hole injuries (Buettmann et al., 2019). This indicates that another cell type besides osteoblasts and chondrocytes is responsible for VEGFA expression in full osteotomies. Considering that drill hole injuries are relatively small injuries that do not require extensive callus formation, it is sometimes referred to as an injury model for intramembranous regeneration. Full osteotomies and fractures, however, represent the process of endochondral regeneration that requires cartilage formation. One could hypothesize that extensive bone injuries initiating endochondral regeneration require an additional source of VEGF. The data of this study indicate that macrophages or mononuclear phagocytes could potentially be this source during the crucial, initial regeneration phase (Stefanowski et al., 2019).

¹⁵ The differentiation and origin of mesenchymal-derived bone cells is discussed in Stefanowski et al. (2019).

During vascularization of full osteotomies, endothelial growth started from the existing vascular network and activated endothelial cells with filopodia were observed (Stefanowski et al., 2020). Vascularization occurred in two waves, a first wave that vascularized the fracture hematoma and a second wave that remodeled the existing network (Stefanowski et al., 2020). Although a high degree of remodeling occurred and continues throughout homeostasis, only one endothelial cell division event was documented (Stefanowski et al., 2020). Similarly, proliferating endothelial cells were not found using histological methods (Reismann et al., 2017). This indicates that endothelial cell division is a rare event. Considering that endothelial cell divisions occur primarily in type H endothelium (Kusumbe et al., 2014) and that the endothelium during regeneration is in fact type H endothelium suggests that proliferation occurs outside of the imaging window using Limbostomy (Stefanowski et al., 2020). Alternatively, one can assume that cell proliferation was simply not captured and to effectively quantify endothelial proliferation, longer time windows should be analyzed (Stefanowski et al., 2020). If sprouting is studied, endothelial cells are divided into proliferating stalk cells and activated tip cells with filopodia (Geudens and Gerhardt, 2011). Although this two-dimensional categorization is not apparent in bone regeneration visualized by Limbostomy, it allows the assumption that growing vasculature can compartmentalize functionally. In combination with the observation that vascularization of the osteotomy gap is rapid (Stefanowski et al., 2020), it seems reasonable to conclude that proliferation of endothelial cells occurs in an environment that stimulates its proliferation before the vascular network expands into the fracture hematoma. Taken into account that endothelial HIF1 α strongly regulates type H endothelial cell expansion, this environment has to be hypoxic for a period long enough to stimulate cell expansion (Kusumbe et al., 2014).

4.4 The Role of CX₃CR1^{hi}Gr1^{lo} Mononuclear Phagocytes

Monocytes, macrophages, and other myeloid cells impact vascularization in a range of physiological and pathological conditions. Their mobilization orchestrates neovascularization after irradiation (Loinard et al., 2017) and it was shown that not only osteoclasts (Romeo et al., 2019) but their progenitors have the capacity to stimulate vascularization and subsequent osteogenesis (Kusumbe and Adams, 2014). In turn, endothelial cells can regulate the conversion of classical Ly6C^{hi} monocytes into Ly6C^{lo} monocytes via monocyte Notch2-signaling (Gamrekelashvili et al., 2016). This suggests that the endothelial-myeloid interaction is important for differentiation and survival.

The data of Clark et al. suggest that an anti-inflammatory polarization bias of macrophages determines healing outcome but not the mere presence of macrophages at the injury site. Clark et al. conclude that inhibition of M-CSF1R inhibits all monocyte recruitment and prevents monocyte-derived macrophage differentiation, but the role of non-classical CX₃CR1^{hi}Ly6C^{lo} monocytes is not considered in their study

(Clark et al., 2020). In this study it is shown that macrophages of the intramedullary callus are primarily F4/80⁺Gr1⁻(Ly6C)CX₃CR1⁺ (Stefanowski et al., 2019). These cells exhibit an immunophenotype resembling non-classical monocytes. Furthermore, the lifetime of CX₃CR1^{hi}Ly6C^{lo} mononuclear phagocytes is estimated to be 5 days (Geissmann et al., 2003; Ginhoux and Jung, 2014) and depends on survival factors beyond CSF1R, including Nur77 and CX₃CR1 (Ginhoux and Jung, 2014). In the study of Clark et al. treatment for monocyte depletion via CSF1R has only started 24 h before the injury (Clark et al., 2020) and thus indicates that only the availability of classical monocytes with a half-life of 20 h but not that of non-classical mononuclear phagocytes has been blocked. In further support of this idea, *cx3cr1* and *il-10* were amongst the lower 2 % of downregulated genes in macrophages from old mice when compared to young mice 3 days post-injury and after treatment (Clark et al., 2020). Additionally, CX₃CR1^{hi}Ly6C^{lo} mononuclear phagocytes are biased precursors for M2-like macrophages which support vascularization during regeneration (Olingy et al., 2017). Whether macrophages of an F4/80⁺Gr1⁻(Ly6C)CX₃CR1⁺ immunophenotype are the descendants of non-classical monocytes, tissue resident macrophages, osteal macrophages (osteomacs) or an intermediate precursor from the bone marrow, requires further research. To assess the contribution of CX₃CR1^{hi} monocytes, the usage of Nur77^{GFP} reporter mice could be a promising option to improve the distinction between CX₃CR1^{hi} non-classical and CX₃CR1^{lo} classical monocytes and their progeny.

Furthermore, Gamrekelashvili et al. described endothelial cells to trigger differentiation of classical monocytes into CX₃CR1^{hi}Ly6C^{lo} mononuclear phagocytes under steady-state conditions (Gamrekelashvili et al., 2016). This process could be exaggerated during inflammation and provide a potential signaling pathway via Dll1/Notch2 during endothelial cell activation and type H vessel growth.

The question how mononuclear phagocytes contribute to vascularization remains unanswered. The role of macrophages during tip cell fusion (anastomosis) is not understood (Geudens and Gerhardt, 2011) but there is evidence that macrophages can act as helper cells (accessory cells) during the function of newly formed vasculature (Gurevich et al., 2018). In this study, CX₃CR1⁺ cells were shown to precede vascularization and closely attach to endothelial cells (Stefanowski et al., 2019). CX₃CR1^{hi}Ly6C^{lo} mononuclear phagocytes are a promising candidate for accessory functions during anastomosis for multiple reasons: First, CX₃CR1^{hi}Ly6C^{lo} mononuclear phagocytes are of generally anti-inflammatory phenotype and are known for IL-10 production in tissues such as the small intestine (Morhardt et al., 2019). Second, they monitor the vasculature and control their disposal (Auffray et al., 2009; Carlin et al., 2013). Third, endothelial cells highly express the CX₃CL1 for adhesion (Bazan et al., 1997; Pan et al., 1997) and fourth, Gurevich et al. described macrophages of anti-inflammatory phenotype to be relevant for anastomosis in the zebrafish (Gurevich et al. 2018). If CX₃CR1⁺ cells also promote anastomosis, could be

analyzed by crossing endothelial cell reporter mice with CX₃CR1 reporter mice. This approach could be combined using CX₃CR1 conditional deletion of factors such as VEGFA to assess their effect on growth.

Apart from directly influencing vascularization CX₃CR1⁺ cells have been shown to be capable of forming vessel-like channels (Barnett et al., 2016). Considering this so-called vessel mimicry, CX₃CR1⁺ cells might have the potential to actively incorporate into the vascular network or drain the surrounding tissue.

It remains unclear to which extent macrophages of M1- or M2-like phenotype contribute to vascularization or regeneration since both macrophage-derived pro- and anti-inflammatory factors such as IL-1 and IL-10, respectively, can contribute to improved wound healing. Sequencing of macrophages, present in the fracture gap, will be helpful to understand their function in detail. Overall, the results of this study support the idea that anti-inflammatory CX₃CR1^{hi} myeloid cells support vascularization throughout the bone regeneration process. The pro-inflammatory milieu switches to an anti-inflammatory milieu as early as one day after injury, marked by a high expression of IL-10 (Schmidt-Bleek et al., 2014b). In the presence of young macrophages, *cx3cr1* and *il-10* are highly upregulated during bone regeneration (Clark et al., 2020). Furthermore, a recent study has shown that IL-10 strongly enhances neovascularization and endothelial progenitor recruitment (Balaji et al., 2020). It could be hypothesized that CX₃CR1^{hi}-derived IL-10 contributes to a general shift from a pro- to an anti-inflammatory milieu.

Various types of osteoclasts promote vascularization and osteogenesis (Kusumbe and Adams, 2014). In the growing bone, osteoclasts develop during embryogenesis (Jacome-Galarza et al., 2019) but during regeneration their origin is elusive. Osteoclasts are a major contributor for bone remodeling, and we have identified some CD80⁺ macrophages in the first two days of regeneration. Considering that osteoclast progenitor cells have been described to express CD80¹⁶ might suggest that some macrophages commit to osteoclastogenesis early in regeneration. These few cells might be sufficient for providing enough progenitors as osteoclasts are long-lived and fuse with circulating monocytes (Jacome-Galarza et al., 2019).

The origin and fate of CX₃CR1^{hi}Ly6C^{lo} mononuclear phagocytes in the osteotomy gap is not known. A possible mechanism could be the same as under homeostatic conditions in which classical monocytes differentiate into CX₃CR1^{hi}Ly6C^{lo} non-classical monocytes. They could also originate from tissue-resident macrophages in the bone marrow. However, it should be first clarified where tissue-resident macrophages themselves derive from. To address their origin, fate map experiments by marking macrophages using tamoxifen-inducible Cre-expression models specific for EMPs (c-Myb) or HSCs (Runx1) are feasible (Ginhoux and Guilliams, 2016). If macrophages which permanently reside in the bone marrow

¹⁶ The role of M1/M2-like macrophages and their markers is discussed in Stefanowski et al. (2019).

self-renew from embryo-derived macrophages (including both yolk-sac and fetal liver), they would be of c-Myb⁺ progeny. If they renew from HSCs (and cMoPs) they would be of Runx1⁺ (or CD135⁺) progeny (Ginhoux and Guilliams, 2016). However, it should be mentioned that the specific spatiotemporal embryonic expression of those markers in macrophage progenitors is still subject to an ongoing debate.

To clarify the fate of CX₃CR1^{hi}Ly6C^{lo} cells in the course of regeneration, a combination of a CX₃CR1 tamoxifen-inducible Cre (CX₃CR1^{CreER}) with a fate indicating universally expressing ROSA26^{mT/mG} mouse that permanently changes fluorescence from red (mT; membrane Tomato) to green (mG; membrane GFP) upon Cre-expression could be used. Tamoxifen induction before, during, or after injury will show osteoclasts in both colors as they fuse with CX₃CR1-expressing myeloid cells.

In summary, this work presents an intravital imaging approach for longitudinal observations suitable to shed light on questions of bone and bone marrow dynamics under homeostatic and pathological conditions. Using LIMB and Limbostomy, previously unknown vessel plasticity of the bone marrow vasculature and a potential role of phagocytes in vascularization during bone regeneration was revealed. This highlights the great potential of this method to improve our understanding of the dynamics in bone homeostasis and diseases, which will contribute to the development of specific treatment approaches in the future.

5 References

- Alexander, K.A., Chang, M.K., Maylin, E.R., Kohler, T., Müller, R., Wu, A.C., van Rooijen, N., Sweet, M.J., Hume, D.A., Raggatt, L.J., Pettit, A.R., 2011. Osteal macrophages promote in vivo intramembranous bone healing in a mouse tibial injury model. *Journal of Bone and Mineral Research* 26, 1517–1532. <https://doi.org/10.1002/jbmr.354>
- Al-Sebaei, M.O., Dauks, D.M., Belkina, A.C., Kakar, S., Wigner, N.A., Cusher, D., Graves, D., Einhorn, T., Morgan, E., Gerstenfeld, L.C., 2014. Role of Fas and Treg Cells in Fracture Healing as Characterized in the Fas-Deficient (lpr) Mouse Model of Lupus. *Journal of Bone and Mineral Research* 29, 1478–1491. <https://doi.org/10.1002/jbmr.2169>
- Auffray, C., Fogg, D., Garfa, M., Elain, G., Join-Lambert, O., Kayal, S., Sarnacki, S., Cumano, A., Lauvau, G., Geissmann, F., 2007. Monitoring of Blood Vessels and Tissues by a Population of Monocytes with Patrolling Behavior. *Science* 317, 666–670. <https://doi.org/10.1126/science.1142883>
- Auffray, C., Sieweke, M.H., Geissmann, F., 2009. Blood Monocytes: Development, Heterogeneity, and Relationship with Dendritic Cells. *Annual Review of Immunology* 27, 669–692. <https://doi.org/10.1146/annurev.immunol.021908.132557>
- Avraham-Davidi, I., Yona, S., Grunewald, M., Landsman, L., Cochain, C., Silvestre, J.S., Mizrahi, H., Faroja, M., Strauss-Ayali, D., Mack, M., Jung, S., Keshet, E., 2013. On-site education of VEGF-recruited monocytes improves their performance as angiogenic and arteriogenic accessory cells. *The Journal of Experimental Medicine* 210, 2611–2625. <https://doi.org/10.1084/jem.20120690>
- Balaji, S., Steen, E., Wang, X., Vangapandu, H. v., Templeman, N., Blum, A.J., Moles, C.M., Li, H., Narmoneva, D.A., Crombleholme, T.M., Butte, M.J., Bollyky, P.L., Keswani, S.G., 2020. IL-10 promotes endothelial progenitor cell driven wound neovascularization and enhances healing via STAT3. *bioRxiv*. <https://doi.org/doi.org/10.1101/760165>
- Barnett, F.H., Rosenfeld, M., Wood, M., Kiosses, W.B., Usui, Y., Marchetti, V., Aguilar, E., Friedlander, M., 2016. Macrophages form functional vascular mimicry channels in vivo. *Scientific Reports* 6, 36659. <https://doi.org/10.1038/srep36659>
- Barretto, R.P.J., Ko, T.H., Jung, J.C., Wang, T.J., Capps, G., Waters, A.C., Ziv, Y., Attardo, A., Recht, L., Schnitzer, M.J., 2011. Time-lapse imaging of disease progression in deep brain areas using fluorescence microendoscopy. *Nature Medicine* 17, 223–228. <https://doi.org/10.1038/nm.2292>
- Bazan, J.F., Bacon, K.B., Hardiman, G., Wang, W., Soo, K., Rossi, D., Greaves, D.R., Zlotnik, A., Schall, T.J., 1997. A new class of membrane-bound chemokine with a CX3C motif. *Nature* 385, 640–644. <https://doi.org/10.1038/385640a0>

- Bigueti, C.C., Vieira, A.E., Cavalla, F., Fonseca, A.C., Colavite, P.M., Silva, R.M., Trombone, A.P.F., Garlet, G.P., 2018. CCR2 Contributes to F4/80+ Cells Migration Along Intramembranous Bone Healing in Maxilla, but Its Deficiency Does Not Critically Affect the Healing Outcome. *Frontiers in Immunology* 9, 1–15. <https://doi.org/10.3389/fimmu.2018.01804>
- Birbrair, A., Frenette, P.S., 2016. Niche heterogeneity in the bone marrow. *Annals of the New York Academy of Sciences* 1370, 82–96. <https://doi.org/10.1111/nyas.13016>
- Bixel, M.G., Kusumbe, A.P., Ramasamy, S.K., Sivaraj, K.K., Butz, S., Vestweber, D., Adams, Ralf.H., 2017. Flow Dynamics and HSPC Homing in Bone Marrow Microvessels. *Cell Reports* 18, 1804–1816. <https://doi.org/10.1016/j.celrep.2017.01.042>
- Buettmann, E.G., McKenzie, J.A., Migotsky, N., Sykes, D.A.W., Hu, P., Yoneda, S., Silva, M.J., 2019. VEGFA From Early Osteoblast Lineage Cells (Osterix+) Is Required in Mice for Fracture Healing. *Journal of Bone and Mineral Research* 34, 1690–1706. <https://doi.org/10.1002/jbmr.3755>
- Buscher, K., Marcovecchio, P., Hedrick, C.C., Ley, K., 2017. Patrolling Mechanics of Non-Classical Monocytes in Vascular Inflammation. *Frontiers in Cardiovascular Medicine* 4, 1–10. <https://doi.org/10.3389/fcvm.2017.00080>
- Carlin, L.M., Stamatziades, E.G., Auffray, C., Hanna, R.N., Glover, L., Vizcay-Barrena, G., Hedrick, C.C., Cook, H.T., Diebold, S., Geissmann, F., 2013. Nr4a1-Dependent Ly6Clow Monocytes Monitor Endothelial Cells and Orchestrate Their Disposal. *Cell* 153, 362–375. <https://doi.org/10.1016/j.cell.2013.03.010>
- Carmi, Y., Voronov, E., Dotan, S., Lahat, N., Rahat, M.A., Fogel, M., Huszar, M., White, M.R., Dinarello, C.A., Apte, R.N., 2009. The Role of Macrophage-Derived IL-1 in Induction and Maintenance of Angiogenesis. *The Journal of Immunology* 183, 4705–4714. <https://doi.org/10.4049/jimmunol.0901511>
- Chang, M.K., Raggatt, L.-J., Alexander, K.A., Kuliwaba, J.S., Fazzalari, N.L., Schroder, K., Maylin, E.R., Ripoll, V.M., Hume, D.A., Pettit, A.R., 2008. Osteal Tissue Macrophages Are Intercalated throughout Human and Mouse Bone Lining Tissues and Regulate Osteoblast Function In Vitro and In Vivo. *The Journal of Immunology* 181, 1232–1244. <https://doi.org/10.4049/jimmunol.181.2.1232>
- Chow, A., Huggins, M., Ahmed, J., Hashimoto, D., Lucas, D., Kunisaki, Y., Pinho, S., Leboeuf, M., Noizat, C., van Rooijen, N., Tanaka, M., Zhao, Z.J., Bergman, A., Merad, M., Frenette, P.S., 2013. CD169+ macrophages provide a niche promoting erythropoiesis under homeostasis and stress. *Nature Medicine* 19, 429–436. <https://doi.org/10.1038/nm.3057>
- Chow, A., Lucas, D., Hidalgo, A., Méndez-Ferrer, S., Hashimoto, D., Scheiermann, C., Battista, M., Leboeuf, M., Prophete, C., van Rooijen, N., Tanaka, M., Merad, M., Frenette, P.S., 2011. Bone marrow CD169+ macrophages promote the retention of hematopoietic stem and progenitor cells in the mesenchymal stem cell niche. *The Journal of Experimental Medicine* 208, 261–271. <https://doi.org/10.1084/jem.20101688>
- Clark, D., Brazina, S., Yang, F., Hu, D., Hsieh, C.L., Niemi, E.C., Miclau, T., Nakamura, M.C., Marcucio, R., 2020. Age-related changes to macrophages are detrimental to fracture healing in mice. *Aging Cell* 19, 1–12. <https://doi.org/10.1111/ace1.13112>
- Corliss, B.A., Azimi, M.S., Munson, J.M., Peirce, S.M., Murfee, W.L., 2016. Macrophages: An Inflammatory Link Between Angiogenesis and Lymphangiogenesis. *Microcirculation* 23, 95–121. <https://doi.org/10.1111/micc.12259>
- Coşkun, S., Chao, H., Vasavada, H., Heydari, K., Gonzales, N., Zhou, X., de Crombrugge, B., Hirschi, K.K., 2014. Development of the Fetal Bone Marrow Niche and Regulation of HSC Quiescence and Homing Ability by Emerging Osteolineage Cells. *Cell Reports* 9, 581–590. <https://doi.org/10.1016/j.celrep.2014.09.013>
- Denk, W., Strickler, J., Webb, W., 1990. Two-photon laser scanning fluorescence microscopy. *Science* 248, 73–76. <https://doi.org/10.1126/science.2321027>
- Einhorn, T.A., Gerstenfeld, L.C., 2015. Fracture healing: mechanisms and interventions. *Nature Reviews Rheumatology* 11, 45–54. <https://doi.org/10.1038/nrrheum.2014.164>
- Elshabrawy, H.A., Chen, Z., Volin, M. v, Ravella, S., Virupannavar, S., Shahrara, S., 2015. The pathogenic role of angiogenesis in rheumatoid arthritis. *Angiogenesis* 18, 433–448. <https://doi.org/10.1007/s10456-015-9477-2>
- Evrard, M., Chong, S.Z., Devi, S., Chew, W.K., Lee, B., Poidinger, M., Ginhoux, F., Tan, S.M., Ng, L.G., 2015. Visualization of bone marrow monocyte mobilization using Cx3cr1 gfp/+ Flt3L -/- reporter mouse by multiphoton intravital microscopy. *Journal of Leukocyte Biology* 97, 611–619. <https://doi.org/10.1189/jlb.1TA0514-274R>
- Fantin, A., Vieira, J.M., Gestri, G., Denti, L., Schwarz, Q., Prykhozhiy, S., Peri, F., Wilson, S.W., Ruhrberg, C., 2010. Tissue macrophages act as cellular chaperones for vascular anastomosis downstream of VEGF-mediated endothelial tip cell induction. *Blood* 116, 829–840. <https://doi.org/10.1182/blood-2009-12-257832>
- Gamrekeshvili, J., Giagnorio, R., Jussofie, J., Soehnlein, O., Duchene, J., Briseño, C.G., Ramasamy, S.K., Krishnasamy, K., Limbourg, A., Häger, C., Kapanadze, T., Ishifune, C., Hinkel, R., Radtke, F., Strobl, L.J., Zimmer-Strobl, U., Napp, L.C., Bauersachs, J., Haller, H., Yasutomo, K., Kupatt, C., Murphy, K.M., Adams, R.H., Weber, C., Limbourg, F.P., 2016. Regulation of monocyte cell fate by blood vessels mediated by Notch signalling. *Nature Communications* 7, 12597. <https://doi.org/10.1038/ncomms12597>
- Geissmann, F., Jung, S., Littman, D.R., 2003. Blood Monocytes Consist of Two Principal Subsets with Distinct Migratory Properties. *Immunity* 19, 71–82. [https://doi.org/10.1016/S1074-7613\(03\)00174-2](https://doi.org/10.1016/S1074-7613(03)00174-2)

- Gerri, C., Marín-Juez, R., Marass, M., Marks, A., Maischein, H.-M., Stainier, D.Y.R., 2017. Hif-1 α regulates macrophage-endothelial interactions during blood vessel development in zebrafish. *Nature Communications* 8, 15492. <https://doi.org/10.1038/ncomms15492>
- Gerstenfeld, L.C., Cho, T.J., Kon, T., Aizawa, T., Tsay, A., Fitch, J., Barnes, G.L., Graves, D.T., Einhorn, T.A., 2003. Impaired fracture healing in the absence of TNF-alpha signaling: the role of TNF-alpha in endochondral cartilage resorption. *J. Bone Miner. Res.* 18, 1584–1592. <https://doi.org/10.1359/jbmr.2003.18.9.1584>
- Geudens, I., Gerhardt, H., 2011. Coordinating cell behaviour during blood vessel formation. *Development* 138, 4569–4583. <https://doi.org/10.1242/dev.062323>
- Ginhoux, F., Williams, M., 2016. Tissue-Resident Macrophage Ontogeny and Homeostasis. *Immunity* 44, 439–449. <https://doi.org/10.1016/j.immuni.2016.02.024>
- Ginhoux, F., Jung, S., 2014. Monocytes and macrophages: developmental pathways and tissue homeostasis. *Nature Reviews Immunology* 14, 392–404. <https://doi.org/10.1038/nri3671>
- Göppert-Mayer, M., 1931. Über Elementarakte mit zwei Quantensprüngen. *Annalen der Physik* 401, 273–294. <https://doi.org/10.1002/andp.19314010303>
- Gordon, S., 2003. Alternative activation of macrophages. *Nature Reviews Immunology* 3, 23–35. <https://doi.org/10.1038/nri978>
- Grüneboom, A., Hawwari, I., Weidner, D., Culemann, S., Müller, S., Henneberg, S., Brenzel, A., Merz, S., Bornemann, L., Zec, K., Wuelling, M., Kling, L., Hasenberg, M., Voortmann, S., Lang, S., Baum, W., Ohs, A., Kraff, O., Quick, H.H., Jäger, M., Landgraeber, S., Dudda, M., Danuser, R., Stein, J. v., Rohde, M., Gelse, K., Garbe, A.I., Adamczyk, A., Westendorf, A.M., Hoffmann, D., Christiansen, S., Engel, D.R., Vortkamp, A., Krönke, G., Herrmann, M., Kamradt, T., Schett, G., Hasenberg, A., Gunzer, M., 2019. A network of trans-cortical capillaries as mainstay for blood circulation in long bones. *Nature Metabolism* 1, 236–250. <https://doi.org/10.1038/s42255-018-0016-5>
- Gurevich, D.B., Severn, C.E., Twomey, C., Greenhough, A., Cash, J., Toye, A.M., Mellor, H., Martin, P., 2018. Live imaging of wound angiogenesis reveals macrophage orchestrated vessel sprouting and regression. *The EMBO Journal* 37, 1–23. <https://doi.org/10.15252/embj.201797786>
- Hawkins, E.D., Duarte, D., Akinduro, O., Khorshed, R.A., Passaro, D., Nowicka, M., Straszowski, L., Scott, M.K., Rothery, S., Ruivo, N., Foster, K., Waibel, M., Johnstone, R.W., Harrison, S.J., Westerman, D.A., Quach, H., Gribben, J., Robinson, M.D., Purton, L.E., Bonnet, D., lo Celso, C., 2016. T-cell acute leukaemia exhibits dynamic interactions with bone marrow microenvironments. *Nature* 538, 518–522. <https://doi.org/10.1038/nature19801>
- Hettinger, J., Richards, D.M., Hansson, J., Barra, M.M., Joschko, A.-C., Krijgsveld, J., Feuerer, M., 2013. Origin of monocytes and macrophages in a committed progenitor. *Nature Immunology* 14, 821–830. <https://doi.org/10.1038/ni.2638>
- Holzwarth, K., Köhler, R., Philipsen, L., Tokoyoda, K., Ladyhina, V., Wählby, C., Niesner, R.A., Hauser, A.E., 2018. Multiplexed fluorescence microscopy reveals heterogeneity among stromal cells in mouse bone marrow sections. *Cytometry Part A* 93, 876–888. <https://doi.org/10.1002/cyto.a.23526>
- Itkin, T., Gur-Cohen, S., Spencer, J.A., Schajnovitz, A., Ramasamy, S.K., Kusumbe, A.P., Ledergor, G., Jung, Y., Milo, I., Poulos, M.G., Kalinkovich, A., Ludin, A., Golan, K., Khatib, E., Kumari, A., Kollet, O., Shakhar, G., Butler, J.M., Rafii, S., Adams, R.H., Scadden, D.T., Lin, C.P., Lapidot, T., 2016. Distinct bone marrow blood vessels differentially regulate haematopoiesis. *Nature* 532, 323–328. <https://doi.org/10.1038/nature17624>
- Jacobsen, R.N., Forristal, C.E., Raggatt, L.J., Nowlan, B., Barbier, V., Kaur, S., van Rooijen, N., Winkler, I.G., Pettit, A.R., Levesque, J.-P., 2014. Mobilization with granulocyte colony-stimulating factor blocks medullar erythropoiesis by depleting F4/80+VCAM1+CD169+ER-HR3+Ly6G+ erythroid island macrophages in the mouse. *Experimental Hematology* 42, 547–561.e4. <https://doi.org/10.1016/j.exphem.2014.03.009>
- Jacome-Galarza, C.E., Percin, G.I., Muller, J.T., Mass, E., Lazarov, T., Eitler, J., Rauner, M., Yadav, V.K., Crozet, L., Bohm, M., Loyher, P.-L., Karsenty, G., Waskow, C., Geissmann, F., 2019. Developmental origin, functional maintenance and genetic rescue of osteoclasts. *Nature* 568, 541–545. <https://doi.org/10.1038/s41586-019-1105-7>
- Jung, S., Aliberti, J., Graemmel, P., Sunshine, M.J., Kreutzberg, G.W., Sher, A., Littman, D.R., 2000. Analysis of Fractalkine Receptor CX3CR1 Function by Targeted Deletion and Green Fluorescent Protein Reporter Gene Insertion. *Molecular and Cellular Biology* 20, 4106–4114. <https://doi.org/10.1128/MCB.20.11.4106-4114.2000>
- Kierdorf, K., Prinz, M., Geissmann, F., Gomez Perdiguero, E., 2015. Development and function of tissue resident macrophages in mice. *Seminars in Immunology* 27, 369–378. <https://doi.org/10.1016/j.smim.2016.03.017>
- Kolar, P., Gaber, T., Perka, C., Duda, G.N., Buttgerit, F., 2011. Human early fracture hematoma is characterized by inflammation and hypoxia, in: *Clinical Orthopaedics and Related Research*. <https://doi.org/10.1007/s11999-011-1865-3>
- Kolar, P., Schmidt-Bleek, K., Schell, H., Gaber, T., Toben, D., Schmidmaier, G., Perka, C., Buttgerit, F., Duda, G.N., 2010. The Early Fracture Hematoma and Its Potential Role in Fracture Healing. *Tissue Engineering Part B: Reviews* 16, 427–434. <https://doi.org/10.1089/ten.teb.2009.0687>
- Komori, T., 2006. Regulation of osteoblast differentiation by transcription factors. *Journal of Cellular Biochemistry* 99, 1233–1239. <https://doi.org/10.1002/jcb.20958>
- Kusumbe, A.P., Adams, R.H., 2014. Osteoclast progenitors promote bone vascularization and osteogenesis. *Nature Medicine* 20, 1238–1240. <https://doi.org/10.1038/nm.3747>

- Kusumbe, A.P., Ramasamy, S.K., Adams, R.H., 2014. Coupling of angiogenesis and osteogenesis by a specific vessel subtype in bone. *Nature* 507, 323–328. <https://doi.org/10.1038/nature13145>
- Kusumbe, A.P., Ramasamy, S.K., Itkin, T., Mäe, M.A., Langen, U.H., Betsholtz, C., Lapidot, T., Adams, R.H., 2016. Age-dependent modulation of vascular niches for haematopoietic stem cells. *Nature* 532, 380–384. <https://doi.org/10.1038/nature17638>
- Lang, A., Schulz, A., Ellinghaus, A., Schmidt-Bleek, K., A., L., A., S., A., E., 2016. Osteotomy models - The current status on pain scoring and management in small rodents. *Laboratory Animals* 50, 433–441. <https://doi.org/10.1177/0023677216675007>
- Langen, U.H., Pitulescu, M.E., Kim, J.M., Enriquez-Gasca, R., Sivaraj, K.K., Kusumbe, A.P., Singh, A., di Russo, J., Bixel, M.G., Zhou, B., Sorokin, L., Vaquerizas, J.M., Adams, R.H., 2017. Cell–matrix signals specify bone endothelial cells during developmental osteogenesis. *Nature Cell Biology* 19, 189–201. <https://doi.org/10.1038/ncb3476>
- Le, V., Lee, Seunghun, Lee, Seungwon, Wang, T., Hyuk Jang, W., Yoon, Y., Kwon, S., Kim, H., Lee, Seung-woo, Hean Kim, K., 2017. In vivo longitudinal visualization of bone marrow engraftment process in mouse calvaria using two-photon microscopy. *Scientific Reports* 7, 44097. <https://doi.org/10.1038/srep44097>
- Li, Y., Kong, N., Li, Z., Tian, R., Liu, X., Liu, G., Wang, K., Yang, P., 2019. Bone marrow macrophage M2 polarization and adipose-derived stem cells osteogenic differentiation synergistically promote rehabilitation of bone damage. *Journal of Cellular Biochemistry* 120, 19891–19901. <https://doi.org/10.1002/jcb.29297>
- Lian, J.B., Gravalles, E.M., Stein, G.S., 2011. Osteoblasts and their Signaling Pathways, in: *Osteoimmunology*. Elsevier, pp. 101–140. <https://doi.org/10.1016/B978-0-12-375670-1.10005-6>
- Lin, H.-H., Faunce, D.E., Stacey, M., Terajewicz, A., Nakamura, T., Zhang-Hoover, J., Kerley, M., Mucenski, M.L., Gordon, S., Stein-Streilein, J., 2005. The macrophage F4/80 receptor is required for the induction of antigen-specific efferent regulatory T cells in peripheral tolerance. *Journal of Experimental Medicine* 201, 1615–1625. <https://doi.org/10.1084/jem.20042307>
- lo Celso, C., Fleming, H.E., Wu, J.W., Zhao, C.X., Miake-Lye, S., Fujisaki, J., Côté, D., Rowe, D.W., Lin, C.P., Scadden, D.T., 2009. Live-animal tracking of individual haematopoietic stem/progenitor cells in their niche. *Nature* 457, 92–96. <https://doi.org/10.1038/nature07434>
- Loinard, C., Vilar, J., Milliat, F., Lévy, B., Benderitter, M., 2017. Monocytes/Macrophages Mobilization Orchestrate Neovascularization after Localized Colorectal Irradiation. *Radiation Research* 187, 549–561. <https://doi.org/10.1667/RR14398.1>
- Ludin, A., Itkin, T., Gur-Cohen, S., Mildner, A., Shezen, E., Golan, K., Kollet, O., Kalinkovich, A., Porat, Z., D’Uva, G., Schajnovitz, A., Voronov, E., Brenner, D.A., Apte, R.N., Jung, S., Lapidot, T., 2012. Monocytes-macrophages that express α -smooth muscle actin preserve primitive hematopoietic cells in the bone marrow. *Nature Immunology* 13, 1072–1082. <https://doi.org/10.1038/ni.2408>
- Marsell, R., Einhorn, T.A., 2011. The biology of fracture healing. *Injury* 42, 551–555. <https://doi.org/10.1016/j.injury.2011.03.031>
- Méndez-Ferrer, S., Lucas, D., Battista, M., Frenette, P.S., 2008. Haematopoietic stem cell release is regulated by circadian oscillations. *Nature* 452, 442–447. <https://doi.org/10.1038/nature06685>
- Mildner, A., Marinkovic, G., Jung, S., 2017. Murine Monocytes: Origins, Subsets, Fates, and Functions, in: *Myeloid Cells in Health and Disease*. American Society of Microbiology, pp. 141–153. <https://doi.org/10.1128/microbiolspec.MCHD-0033-2016>
- Morhardt, T.L., Hayashi, A., Ochi, T., Quirós, M., Kitamoto, S., Nagao-Kitamoto, H., Kuffa, P., Atarashi, K., Honda, K., Kao, J.Y., Nusrat, A., Kamada, N., 2019. IL-10 produced by macrophages regulates epithelial integrity in the small intestine. *Scientific Reports* 9, 1223. <https://doi.org/10.1038/s41598-018-38125-x>
- Murray, P.J., Allen, J.E., Biswas, S.K., Fisher, E.A., Gilroy, D.W., Goerdt, S., Gordon, S., Hamilton, J.A., Ivashkiv, L.B., Lawrence, T., Locati, M., Mantovani, A., Martinez, F.O., Mege, J.-L., Mosser, D.M., Natoli, G., Saeij, J.P., Schultze, J.L., Shirey, K.A., Sica, A., Suttles, J., Udalova, I., van Ginderachter, J.A., Vogel, S.N., Wynn, T.A., 2014. Macrophage Activation and Polarization: Nomenclature and Experimental Guidelines. *Immunity* 41, 14–20. <https://doi.org/10.1016/j.immuni.2014.06.008>
- Nevius, E., Pinho, F., Dhodapkar, M., Jin, H., Nadrah, K., Horowitz, M.C., Kikuta, J., Ishii, M., Pereira, J.P., 2015. Oxysterols and EBI2 promote osteoclast precursor migration to bone surfaces and regulate bone mass homeostasis. *Journal of Experimental Medicine* 212, 1931–1946. <https://doi.org/10.1084/jem.20150088>
- Olingy, C.E., San Emeterio, C.L., Ogle, M.E., Krieger, J.R., Bruce, A.C., Pfau, D.D., Jordan, B.T., Peirce, S.M., Botchwey, E.A., 2017. Non-classical monocytes are biased progenitors of wound healing macrophages during soft tissue injury. *Scientific Reports* 7, 447. <https://doi.org/10.1038/s41598-017-00477-1>
- Palframan, R.T., Jung, S., Cheng, G., Weninger, W., Luo, Y., Dorf, M., Littman, D.R., Rollins, B.J., Zwerink, H., Rot, A., von Andrian, U.H., 2001. Inflammatory Chemokine Transport and Presentation in HEV. *Journal of Experimental Medicine* 194, 1361–1374. <https://doi.org/10.1084/jem.194.9.1361>
- Pan, Y., Lloyd, C., Zhou, H., Dolich, S., Deeds, J., Gonzalo, J.-A., Vath, J., Gosselin, M., Ma, J., Dussault, B., Woolf, E., Alperin, G., Culpepper, J., Gutierrez-Ramos, J.C., Gearing, D., 1997. Neurotactin, a membrane-anchored chemokine upregulated in brain inflammation. *Nature* 387, 611–617. <https://doi.org/10.1038/42491>

- Praemer, A., Furner, S., Rice, D.P., 1999. Musculoskeletal Conditions in the United States. American Academy of Orthopaedic Surgeons.
- Raggatt, L.J., Wulschleger, M.E., Alexander, K.A., Wu, A.C.K., Millard, S.M., Kaur, S., Maughan, M.L., Gregory, L.S., Steck, R., Pettit, A.R., 2014. Fracture Healing via Periosteal Callus Formation Requires Macrophages for Both Initiation and Progression of Early Endochondral Ossification. *The American Journal of Pathology* 184, 3192–3204. <https://doi.org/10.1016/j.ajpath.2014.08.017>
- Ramasamy, S.K., Kusumbe, A.P., Adams, R.H., 2015. Regulation of tissue morphogenesis by endothelial cell-derived signals. *Trends in Cell Biology* 25, 148–157. <https://doi.org/10.1016/j.tcb.2014.11.007>
- Ramasamy, S.K., Kusumbe, A.P., Itkin, T., Gur-Cohen, S., Lapidot, T., Adams, R.H., 2016. Regulation of Hematopoiesis and Osteogenesis by Blood Vessel-Derived Signals. *Annual review of cell and developmental biology* 1–27. <https://doi.org/10.1146/annurev-cellbio-111315-124936>
- Ramasamy, S.K., Kusumbe, A.P., Wang, L., Adams, R.H., 2014. Endothelial Notch activity promotes angiogenesis and osteogenesis in bone. *Nature* 507, 376–380. <https://doi.org/10.1038/nature13146>
- Reismann, D., Stefanowski, J., Günther, R., Rakhymzhan, A., Matthys, R., Nützi, R., Zehentmeier, S., Schmidt-Bleek, K., Petkau, G., Chang, H.-D., Naundorf, S., Winter, Y., Melchers, F., Duda, G., Hauser, A.E., Niesner, R.A., 2017. Longitudinal intravital imaging of the femoral bone marrow reveals plasticity within marrow vasculature. *Nature Communications* 8, 2153. <https://doi.org/10.1038/s41467-017-01538-9>
- Romeo, S.G., Alawi, K.M., Rodrigues, J., Singh, A., Kusumbe, A.P., Ramasamy, S.K., 2019. Endothelial proteolytic activity and interaction with non-resorbing osteoclasts mediate bone elongation. *Nature Cell Biology* 21, 430–441. <https://doi.org/10.1038/s41556-019-0304-7>
- Sapozhnikov, A., Pewzner-Jung, Y., Kalchenko, V., Krauthgamer, R., Shachar, I., Jung, S., 2008. Perivascular clusters of dendritic cells provide critical survival signals to B cells in bone marrow niches. *Nature Immunology* 9, 388–395. <https://doi.org/10.1038/ni1571>
- Sass, F.A., Schmidt-Bleek, K., Ellinghaus, A., Filter, S., Rose, A., Preininger, B., Reinke, S., Geissler, S., Volk, H.-D., Duda, G.N., Dienelt, A., 2017. CD31+ Cells From Peripheral Blood Facilitate Bone Regeneration in Biologically Impaired Conditions Through Combined Effects on Immunomodulation and Angiogenesis. *Journal of Bone and Mineral Research* 32, 902–912. <https://doi.org/10.1002/jbmr.3062>
- Sato, K., Suematsu, A., Okamoto, K., Yamaguchi, A., Morishita, Y., Kadono, Y., Tanaka, S., Kodama, T., Akira, S., Iwakura, Y., Cua, D.J., Takayanagi, H., 2006. Th17 functions as an osteoclastogenic helper T cell subset that links T cell activation and bone destruction. *Journal of Experimental Medicine* 203, 2673–2682. <https://doi.org/10.1084/jem.20061775>
- Scheiermann, C., Kunisaki, Y., Frenette, P.S., 2013. Circadian control of the immune system. *Nature Reviews Immunology* 13, 190–198. <https://doi.org/10.1038/nri3386>
- Schlundt, C., el Khassawna, T., Serra, A., Dienelt, A., Wendler, S., Schell, H., van Rooijen, N., Radbruch, A., Lucius, R., Hartmann, S., Duda, G.N., Schmidt-Bleek, K., 2018. Macrophages in bone fracture healing: Their essential role in endochondral ossification. *Bone* 106, 78–89. <https://doi.org/10.1016/j.bone.2015.10.019>
- Schmidt-Bleek, K., Petersen, A., Dienelt, A., Schwarz, C., Duda, G.N., 2014a. Initiation and early control of tissue regeneration – bone healing as a model system for tissue regeneration. *Expert Opinion on Biological Therapy* 14, 247–259. <https://doi.org/10.1517/14712598.2014.857653>
- Schmidt-Bleek, K., Schell, H., Lienau, J., Schulz, N., Hoff, P., Pfaff, M., Schmidt, G., Martin, C., Perka, C., Buttgerit, F., Volk, H., Duda, G., 2014b. Initial immune reaction and angiogenesis in bone healing. *Journal of Tissue Engineering and Regenerative Medicine* 8, 120–130. <https://doi.org/10.1002/term.1505>
- Shi, C., Pamer, E.G., 2011. Monocyte recruitment during infection and inflammation. *Nature Reviews Immunology* 11, 762–774. <https://doi.org/10.1038/nri3070>
- Shiu, H.T., Leung, P.C., Ko, C.H., 2018. The roles of cellular and molecular components of a hematoma at early stage of bone healing. *Journal of Tissue Engineering and Regenerative Medicine* 12, e1911–e1925. <https://doi.org/10.1002/term.2622>
- Sica, A., Mantovani, A., 2012. Macrophage plasticity and polarization: in vivo veritas. *Journal of Clinical Investigation* 122, 787–795. <https://doi.org/10.1172/JCI59643>
- Simkin, J., Sammarco, M.C., Marrero, L., Dawson, L.A., Yan, M., Tucker, C., Cammack, A., Muneoka, K., 2017. Macrophages are required to coordinate mouse digit tip regeneration. *Development* 144, 3907–3916. <https://doi.org/10.1242/dev.150086>
- Spencer, J.A., Ferraro, F., Roussakis, E., Klein, A., Wu, J., Runnels, J.M., Zaher, W., Mortensen, L.J., Alt, C., Turcotte, R., Yusuf, R., Côté, D., Vinogradov, S.A., Scadden, D.T., Lin, C.P., 2014. Direct measurement of local oxygen concentration in the bone marrow of live animals. *Nature* 508, 269–273. <https://doi.org/10.1038/nature13034>
- Stefanowski, J., Fiedler, A.F., Köhler, M., Günther, R., Liublín, W., Tschaikner, M., Rauch, A., Reismann, D., Matthys, R., Nützi, R., Bixel, M.G., Adams, R.H., Niesner, R.A., Duda, G.N., Hauser, A.E., 2020. Limbostomy: Longitudinal Intravital Microendoscopy in Murine Osteotomies. *Cytometry Part A* 97, 483–495. <https://doi.org/10.1002/cyto.a.23997>
- Stefanowski, J., Lang, A., Rauch, A., Aulich, L., Köhler, M., Fiedler, A.F., Buttgerit, F., Schmidt-Bleek, K., Duda, G.N., Gaber, T., Niesner, R.A., Hauser, A.E., 2019. Spatial Distribution of Macrophages During Callus Formation and Maturation Reveals Close Crosstalk Between Macrophages and Newly Forming Vessels. *Frontiers in Immunology* 10. <https://doi.org/10.3389/fimmu.2019.02588>

- Takayanagi, H., Kim, S., Taniguchi, T., 2002. Signaling crosstalk between RANKL and interferons in osteoclast differentiation. *Arthritis research* 4 Suppl 3, S227-32. <https://doi.org/10.1186/ar581>
- Tsakasaki, M., Takayanagi, H., 2019. Osteoimmunology: evolving concepts in bone-immune interactions in health and disease. *Nature Reviews Immunology* 19, 626-642. <https://doi.org/10.1038/s41577-019-0178-8>
- Udalova, I.A., Mantovani, A., Feldmann, M., 2016. Macrophage heterogeneity in the context of rheumatoid arthritis. *Nature Reviews Rheumatology* 12, 472-485. <https://doi.org/10.1038/nrrheum.2016.91>
- Upadhaya, S., Krichevsky, O., Akhmetzyanova, I., Sawai, C.M., Fooksman, D.R., Reizis, B., 2020. Intravital Imaging Reveals Motility of Adult Hematopoietic Stem Cells in the Bone Marrow Niche. *Cell Stem Cell* 27, 336-345.e4. <https://doi.org/10.1016/j.stem.2020.06.003>
- Vi, L., Baht, G.S., Soderblom, E.J., Whetstone, H., Wei, Q., Furman, B., Puviindran, V., Nadesan, P., Foster, M., Poon, R., White, J.P., Yahara, Y., Ng, A., Barrientos, T., Grynypas, M., Mosely, M.A., Alman, B.A., 2018. Macrophage cells secrete factors including LRP1 that orchestrate the rejuvenation of bone repair in mice. *Nature Communications* 9, 5191. <https://doi.org/10.1038/s41467-018-07666-0>
- Vi, L., Baht, G.S., Whetstone, H., Ng, A., Wei, Q., Poon, R., Mylvaganam, S., Grynypas, M., Alman, B.A., 2015. Macrophages Promote Osteoblastic Differentiation In Vivo: Implications in Fracture Repair and Bone Homeostasis. *Journal of Bone and Mineral Research* 30, 1090-1102. <https://doi.org/10.1002/jbmr.2422>
- Wang, T., Ouzounov, D.G., Wu, C., Horton, N.G., Zhang, B., Wu, C.-H., Zhang, Y., Schnitzer, M.J., Xu, C., 2018. Three-photon imaging of mouse brain structure and function through the intact skull. *Nature Methods* 15, 789-792. <https://doi.org/10.1038/s41592-018-0115-y>
- Watkins-Castillo, S., Andersson, G., 2014. United States Bone and Joint Initiative: The Burden of Musculoskeletal Diseases in the United States (BMUS), The Burden of Musculoskeletal diseases in the United States.
- Wei, Q., Frenette, P.S., 2018. Niches for Hematopoietic Stem Cells and Their Progeny. *Immunity* 48, 632-648. <https://doi.org/10.1016/j.immuni.2018.03.024>
- Winkler, I.G., Sims, N. a, Pettit, A.R., Barbier, V., Nowlan, B., Helwani, F., Poulton, I.J., van Rooijen, N., Alexander, K.A., Raggatt, L.J., Lévesque, J.-P., 2010. Bone marrow macrophages maintain hematopoietic stem cell (HSC) niches and their depletion mobilizes HSCs. *Blood* 116, 4815-4828. <https://doi.org/10.1182/blood-2009-11-253534>
- Wynn, T.A., Chawla, A., Pollard, J.W., 2013. Macrophage biology in development, homeostasis and disease. *Nature* 496, 445-455. <https://doi.org/10.1038/nature12034>
- Zehentmeier, S., Roth, K., Cseresnyes, Z., Sercan, Ö., Horn, K., Niesner, R. a, Chang, H.-D., Radbruch, A., Hauser, A.E., 2014. Static and dynamic components synergize to form a stable survival niche for bone marrow plasma cells. *European Journal of Immunology* 44, 2306-2317. <https://doi.org/10.1002/eji.201344313>

6 Statutory Declaration

I, Jonathan Stefanowski, by personally signing this document in lieu of an oath, hereby affirm that I prepared the submitted dissertation on the topic *Elucidating the mechanisms of bone regeneration using longitudinal intravital multiphoton endomicroscopy in the murine bone marrow* (Ergründung der Mechanismen der Knochenregeneration mit Hilfe longitudinaler intravitale Multiphotonen-Endomikroskopie) independently and without the support of third parties, and that I used no other sources and aids than those stated.

All parts which are based on the publications or presentations of other authors, either in letter or in spirit, are specified as such in accordance with the citing guidelines. The sections on methodology (in particular regarding practical work, laboratory regulations, statistical processing) and results (in particular regarding figures, charts and tables) are exclusively my responsibility.

Furthermore, I declare that I have correctly marked all of the data, the analyses, and the conclusions generated from data obtained in collaboration with other persons, and that I have correctly marked my own contribution and the contributions of other persons (cf. declaration of contribution). I have correctly marked all texts or parts of texts that were generated in collaboration with other persons.

My contributions to any publications to this dissertation correspond to those stated in the below joint declaration made together with the supervisor. All publications created within the scope of the dissertation comply with the guidelines of the ICMJE (International Committee of Medical Journal Editors; www.icmje.org) on authorship. In addition, I declare that I shall comply with the regulations of Charité – Universitätsmedizin Berlin on ensuring good scientific practice.

I declare that I have not yet submitted this dissertation in identical or similar form to another Faculty.

The significance of this statutory declaration and the consequences of a false statutory declaration under criminal law (Sections 156, 161 of the German Criminal Code) are known to me.

Date

Signature

7 Declaration of Contribution

Jonathan Stefanowski contributed to the selected publication as followed:

1. Reismann, D.*, **Stefanowski, J.***, Günther, R., Rakhymzhan, A., Matthys, R., Nützi, R., Zehentmeier, S., Schmidt-Bleek, K., Petkau, G., Chang, H.-D., Naundorf, S., Winter, Y., Melchers, F., Duda, G., Hauser, A.E., Niesner, R.A., 2017. Longitudinal intravital imaging of the femoral bone marrow reveals plasticity within marrow vasculature. *Nat. Commun.* 8, 2153. Impact Factor 12.353 <https://doi.org/10.1038/s41467-017-01538-9> (*shared first-coauthor)

- Data collection μ CT (Fig. 2)
- Microendoscope implantation procedure (Supp. Fig. 3)
- Bone sample preparation, bone sample cryosectioning, establishing and performing immunofluorescence histology and histochemistry, confocal and widefield microscopy (Fig. 3, 7; Supp. Fig. 4, 8)
- Establishing, performing, and analyzing FACS measurement of immune cell populations (Fig. 3; Supp. Fig. 5)
- Acquiring and analyzing cell populations using the LIMB implant. Analyzing calvarial imaging data (Fig. 4 e)
- Manuscript writing (figure captions) and revisiting the manuscript prior to resubmission

2. **Stefanowski, J.***, Lang, A.*, Rauch, A., Aulich, L., Köhler, M., Fiedler, A.F., Buttgereit, F., Schmidt-Bleek, K., Duda, G.N., Gaber, T., Niesner, R.A., Hauser, A.E., 2019. Spatial Distribution of Macrophages During Callus Formation and Maturation Reveals Close Crosstalk Between Macrophages and Newly Forming Vessels. *Front. Immunol.* 10. Impact Factor 3.124 <https://doi.org/10.3389/fimmu.2019.02588> (*shared first-coauthor)

- Surgery and sample preparation internal fixation
- Establishing and performing immunofluorescence and histochemistry histology (TRAP), confocal and widefield microscopy (Fig. 1 B-D; Fig. 3 A, B, D; Supp. Fig. 3 B-D; Fig. 4 A-D; Fig. 5 A; Supp. Fig. 6)
- Proximity analysis of F4/80 cells in *Emcn*^{hi/lo} areas (Fig. 3 E, F)
- Polarization analysis (Fig. 5 B; Supp. Fig. 4)
- Intravital LIMB implantation and imaging (Fig. 5 H; Supp. Movie 1-4)
- Manuscript writing (respective figure captions, respective methods, introduction, respective results, discussion)

3. **Stefanowski, J.***, Fiedler, A.F.*, Köhler, M., Günther, R., Liublin, W., Tschaikner, M., Rauch, A., Reismann, D., Matthys, R., Nützi, R., Bixel, M.G., Adams, R.H., Niesner, R.A., Duda, G.N., Hauser, A.E., 2020. Limbostomy: Longitudinal Intravital Microendoscopy in Murine Osteotomies. *Cytom. Part A* 97, 483–495. Impact Factor N.A <https://doi.org/10.1002/cyto.a.23997> (*shared first-coauthor)
- Participation in the development of an optimized design, lens gluing of the Limbostomy microendoscope (Fig. 1; Supp. Movie 1)
 - Establishing and implanting of the Limbostomy microendoscope and its documentation (Fig. 3 A-I)
 - Animal experiment proposal writing, animal observation and documentation (Fig. 3)
 - Multi-photon imaging (Fig. 2; Fig. 4 A-C; Supp. Movies 2-4; Supp. Fig. 3, 4)
 - Analyzing osteotomy gap size (Fig. 3 J, K)
 - Establishing and performing immunofluorescence histology, confocal microscopy (Fig. 3, Supp. Fig. 4)
 - Establishing and performing movie analysis, object identification (Fig. 4)
 - Manuscript writing (respective figure captions, respective methods, introduction, respective results, discussion)

Signature of the doctoral candidate

8 Selected Publications

8.1 Reismann et al., 2017 – Longitudinal Intravital imaging of the Femoral Bone Marrow Reveals Plasticity within Marrow Vasculature

The following presents the publication

Reismann, D.*, **Stefanowski, J.***, Günther, R., Rakhymzhan, A., Matthys, R., Nützi, R., Zehentmeier, S., Schmidt-Bleek, K., Petkau, G., Chang, H.-D., Naundorf, S., Winter, Y., Melchers, F., Duda, G., Hauser, A.E., Niesner, R.A., 2017. Longitudinal intravital imaging of the femoral bone marrow reveals plasticity within marrow vasculature. Nat. Commun. 8, 2153. Impact Factor 12.353 <https://doi.org/10.1038/s41467-017-01538-9> (*shared first-coauthor)

as a part of this dissertation. For optimal pdf and image quality or the publication's digital supporting information, such as movies access the publisher's website under the digital object identifiers of the selected publication. All information is publicly available.

ARTICLE

DOI: 10.1038/s41467-017-01538-9

OPEN

Longitudinal intravital imaging of the femoral bone marrow reveals plasticity within marrow vasculature

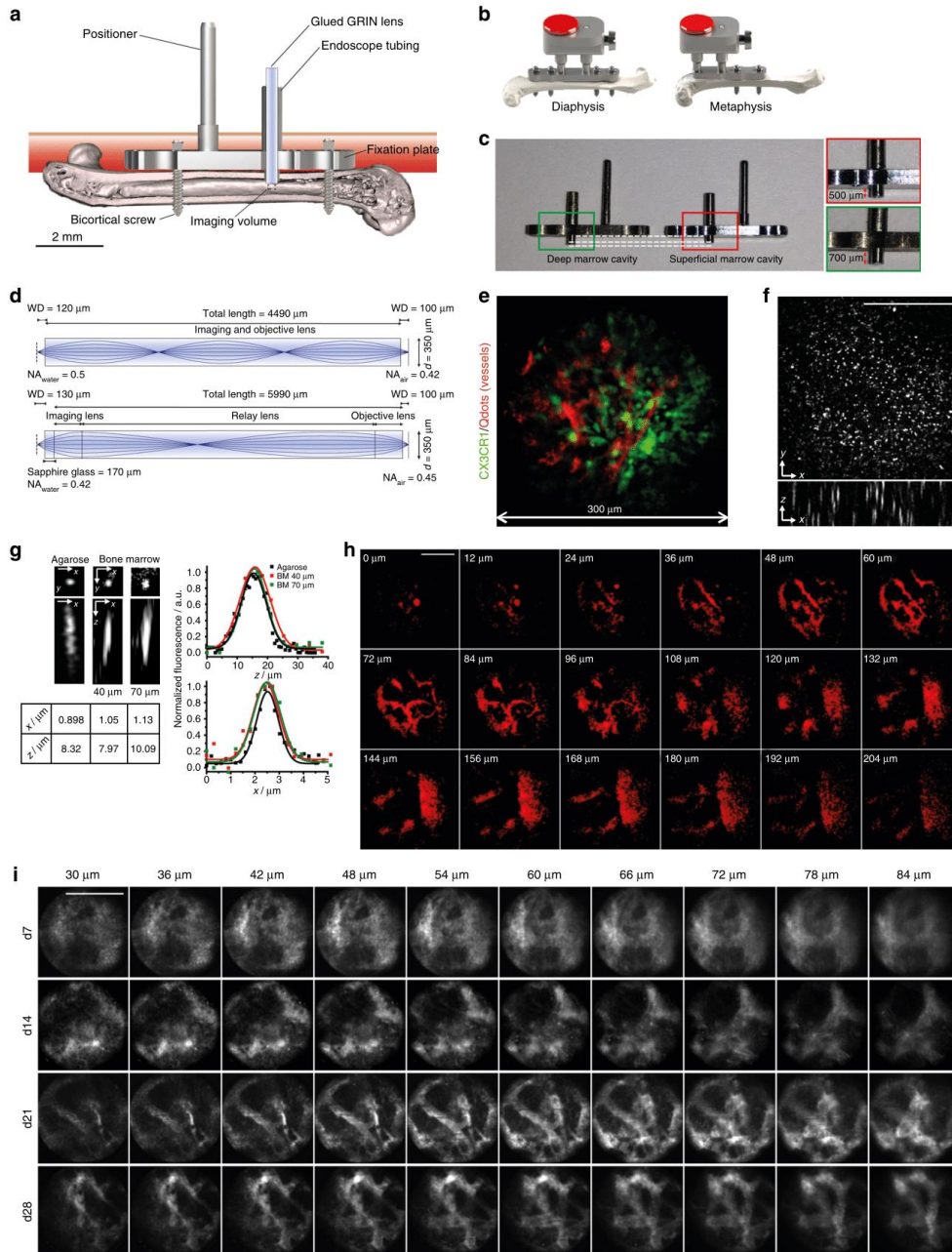
David Reismann¹, Jonathan Stefanowski^{1,2}, Robert Günther¹, Asylkhan Rakhymzhan¹, Romano Matthys³, Reto Nützi³, Sandra Zehentmeier^{1,2,6}, Katharina Schmidt-Bleek⁴, Georg Petkau¹, Hyun-Dong Chang¹, Sandra Naundorf¹, York Winter⁵, Fritz Melchers¹, Georg Duda⁴, Anja E. Hauser^{1,2} & Raluca A. Niesner¹

The bone marrow is a central organ of the immune system, which hosts complex interactions of bone and immune compartments critical for hematopoiesis, immunological memory, and bone regeneration. Although these processes take place over months, most existing imaging techniques allow us to follow snapshots of only a few hours, at subcellular resolution. Here, we develop a microendoscopic multi-photon imaging approach called LIMB (longitudinal intravital imaging of the bone marrow) to analyze cellular dynamics within the deep marrow. The approach consists of a biocompatible plate surgically fixated to the mouse femur containing a gradient refractive index lens. This microendoscope allows highly resolved imaging, repeatedly at the same regions within marrow tissue, over months. LIMB reveals extensive vascular plasticity during bone healing and steady-state homeostasis. To our knowledge, this vascular plasticity is unique among mammalian tissues, and we expect this insight will decisively change our understanding of essential phenomena occurring within the bone marrow.

¹Deutsches Rheuma-Forschungszentrum, A Leibniz Institute, Charitéplatz 1, 10117 Berlin, Germany. ²Immune Dynamics, Charité—Universitätsmedizin, Charitéplatz 1, 10117 Berlin, Germany. ³RISystem AG, Talstraße 2A, 7270 Davos Platz, Switzerland. ⁴Julius Wolff Institute, Charité—Universitätsmedizin, Augustenburger Platz 1, 13353 Berlin, Germany. ⁵Humboldt-Universität zu Berlin, Unter den Linden 6, 10099 Berlin, Germany. ⁶Present address: Department of Immunobiology, Yale University School of Medicine, New Haven, CT 06519, USA. David Reismann and Jonathan Stefanowski contributed equally to this work. Anja E. Hauser and Raluca A. Niesner jointly supervised this work. Correspondence and requests for materials should be addressed to A.E.H. (email: hauser@dfz.de) or to R.A.N. (email: niesner@dfz.de)

The bone marrow is the birthplace of hematopoietic cells in adult mammals. As such, it is a highly dynamic environment, where new blood cells are constantly generated from proliferating hematopoietic precursors and exit the bone marrow into the circulation¹. At the same time, the bone marrow serves as a harbor for memory cells of the immune system, which reside in

the various subtly different microenvironments that support specific immune cell types². These microenvironments are characterized by specialized stromal cell populations, which compose stable components of the niches³ and provide essential signals for the differentiation and survival of the hematopoietic cells that occupy these niches.



In order to fulfill these functions, the bone marrow tissue is traversed by a dense system of blood vessels comprising arteries, distal arterioles, and sinusoids. These are responsible for transporting cells entering and exiting the bone marrow^{4, 5}, and also for delivering oxygen, nutrients, and growth factors¹. The marrow vasculature plays a key role in the regulation of hematopoiesis⁶, and hematopoietic stem cell niches are located perivascularly. Recently, a strong link between angiogenesis and osteogenesis, mediated by a defined vessel subtype, characterized by CD31^{hi}Emcn^{hi} (type H) endothelium has been described in the bone marrow. This finding revealed a previously unknown heterogeneity among blood vessels in the bone marrow, supporting the notion of tight functional interactions between marrow and bone⁷.

In the recent decade, intravital two-photon microscopy has significantly advanced our understanding of dynamic processes within the immune system. Within the bone marrow, intravital microscopy has helped to elucidate mechanisms of hematopoiesis⁸, mobilization of hematopoietic cells^{5, 9}, and the maintenance of immunological memory^{3, 10}. In mice, intravital imaging of bone marrow in areas close to the bone cortex has been performed either in the calvarium^{11–13}, in the tibia^{3, 14}, or in the femur^{15, 16}. The calvarial preparation takes advantage of the thin sheet of flat bone covering the marrow in this area. Imaging the bone marrow of long bones is more invasive, as it requires the surgical ablation of cortical bone. Both methods have been used mainly as terminal procedures, although imaging at multiple time points has been used for intravital microscopy of both calvarium^{17, 18} and long bones (femur and tibia) for imaging durations of hours, over a maximum of 40 days^{15, 16}. Nevertheless, up to now there is no available method enabling longitudinal intravital microscopy of the deeper marrow regions in long bones, at sub-cellular resolution, over the time course of several weeks or even months, i.e., both during bone healing and during homeostasis. In order to understand the cellular dynamics occurring in those marrow regions over longer periods of time, an intravital imaging approach allowing longitudinal observation of a fixed region within the bone marrow in one and the same subject is needed.

The development of permanent windows for the brain cortex¹⁹ or of the spinal cord²⁰ solved the challenge of longitudinal imaging, but limitations regarding the accessibility of deep tissue areas still remained. An elegant solution for this problem was provided by the lab of Marc Schnitzer²¹, who used gradient refractive index (GRIN) endoscopic lenses implanted into the brain cortex in order to image deep cortical layers over several weeks. An endoscopic approach was also used previously for single-photon imaging in the femur, by introducing a fiber-optic probe into the femoral cavity through the knee area. This method

was used for imaging within a single-plane circular field of view of 300 μm diameter and at a lateral resolution of 3.3 μm . The imaged tissue areas were located at 10–15 μm distance from the endoscope tip²².

Here, we present a novel method called longitudinal intravital imaging of the bone marrow (LIMB), which allows repeated imaging of the same tissue region in the bone marrow of living mice over the time course of up to 115 days. The approach enables sub-cellular resolution multi-photon imaging of cylindrical tissue volumes (300 \times 300 \times 200 μm^3) and is based on the use of a GRIN endoscopic lens mounted on a specialized holder that is surgically fixated to the femur of the mouse. By 28 days post-surgery, reactive processes of the organism to the implant completely cease, and the tissue reaches equilibrium. Using our technique, we are able to demonstrate a high degree of structural plasticity of deep bone marrow vessels not only during bone healing following lens implantation, but also in steady-state homeostasis, with implications for the concepts of micro-environmental stability and niche formation.

Results

Characterization and optical performance of the LIMB implant. In order to understand tissue and cellular dynamics in the bone marrow on a longer time scale, we developed a bi-compatible implant—the LIMB implant, which allows micro-endoscopic imaging of the femoral bone marrow.

The implant is based on a fixation plate originally developed to stabilize the mouse femur after osteotomy²³. Based on the principles of low contact plates developed for fracture healing^{23–27}, stability is achieved via two angle-stable bi-cortical screws (Fig. 1a, Supplementary Fig. 1d), which fix the plate in a “bridging” position above the bone, to avoid direct contact to the bone surface. This prevents any compression of the bone.

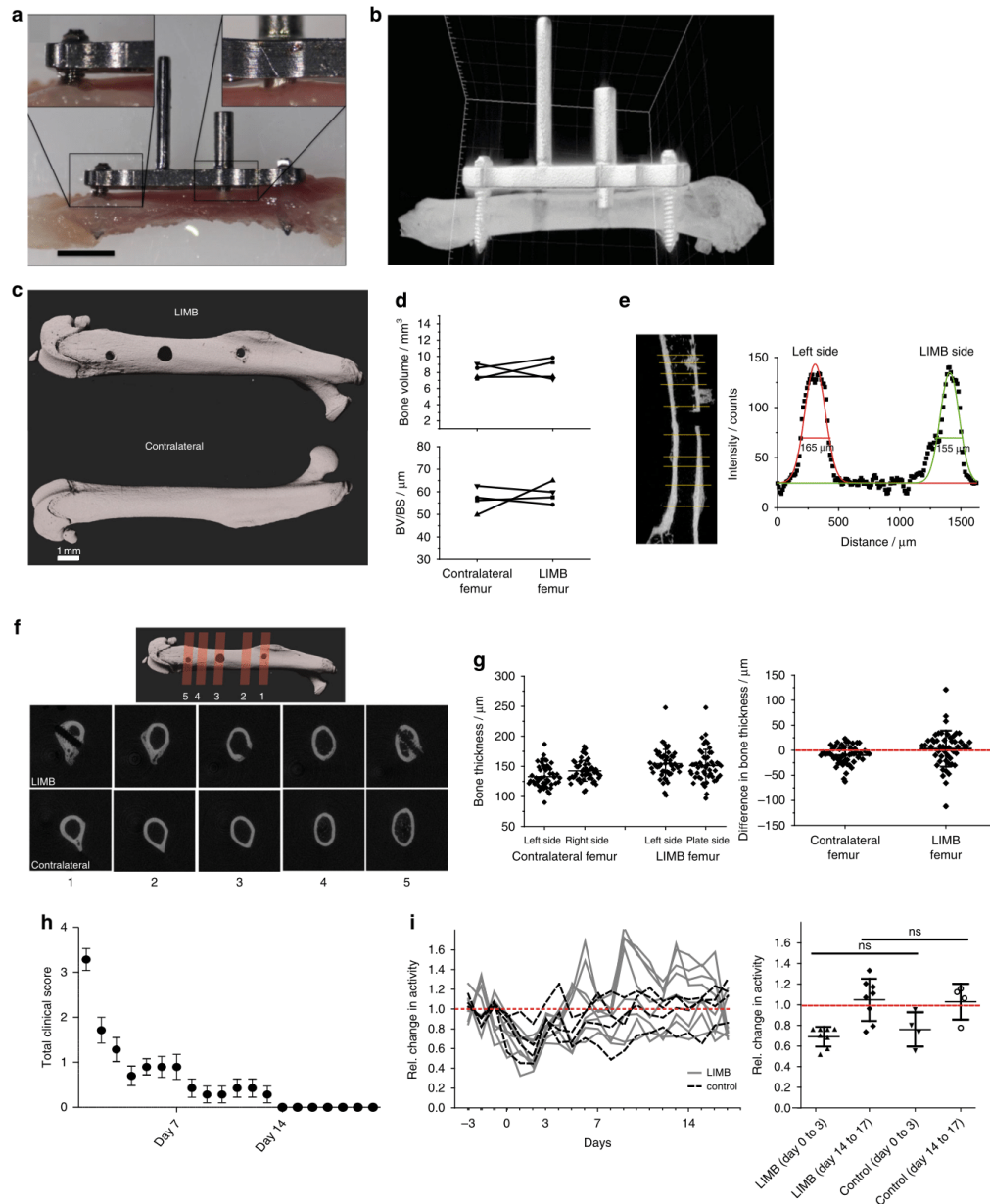
In order to allow repeated intravital imaging deep within the femoral bone marrow, a titanium alloy tube of 600 μm outer diameter and 450 μm inner diameter is mounted onto the fixation plate (Fig. 1a; Supplementary Fig. 1). To account for tissue heterogeneity and to visualize the different bone marrow areas of the femur, two types of implants were designed, allowing us to access either diaphyseal or metaphyseal regions (Fig. 1b). By varying the length of the endoscopic tubing in the marrow cavity (e.g., 500 vs. 700 μm , Fig. 1c), we can image pericortical tissue areas or areas deep in the marrow. For instance, by using a long microendoscopic tubing, we can visualize the endosteum on the opposite side of the bone cortex, in a contact-free manner.

A GRIN lens (Fig. 1d) is positioned in the endoscope tubing and used as a lens for imaging. We use two GRIN lens designs,

Fig. 1 LIMB allows murine long bone imaging in various locations with high resolution. **a** Design and positioning of LIMB implant for longitudinal bone marrow imaging. The LIMB implant is fixed onto the femur using bi-cortical angle-stable screws. GRIN lens systems are placed within the endoscope tubing for imaging and sealed to ensure sterility. The positioner allows adjustment and alignment of GRIN and microscope optical axes. **b** In order to account for tissue heterogeneity, i.e., metaphyseal vs. diaphyseal regions, alternative LIMB designs have been developed. LIMB fixation with four screws allows higher bone stability after osteotomies. **c** Tubing lengths of 500 and 700 μm , respectively, allow access to either peri-cortical or deep marrow regions. **d** Two GRIN lens systems are used for imaging. The single GRIN lens (upper panel) combines the imaging and objective lens function and is glued into the endoscope tubing. The symmetric triple GRIN lens (lower panel) is exchangeable and a sapphire window seals the endoscope tubing. **e** 3D fluorescence image of the bone marrow of a CX₃CR1:GFP mouse using the single GRIN lens (myeloid CX₃CR1⁺ cells - green; vasculature labeled by Qdots - red). The maximum field of view is circular, with 280 μm diameter. **f** The PSF was measured on 100 nm beads ($\lambda_{\text{em}} = 605 \text{ nm}$, $\lambda_{\text{exc}} = 850 \text{ nm}$) in agarose, using the single GRIN lens. No significant wave-front distortions affecting the PSF are observed. **g** Qdots are used to estimate PSF in marrow tissue. They reveal slight resolution deterioration with increasing imaging depth. **h** 2D fluorescence images of Qdots-labeled femoral vasculature, 35 days post-surgery, at various z-positions between the surface of the single GRIN lens and 204 μm tissue depth. They reveal fine vascularization in the upper layers and a large blood vessel (~100 μm diameter) with emerging branches in the deep marrow. **i** 2D fluorescence images of femoral vasculature acquired at various depths and time points post-surgery, using the triplet GRIN lens. The tissue at the contact surface with the window is characterized by de novo micro-vascularization, i.e., granulation tissue. Its thickness varies between individuals and decreases over time after implantation. Scale bars = 100 μm

both with a diameter of 350 μm . The first design (Fig. 1d, upper panel) consists of one single GRIN lens of 4.49 mm in length, a numerical aperture (NA) of 0.5 at the object side and a field of view of 280 μm in diameter (Fig. 1e). The lens is permanently and stably glued into the tubing, thereby sealing it to maintain sterility within the marrow cavity and ensuring fixed positioning of the optical path. The second design (Fig. 1d, lower panel) consists of a system of three GRIN lenses with NA 0.42 at the object side,

5.99 mm in length and a field of view of 150 μm diameter. This GRIN system requires a 170 μm thick sapphire window for optimal optical performance, which is attached to the tubing and seals the implant. Thus, this design allows flexible replacement of the GRIN lens system for applications requiring different optical properties. A 45° prism can be glued at the end of the GRIN lens to achieve a side view of the marrow tissue and access additional tissue areas.



The LIMB implant is surgically fixated onto the right femur of mice (Supplementary Figs. 2b, 3) to intravital visualize tissue dynamics by multi-photon microscopy. The use of multi-photon excitation permits imaging deep into tissue. The implant is completed by a titanium-alloy reference plate (Fig. 1b, Supplementary Figs. 1, 2a) mounted onto the positioner and the endoscope tubing, which allows stable, reproducible positioning of the mice under the microscope. This reference plate couples with a custom-built adapter used to align the optical axes of the microscope objective lens (20 \times , NA 0.45) and of the GRIN lens, thereby transferring the focus from the microscope objective through the GRIN lens into the marrow tissue (Supplementary Figs. 2b, 3h).

To characterize the optical properties of LIMB, we first determined the point spread function (PSF) of the GRIN lens systems using 100 nm fluorescent beads (emission at 605 nm, excitation at 850 nm) in agarose. Using the one-lens GRIN design, the spatial resolution was $0.8 \pm 0.1 \mu\text{m}$ (s.d.) laterally and $5.2 \pm 0.5 \mu\text{m}$ axially, corresponding to theoretical values for NA 0.5 ($n = 23$ beads). The three-dimensional PSF was not distorted by optical aberrations over the entire field of view (Fig. 1f). Using the three-lens GRIN system with the sapphire glass window, we measured a spatial resolution of $0.9 \pm 0.2 \mu\text{m}$ laterally and $8.0 \pm 1.1 \mu\text{m}$ axially (Fig. 1g), also corresponding to the theoretical values for NA 0.42 ($n = 18$ beads).

Within the bone marrow, the spatial resolution was evaluated using quantum dots 655 (Qdots). While most of these nanoparticles remained within the blood vessels, some Qdots entered the parenchyma due to the fenestrated sinusoids of the bone marrow and were observed as single fluorescent spheres of sub-resolution sizes. Typically, resolution values of $1.0 \pm 0.1 \mu\text{m}$ laterally and $7.4 \pm 1.6 \mu\text{m}$ axially were achieved within the imaging volume between 40 and 70 μm distance from the surface of the GRIN lens (at each depth, $n = 8$ Qdots).

The maximum extent of the imaging volume within the bone marrow using the one-lens GRIN system started from the endoscope surface at 0 μm and reached down to 204 μm within the bone marrow (Fig. 1h). It included regions with superficial small sinusoids and arterioles, as well as deeper-laying large blood vessels including the central sinus. We reliably achieved a signal-to-noise ratio of at least 5, independent of inter-individual variance and of the imaging time point after surgery.

At early time points post-surgery, we typically visualized granulation tissue, characterized by a tight network of small blood vessels within a large area in the imaging volume ($\sim 30\text{--}85 \mu\text{m}$ in depth). Over time, this granulation tissue retracted to the area next to the GRIN optics and was replaced by normal-appearing bone marrow vasculature, resembling the vasculature as observed

by calvarial and tibial imaging preparations. At late time points post-surgery, from 28 days onwards, we observed complete resolution of this granulation layer (Fig. 1i).

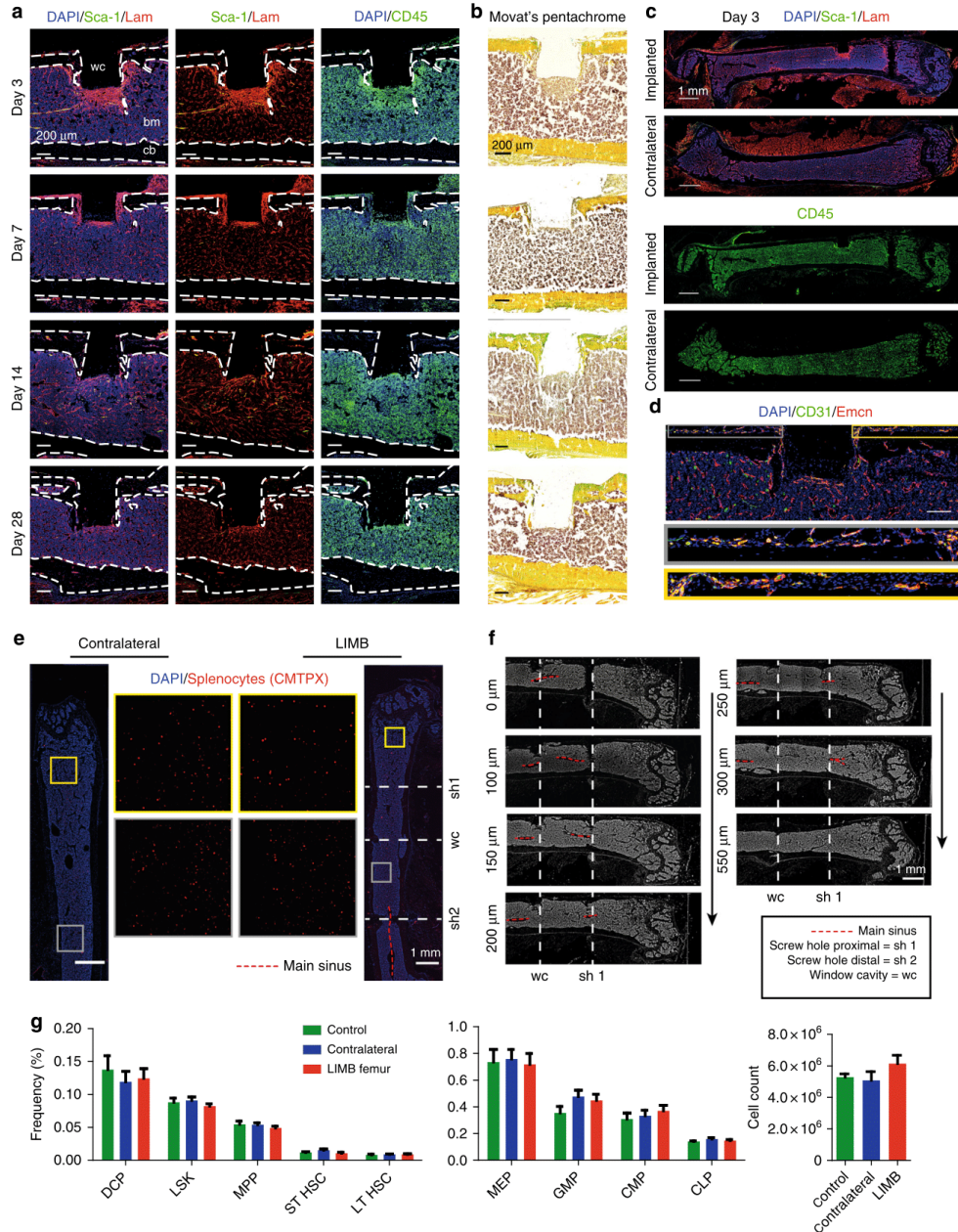
Local and overall tissue recovery after implantation. First, we determined to what extent the surgical procedure and the presence of the implant itself affected the mice and impacted on bone physiology. As shown in Fig. 2a, b and Supplementary Movie 1, we confirmed that the low contact plate design does not compress the bone, instead, a gap of at least 100 μm remained between bone surface and plate. After removal of the plate (day 7 post-implantation), reconstructed μCT images of the bone surface appeared smooth in the area where the plate had been, comparable to the surface of contralateral bones (Fig. 2c). Furthermore, no differences in bone volume, ratio of bone volume to bone surface (BV/BS), bone shape or thickness were found between the LIMB-implanted and contralateral femurs (Fig. 2d–g). In order to determine the impact of the surgery on the mice, we clinically scored the animals immediately after LIMB implantation, taking parameters such as weight, general appearance, and vitality into account. The data recorded from 79 mice indicate that the animals reached a low level of burden (as reflected in a score of 1) by post-surgical day 3, and normal values for all parameters were reached within 14 days after surgery (Fig. 2h). In addition, the general activity of mice that received the LIMB implant was recorded, starting 3 days pre-surgery until 18 days post-surgery (Fig. 2i, left panel). By transponder-based tracking, we recorded the movement of each mouse, thereby generating individual motility profiles of LIMB-implanted and co-housed mice, which had undergone sham treatment (without implantation). The mean activity levels dropped to a similar extent in both implanted and sham-treated groups within 3 days post-surgery, when compared to pre-surgical levels. By day 14 after surgery, at a time point when clinical scores were normal again (Fig. 2h), the activity of the mice in both groups also returned to pre-surgical levels (Fig. 2i, right panel). Interestingly, at both early and late time points post-surgery, there were no significant differences between sham-treated and LIMB-implanted mice. In order to analyze the effects of the surgical intervention and of the implant on the gait of the animals, the open-field behavior of the mice was recorded (Supplementary Movie 2) at day 2, 6, 9, 13, and 21 post-surgery. No severe gait abnormalities were observed at any time ($n = 79$).

In order to assess the effects of the LIMB implant on the bone with respect to post-surgical inflammation and bone formation adjacent to the LIMB microendoscope, we performed immunofluorescence and histochemical analysis (Fig. 3a–c). The most striking changes within the marrow of the implant-bearing

Fig. 2 Effect of LIMB implantation on bone tissue, general health, and activity of the mice. **a** Picture of an explanted femur including the LIMB implant shows the fixation plate bridging between the angle-stable screws, thereby preventing direct contact to the bone surface/periosteum. Scale bar = 2 mm. **b** 3D reconstructed μCT images of a femur bearing the LIMB implant confirm no direct contact between bone and fixation plate. Shadows below the positioner are beam hardening artifacts of the high attenuation titanium alloy. **c** 3D reconstructed μCT images of an intact femur (lower panel) and a femur after removal of the LIMB implant (upper panel). Bone surface under the fixation plate 7 days after implantation appears similar to the bone surface of the intact femur. Bone growth is observed only around the bicortical screws. **d** Total bone volume (upper panel) and BV/BS (lower panel) of LIMB and contralateral femur, respectively ($n = 4$ mice). **e** Longitudinal cross-section through a μCT reconstruction of a femur after implant removal (left panel). Yellow lines represent the positions chosen to measure the bone thickness. For each position, the intensity profile was approximated with two Gaussian curves as indicated in the left graph. **f** 3D reconstruction of μCT data showing the planes of transverse cross-sections displayed in the lower two panels. At day 21 after implantation, calcified bone forms around the bicortical screws, but not around the endoscope tubing. Cross-section μCT images at the sites of the screws show enough space for the bone marrow tissue to connect the diaphysis with the metaphysis. **g** No differences in bone thickness between contralateral and LIMB femurs are measured ($n = 5$ mice). **h** Total clinical score over 3 weeks post-surgery based on behavior and appearance of the individual mice ($n = 79$ mice). **i** Physical activity of LIMB implanted mice, pre-surgery and post-surgery, and of co-housed control mice. The LIMB-implanted mice reach their pre-surgical activity level within the same time as sham-treated controls (right graph) (two independent experiments; $n = 8$

femurs were an accumulation of CD45⁺ cells, and enhanced expression of the extracellular matrix (ECM) component laminin in tissue regions around the implant, peaking at day 3 post-surgery. Some of the cells with hematopoietic morphology were Sca-1⁺ckit⁺ and may represent progenitors (Supplementary Fig. 4a). We also detected CD45⁺Sca-1⁺ cells in elongated structures surrounded by laminin, likely representing arterioles

sprouting into the injured area (Supplementary Fig. 4b). These changes occurred around the sides of the implanted tube and in front of the sapphire glass window, reaching a depth of up to 400 μ m. By day 7, the inflamed area as indicated by laminin, Sca-1 and CD45 shrunk to a thickness of ~100 μ m. The tissue structure further normalized at day 14 and by day 28, the area in front of the imaging window typically consisted of laminin⁺ vessels



surrounded by CD45⁺ hematopoietic parenchyma, in a pattern resembling the other regions of the bone marrow and the contralateral (non-implant-bearing) femur. Movat's pentachrome staining showed that, although in some mice bone formation occurred lateral to the implanted tube emanating from the cortex, no new bone formed in front of the imaging window. Besides these changes in the tissue occurring adjacent to the implant and screws, the overall structure of the bone marrow was unaltered with respect to the overall distribution of leukocytes, ECM components, and vessels when compared to the contralateral bone (Fig. 3c). At the site of the periosteum, vascularization was detected (Fig. 3d). In order to test whether the implant impairs blood flow throughout the bone, we adoptively transferred CMTPX-labeled splenocytes via the tail vein, harvested the bones 4 h later and analyzed the distribution of CMTPX⁺ cells by fluorescence histology. In histological sections, CMTPX⁺ cells were distributed throughout the marrow in both the contralateral and the LIMB-implanted femurs (Fig. 3e). Importantly, engraftment occurred on both sides of the bicortical screws. Consistent with this observation, longitudinal serial sections showed clearly that the bicortical screw did not completely separate the bone marrow and did not impair the blood flow in any part of the marrow. Additionally, we performed μ CT of implanted bones, which also showed clearly that the bone marrow was not completely separated by the bicortical screws (Fig. 3f and Supplementary Movie 1). In order to verify whether hematopoiesis within the bone marrow was altered, we performed flow cytometry on bone marrow cells of LIMB-implanted mice, and quantified the major hematopoietic progenitor populations. No significant differences in the frequencies or total cell counts of the analyzed populations were observed compared to bone marrow from contralateral femurs or bone marrow from non-treated mice (Fig. 3g and Supplementary Fig. 5).

B lymphocyte motility in femur, calvarium, and tibia. In order to observe the dynamics of B-lineage cells within the femoral marrow, we chose *CD19:tdRFP* mice as recipients of the LIMB implant. In these mice, Cre recombinase activity in CD19-expressing cells leads to the removal of a STOP cassette and expression of tdRFP in the B cell lineage, starting in the late pro-B cell stage. The vasculature was labeled using Qdots. Mice were imaged starting at day 7 (Fig. 4a; Supplementary Movies 3, 5–7), up to maximally day 115 post-surgery (Supplementary Movie 12).

Using LIMB in *CD19:tdRFP* mice, under homeostatic conditions, i.e., at day 60 or 90 post-surgery, we found that tdRFP⁺ cells of various volumes displayed different motility patterns. We distinguished the subtypes of B lymphocytes based on their size,

and tracked them to assess their velocity and displacement rate. A maximum diameter of 10 μ m corresponds to a spherical volume of \sim 500 μ m³, therefore these cells presumably represent B cells, displaying a high degree of directed motility, in line with previous reports⁵. Larger tdRFP⁺ cells in this system represent rather static plasma cells, consistent with the concept of their residence in bone marrow niches (Fig. 3c) and with our previous work³. In order to compare the motility of B-lineage cells in the femur to other bone marrow compartments, we performed intravital imaging of calvaria and tibia of *CD19:tdRFP* mice. Notably, we found no significant differences in the motility of bone marrow B and plasma cells when comparing femur (LIMB), calvarium, and tibia (Supplementary Movies 4, 8, 9; Fig. 4b–e).

Long-term stability of the LIMB implant. In order to test the positional stability of the LIMB implant, the microendoscope was implanted in mice ubiquitously expressing photoactivatable green fluorescent protein (paGFP). Prior to photoactivation, paGFP is non-fluorescent upon 940 nm illumination. Photoactivation at 840 nm leads to 100-fold increase in green fluorescence upon excitation at 940 nm²⁸. *PaGFP* mice were injected with Qdots to label the vasculature and were imaged before and after photoactivation (Fig. 5a, two upper rows). The photoactivation area was either 75 \times 75 or 100 \times 100 μ m³ positioned within the center of the field of view (Supplementary Fig. 6). We analyzed paGFP fluorescence by repeated imaging every 6–12 h (Fig. 5a, third to last row) and detected paGFP fluorescence at the same area at least 36 h after photoactivation. Thus, we confirmed the high positioning stability of the LIMB implant with respect to the implantation/imaging site in the bone. The fluorescence signal of paGFP decreases over the time span of hours/days due to the emigration of hematopoietic cells out of the photoactivated region (Supplementary Movies 9, 10) and due to protein turnover, causing fluorescent paGFP to be replaced by newly synthesized, non-fluorescent paGFP. The imaging data acquired in *paGFP* mice reveal that while the field of view labeled by photoactivation remains stable, morphological changes of the vascular system do not cease after day 28 post-surgery and seem to depend on the vessel diameter (Fig. 5a). In order to exclude that such changes are caused by the LIMB implant itself, we performed longitudinal imaging in the calvarium of *paGFP* mice, over a volume of 500 \times 500 \times 66 μ m³. We were able to repeatedly detect paGFP fluorescent areas in the calvarial marrow islets for up to 72 h after photoactivation, and observed paGFP cells leaving this area. Similarly to LIMB, we also detected drastic changes in the marrow vasculature, most prominent in smaller vessels (Fig. 5b; Supplementary Fig. 7).

Fig. 3 The bone marrow within the imaging volume reaches steady-state comparable to homeostasis 28 days after LIMB implantation. **a** Immunofluorescence analysis of bone sections after removal of the LIMB implant over the time course of 4 weeks. ECM formation was identified by the marker Laminin (Lam). Stem-cell antigen 1 (Sca-1) is highly expressed in arterioles. The leukocyte marker CD45 indicates localization of inflammatory cells adjacent to the window cavity (wc). Lam is highly expressed around the implant during the first week and completely normalizes after 2–4 weeks. CD45⁺ cell accumulations are found during the first weeks in proximity to the wc. **b** Movat's pentachrome stain detects connective tissues and reveals remodeling of bone primarily on the periosteal interface near the fixation plate. **a, b** Images are representative for 3–5 mice per time point post-surgery. **c** Overview immunofluorescence images of the femoral bones from an individual mouse 3 days post-surgery. Note the specific reaction to the implant-bone marrow interfaces indicated by accumulations of CD45⁺ cells, and Lam⁺ and Sca1⁺ arteries (yellow). bm bone marrow, cb cortical bone. **d** Immunofluorescence image of the region around the endoscope tubing in a LIMB-implanted femur 7 days post-surgery, including the bone cortex and periosteum under the plate. The presence of various blood vessel subsets indicated by CD31 and Emcn demonstrates intact blood supply to the periosteum and to the bone. Scale bar = 100 μ m. **e** Blood supply is intact throughout the marrow cavity, indicated by CMTPX-labeled splenocytes, which localize in the bone marrow 4 h after transplantation in both contralateral and LIMB-implanted femurs at 42 days post-surgery ($n = 3$ mice). **f** Histological DAPI stain (gray) shows intact tissue structure, with no separation of the bone marrow and the vasculature by the screws or endoscope tubing. **g** Flow cytometry analysis of femurs with the LIMB implant, their contralateral femurs and femurs of control mice. Similar frequencies and cell counts of various cell populations shows no effect of the LIMB implant on bone marrow cell composition ($n = 8$ LIMB-implanted mice, $n = 8$ controls, two independent experiments). Error bars represent s.e.m. values. Statistical analysis was performed using t-test

Vascular plasticity during healing phase and homeostasis. Using LIMB, we observed drastic changes in the vascular morphology within the femoral marrow after implantation, both during the healing phase and after reaching steady-state. These

changes were not caused by instability of the microendoscope or by inaccuracy during repeated selection of the imaging volume, as demonstrated by the results of our photoactivation experiments.

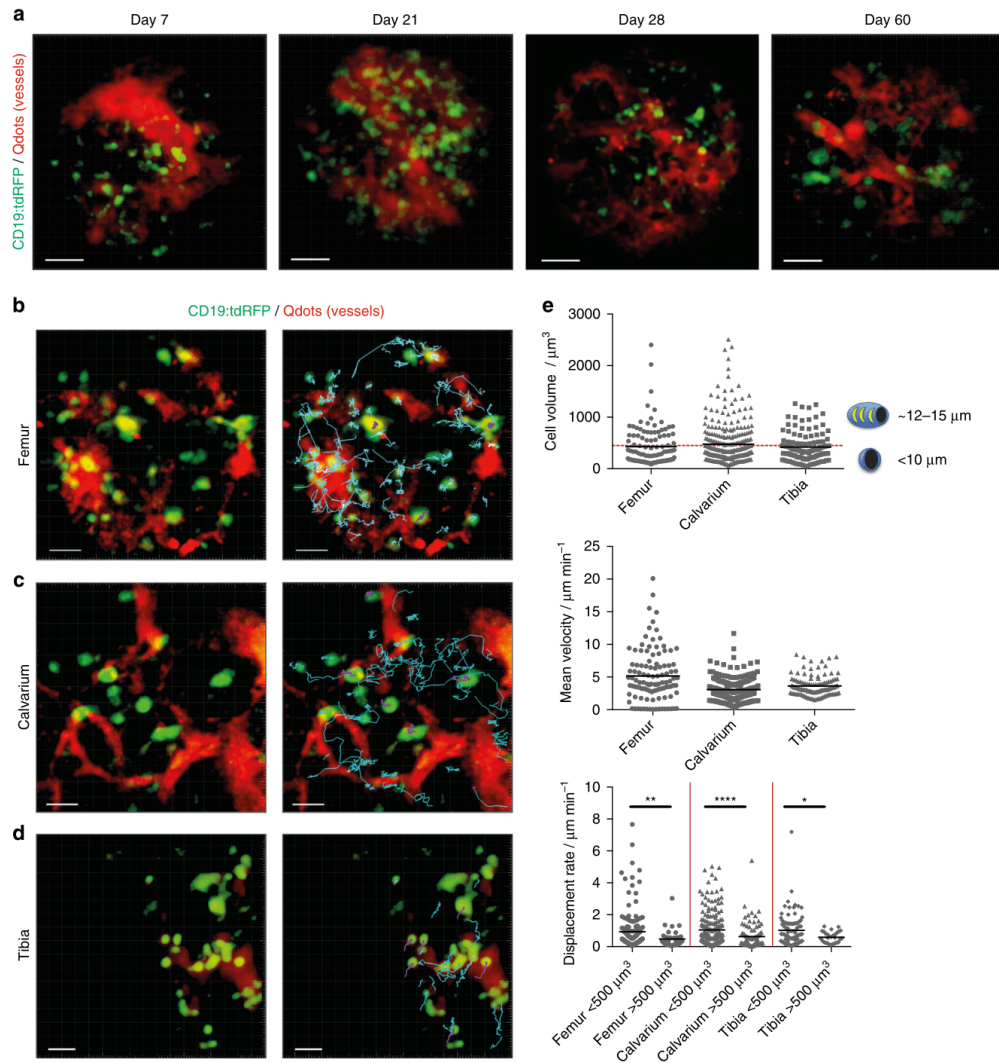


Fig. 4 Immune cell dynamics in different bone types show comparable motility patterns. **a** 3D fluorescence images acquired by LIMB in the femoral marrow of a *CD19:tdRFP* mouse at day 7, day 14, day 28, and day 60 after surgery. Mature B lymphocytes express tdRFP and are displayed in green, whereas the vasculature was labeled with Qdots and is displayed in red. Scale bar = 50 μm . All images are snapshots of 45 min movies, with images acquired every 30 s. The movies are provided as Supplementary Material. **b** Time-lapse 3D fluorescence image acquired by LIMB in the bone marrow of a *CD19:tdRFP* mouse at day 90 post-surgery. The tracks of the B lymphocytes smaller than $500 \mu\text{m}^3$ (defined as B cells with a maximum diameter of $10 \mu\text{m}$) are shown in cyan, whereas those with a volume larger than $500 \mu\text{m}^3$ (defined as plasma cells) are shown in violet. Scale bar = 30 μm . **c** Similar to **b**, time lapse 3D image of the bone marrow of a *CD19:tdRFP* mouse with corresponding tracks of B and plasma cells in the calvarium and **d** the tibia. Scale bar = 30 μm . Representative movies with cell motility tracks for LIMB, calvarial, and tibial imaging are provided as Supplementary Material. **e** Quantification of cell volumes, mean velocities, and displacement rates of B lymphocytes from movies acquired by LIMB ($n = 4$ mice), within the calvarial bone ($n = 3$ mice), and the tibia ($n = 2$ mice). Similar cell subset frequencies and mean velocities of B lymphocytes were measured by LIMB in the femoral bone marrow, by calvarial imaging as well as by tibial imaging. We statistically analyzed the data in **e** using t-test (* $p < 0.05$; ** $p < 0.01$; *** $p < 0.001$)

As expected, we observed dynamic blood vessel re-organization between day 7 and 21 post-surgery. Interestingly, even between day 27 and 60, a time span in which the tissue composition in front of the microendoscope is comparable to non-implanted bone marrow (Figs. 2, 3), the vasculature continued to change massively (Fig. 6a). Starting from day 27 post-surgery, with a time

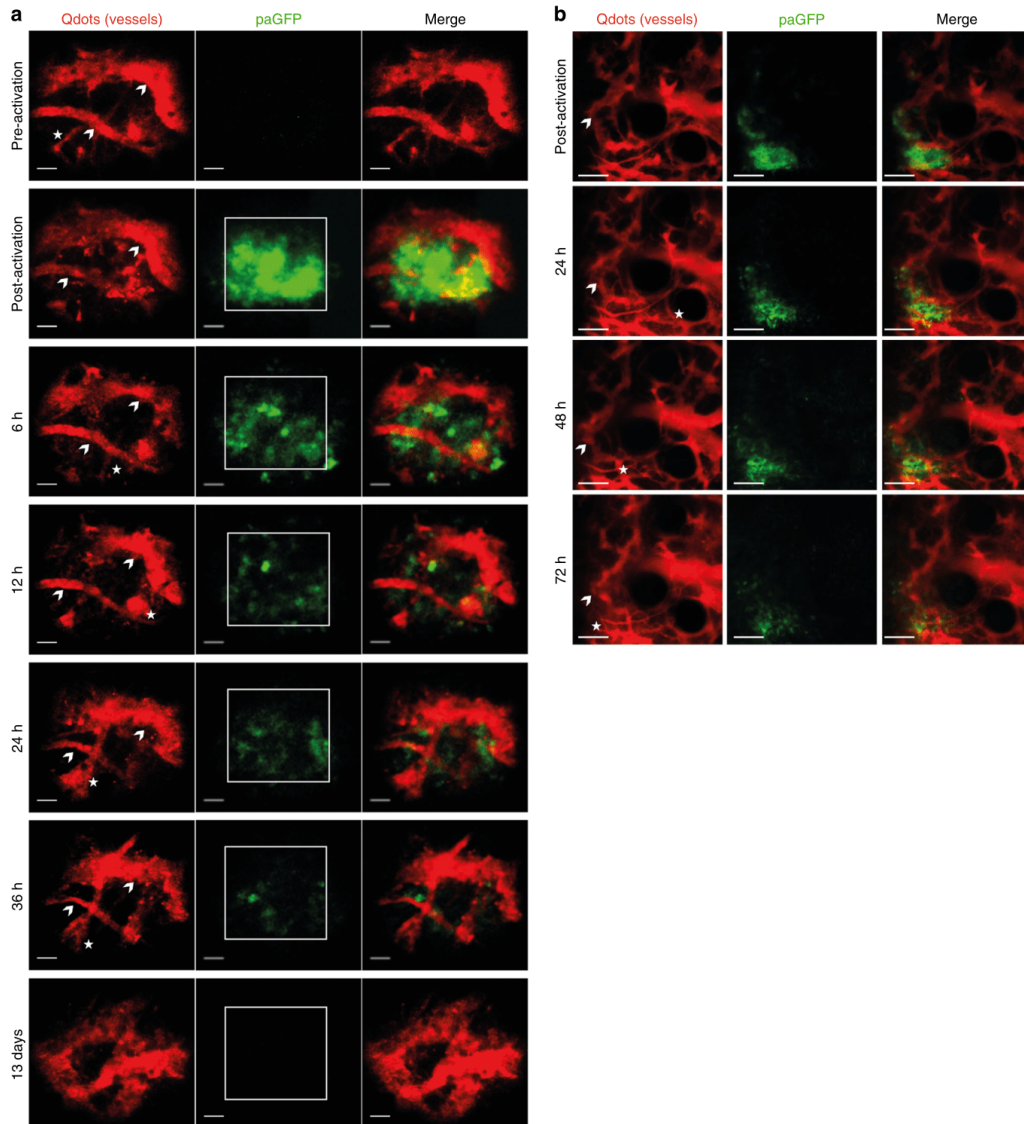
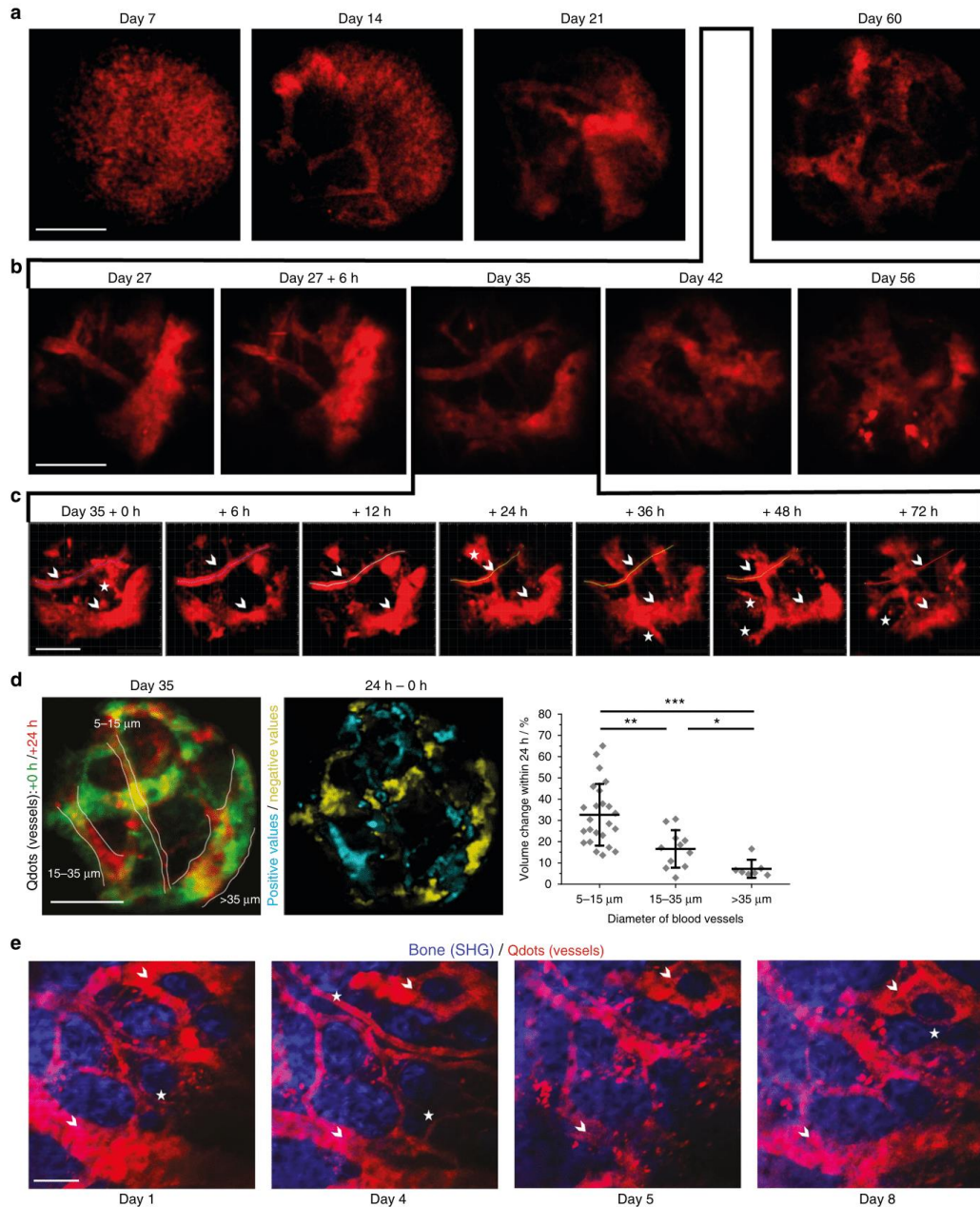


Fig. 5 Imaging of locally activated paGFP in murine deep femoral marrow reveals high positioning stability of the LIMB implant. **a** paGFP mice were implanted with a LIMB microendoscope ($n = 3$ mice). After 35 days, the mice were injected intravenously with Qdots to label the vasculature. Photoactivation of paGFP was performed at a wavelength of 840 nm in a $75 \times 75 \times 30 \mu\text{m}^3$ square area in the center of the field of view. Additional injections of Qdots were given before each recording. We performed the described photoactivation experiments repeatedly, up to three times in the same animal at day 27, 35, and 56 post-surgery, during homeostasis with similar results. Blood vessels which could be observed over the whole period of 36 h are indicated by arrowheads, whereas those that appear or disappear within this time period are labeled by asterisks. Scale bar = $30 \mu\text{m}$. **b** Similarly to **a**, photoactivation of a $150 \times 150 \times 9 \mu\text{m}^3$ region within the $500 \times 500 \times 66 \mu\text{m}^3$ field of view in a paGFP mouse with a permanent calvarial imaging window let us easily identify the photoactivated area. The paGFP fluorescence could be visualized over several imaging sessions. Scale bar = $100 \mu\text{m}$. During these time windows we observed changes of the vasculature in both, the deep femoral marrow and bone marrow islets of the calvarium

resolution of 7 days between imaging sessions, the pattern of large blood vessels ($>50\ \mu\text{m}$) changed between consecutive time points, making their use as tissue landmarks impossible (Fig. 6b). Only by further increasing the time resolution in LIMB, during the homeostatic phase, i.e., shortening the interval between imaging sessions to every 6–24 h (Fig. 6c), were the vessels stable enough

to be used for orientation. We found that blood vessels with diameters in the range of 5–15 μm had the highest degree of volume change within the time span of 24 h (Fig. 6d, Supplementary Movie 13). Within the same period, large blood vessels ($>35\ \mu\text{m}$) changed rather slowly, whereas middle-sized blood vessels with a diameter between 15–35 μm displayed an



intermediate degree of remodeling. Notably, we observed a comparable remodeling in the vascular compartment of the marrow islets of the calvarium, over a time course of 8 days (Fig. 6e). As the surgery for longitudinal calvarial imaging does not disrupt the integrity of the bone, we can rule out that the vascular plasticity was an effect caused by the femoral implant and confirm the physiological nature of this vascular remodeling. However, due to the fact that calvarial marrow islets are rather small as compared to the cortical bone areas, the dramatic vascular plasticity remained underestimated until now. Only by using LIMB, we were able to observe and quantify these changes.

Possible mechanisms of femoral vascular plasticity. In order to investigate whether vascular remodeling was the result of active angiogenesis related to de novo bone formation, we performed immunofluorescence analysis of bone sections (Fig. 7). A recent publication described CD31^{hi} Endomucin (Emcn)^{hi} (type H) bone marrow endothelium to be involved in osteogenesis-related angiogenesis in the bone marrow⁷. In line with previous reports²⁹, we found type H vessels to be abundant at the growth plate of young mice, but only few type H vessels were present in aged mice (Supplementary Fig. 8a). In contrast, type H vessels close to the bone cortex were found at all ages (Supplementary Fig. 8a), consistent with age-independent bone remodeling at this site. We examined the bone marrow for the presence of type H vessels following implantation (Fig. 7a) and detected them during the early healing phase (days 3–14) in tissue areas next to the microendoscope. At day 28 post-surgery, only few type H vessels were found in proximity of the microendoscope and their shape and abundance were comparable to the vessels present at bone–bone marrow interfaces. Together, this indicates a state of homeostasis, consistent with the previously observed time course of regeneration (Fig. 3).

In line with the vascular remodeling within the bone marrow, we observed marked changes in the stromal network in *Prx-1:YFP* mice (Supplementary Fig. 9). During homeostasis, the stromal network remodeling continues, similar to the vascular reorganization. Repeated imaging experiments in *paGFP* mice every 6–12 h after photoactivation, over a total time of 36 h (Fig. 5), revealed fluorescent cells, presumably stromal cells, persisting over the whole time span of 36 h, as well as highly motile fluorescent cells, presumably hematopoietic cells, leaving the photoactivated volume. Over the course of these 36 h the vasculature continuously changed its shape. In order to assess whether the remodeling process involves proliferation of the endothelial cells, we administered the thymidine analog EdU to label newly synthesized DNA³ to mice that had received a LIMB implant either 3 or 42 days earlier. EdU labeled a similar fraction and

comparable pattern of hematopoietic cells distributed over the whole bone marrow in both cohorts ($n = 3$ mice in each cohort). We did not detect an overt proliferation of endothelial cells in the tissue surrounding the implant (Fig. 7b). Similarly, staining for the proliferation marker Ki67 did not show any accumulation of proliferating endothelial cells at the implant site, at any time point (Supplementary Fig. 8b). Taken together, these data support the hypothesis that the observed dynamics are the result of passive displacement of the vessels, probably caused by dynamics and cell proliferation in the surrounding tissue (Fig. 7c; Supplementary Movies 10, 11), rather than active proliferation in the vascular compartment. The exact kinetics and mechanisms of the vascular and stromal remodeling during the steady-state will be subject of further studies, as they impact on many processes taking place in the bone marrow.

Discussion

While intravital imaging of the bone marrow has previously been performed^{3, 11–18, 22}, longitudinal multi-photon imaging in the deep marrow of long bones over the time course of months was not feasible. Longitudinal microscopic and microendoscopic imaging of the CNS^{20, 21}, retina³⁰, or lymph nodes transplanted into the ear of mice³¹ has been reported, and blood vessels have been used as anatomical reference points, allowing the recognition and imaging of the same regions within the tissue.

The bone marrow contains quiescent and activated hematopoietic stem cells in dedicated perivascular tissue niches^{6, 29}, and is the tissue in which most leukocytes complete their development. The bone marrow actively participates in immune reactions^{32, 33} and is an important site for the maintenance of immunological memory^{3, 10, 34, 35}. The interaction of hematopoietic cells with stromal cells plays a crucial role in these processes: subtypes of vascular cells provide niches for the maintenance of hematopoietic stem cell quiescence⁶, and stromal cells in the bone marrow provide cytokines, which support the survival and differentiation of developing hematopoietic cells. Endothelial cells mediate leukocyte trafficking between the circulation and the bone marrow parenchyma⁹, guiding immune memory cells back into the bone marrow together with stromal cells, which provide chemotactic cues and anchor the memory cells in their niches³⁶. Moreover, the role of the immune, vascular and bone compartments during distinct phases of bone regeneration still remain elusive. Hence, there is a clear need for longitudinal imaging technologies to allow the investigation of dynamic processes at the cellular and sub-cellular level in this organ.

The GRIN lens microendoscopic implant presented in this work allows for the first time imaging of dynamic cellular

Fig. 6 LIMB approach reveals kinetics of vascular remodeling during bone healing and homeostasis on time scales from hours to months. *C57/B6J* mice received the LIMB implant and were injected intravenously with Qdots (red) prior to each LIMB imaging session to label the vasculature. Vessels were three-dimensionally imaged at increasing time resolution over the course of **a** weeks **b** days and **c** several hours. In line with our previous observations, we noted prominent changes in the vasculature, which continued over the whole monitoring time period, even after homeostasis is reached ($n = 5$ mice, two independent experiments, scale bar = 50 μm). Small vessels continuously appear and disappear, larger vessels change their position and shape. The trace of such a larger vessel is displayed at all time points as a line in **c**. Blood vessels which can be used as landmarks are labeled by arrowheads and those that completely disappear within days are labeled by asterisks. **d** Overlap of the 3D projections of blood vessels in a mouse 35 days post-surgery (+0 h, green) and 24 h later (+24 h, red). A differential image between the two 3D images was generated. Blood vessel volume change was calculated by dividing the fraction of the volume difference between +24 h and 0 h (cyan areas in the middle panel indicate positive values, i.e., appearance of blood vessels; yellow areas indicate negative values, i.e., disappearance of blood vessels) by the total volume of the blood vessel at +24 h (delineated by white lines in the left panel) to obtain a normalized parameter of vessel volume change. The normalized volume changes (right panel) are dependent on the blood vessel diameter, with small vessels remodeling more rapidly than large vessels ($n = 6$ mice, scale bar = 100 μm). **e** Similar to the observations in the deep femoral marrow, repeated imaging of blood vessels in calvarial bone and bone marrow also showed remodeling of the vasculature ($n = 3$ mice, two independent experiments). Scale bar = 100 μm . Error bars represent s.d. values. Statistical analysis in **d** was performed using an ANOVA test (* $p < 0.05$; ** $p < 0.01$; *** $p < 0.001$)

processes in the deep femoral marrow, repeatedly, over a time period of up to several months. The central marrow represents an area, which has been inaccessible to intravital multi-photon

imaging until now; our technique permits imaging of this tissue for the unprecedented duration of 4 months within the same bone marrow region. Importantly, this time period covers not

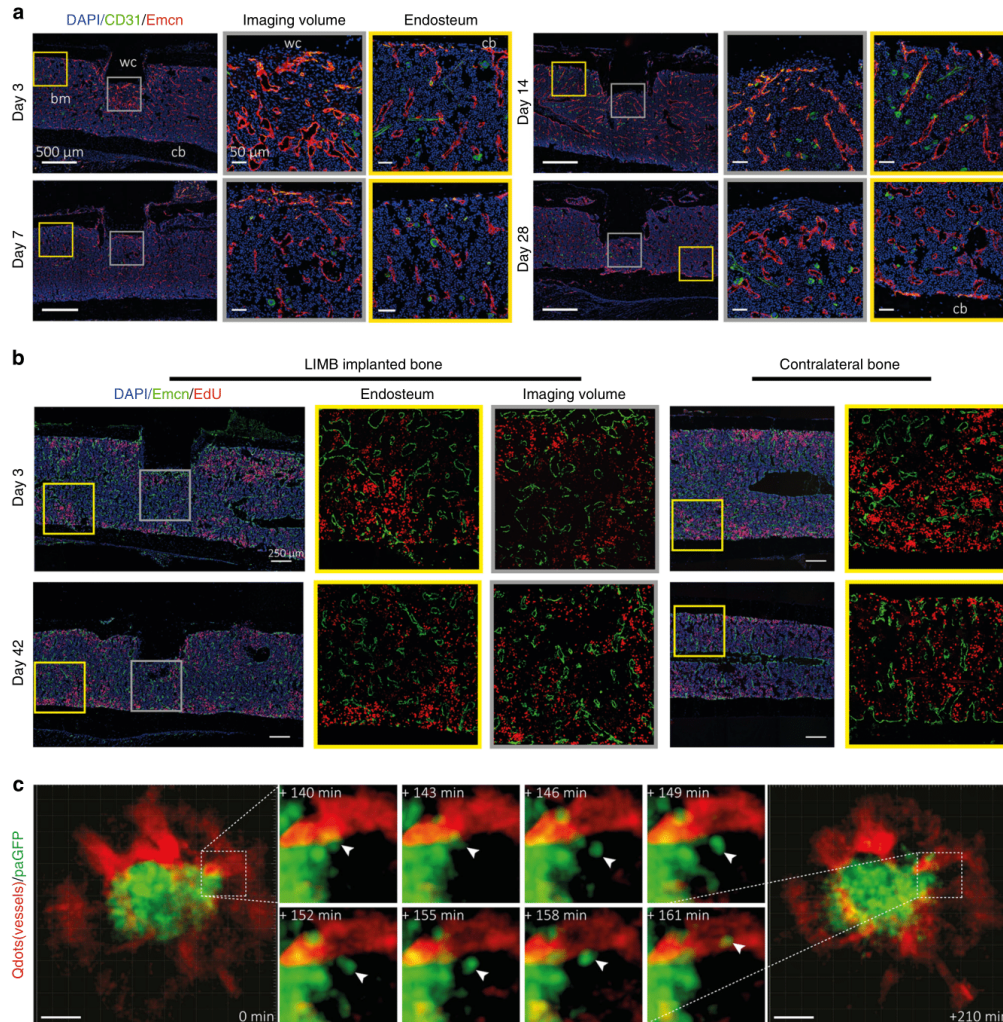


Fig. 7 LIMB and immunofluorescence analysis indicate possible mechanisms of vascular morphological changes deep in the femoral bone marrow, during regeneration, and in steady-state homeostasis. **a** Immunofluorescence analysis shows that type H vessels, characterized by $CD31^{hi}Emcn^{hi}$ -expressing endothelial cells, are induced and present around the implant at day 3 after LIMB implantation. Their presence may vary individually but normalizes within 28 days post-surgery. Sinusoidal and type H vessel morphology adjacent to the wc is irregular in the first week and completely reorganizes to an appearance comparable to vessels found at endosteal areas distant from the injury site ($n = 3$ mice). bm bone marrow, cb cortical bone. Scale bar = 500 μm (left panels). **b** Immunofluorescence analysis after EdU pulse-chase experiments indicates similar EdU-uptake in the bone marrow of LIMB-implanted femurs and contralateral bones. Proliferating endothelial cells were rarely present at late time points after implantation. This result also supports the conclusion that 28 days after LIMB implantation both the bone and the bone marrow reach homeostasis ($n = 3$ mice in each cohort). **c** 3D fluorescence image ($300 \times 300 \times 66 \mu m^3$, left and right panel) acquired by LIMB 26 days post-surgery, in a *paGFP* mouse with the vasculature labeled by Qdots. Photoactivation was performed within a volume of $100 \times 100 \times 9 \mu m^3$ in the center of the image. The fluorescence image was acquired 2 h post activation. Scale bar = 50 μm . The middle panel shows time-lapse 3D images of the inset from the left panel, indicating that *paGFP* fluorescent cells outside the initial photoactivation volume are present 3 h after photoactivation and that they fluctuate in number and position within the tissue. Passive displacement of the relatively immobile stromal and vascular compartments by continuous proliferation and movement of hematopoietic cells is a possible mechanism of tissue and vascular re-localization during homeostasis (see Supplementary Movies 10, 11)

only the bone healing phase, but also allows imaging during post-operative steady-state homeostasis, as demonstrated in this work.

As a microendoscopic approach, LIMB allows imaging of areas between 100 and 500 μm deep within bone marrow tissue, which are not accessible to existing intravital microscopy preparations. Whereas the maximum field of view of 280 μm in diameter and the spatial resolution are comparable to those achieved by the established longitudinal conventional intravital multi-photon microscopy, the imaging volume is fixed. This represents both a benefit, since the implant itself functions as a landmark for orientation in tissue, but also a limitation, since covering the relevant tissue areas can be more challenging than with other imaging methods.

Along that line, as we and others have previously shown³, the deep bone marrow in diaphyseal regions does not show a supra-cellular compartmentalization, in contrast to secondary lymphoid organs, which are divided into zones that primarily host certain immune cell subtypes. In order to address tissue heterogeneity in the bone marrow, we developed various designs of our implant that allow positioning of the GRIN lens at various locations within the bone marrow, based on known anatomical compartmentalization. Hence, LIMB allows the imaging of diaphyseal or metaphyseal areas as well as peri-cortical vs. deep-marrow regions, which are known to differ in their cellular composition. As we demonstrated by imaging sessile plasma cells (which are present in the bone marrow in frequencies of less than 1% of all hematopoietic cells), LIMB is suitable for the analysis of rare cells, despite the rather small field of view. This kind of analysis is crucial to improve our understanding of both hematopoiesis and immunological memory.

Upon fluorescently marking the lumina of blood vessels as a way to identify the same tissue regions in different imaging sessions^{21, 31}, we unexpectedly found the vasculature to be markedly dynamic during steady-state homeostasis. As compared to other tissues, the bone marrow is characterized by a much higher frequency of proliferating cells³, and an additional level of dynamics is added by the motility of hematopoietic cells. There is a constant egress of cells⁵, but cells can also enter the marrow tissue, as in the case of memory T cells or plasma blasts^{34, 37}. Currently, our experiments using different strategies in order to label proliferating cells indicate that dynamics occurring in the non-vascular compartment may affect the positioning of the vessels rather than proliferation of the endothelial cells. Future studies based on LIMB analysis will show whether the observed dynamics are solely caused by a passive displacement of the vessels induced by proliferation or motility of bone marrow cells, or whether they are the result of an active process such as neovascularization, especially in light of recently published findings, which indicate that angiogenesis in the bone marrow mechanistically differs from other organs³⁸. In any case, we expect that our results will have implications on our understanding of bone marrow microenvironment organization. They add complexity to the concept of how various tissue niches within the bone marrow are regulated. In the future we will investigate the impact of stromal network dynamics on the niches, since stromal cells may also contribute to the stability of those niches by acting as a scaffold in the tissue.

Concluding, LIMB is a unique method, which enables us to longitudinally analyze the same tissue areas in the deep bone marrow of individual mice by intravital multi-photon microscopy. Our technique will open up new ways for analyzing both long-term processes occurring with slow dynamics as well as short-term processes, characterized by fast cellular dynamics. LIMB can be applied to image any process occurring in the bone marrow, including regenerative processes, such as bone formation

in adaptation or after injury, as well as tumor formation and bone marrow metastasis, to name only a few examples.

Methods

Two-photon laser-scanning microscopy. Multi-photon fluorescence imaging experiments were performed using a specialized laser-scanning microscope based on a commercial scan head (TriMScope II, LaVision BioTec GmbH, Bielefeld, Germany). We used a 20 \times objective lens (IR-coating, NA 0.45, Olympus, Hamburg, Germany) combined with GRIN lenses (Fig. 1, GRINtech GmbH, Jena, Germany) to focus the excitation laser radiation into the sample and to collect the emitted fluorescence. Detection of the fluorescence signals was accomplished with photomultiplier tubes in the ranges of (466 \pm 20) nm, (525 \pm 25) nm, (593 \pm 20) nm, and (655 \pm 20) nm. paGFP was photoactivated at 840 nm. Both, activated paGFP and GFP were excited at 940 nm and detected at (525 \pm 25) nm. eYFP (*Prx-1:YFP* mice) was excited at 940 nm and detected at (525 \pm 20) nm and (593 \pm 20) nm, while tdRFP was excited at 1100 nm and detected at (593 \pm 20) nm. Blood vessels were labeled with Qdots excited at 940 or 1100 nm and detected at (593 \pm 20) nm. In all imaging experiments we used an average maximum laser power of 10 mW to avoid photodamage, at a typical pixel dwell time of 2 μs . The maximum peak photon flux was 10²⁹ photons $\text{cm}^{-2} \text{s}^{-1}$, in accordance to the values measured using conventional two-photon microscopy. The acquisition time for an image with a field of view of 150 \times 150 μm^2 and a digital resolution of 497 \times 497 pixel was 800 ms, as well as for a field of view of 350 \times 350 μm^2 and a digital resolution of 507 \times 507 pixel. We acquired 70 μm z-stacks (z-step size 6 μm) each 30 s over a total time course of typically 45 min. Calvarial and tibial imaging were performed using the same microscope setup. In contrast to LIMB, we used a 20 \times water-immersion objective for focusing (IR coated, NA 0.95, Olympus, Hamburg, Germany).

Data analysis. Image segmentation and tracking of all cells was performed using segmentation, object-recognition, and tracking plugins in Imaris (Bitplane AG, Zurich, Switzerland). Cell tracks that were present in the field of view for more than 10 recorded time points (i.e., 5 min) were included in the analysis. Statistical analysis of the data was performed using Prism (Graph Pad Software Inc., San Diego, USA).

Mice. All mice used were on a *C57/Bl6J* background. *CD19:tdRFP* fate mapping mice were generated in our lab by crossing *CD19:Cre*²⁸ onto *ROSA26:tdRFP*²⁹ mice. *Prx-1:Cre* mice³⁰ were crossed onto *ROSA26:eYFP* mice (*Prx-1:YFP*). Photoactivatable GFP (*paGFP*) mice, which ubiquitously express paGFP¹⁸, were kindly provided by Prof. M. Nussenzweig. *CX3CR1:GFP* mice express EGFP in monocytes, dendritic cells, NK cells, and brain microglia under control of the endogenous *Cx3cr1* locus³⁹. All mice were bred in the animal facility of the DREZ. All animal experiments were approved by Landesamt für Gesundheit und Soziales, Berlin, Germany, in accordance with institutional, state, and federal guidelines.

Surgical preparation for longitudinal intravital imaging. We used a lateral approach to expose the femoral shaft of the right hind limb of mice anaesthetized with 1.5–2.0% isoflurane. Initially, an incision of ~1.5 cm was made into the shaved and disinfected skin between the knee and hip joint, parallel to the femur. The underlying muscles were dissected and retracted along the delimiting fascia. Then, a 0.65 mm pilot hole in the distal half of the diaphysis was drilled through the cortex using an electric precision drill (FBS 240/E Proxxon GmbH, Föhren, Germany) mounted on a stand to ensure minimal damage to the underlying bone marrow tissue. Ring forceps were applied to fix the bone in position. We placed the TiCP grade 4 implant parallel onto the femoral shaft and drilled the other two pilot holes (0.31 mm) for the bicortical screws manually through the complete shaft. Here, the holes in the implant act as drill templates. When fully inserted, the bone screws lock in the fixation plate, and thus prevent any movement or rotation. The wound was frequently washed during surgery with sterile NaCl solution and sewed with an absorbable surgical thread (Surgicryl Rapid PGA, USP 6-0, SMI, St. Vith, Belgium). Finally, we attached the reference plate. All animals were kept on a temperature-controlled heating device throughout the surgery (Supplementary Fig. 2). For longitudinal calvarial imaging we used a permanent window glued with bone cement onto the calvarial bone, leaving a circular window freely accessible⁴⁰. The window glass was supported by a customized metal ring kindly provided by Dr. Rinnenthal, J.-L. (Charité—Universitätsmedizin, Berlin, Germany).

Clinical scoring system. Total clinical scoring post-surgery was based on behavior and appearance of the individual mice. The total clinical score represents the sum of eight factors (physical appearance, state of mucosae, motoric ability, wound healing, body weight loss, food and water consumption, response to provocation) rated on a scale of 0–3. No animal was scored to a total clinical score higher than 4.

Histochemistry. Femurs were fixed in 4% paraformaldehyde and transferred to 10–30% sucrose/PBS for cryoprotection. Fixed bone sample and implant were covered with Kawamoto's medium (SCEM, Section-Lab Co. Ltd., Hiroshima, Japan) in order to avoid air bubbles during separation. Bones were frozen and cryo-

sectioned using Kawamoto's film method⁴¹. Movat's pentachrome stainings were performed on 7 μm sections⁴². Brightfield images were generated by three-dimensional tile scanning on a Biorevo (BZ-9000, Keyence GmbH, Neu Isenburg, Germany) using the BZ-II Viewer with a 10 \times , NA 0.45 (air) objective lens. Images were stitched using BZ-II Analyzer and processed with Fiji software.

Fluorescence microscopy. Bones were fixed and sectioned as described above. Sections of 7 μm were blocked with 5% FCS/PBS for 30 min and stained with antibodies in 5% FCS/PBS/0.1% Tween for 1–2 h at room temperature: CD45 (1:100, ThermoFisher eBioscience, Frankfurt, Germany, 30-F11), Sca-1-APC (1:200, eBioscience, 17-5981-82), Laminin (1:200, Sigma-Aldrich, Taufkirchen, Germany, L9393), c-kit-PE (1:100, 130-102-542, Miltenyi, Bergisch Gladbach, Germany), Ki-67-bio (1:100, eBioscience, 14-5698-82), Endomucin (1:100, Santa Cruz, sc-65495), CD31-A488 (1:100, R&D Systems, FAB3628G). Sections were washed with PBS/0.1% Tween three times and incubated with secondary Abs (LifeSciences-Sigma-Aldrich, Taufkirchen, Germany) for 1 h at room temperature. Nuclei were stained with 1 $\mu\text{g ml}^{-1}$ DAPI (Sigma-Aldrich) in PBS and mounted with Fluorescent Mounting Medium (DAKO, Hamburg, Germany). Overview images were generated by three-dimensional tile scanning on a LSM710 (Carl Zeiss Microimaging, Jena, Germany) using Zen 2011 software, with either a 10 \times , NA 0.3 (air) objective lens for complete femoral bone marrow sections, or a 20 \times , NA 0.5 (air) objective lens for partial scans (implant area, distal bone). Maximum intensity projection images and stitched overviews were created using Zen 2011 and processed with Fiji. For tracking of CMTPX-labeled transferred cells, splenocytes were isolated and incubated with CellTracker Red CMTPX, according to the manufacturer's protocol (ThermoFisher, Frankfurt, Germany). 1×10^6 splenocytes were transferred to recipient mice. Bones were harvested 4 h after transplantation and femurs were processed as described in the immunofluorescence method section. Sections were stained with DAPI and fluorescent images were generated by three-dimensional tile scanning on a Biorevo (BZ-9000, Keyence GmbH, Neu Isenburg, Germany) using BZ-II Viewer with a 10 \times , NA 0.45 (dry) objective lens. Images were stitched using BZ-II Analyzer and processed with Fiji software.

EdU labeling and staining. Proliferating cells were labeled using EdU at 1.6 mg kg⁻¹ mouse weight injected in PBS intraperitoneally 2 h before sacrifice. Femoral bone sections were stained using the Click-iT EdU Alexa Fluor 647 kit (LifeSciences-Sigma-Aldrich, Taufkirchen, Germany), according to the manufacturer's protocol.

Flow cytometry. Diaphyseal ends including growth plate and secondary ossification centers of femurs were cut off and discarded. An 18 gauge needle was inserted into the distal end of the long bone and the bone marrow was thoroughly flushed out with 5 ml of cold (4°C) MACS buffer (0.5% BSA, 2 mM EDTA in PBS). LIMB implants were removed after flushing. Cells were re-suspended, filtered with a 50 μm cell strainer, spun down 6 min at 75 \times g, and re-suspended in an erythrocyte lysis buffer. After washing, FcR were blocked using antibodies against CD16/32 (DRFZ in house clone 2.4G2, 5 $\mu\text{g ml}^{-1}$) and stained with antibodies on ice for 40 min. After washing the cells were acquired with a FACSsymphony (BD Bioscience, Heidelberg, Germany) system and populations analyzed in FlowJo10. Cell counts were performed on $n = 6$ individuals. Live lymphocytes were divided into the following populations: progenitors: LSK cell (lin⁻sca1⁺ckit⁺), long-term hematopoietic stem cell (LT HSC, lin⁻sca1⁺ckit⁺CD150⁺CD48⁻), short-term HSC (ST HSC, lin⁻sca1⁺ckit⁺CD150⁺CD48⁺), multi-potent progenitor (MPP, lin⁻sca1⁺ckit⁺CD150⁺CD48⁺), common lymphoid progenitor (CLP, LSK⁻IL7R⁺Flk2⁺), common myeloid progenitor (CMP, lin⁻sca1⁻ckit⁺CD34⁺CD16/32⁻), megakaryocyte-erythroid progenitor (MEP, lin⁻sca1⁻ckit⁺CD34⁺CD16/32⁺) and granulocyte-macrophage progenitor (GMP, lin⁻sca1⁻ckit⁺CD34⁺CD16/32⁺), dendritic cell progenitor (DCP, lin⁻sca1⁻Flk2⁺IL7R⁺) B cells: propeB (B220⁺CD19⁻ckit⁺Flk2⁺), preB1 (B220⁺CD19⁺ckit⁺), preB11 (B220⁺CD19⁺ckit⁺IgM⁻CD25⁺), immature B cells (B220⁺CD19⁺ckit⁺IgM⁺IgD⁻), mature B cells (B220⁺CD19⁺ckit⁺IgM⁺IgD⁺), plasma cells (CD138high) T cells CD4 T cells (CD3⁺CD4⁺), CD8 T cells (CD3⁺CD8⁺) innate immune cells: natural killer cells (NK cells, NK1.1⁺), granulocytes (CD11b⁺Gr1⁺), monocytes/macrophages (CD11b⁺Gr1⁻), dendritic cells (DCs, CD11c⁺). Antibodies used: CD19-FITC (1:800, BioLegend, Fell, Germany, 115506), B220-FITC (1:800, BioLegend 103206), Gr1-FITC (1:800, BioLegend 108406), CD3-FITC (1:800, BioLegend 100204), CD11b-FITC (1:800, BioLegend 101206), Ter119-FITC (1:800, BioLegend 116206), IL7R-PE-Cy7 (1:100, BioLegend 135014), B220-BV510 (1:400, BioLegend 103247), CD34-A647 (1:200, eBioscience 51-0341-82), CD16/32-A450 (1:800, eBioscience 48-0161-82), sca1-APC-Cy7 (1:400, BioLegend 108126), Flk2-PE (1:100, BioLegend 135306), CD19-BV650 (1:400, BioLegend 115541), ckit-A700 (1:200, eBioscience 56-1172-82), c-fms-APC (1:200, eBioscience 17-1152-82), ckit-APC (1:200, BioLegend 135108), CD150-PE (1:800, BioLegend 115904), CD48-PE-Cy7 (1:800, BioLegend 560731), sca1-A700 (1:200, eBioscience 56-5981-82), CD138-BV421 (1:800, BioLegend 142508), IgM-APC (1:400, BioLegend 406509), CD25-APC-Cy7 (1:400, BioLegend 102026), IgD-A488 (0.7 $\mu\text{g ml}^{-1}$, in house, clone 11.26c), CD4-PE-Cy7 (1:800, eBioscience 25-0042-82), CD8-APC (1:800, BioLegend 100712), CD3-APC-Cy7 (1:200, eBioscience 47-0031-82), CD11c-FITC (1:800, BioLegend 117306), NK1.1-PE (1:800, BioLegend

108707), Gr1-PB (1:800, BioLegend 108429), CD11b-A700 (1:800, eBioscience 56-0112-82).

Mouse activity analysis. Analysis of mouse activity and motility was performed using radio-frequency identification (RFID) technology to identify and track individual mice within a cage. Animals were subcutaneously tagged with bio-compatible glass-encapsulated RFID transponders (EURO I.D., Frechen, Germany) and were detected by a 2 \times 4 sensor plate system (Phenosys, Berlin, Germany) underneath the cage. The frequency of crossed sensors serves as an approximate activity measure. Physical activity was normalized to the mean value of activity measured over 3 days before surgery. Before that, mice had been placed in the cage for at least 2 days. The relative change in activity for each mouse is displayed. For sham treatment, animals were put under anesthesia.

Ex vivo μCT . Femoral bones were harvested and fixed as described above. Fixed bones were measured in 20–30% sucrose solution using the vivaCT 40 (Scanco Medical AG, Brüttisellen, Switzerland). Scans were performed with 70 kVp and an isotropic voxel size of 10.5 μm . Reconstructed scans were converted into tiff-stacks for further data analysis. Bone morphological measurements from μCT 3D reconstructions were performed using the intensity. For bone thickness under the fixation plate and on the opposite site of the bone, areas were chosen as shown in Fig. 2e. For each position, the intensity profile was approximated with two Gaussian curves. The width of each Gaussian curve was considered to represent bone thickness at the respective position. For intact contralateral femurs, we performed the same measurements choosing a mirrored position of the bone to account for the fact that the LIMB femurs are always right femurs and the contralateral bones are left femurs.

Data availability. All relevant data are saved on the institutional servers. The data that support the findings of this study are available from the corresponding authors upon reasonable request.

Received: 14 March 2017 Accepted: 25 September 2017

Published online: 18 December 2017

References

- Ramasamy, S. K. et al. Regulation of hematopoiesis and osteogenesis by blood vessel-derived signals. *Annu. Rev. Cell Dev. Biol.* **32**, 649–675 (2016).
- Tokoyoda, K., Hauser, A. E., Nakayama, T. & Radbruch, A. Organization of immunological memory by bone marrow stroma. *Nat. Rev. Immunol.* **10**, 193–200 (2010).
- Zehentmeier, S. et al. Static and dynamic components synergize to form a stable survival niche for bone marrow plasma cells. *Eur. J. Immunol.* **44**, 2306–2317 (2014).
- Roth, K. et al. Tracking plasma cell differentiation and survival. *Cytometry A* **85**, 15–24 (2014).
- Beck, T. C., Gomes, A. C., Cyster, J. G. & Pereira, J. P. CXCR4 and a cell-extrinsic mechanism control immature B lymphocyte egress from bone marrow. *J. Exp. Med.* **211**, 2567–2581 (2014).
- Itkin, T. et al. Distinct bone marrow blood vessels differentially regulate haematopoiesis. *Nature* **532**, 323–328 (2016).
- Kusumbe, A. P., Ramasamy, S. K. & Adams, R. H. Coupling of angiogenesis and osteogenesis by a specific vessel subtype in bone. *Nature* **507**, 323–328 (2014).
- Junt, T. et al. Dynamic visualization of thrombopoiesis within bone marrow. *Science* **317**, 1767–1770 (2007).
- Kohler, A. et al. G-CSF-mediated thrombopoietin release triggers neutrophil motility and mobilization from bone marrow via induction of Cxcr2 ligands. *Blood* **117**, 4349–4357 (2011).
- Mazo, I. B. et al. Bone marrow is a major reservoir and site of recruitment for central memory CD8⁺ T cells. *Immunity* **22**, 259–270 (2005).
- Mazo, I. B. & von Andrian, U. H. Adhesion and homing of blood-borne cells in bone marrow microvessels. *J. Leukoc. Biol.* **66**, 25–32 (1999).
- Lo Celso, C., Lin, C. P. & Scadden, D. T. In vivo imaging of transplanted hematopoietic stem and progenitor cells in mouse calvarium bone marrow. *Nat. Protoc.* **6**, 1–14 (2011).
- Wu, J. W., Runnels, J. M. & Lin, C. P. Intravital imaging of hematopoietic stem cells in the mouse skull. *Methods Mol. Biol.* **1185**, 247–265 (2014).
- Kohler, A. et al. Altered cellular dynamics and endosteal location of aged early hematopoietic progenitor cells revealed by time-lapse intravital imaging in long bones. *Blood* **114**, 290–298 (2009).
- Chen, Y., Maeda, A., Bu, J. & DaCosta, R. Femur window chamber model for in vivo cell tracking in the murine bone marrow. *J. Vis. Exp.* **113**, e54205 (2016).

16. Kim, S., Lin, L., Brown, G. A., Hosaka, K. & Scott, E. W. Extended time-lapse in vivo imaging of tibia bone marrow to visualize dynamic hematopoietic stem cell engraftment. *Leukemia* **31**, 1582–1592 (2017).
17. Park, D. et al. Endogenous bone marrow MSCs are dynamic, fate-restricted participants in bone maintenance and regeneration. *Cell Stem Cell* **10**, 259–272 (2012).
18. Hawkins, E. D. et al. T-cell acute leukaemia exhibits dynamic interactions with bone marrow microenvironments. *Nature* **538**, 518–522 (2016).
19. Trachtenberg, J. T. et al. Long-term in vivo imaging of experience-dependent synaptic plasticity in adult cortex. *Nature* **420**, 788–794 (2002).
20. Farrar, M. J., Wise, F. W., Fetcho, J. R. & Schaffer, C. B. In vivo imaging of myelin in the vertebrate central nervous system using third harmonic generation microscopy. *Biophys. J.* **100**, 1362–1371 (2011).
21. Barretto, R. P. et al. Time-lapse imaging of disease progression in deep brain areas using fluorescence microendoscopy. *Nat. Med.* **17**, 223–228 (2011).
22. Lewandowski, D. et al. In vivo cellular imaging pinpoints the role of reactive oxygen species in the early steps of adult hematopoietic reconstitution. *Blood* **115**, 443–452 (2010).
23. Matthys, R. & Perren, S. M. Internal fixator for use in the mouse. *Injury* **40**, S103–S109 (2009).
24. Perren, S. M. Evolution of the internal fixation of long bone fractures. The scientific basis of biological internal fixation: choosing a new balance between stability and biology. *J. Bone Joint Surg. Br.* **84**, 1093–1110 (2002).
25. Gerber, C., Mast, J. W. & Ganz, R. Biological internal fixation of fractures. *Arch. Orthop. Trauma Surg.* **109**, 295–303 (1990).
26. Perren S. M., Cordey J., Rahn B. A., Gautier E. & Schneider E. Early temporary porosis of bone induced by internal fixation implants. A reaction to necrosis, not to stress protection? *Clin. Orthop. Relat. Res.* **232**, 139–151 (1988).
27. Hyldahl, C., Pearson, S., Tepic, S. & Perren, S. M. Induction and prevention of pin loosening in external fixation: an in vivo study on sheep tibiae. *J. Orthop. Trauma* **5**, 485–492 (1991).
28. Victoria, G. D. et al. Germinal center dynamics revealed by multiphoton microscopy with a photoactivatable fluorescent reporter. *Cell* **143**, 592–605 (2010).
29. Kusumbe, A. P. et al. Age-dependent modulation of vascular niches for haematopoietic stem cells. *Nature* **532**, 380–384 (2016).
30. Bremer, D. et al. Longitudinal intravital imaging of the retina reveals long-term dynamics of immune infiltration and its effects on the glial network in experimental autoimmune uveoretinitis, without evident signs of neuronal dysfunction in the ganglion cell layer. *Front. Immunol.* **7**, 642 (2016).
31. Gibson, V. B. et al. A novel method to allow noninvasive, longitudinal imaging of the murine immune system in vivo. *Blood* **119**, 2545–2551 (2012).
32. Sapozhnikov, A. et al. Perivascular clusters of dendritic cells provide critical survival signals to B cells in bone marrow niches. *Nat. Immunol.* **9**, 388–395 (2008).
33. Cariappa, A. et al. Perisinusoidal B cells in the bone marrow participate in T-independent responses to blood-borne microbes. *Immunity* **23**, 397–407 (2005).
34. Tokoyoda, K. et al. Professional memory CD4⁺ T lymphocytes preferentially reside and rest in the bone marrow. *Immunity* **30**, 721–730 (2009).
35. Sercan Alp, O. et al. Memory CD8(+) T cells colocalize with IL-7(+) stromal cells in bone marrow and rest in terms of proliferation and transcription. *Eur. J. Immunol.* **45**, 975–987 (2015).
36. Tokoyoda, K., Egawa, T., Sugiyama, T., Choi, B. I. & Nagasawa, T. Cellular niches controlling B lymphocyte behavior within bone marrow during development. *Immunity* **20**, 707–718 (2004).
37. Hauser, A. E. et al. Chemotactic responsiveness toward ligands for CXCR3 and CXCR4 is regulated on plasma blasts during the time course of a memory immune response. *J. Immunol.* **169**, 1277–1282 (2002).
38. Ramasamy, S. K., Kusumbe, A. P., Wang, L. & Adams, R. H. Endothelial Notch activity promotes angiogenesis and osteogenesis in bone. *Nature* **507**, 376–380 (2014).
39. Jung, S. et al. Analysis of fractalkine receptor CX(3)CR1 function by targeted deletion and green fluorescent protein reporter gene insertion. *Mol. Cell Biol.* **20**, 4106–4114 (2000).
40. Fuhrmann, M., Mitteregger, G., Kretzschmar, H. & Herms, J. Dendritic pathology in prion disease starts at the synaptic spine. *J. Neurosci.* **27**, 6224–6233 (2007).
41. Kawamoto, T. Use of a new adhesive film for the preparation of multi-purpose fresh-frozen sections from hard tissues, whole-animals, insects and plants. *Arch. Histol. Cytol.* **66**, 123–143 (2003).
42. Movat, H. Z. Demonstration of all connective tissue elements in a single section; pentachrome stains. *AMA Arch. Pathol.* **60**, 289–295 (1955).

Acknowledgements

We thank Patrick Thiemann and Manuela Ohde for assistance with animal care. This work was supported by DFG FOR 2165 (NI1167/4-1 and NI1167/4-2 to R.A.N. and HA5354/6-1 and HA5354/6-2 to A.E.H.), TRR130, TPC01 (to R.A.N. and A.E.H.), TP17 (to A.E.H.) and TP16 (to H.D.C.) and HA5354/8-1 to A.E.H. D.R. and J.S. are members of the Berlin-Brandenburg School for Regenerative Therapies (BSRT). We would like to thank the Charité-Universitätsmedizin Electron Microscopy Facility (Prof. S. Bachmann) for help with experiments. The authors thank Randy Lindquist for proofreading of the manuscript.

Author contributions

R.A.N., A.E.H., D.R. and J.S. designed the study, analyzed data and interpreted results. R.A.N., A.E.H., D.R., J.S., R.G., G.P., A.R. and S.Z. performed experiments. R.M., R.N., K.S.-B. and G.D. provided expertise for the implant design, surgery and Movat's pentachrome histochemical staining. F.M. provided expertise in the analysis of HSCs subsets frequencies and interpretation of these data with respect to the characterization of post-surgical homeostasis. Y.W., H.-D.C. and S.N. helped with mouse activity analysis. R.A.N. and A.E.H. wrote the manuscript.


Additional information

Supplementary Information accompanies this paper at <https://doi.org/10.1038/s41467-017-01538-9>.

Competing interests: R.M. and R.N. (RISystem AG, Davos, Switzerland) declare competing financial interests. The implant for longitudinal imaging will be commercialized by RISystem AG, Davos, Switzerland. The remaining authors declare no competing financial interests.

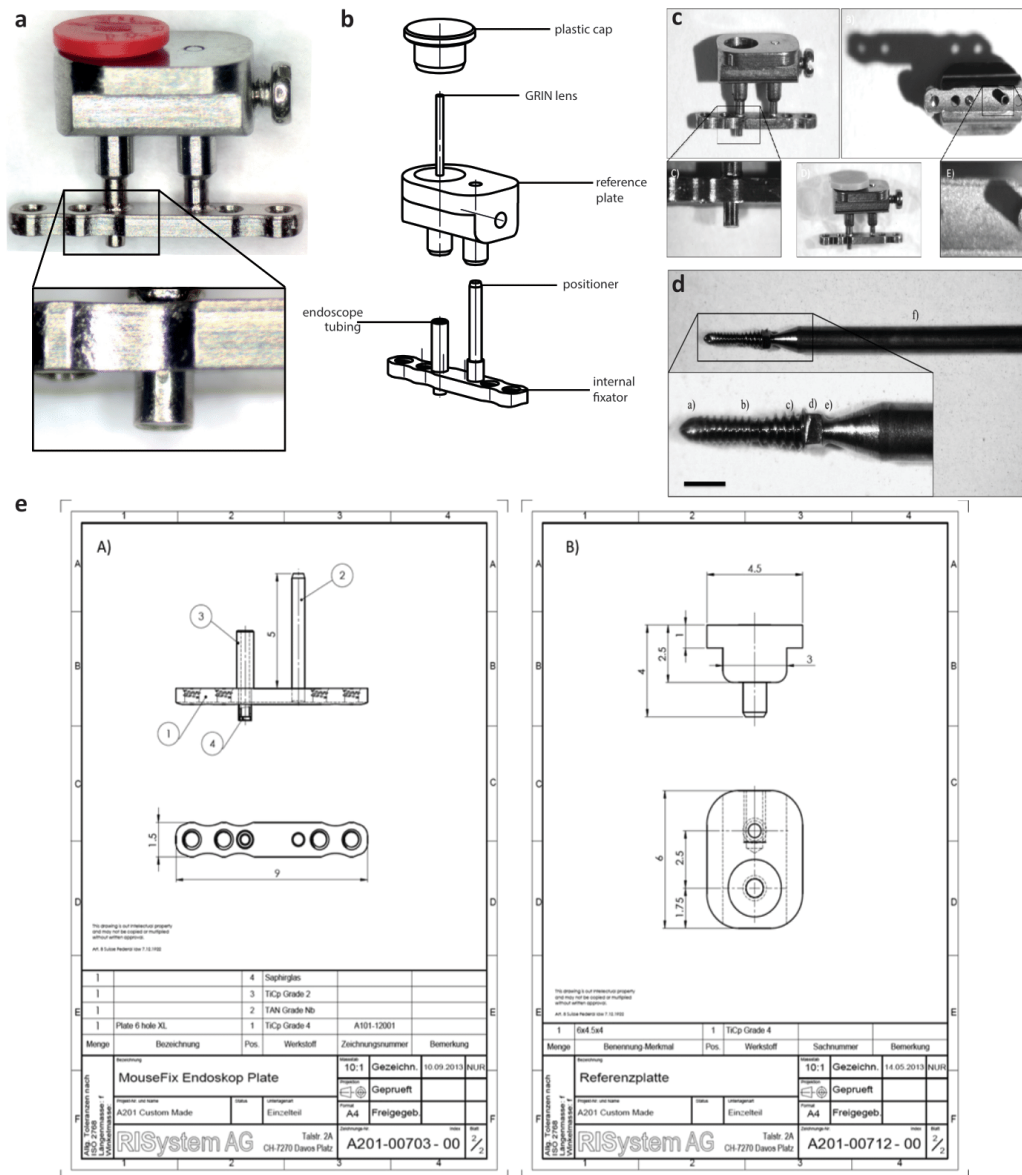
Reprints and permission information is available online at <http://npg.nature.com/reprintsandpermissions/>

Publisher's note: Springer Nature remains neutral with regard to jurisdictional claims in published maps and institutional affiliations.

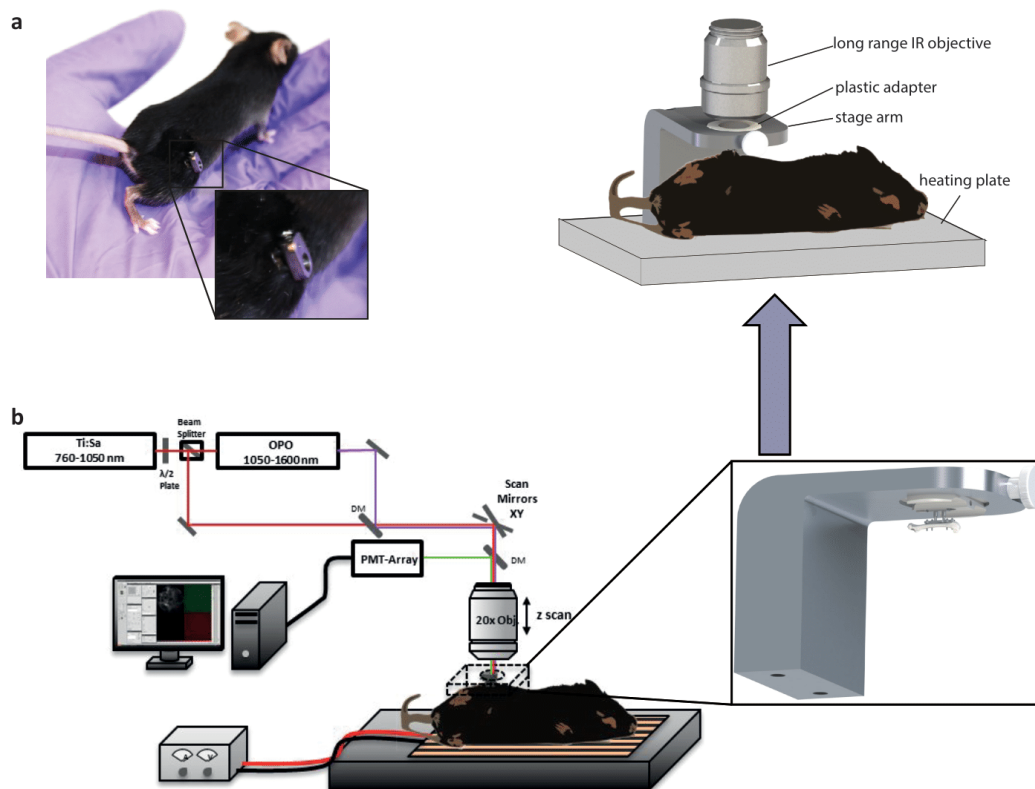
 **Open Access** This article is licensed under a Creative Commons Attribution 4.0 International License, which permits use, sharing, adaptation, distribution and reproduction in any medium or format, as long as you give appropriate credit to the original author(s) and the source, provide a link to the Creative Commons license, and indicate if changes were made. The images or other third party material in this article are included in the article's Creative Commons license, unless indicated otherwise in a credit line to the material. If material is not included in the article's Creative Commons license and your intended use is not permitted by statutory regulation or exceeds the permitted use, you will need to obtain permission directly from the copyright holder. To view a copy of this license, visit <http://creativecommons.org/licenses/by/4.0/>.

© The Author(s) 2017

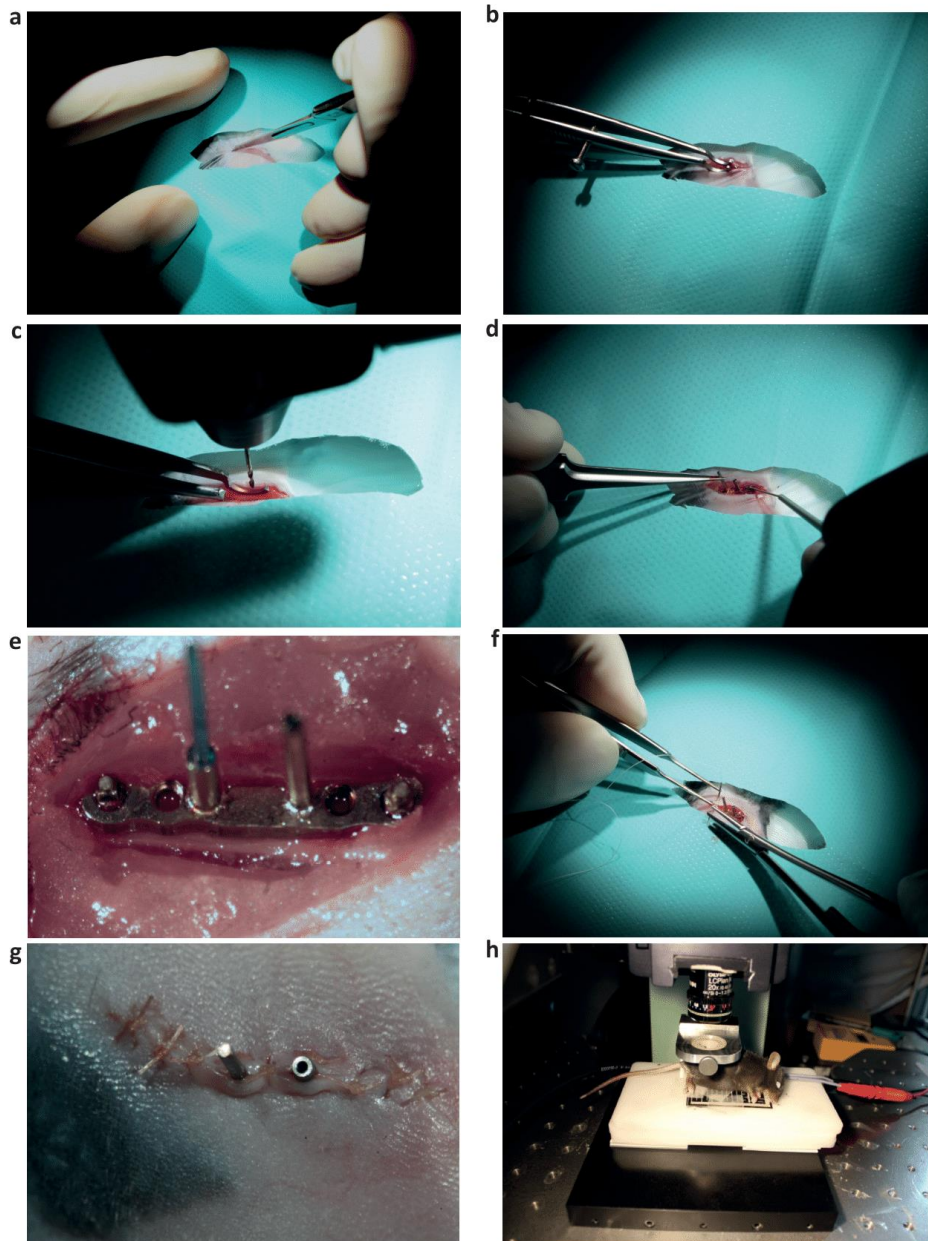
8.2 Reismann et al., 2017 – Supporting Material



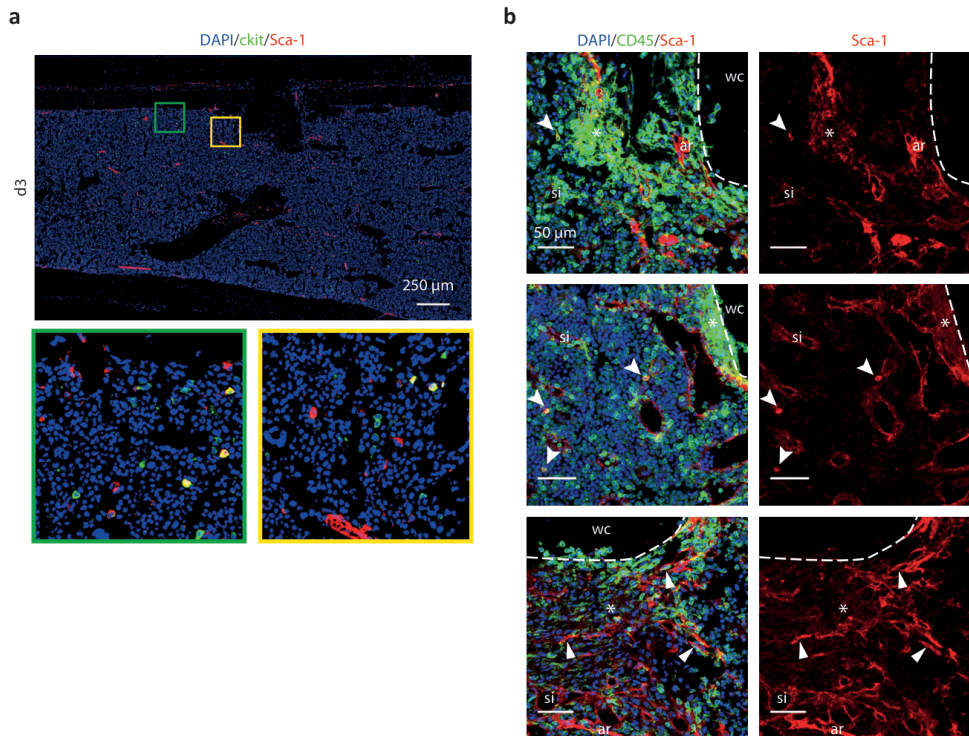
Supplementary Figure 1 | Assembly and technical specifications of the LIMB microendoscope implant. **(a)** The titanium alloy (medical grade) implant consists of two parts that are assembled at the end of the surgery. The extracorporeal reference plate is attached to the positioner and the endoscope tubing and fixed with a screw (M1x2). **(b)** Exploded assembly drawing of the LIMB setup. The plastic cap prevents the endoscope from dust and smaller particles of the cage bedding. The GRIN lens is fit into the endoscope tubing. The endoscope tubing has an inner diameter of 450 μm and an outer diameter of 650 μm . Both, endoscope tubing and positioner, are micro-welded to the internal fixator. **(c)** The sapphire window ($d = 500 \mu\text{m}$), which seals the tubing at the intramedullary end, is pressed into a recess (right inset). The outer tip ends in the conical recess of the reference plate (left inset) and can be accessed by the microscope objective, when the plastic cap is removed. The reference plate is used for the alignment of the GRIN lens with respect to the microscope objective. It holds the implant and the femur in a stable position under a customized imaging stage (Supplementary Figure 2). **(d)** The bicortical screw (RISystem, Davos, Switzerland) has two different threads b) and c), whereas b) locks into the bone and c) into the fixator plate. d) is the square box wrench for removal of the screw and e) the predetermined breaking point to shear off the shaft f) from the screw at a defined torque. All implanted materials can be autoclaved and are resistant to organic solvents. **(e)** Technical drawings of both parts with relevant dimensioning.



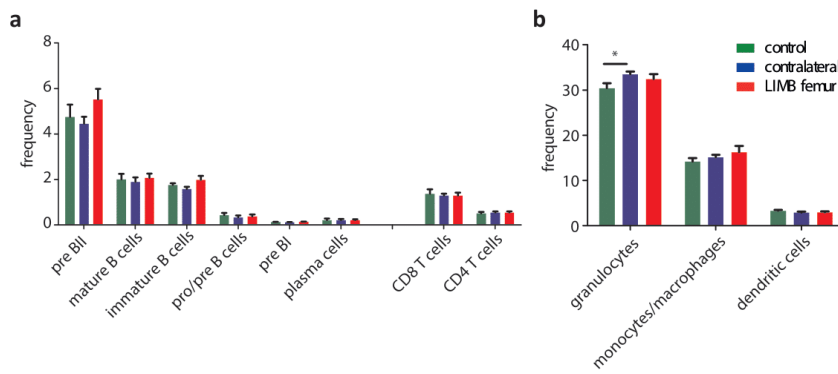
Supplementary Figure 2 | Microscope setup for longitudinal intravital imaging of the bone marrow in mice. (a) Photograph of a mouse carrying the LIMB implant 28 days post-surgery. Externally, only the reference plate is visible (inset). (b) The mouse is positioned under the two-photon microscope using a customized plastic adapter and stage, so that the GRIN lens is aligned parallel to the optical axis of the microscope objective lens for optimal illumination of the bone marrow tissue. During time lapse image acquisition the animals lay on a controlled heating plate to maintain a constant body temperature.



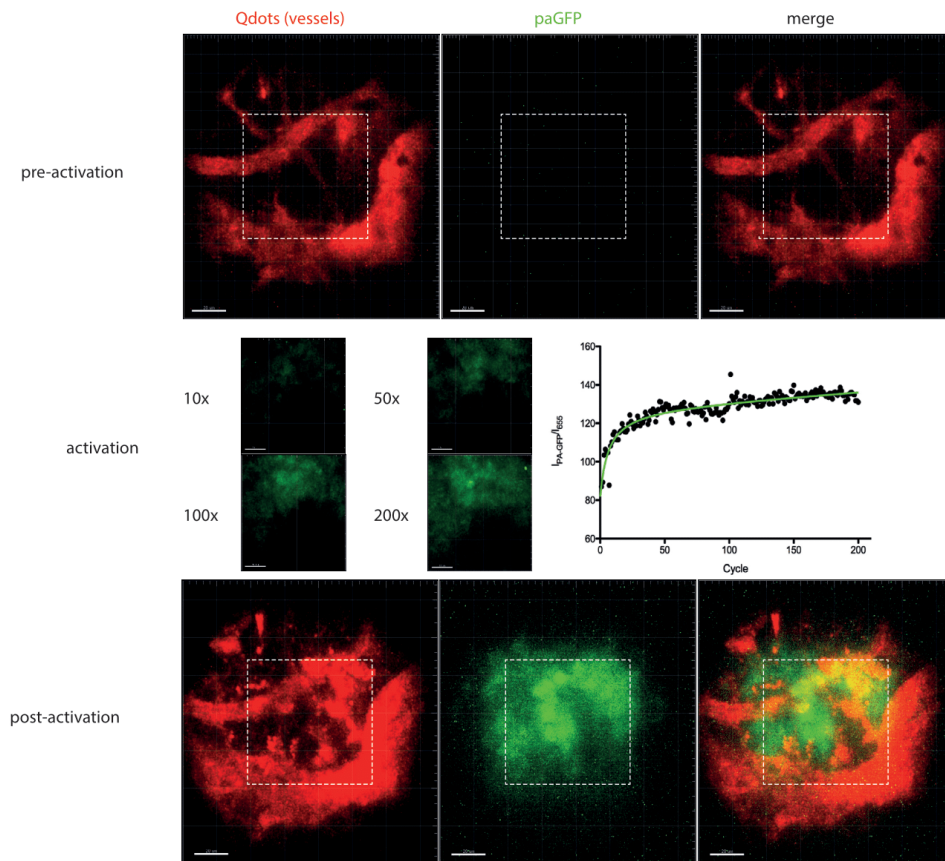
Supplementary Figure 3 | Surgical procedure for implantation of the LIMB-implant. (a) A surgical incision is placed into the shaved and disinfected skin between the knee and hip joint, parallel to the femur in order to expose the femoral shaft of the right hind limb. (b) A ring forceps is used to fixate the bone. (c) For drilling of the pilot hole in the distal half of the diaphysis an electric precision drill and a stand is used. (d) The LIMB implant system is placed parallel onto the femur and (e) bicortical screws are inserted to complete the fixation. (f) The wound was closed with a absorbable surgical thread. In (g) the implant after wound closure and before attachment of the reference plate is shown. (h) Anesthetized mouse under the two-photon microscope.



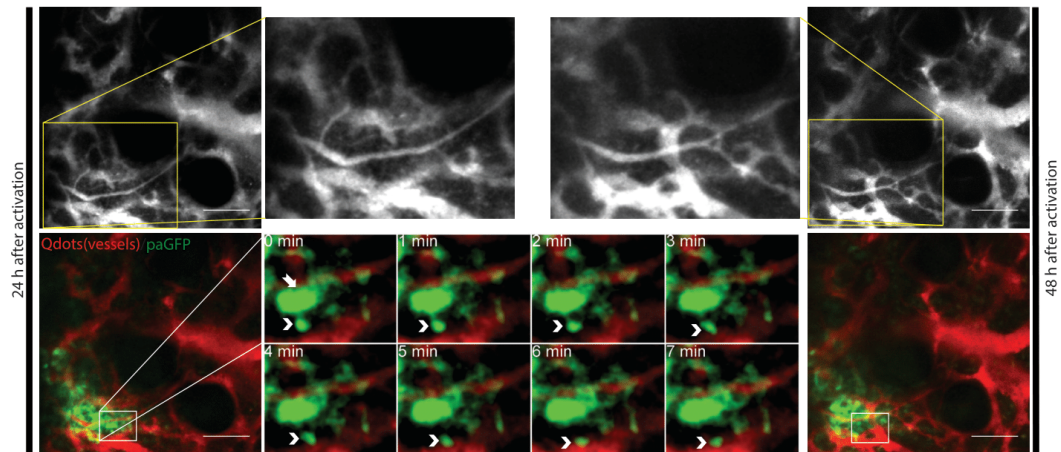
Supplementary Figure 4 | Immunofluorescence analysis early post-surgery. **(a)** Immunofluorescence staining for ckit+sca1+ cells (yellow) shows presence of this HSPC enriched population in endosteal areas and adjacent to the implant window as early as 3 days post-surgery indicating the maintenance of hematopoietic precursor retention in the presence of the LIMB implant **(b)** The tissue adjacent to the window cavity (wc) after removal of the implant displays CD45+ cell (green) accumulations 3 days post-surgery with predominantly rounded nuclei and areas of dim Sca-1 expression (asterisks). Sca-1hi arteriolar endothelial cells with elongated nuclei (triangles) spread into the damaged tissue indicating vascularization. Some cells are Sca-1+CD45+ (arrow heads), and might represent hematopoietic precursors. Sinusoids, si; arterioles, ar.



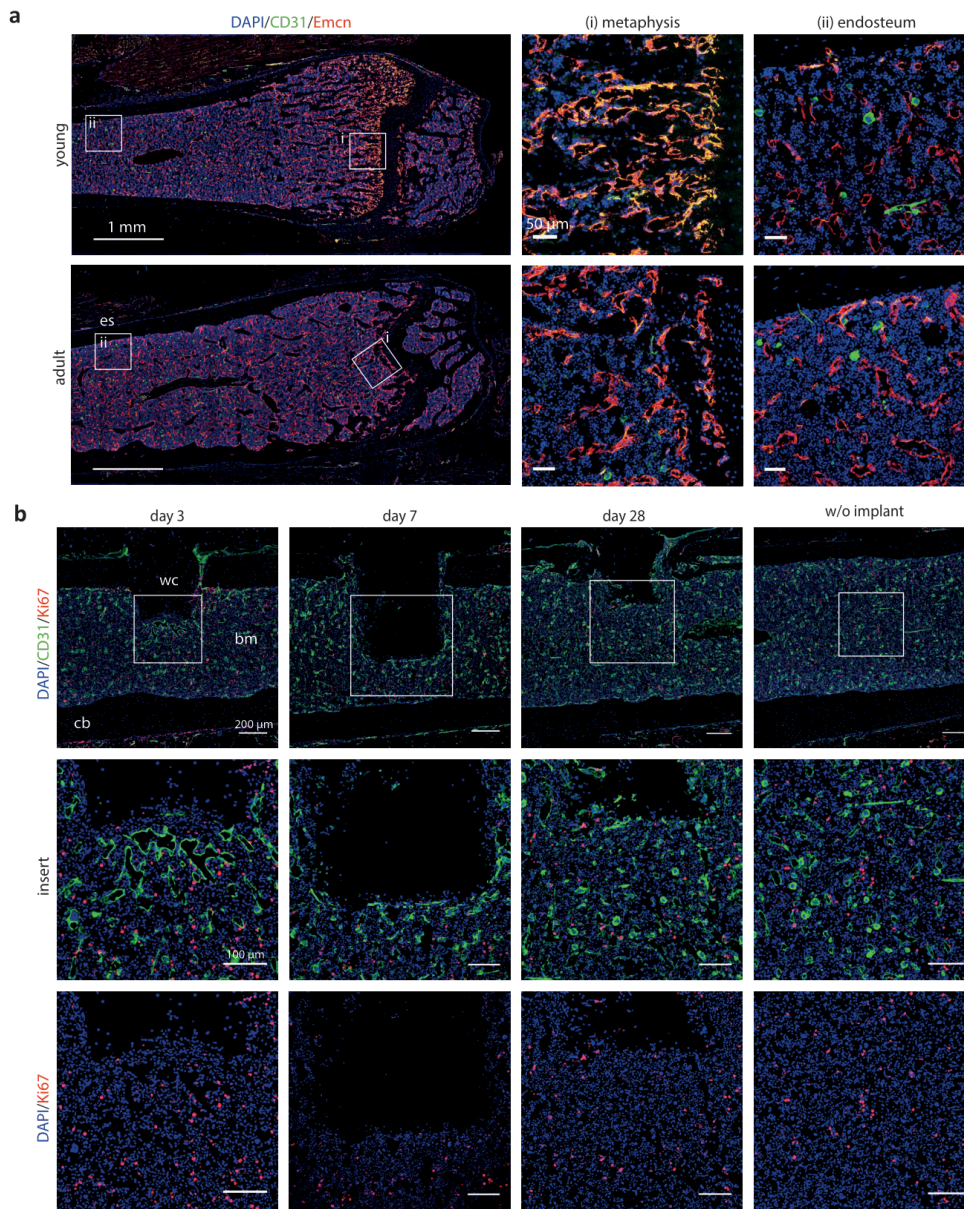
Supplementary Figure 5 | Flow cytometric analysis demonstrates that LIMB has no effect on bone marrow cell populations. Flow cytometry analysis of femurs with the LIMB implant, their contralateral femurs and femurs of control mice. Similar frequencies and cell counts of various leukocyte populations indicate no effect of the presence of the LIMB implant on bone marrow cell composition for (a) B and T cell populations and (b) innate immune cells. (error bars represent s.e.m., statistical analysis: t-test, * - $p = 0.0318$, $n = 8$ LIMB-implanted mice, $n = 8$ control mice, two independent experiments).



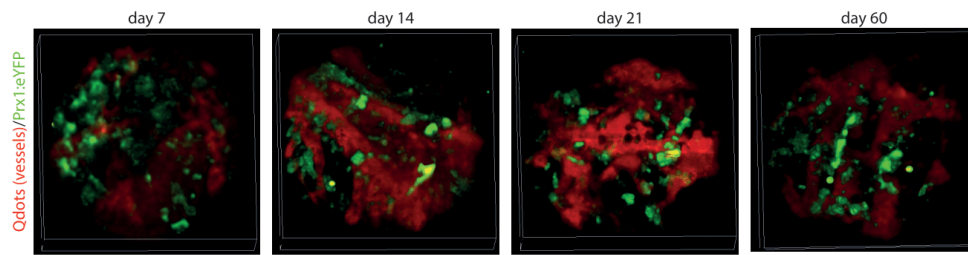
Supplementary Figure 6 | Photoactivation in the bone marrow of paGFP mice using LIMB. Mice ubiquitously expressing paGFP received the LIMB implant and were injected prior to the imaging session with Qdots to label the vasculature. In the course of a photoactivation experiment, first, the pre-activation state of the tissue in the volume-of-view was recorded (upper panel). The vessels were clearly visible but no signal above background was recorded in the paGFP-channel at an excitation wavelength of 940 nm. For photoactivation, the excitation wavelength was tuned to 840 nm and the scanning volume (x, y, z) was reduced from $150 \times 150 \times 30 \mu\text{m}^3$ to $75 \times 75 \times 30 \mu\text{m}^3$ (step size $3 \mu\text{m}$ each) or from $300 \times 300 \times 70 \mu\text{m}^3$ to $100 \times 100 \times 9 \mu\text{m}^3$ (step size $3 \mu\text{m}$ each). During the 200 activation cycles over the time course of 40 min, we recorded the fluorescence signals from the Qdots (vessels) and paGFP as shown in the middle panel. The increase in fluorescence intensity of paGFP ($I_{\text{PA-GFP}}$) normalized to the fluorescence intensity of the vessels (I_{655}) over the number of activation cycles is given in the graph. For multi-photon image acquisition post-activation the excitation wavelength was tuned back to 940 nm and the volume-of-view increased. The same channels were used to record again a $150 \times 150 \times 30 \mu\text{m}^3$ volume, which clearly shows the activated paGFP inside the cells (lower panel). Scale bar = $20 \mu\text{m}$ in the upper and lower panel, scale bar = $15 \mu\text{m}$ in the middle panel.



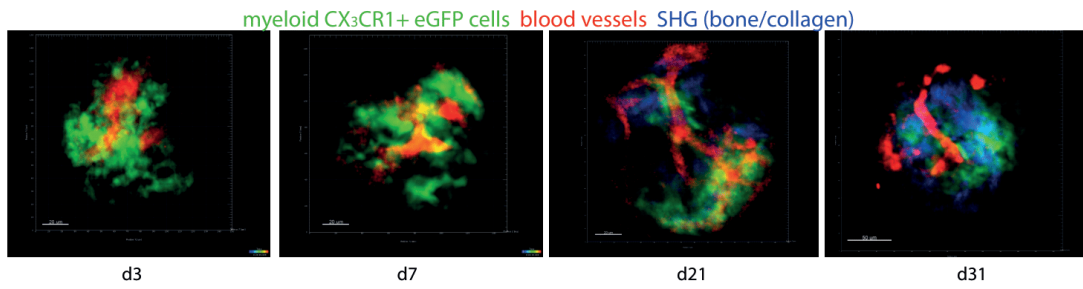
Supplementary Figure 7 | Similar motility patterns of hematopoietic cells in the calvarial bone marrow after photoactivation as compared to the femoral bone marrow. The photoactivation was performed within a volume of a $150 \times 150 \times 9 \mu\text{m}^3$ region within the $500 \times 500 \times 66 \mu\text{m}^3$ field of view. The fluorescence images were longitudinally acquired 24 h and 48 h after activation. The upper panel shows the vessel network in the calvarial bone and bone marrow (gray) 24 h after activation and 48 h after activation with enlarged inserts demonstrating changes in the vasculature within one day. The lower panel shows vessels in red and activated paGFP in green. The lower middle panel shows time-lapse 3D images of the inset in the left panel, indicating paGFP fluorescent cells migrate out of the initial photoactivation volume 24 h after photoactivation. They are fluctuating in number and position within the tissue within short periods of time (7 min). Scale bars = 100 μm .



Supplementary Figure 8 | Presence of type H vessels in the bone marrow in different age cohorts and proliferation of bone marrow cells assessed by KI-67 staining. **(a)** Immunofluorescence analysis shows that type H vessels (Emcn^{hi}CD31^{hi}) are more abundant at the femoral growth plate of young mice (4 weeks old) as compared to old mice (18 weeks old). **(b)** Immunofluorescence analysis of nuclear Ki67 hardly stains for endothelial cells. Proliferation was heterogeneously distributed at different times, similar to bones without (w/o) implant.



Supplementary Figure 9 | LIMB analysis in Prx1:YFP mice reveals continuous remodeling of the stroma compartment in the mouse femur over months. Prx1:YFP mice, which express eYFP in stromal and endothelial cells, received the LIMB implant and were injected prior to each imaging session with Qdots to label the vasculature. During the bone healing phase, at day 7, 14 and 21 post-surgery, a strong reshaping of the stromal network becomes evident from 3D fluorescence imaging in the same individual. The changes continue also at day 60 post-surgery under homeostatic conditions. Imaging volume $150 \times 150 \times 66 \mu\text{m}^3$.



Supplementary Figure 10 | Repeated LIMB imaging using a short (500 μm long) endoscope tubing in a CX₃CR1 eGFP mouse. 3D reconstructions of fluorescence images at day 3, 7, 21 and 31 post-surgery are depicted. Myeloid CX₃CR1+ cells are depicted in green, blood vessels labeled by Qdots in red and second harmonic generation (SHG) originating from collagen and bone in blue. This time course reveals the initial inflammatory phase, followed by vascular remodeling and finally by soft tissue and bone growth, after drill hole injury. Hence, after 31 days we observe in front of the LIMB microendoscope a situation similar to that expected in endosteal regions.

8.3 Stefanowski et al., 2019 – Spatial Distribution of Macrophages During Callus Formation and Maturation Reveals Close Crosstalk Between Macrophages and Newly Forming Vessels

The following presents the publication

Stefanowski, J.*, Lang, A.*, Rauch, A., Aulich, L., Köhler, M., Fiedler, A.F., Buttgereit, F., Schmidt-Bleek, K., Duda, G.N., Gaber, T., Niesner, R.A., Hauser, A.E., 2019. Spatial Distribution of Macrophages During Callus Formation and Maturation Reveals Close Crosstalk Between Macrophages and Newly Forming Vessels. *Front. Immunol.* 10. Impact Factor 3.124 <https://doi.org/10.3389/fimmu.2019.02588> (*shared first-coauthor)

as a part of this dissertation. For optimal pdf and image quality or the publication's digital supporting information, such as movies access the publisher's website under the digital object identifiers of the selected publication. All information is publicly available.



Spatial Distribution of Macrophages During Callus Formation and Maturation Reveals Close Crosstalk Between Macrophages and Newly Forming Vessels

OPEN ACCESS

Edited by:

Anita Ignatius,
University of Ulm, Germany

Reviewed by:

Markus H. Hoffmann,
University of Erlangen
Nuremberg, Germany
Jan Tuckermann,
University of Ulm, Germany

*Correspondence:

Anja E. Hauser
hauser@drfz.de;
anja.hauser-hankeln@charite.de

† These authors have contributed
equally to this work

Specialty section:

This article was submitted to
Molecular Innate Immunity,
a section of the journal
Frontiers in Immunology

Received: 30 July 2019

Accepted: 18 October 2019

Published: 26 November 2019

Citation:

Stefanowski J, Lang A, Rauch A,
Aulich L, Köhler M, Fiedler AF,
Buttgereit F, Schmidt-Bleek K,
Duda GN, Gaber T, Niesner RA and
Hauser AE (2019) Spatial Distribution
of Macrophages During Callus
Formation and Maturation Reveals
Close Crosstalk Between
Macrophages and Newly Forming
Vessels. *Front. Immunol.* 10:2588.
doi: 10.3389/fimmu.2019.02588

Jonathan Stefanowski^{1,2†}, Annemarie Lang^{1,2,3†}, Ariana Rauch², Linus Aulich², Markus Köhler², Alexander F. Fiedler², Frank Buttgereit^{1,2,3}, Katharina Schmidt-Bleek^{3,4}, Georg N. Duda^{3,4}, Timo Gaber^{1,2,3}, Raluca A. Niesner^{2,5} and Anja E. Hauser^{1,2*}

¹ Department of Rheumatology and Clinical Immunology, Charité—Universitätsmedizin Berlin, Corporate Member of Freie Universität Berlin, Humboldt-Universität zu Berlin, and Berlin Institute of Health, Berlin, Germany, ² German Rheumatism Research Centre (DRFZ) Berlin, a Leibniz Institute, Berlin, Germany, ³ Berlin-Brandenburg Center for Regenerative Therapies, Charité—Universitätsmedizin Berlin, Corporate Member of Freie Universität Berlin, Humboldt-Universität zu Berlin, and Berlin Institute of Health, Berlin, Germany, ⁴ Julius Wolff Institute for Biomechanics and Musculoskeletal Regeneration, Charité—Universitätsmedizin Berlin, Corporate Member of Freie Universität Berlin, Humboldt-Universität zu Berlin, and Berlin Institute of Health, Berlin, Germany, ⁵ Dynamic and Functional in vivo Imaging, Department of Veterinary Medicine, Freie Universität Berlin, Berlin, Germany

Macrophages are essential players in the process of fracture healing, acting by remodeling of the extracellular matrix and enabling vascularization. Whilst activated macrophages of M1-like phenotype are present in the initial pro-inflammatory phase of hours to days of fracture healing, an anti-inflammatory M2-like macrophage phenotype is supposed to be crucial for the induction of downstream cascades of healing, especially the initiation of vascularization. In a mouse-osteotomy model, we provide a comprehensive characterization of vessel (CD31⁺, Emcn⁺) and macrophage phenotypes (F4/80, CD206, CD80, Mac-2) during the process of fracture healing. To this end, we phenotype the phases of vascular regeneration—the expansion phase (d1–d7 after injury) and the remodeling phase of the endothelial network, until tissue integrity is restored (d14–d21 after injury). Vessels which appear during the bone formation process resemble type H endothelium (CD31^{hi}Emcn^{hi}), and are closely connected to osteoprogenitors (Runx2⁺, Osx⁺) and F4/80⁺ macrophages. M1-like macrophages are present in the initial phase of vascularization until day 3 post osteotomy, but they are rare during later regeneration phases. M2-like macrophages localize mainly extramedullary, and CD206⁺ macrophages are found to express Mac-2⁺ during the expansion phase. VEGFA expression is initiated by CD80⁺ cells, including F4/80⁺ macrophages, until day 3, while subsequently osteoblasts and chondrocytes are main contributors to VEGFA production at the fracture site. Using Longitudinal Intravital Microendoscopy of the Bone (LIMB) we observe changes in the motility and organization of CX3CR1⁺ cells,

which infiltrate the injury site after an osteotomy. A transient accumulation, resulting in spatial polarization of both, endothelial cells and macrophages, in regions distal to the fracture site, is evident. Immunofluorescence histology followed by histocytometric analysis reveals that $F4/80^+CX3CR1^+$ myeloid cells precede vascularization.

Keywords: bone regeneration, macrophage, endothelial cell, H-type vessel, intravital microscopy, LIMB, CX3CR1 myeloid cells

INTRODUCTION

Bone healing is a spatiotemporally regulated regeneration process, ideally leading to complete restoration of the broken bone without fibrous scar formation (1). Naturally, this regeneration process undergoes endochondral bone formation, if interfragmentary movements strain the fracture gap (2). In the majority of clinical cases, fracture healing follows the endochondral route and may be sub-divided into five phases, namely an (i) initial pro-inflammatory phase, (ii) anti-inflammatory phase, (iii) fibrocartilaginous or soft callus phase, (iv) mineralization or hard callus phase and (v) remodeling phase in which bone tissue regains its physiological shape with a restored bone marrow cavity. While fracture healing occurs in most cases without delay, still 5–10% of patients suffer from delayed healing or non-union. To avoid delayed healing and overcome non-unions, it is important to understand the finely orchestrated processes of bone regeneration (3, 4).

Upon a fracture, the vessels get disrupted and nutrient supply is lacking at the injury site. However, the vascular system is essential for healing, by supplying cells with oxygen and nutrients, removing debris and allowing the recruitment of circulating cells. Endothelial progenitors ($CD31^+$) migrate to the fracture site from the bone marrow or from pre-existing vessels of the periosteum (5–9). In earlier work, we could show that revascularization peaks during two phases of fracture healing: around day 7 (end of the inflammatory phase) and around day 21 (woven bone formation) in sheep (6). Drastic vascular structural plasticity has also been shown during bone marrow regeneration between 7 and 21 days by our group using a longitudinal microendoscopic method at cellular resolution (10). Angiogenic factors, such as vascular endothelial growth factor (VEGF) are of great importance in order to induce vascularization. Street et al. showed that the circulating plasma levels of VEGF are highly increased in patients with fractures and that the fibrin matrix within the fracture hematoma acts like a VEGF reservoir (11). In addition, we reported in a previous study that cells within the fracture hematoma exhibit upregulated VEGF expression and secretion (12, 13). Osteoprogenitor cells also produce VEGF as a consequence of the hypoxic environment, leading to enhanced transcriptional activity of hypoxia-inducible factor 1- α (HIF-1 α) (14, 15). Buettmann et al. most recently showed that especially the release of VEGFA by Osterix (Osx)⁺ osteoprogenitors/pre-osteoblasts is critical for vessel formation during fracture healing (16). It is well-known that the crosstalk between endothelium and bone cells is essential for the integrity and formation of bone. Osteoblasts support the vasculature by

producing VEGF and basic fibroblast growth factor (bFGF) while endothelial cells (ECs) provide factors that further osteoblast differentiation and activity (17). Furthermore, pre-osteoclasts and non-bone-resorbing osteoclasts have been described to enhance vascularization and osteogenesis in the growth plate area by releasing platelet-derived growth factor-BB (PDGF-BB) or supporting vessel anastomosis (18, 19). While the production of angiogenic factors by osteoprogenitors is well-known, there is evidence accumulating that, conversely, endothelial cells can also impact on bone formation, at least during bone development (7). Bone development is initiated by blood vessel invasion, and the arrival of osteoprogenitors. Subsequently, specialized type H blood vessels secrete osteogenic factors, required for the induction of bone formation and growth (20). Although the presence of type H vessels has been reported at sites of bone regeneration (10, 21), early events inducing the formation of these vessels in those situations have not yet been investigated.

Next to the adaptive immunity, the importance of the innate immune system for regenerative processes has been shown by several studies (22–26). Macrophages have been identified as key players for the recovery of tissue integrity and function. Several different types of myeloid-lineage cells can be distinguished in bone regeneration (23). Tissue-resident macrophages (also termed osteomacs) which express F4/80, can be found closely to bone-lining cells, and support intramembranous bone formation as well as endochondral ossification (22, 25, 26). Recruited immune macrophages (M1-like/M2-like) are more pivotal in endochondral ossification, which has been shown by Schlundt et al., who deleted macrophages in osteotomized mice by treatment with clodronate liposomes, and Alexander et al. who examined macrophage subsets close to the periosteum during regeneration (24, 25). Furthermore, osteoclasts are multinucleated tartrate-resistant acid phosphatase (TRAP)⁺F4/80[−] myeloid cells, which derive from fusion events (22).

In other tissues or scenarios, macrophages are essential for vascularization and angiogenesis. They are able to degrade extracellular matrix (ECM) and release pro-angiogenic factors. Degradation of the ECM enables the migration of endothelial progenitors and activates the angiogenic potential of some ECM molecules, as has been shown for fragments of hyaluronic acid (27). In addition, macrophages also release factors that attract, activate or even inhibit angiogenic cells depending on the phase of vascularization (28). Studies during mouse development revealed the tight association of macrophages with capillaries and the subsequent enhancement of angiogenesis (29, 30). Macrophages have also been shown to regulate vessel

permeability comparable to pericytes (31). *Vice versa*, endothelial cells (ECs) also promote the selective growth and differentiation of macrophages, especially the switch towards an M2-like phenotype, which requires direct contact with the endothelium and the regulation via macrophage colony-stimulating factor (M-CSF) signaling (32). However, a potential crosstalk between macrophages and ECs and the details of such interactions during bone regeneration have not been studied so far.

Within this study, we aim to analyze the initial phases of angiogenesis in bone healing with vascular regeneration and their dependence on the presence of macrophages. We focus on the early regeneration events, until the shift from pro- to anti-inflammatory phase, where a close crosstalk of blood vessels with macrophages is most prominent (d1–d7 after injury) and compare this to the bone remodeling phase driven by osteoprogenitors and mineralized tissue formation (d14–d21 after injury).

METHODS

Animal Husbandry, Housing, and Surgery Mouse-Osteotomy-Model

All animal experiments were approved by the local animal protection authority (LaGeSo; permit numbers: G0039/16 and G0111/13) following the German Animal Welfare Act.

Female C57BL/6N mice aged 10 weeks were ordered from Charles River Laboratories (Sulzfeld, Germany) and underwent surgery at the age of 12 weeks with an average body weight of 22 g. Housing took place in a conventional, semi-barrier (non-SPF) facility and randomly split in groups with at least 2 mice per cage housed in Eurostandard Type II clear-transparent plastic cages with a wire lid and filter top. Fine wood chips (Lignocel FS 14, J. Rettenmaier & Söhne GmbH + Co. KG, Germany) and nesting material (EnviroDri[®], Shepherd Specialty Papers, USA) was provided. Houses and pipes were removed after surgery to avoid injuries due to the external fixator. Food (Standard mouse diet, Ssniff Spezialdiäten, Germany) and tap water was provided *ad libitum*, and room temperature was between 20 and 22°C with a humidity of 45–50%. The light/dark cycle was a 12/12-h cycle. Animals were tail and cup handled. Anesthesia was induced at 2.5% isoflurane (CP-Pharma, Germany) and maintained at 1.5%. In order to cover pain after the surgery prior to surgery, all animals received Buprenorphine (0.03 mg/kg; Temgesic, Indivior Eu Ltd., UK) s.c. as analgesic, an eye ointment and clindamycin (0.02 ml; Ratiopharm, Germany). After shaving and disinfecting the left femur area animals were placed on a heating mat and osteotomy was performed under aseptic conditions as described earlier (21, 24). In short, the femur was prepared bluntly, after a lateral longitudinal incision of the skin between hip and knee. The external fixator (MouseExFix, RISystem, Switzerland) was placed parallel to the femur by serial drilling of the pins (0.45 mm diameter). With a Gigli wire saw (RISystem, Davos, Switzerland), a 0.70 mm osteotomy gap was created in the middle of the femur and flushed with NaCl. Following skin closure, mice received pre-warmed NaCl (0.2 ml) s.c., permeable wound dressing spray and could recover from anesthesia in their home cage under

infrared light and close monitoring. Tramadol was applied via the drinking water (0.1 mg/ml; Grünenthal, Germany) for 3 days after osteotomy (33). Given the short time period of treatment, we expect no negative influence of the analgetics on the fracture healing outcome (33). Surgery was performed by two trained veterinarians. For general scoring and humane endpoints, optimized protocols were used which has been summarized in Lang et al. (34).

Combined Osteotomy and Intravital Imaging Model

All animal experiments were approved by the local animal protection authority (LaGeSo; permit numbers: G0302/17) following the German Animal Welfare Act.

Cx3cr1^{tm1Litt} (CX3CR1:GFP), a fractalkine receptor (CX3CR1) reporter mouse, and C57BL/6J animals were bred in our colony. Heterozygous female mice were 14 weeks of age when osteotomy was performed. Housing took place in a conventional SPF barrier facility. Prior to surgery, all animals received Buprenorphine (0.03 mg/kg; Temgesic, Indivior Eu Ltd., UK) s.c. as analgesic and eye ointment. After shaving and disinfecting the left femur area animals were placed on a heating mat and osteotomy was performed under aseptic conditions. Surgery was performed as previously described (10), using four bi-cortical screws, and combined with osteotomy. In short, the internal fixator's Gradient Refractive Index (GRIN) lens tubing was modified to be screwed into the fixator plate after implantation and osteotomy. Osteotomy was performed using a 0.22 mm Gigli wire saw (RISystem, Switzerland) and two cuts for an osteotomy gap size of ~816 μm (CI: 787–844 μm; SD = 85 μm; *n* = 37). After removing the generated bone piece, the lens tube was positioned into the osteotomy gap and screwed into the fixator plate. Analgetics (Tramadol, Buprenorphine) were applied as described above. For antibiotic treatment mice received one injection of 0.04% Enrofloxacin (Baytril, 10 mg/kg body weight Bayer AG, Germany) before surgery.

Bone Sample Preparation

Femoral bones were explanted, muscles largely removed in a way that osteotomized bone parts maintained one entity. Tissue was fixed using 4% electron microscopy-grade PFA in PBS for 4 h at 4°C, washed in PBS, and ran through a sucrose gradient (10%, 20%, 30%; á 12–24 h). The fixators were removed from the fixed samples, underwent μCT measurement, bones were frozen in SCEM medium (Sectionlab, Japan), cut into slices of 7 μm using Kawamoto's film method (35), and stored at –80°C.

Histology

Movat's Pentachrome staining was conducted as described previously (21, 24). TRAP staining for quantification was performed using a kit following the manufacturer's instructions (Thermo Scientific, 386A-1KT, MA, US). Individual slides were stained using small volumes of staining solutions on a heating plate at 37°C. For immunofluorescence, individual sections were thawed, rehydrated in PBS, blocked with 10% donkey serum, and stained with antibodies in PBS/0.1% Tween 20/5% donkey serum containing DAPI for 1–2 h. Target

proteins were identified using antibodies against CD31/PECAM-1 (goat polyclonal unconjugated, AF2628, R&D Systems, 1:100), CD206/MMR (C068C2 conjugated to AF594, BLD-141726, 1:100), CD80 (goat polyclonal unconjugated, AF740-SP, 1:100), Endomucin (Emcn) (V.7C7 unconjugated, sc-65495, 1:100), F4/80 (Cl:A3-1 unconjugated, MCA497G, 1:400), GFP (goat polyclonal conjugated to AF488, 600-101-215, 1:100), Ly-6C (ERPMP20 biotinylated, MA5-16666, 1:20), Ly-6G (1A8 biotinylated, BLD-127603, 1:200), Mac-2/Galectin-3 (M3/38 unconjugated, BLD-125401, 1:100), Osx (rabbit polyclonal, sc-22536-R, 1:200), Runx2 (EPRI14334 conjugated AF647, ab215955, 1:100), Sox9 (EPRI14335 unconjugated, ab185230, 1:200), VEGFA (rabbit polyclonal unconjugated, ab46154, 1:100). Primary antibodies were stained with secondary antibodies when unconjugated (1:500, Thermo Fisher, anti-rat conjugated AF488, A21208; anti-rat conjugated AF546, A11081; anti-rat conjugated AF594, A21209; anti-rabbit conjugated AF488, A21206; anti-rabbit conjugated AF546, A10040; anti-rabbit conjugated AF647, A31573; anti-goat conjugated AF647, A21447; or streptavidin conjugated AF546, S11225). Samples were washed between steps and after staining with PBS/0.1 % Tween 20 for 3×5 min. Stained samples were kept in PBS for 5 min and embedded using aqueous mounting medium (Fluoromount, Thermo Fisher, MA, US) and analyzed microscopically within 6 days. Simultaneous detection of Ly6C and Ly6G was considered to indicate presence of the Gr-1 protein.

Movat's Pentachrome images were taken with a light microscope in a $2.5 \times$ magnification and the program AxioVision (both Carl Zeiss Microscopy GmbH, Germany). For **Figure 2**, images (CD31 & Emcn) were taken with a Keyence microscope (BZ 9000) using a 10x or 4x objective. All other images were acquired at a Zeiss LSM880 in tile scan mode at a resolution of 2048×2048 using a 20x objective, unless specified otherwise. For display, pictures were background subtracted and contrast adjusted using ImageJ 1.52i.

Image Analysis

Image analysis of cell and tissue distribution (**Figure 2**) was performed with ImageJ and an own developed pipeline which has been published and described in detail previously (21). Mean intensity was determined with ImageJ within the marked ROIs distinguishing between the gap, the adjacent to the gap and the bone marrow area. Mean intensities were normalized to the maximum intensity of the image.

Quantification was performed in *CellProfiler 3.1.8* (36) (**Supplementary Figure 1**). Macrophage subsets were described via the co-localization of identified CX3CR1⁺, Gr-1⁺, and F4/80⁺ objects. CX3CR1⁺F4/80⁺Gr1⁺ objects, representing cells were divided by roundness based on object shape features (FormFactor, Perimeter, Min Feret Diameter, **Supplementary Figure 5**). Objects were only considered cells when they overlapped with a nucleus (DAPI) signal. In a second pipeline localization of F4/80⁺ macrophages towards the Emcn⁺ endothelium was analyzed by examination of the direct ($\leq 3.5 \mu\text{m}$) and distant ($> 7 \mu\text{m}$) neighborhood of the subset. Localization of the identified subsets was analyzed by counting the identified objects in regions of interests

(ROIs). ROIs for the osteotomy gap were determined as shown in **Figure 5E**. For neighborhood analysis and frequency determination (**Figures 3E,F**) either Emcn^{hi} or Emcn^{lo} areas within the osteotomy gap or distant thereof were encircled freehand using ImageJ 1.52i, respectively (**Figure 3D**). Areas close to Sox9⁺ chondrocytes were excluded as they did contain few, if any macrophages. Emcn^{hi} areas largely overlapped with F4/80^{hi} areas.

Object Identification and Neighborhood Analysis

For the segmentation, the model-based approach was applied (37). *Otsu* was used as a segmentation algorithm calculating the thresholds for the object edge identification. Mid-level pixels were assigned to the background. The threshold calculation was performed adaptively, which allows adaptation of the threshold to different image sub-regions. For each channel, the parameters were manually optimized by visually inspecting the segmentation results. To aid the segmentation, channel specific object ranges were estimated (e.g., nuclei = $3.1\text{--}12.5 \mu\text{m}$). Clumped cells were separated based on their intensity distribution. Only partly visible cells touching the border of the image were removed from the segmentation process. Nuclei, CX3CR1, F4/80, and Emcn primary objects were identified based exclusively on the image. Due to the dense packing of Gr-1⁺ cells, segmentation was performed via secondary object identification with prior segmented nuclei as cellular reference. The segmentation was channel dependently refined based on various object features (**Supplementary Figure 1B**). Objects features were extracted on the boundaries of the objects for shape (e.g., perimeter, area, radius; **Supplementary Figure 5**), and intensity, computed from the signal intensity values of the object area within a defined image channel. Filter and thresholds were determined by visual evaluation of specific phenotypic measurements of individual objects within the image and the global distribution of the phenotypic measurement within the whole image.

Spatial Polarization Scoring

Bone orientation was determined using Movat's Pentachrome overview images. Scores were determined for individual channels (DAPI, F4/80, or CD31). Scores were determined considering the staining intensity and abundance of the signal in parts of the bone marrow not affected by the injury (homeostatic control), on the same slide in at least $400 \mu\text{m}$ distance from the injury site. Scores were: -2 for the absence of staining in the area or reduced signal abundance and intensity throughout the entire area.; -1 for signal either reduced in intensity but displaying comparable abundance, or reduced abundance and comparable intensity; 0 for appearance that resembles homeostasis (unaffected bone marrow in the same section); 1 for higher intensity at comparable or increased abundance that localized only partially along the line between the gap and the adjacent tissue. Adjacent tissue is tissue along the contour between bone marrow and hematoma, bone fragments, and callus; 2 for higher intensity at comparable or increased abundance along the entire length of the line between the gap and the adjacent tissue or in large areas extending $> 400 \mu\text{m}$ distance from the gap in the bone marrow tissue. Regions often

showed enlarged and unstructured vessel organization, with very bright F4/80 cells between the endothelial lines. Samples were considered spatially polarized when the scored values for F4/80 and vessel marker of proximal and distal to the fracture gap resulted in a difference >2 favoring one side (proximal, distal). Samples which scored a difference of <2 were considered neutral. In total $n = 20$ samples were analyzed, 9 samples scored values other than 0 of which 2 samples were considered neutral, 1 polarized proximally and 6 polarized distally (Supplementary Figure 4A).

Longitudinal Intravital Microendoscopy of Murine Osteotomy

As a GRIN lens system, we used custom singlet GRIN needle microendoscope (length ca. 5.07 mm, diameter = 0.60 mm; NEM-060-10-10-850-S-1.0p, GRINTECH Jena, Germany). The GRIN lens was glued into the lens tubing to a final penetration depth of 650 μm when screwed into the fixator plate. CX3CR1:GFP mice were anesthetized and mounted to the microscope as previously described (10). Qtracker 655 Vascular Label (Thermo Fisher, MA, US) were injected and images were acquired (505 \times 505 px, 500 \times 500 μm , unidirectional, line average 4, step size 4.5–6.5 μm , ca. 18 steps, stack time 60 sec). Image stacks were loaded into Imaris 9.3.0 software (Bitplane Zürich, Switzerland), median filter (3 \times 3 \times 3) was applied. Videos were exported (1024 \times 1024, 4 fps) and images were angled maximum intensity projections. Individual mice were measured at 940–950 nm on day 2, 3, 4, 5 after osteotomy.

Statistical Analysis

Statistical analysis was carried out with GraphPad Prism V.5 or V.8 software. All values are expressed as the mean \pm SD if not stated otherwise. Mann-Whitney *U*-test, Wilcoxon-signed rank test and Friedman test with Dunn's *post-hoc* test were mainly used, since Gaussian distribution was not expected due to inter-individual variations. A $p < 0.05$ was considered statistically significant. Image analysis was blinded for time points.

RESULTS

Emcn^{hi}CD31^{hi} Endothelium Is Present During Endochondral Bone Formation in the Osteotomy Gap

Fracture healing consists of consecutive phases. Progression into each phase depends on the undisturbed and error-free course of the respective previous phase (38). In the mouse-osteotomy model used in this study, residuals of cells in the fracture hematoma are visible in Movat's Pentachrome staining at day 3, while the osteotomy gap is filled with a mixture of bone marrow cells including hematopoietic cells at day 7, and endochondral bone formation occurs between day 14 and day 21 (Figure 1A). Using immunofluorescence histology, a positive signal for CD31 (Platelet endothelial cell adhesion molecule 1) is seen in elongated

cells inside the fracture hematoma, which include no detectable nuclei (Supplementary Figures 2A–C), probably indicating that these residuals represent endothelial cells that may have lost their integrity. In order to further characterize the cellular composition within the fracture area, immunofluorescence staining for key transcription factors of mesenchymal differentiation was performed on serial sections of the same bones (Figure 1B). Already at day 3, osteoblast progenitors characterized by nuclear expression of Runt-related transcription factor 2 (Runx2) are dispersed in the fracture gap. By day 7, their number has increased, leading to a dense population of the gap, whilst sparing a region in the center. The peripheral borders of the gap and adjacent periosteal regions are populated by cells co-expressing Runx2 and SRY-box transcription factor 9 (Sox9) in the nucleus, indicating their potential for either osteogenic or chondrogenic differentiation (Figure 1B). This is in accordance with the blue-greenish color in corresponding regions of Movat's Pentachrome staining, indicative of cartilaginous tissue (Alcian blue positive). At day 14, Runx2⁺ cells are found to localize on both sides of the gap. Single Runx2⁺ cells are surrounded by areas characterized by the presence of only a few nuclei, in line with the presence of mineralized bone in those areas, as visualized by Movat's Pentachrome staining (compare: Figures 1A,B). Sox9⁺ cells are exclusively present in the center of the gap at this time point. Notably, the majority of these cells do not co-express Runx2. In contrast, at day 21, a time point when mineralization of the gap is complete, the progenitors identified in this area are almost exclusively Runx2⁺. In a next step, Osterix (Osx) and CD31 stainings were performed on serial slides from the same individuals. Direct comparison reveals that at day 3, only some Runx2⁺ cells are also Osx⁺, indicating various degrees of osteogenic differentiation. From day 7 on, Runx2⁺ cells are also positive for Osx⁺, consistent with ongoing maturation of osteoblasts. Osx⁺ osteoblasts localize in the fracture gap alongside existing and newly formed bone, as indicated by differential interference contrast (DIC) signal. Sox9⁺ cells can be found at day 14 and 21 in areas with cartilage and close to Osx⁺ cells, indicating ongoing further differentiation and mineralization, which is accompanied by vascularization. For further quantitative analysis of the vasculature sprouting into the gap, we defined the gap as a rectangular region between the cortical ends and analyzed CD31⁺ vessels and Osx⁺ bone cells in this region (Figure 1C). At day 3, CD31⁺ matrix (residuals of the fracture hematoma) and some CD31⁺ cells are present (compare to Supplementary Figures 2A–C), while Osx⁺ cells enter the osteotomy gap at later time points, between day 7–21 (Figures 1C,E). At later phases of fracture healing, endothelial cells displaying the phenotype of type H vessels (Emcn^{hi}CD31^{hi}) closely associate with Osx⁺ osteoprogenitors/pre-osteoblasts (Figure 1C). Investigating the co-localization of Runx2⁺ and Sox9⁺ cells with respect to CD31⁺ endothelium reveals a close localization of Runx2⁺ cells around vascularized areas, while Sox9⁺ cells are only found in less vascularized areas (Figure 1D). Our results confirm a close relationship between vessel formation and osteoprogenitors/osteoblasts and extend previous reports of this phenomenon, which focused on bone development (7), to a regenerative scenario.

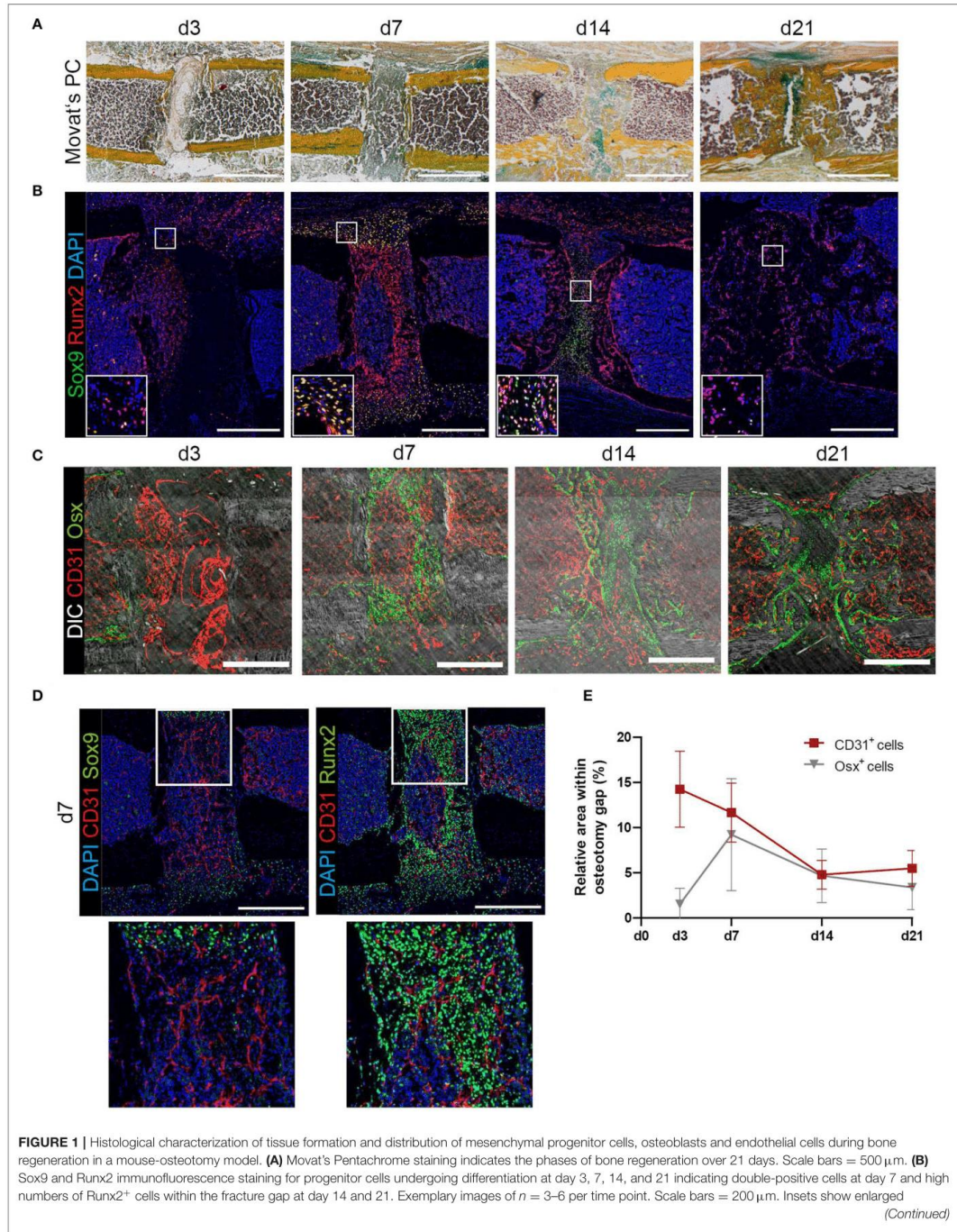


FIGURE 1 | representative areas marked by white frames. **(C)** Exemplary images at day 3, 7, 14, and 21 displaying the distribution of CD31⁺ ECs and Osx⁺ osteoprogenitors/pre-osteoblasts revealing close proximity between CD31⁺ endothelium and Osx⁺ cells. Scale bars = 200 μ m. **(D)** Exemplary images for Sox9 or Runx2 and CD31 staining at day 7. Insets show enlarged representative areas marked by white frames. While Runx2⁺ cells can be found closed to endothelial cells, Sox9⁺ cells can be found in not yet vascularized areas. **(E)** Quantification of cellular compartments present in the fracture gap during regeneration. Endothelial cells (ECs; CD31⁺) and osteoprogenitors/pre-osteoblasts (Osx⁺) were quantified based on the relative presence of positive pixels with the respective markers in immunofluorescence images supporting the descriptive analysis on the spatiotemporal distribution of progenitor cells, osteoblasts and endothelial cells over time. Data show mean \pm SD for $n = 3-6$.

Localization and Morphologic Characterization of Emcn^{hi}CD31^{hi} Type H Endothelium

While Emcn^{hi}CD31^{hi} endothelium can be found directly in the osteotomy gap and in the adjacent tissue, Emcn^{lo}CD31^{lo} endothelium is prominent in bone marrow regions not affected by the injury. Pixel intensity analysis confirms the differences between the Emcn⁺ and/or CD31⁺ cells in and adjacent to the osteotomy gap, compared to the bone marrow (Figures 2A,B).

We further characterized the type H vessels in the fracture gap (Figures 2C,D). During vascularization of cartilaginous tissue, invading vessel buds (distal loops), previously described as a morphological criterion for type H endothelium (7), can be identified (Figure 2E, first row marked by arrows). Furthermore, CD31⁺ arterioles, which are negative for Emcn, are found within the osteotomy gap. However, a second morphological criterion described to be typical for type H vessels in the growth plate areas, namely their columnar structure, does not appear during regeneration, suggesting that this ordered arrangement is a specific feature of bones undergoing longitudinal growth. Taken together, our data reveal the appearance of Emcn^{hi}CD31^{hi} in the fracture gap, which share additional distinct morphological features with the previously described type H vessels, although they are not organized in columnar structures. This finding suggests an important role of this osteogenic vessel type not only during bone development, but also during regenerative processes of the bone.

M2-Like Macrophages Localize Preferentially Extramedullary

In order to determine the role of macrophages in the context of vascularization during bone regeneration, we analyzed macrophage subsets and their spatial localization relative to type H vessels. Based on the pan-macrophage marker F4/80, which includes also osteomacs, we defined M1- and M2-like macrophages labeled by CD80 and CD206 (Mannose receptor), respectively, as well as Mac-2 (Galectin-3), a marker associated with pro-inflammatory macrophages (22). Over the course of endochondral bone regeneration, F4/80⁺ cells localize throughout the bone marrow, as well as on the border to bone surfaces, accumulating in various areas (Figure 3A). At day 3 post-osteotomy, high numbers of F4/80^{hi} cells localize in periosteal regions adjacent to the osteotomy gap. They can be found periosteal in varying numbers throughout the regeneration process, until the bone remodeling phase at day 21. At day 14, F4/80^{hi} cells are found exclusively in periosteal regions, whereas they are found in both the medulla and the periost at day 21.

Extra-medullary F4/80⁺ macrophages are positive for the anti-inflammatory M2(a) macrophage marker CD206 (Figure 3A, blue framed inset). Those M2-like cells are not abundant in the marrow or at sites of vascularization, where expression of CD206 is generally lower and macrophage morphology rather ramified (Figure 3A, yellow and orange framed insets). CD206 expression is also found in cells resembling the morphology of endothelia (Emcn⁺), which are F4/80⁻ throughout the regeneration process as well as under homeostatic conditions (Figure 3A, yellow framed inset; Supplementary Figures 3C,D). M1-like macrophages, defined by expression of CD80, are extremely rare and only few are found at day 3, with their abundance comparable to control tissue (Supplementary Figures 3B,D). Using the marker Mac-2 in addition, almost all CD206⁺ macrophages are found to be positive for Mac-2 at day 3, however, not all Mac-2⁺ cells are CD206⁺ (Figure 3B). Mac-2 positive cells localize in the fracture gap and in proximity to the bone surfaces. Over the course of regeneration, double-positive Mac-2⁺ and CD206⁺ cells vanish and cells which are single positive for each of the two markers are detected at day 21, a time point when remodeling is ongoing (Figure 3B). Quantitative pixel-based area analysis of F4/80 macrophages, CD31 and TRAP shows that CD31⁺ and F4/80⁺ cells are reduced over time, while the number of TRAP⁺ cells (osteoclasts or activated macrophages) increases (Figure 3C; Supplementary Figure 3A).

CD206⁺ macrophages are present throughout the healing process with no apparent preferential localization towards the vasculature, and they are mainly Mac-2⁺ in the early phase of regeneration. Over the course of regeneration, F4/80-expression decreases in regions adjacent to the callus, and at later time points only few areas, which contain cells expressing F4/80 at intermediate levels, are observed.

F4/80⁺ and CD80⁺ Cells Produce VEGFA During Early Regeneration and Osteoblasts and Chondrocytes Are the Main Producers at Later Time Points

Since we could not find substantial amounts of CD80⁺ cells at day 3 post-osteotomy, we analyzed the regeneration at day 1 and day 2. Some CD80⁺ cells were found at day 1, and they were abundant in higher numbers at day 2 post-osteotomy (Figure 4A). Some of those are F4/80⁺CD80⁺ macrophages, which localize in areas adjacent to the osteotomy gap. CD80⁺ cells are located directly at the injury site (Figure 4A, day 2). Macrophages are known to support vascularization via VEGFA during tissue regeneration, which is why next, we analyzed VEGFA using immunofluorescence histology over the time

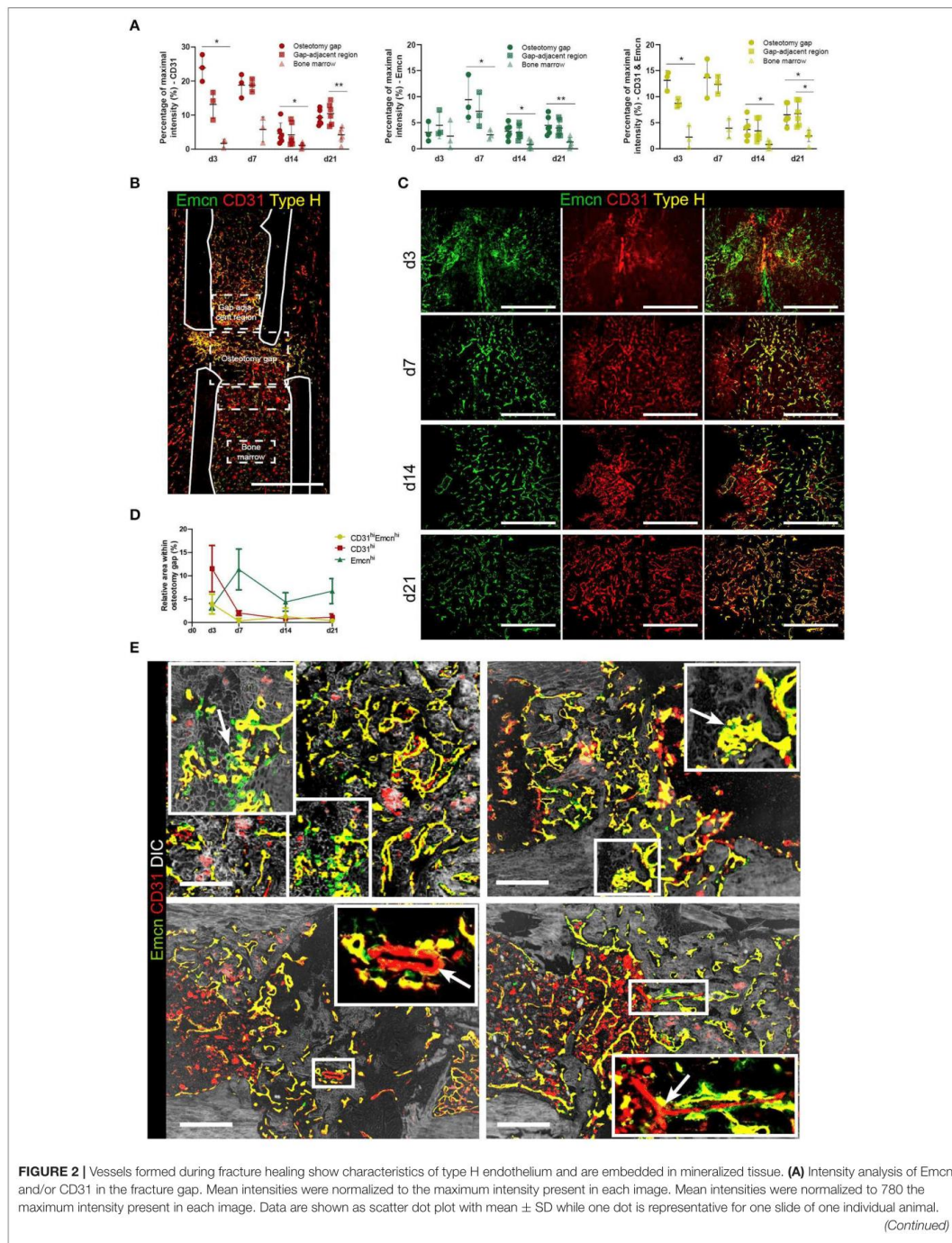


FIGURE 2 | Friedman test with Dunn's *post-hoc* test were performed to determine statistical differences; *p*-values are indicated with **p* < 0.05, ***p* < 0.01. **(B)** Emcn^{hi} CD31^{hi} endothelium shows spatial differences in abundance throughout the bone. Exemplary image showing the definition for the osteotomy gap, the gap adjacent regions and the bone marrow area, as used in our analyses. Scale bar = 200 μm . **(C)** Images of Emcn^{hi} CD31^{hi} endothelium at day 3, 7, 14, and 21. Data are representative for *n* = 3 (d3/7) and *n* = 6 (d14/21). **(D)** Quantification of areas occupied by Emcn^{hi} CD31^{hi} type H endothelium during the time course of bone healing. Data are shown as Mean \pm SD. **(E)** Emcn and CD31 staining combined with phase contrast images (DIC) in the soft to hard callus transition of fracture healing highlight morphological characteristics also present in growth plate bone growth. Upper panels: invasion of vessels in cartilaginous tissue and type H vessel-like budding is indicated by arrows. Lower panels: CD31^+ only vessels are assumed to be arterioles (arrows) (7). Scale bars = 200 μm .

course of bone regeneration (Figures 4B–D). VEGFA is not expressed by F4/80^+ CD80^- macrophages throughout the entire process, but CD80^+ F4/80^- and a fraction of CD80^+ F4/80^+ cells express VEGFA. This expression was restricted to very early time points, namely day 1 and day 2 (Figures 4B,C). From day 3 on, VEGFA is found to be expressed in the fracture gap and along bone surfaces (endosteal, periosteal) and in the bone forming areas (Figure 4D). The signal for VEGFA at day 14 is pronounced in areas, which also contain Sox9^+ and Runx2^+ cells (Figures 1B, 4D). Taken together, VEGFA expression is observed in CD80^+ cells, including a fraction of F4/80^+ cells, in the early phase until day 3, after that, VEGFA is expressed predominantly by osteoblasts and chondrocytes in bone forming areas.

Cells Within the Osteotomy Gap Localize in Proximity to the Endothelium

High abundance and expression of the vascular markers CD31 and Emcn is observed in both, the damaged tissue in the early regeneration, and in bone forming tissue over the subsequent course of regeneration in the osteotomy gap (Figure 2C). These areas rich in type H vessels, simultaneously contain F4/80^{hi} cells (Figures 3A,D). In order to evaluate the proximity in localization between macrophages and type H endothelium, we defined two regions for each sample, the Emcn^{hi} region and the Emcn^{lo} region (Figure 3E). Objects in these regions were segmented based on marker expression of Emcn , F4/80 and DAPI. Over the course of regeneration, similar frequencies of 25.0 ± 11.6 % F4/80^+ cells are present in both, the Emcn^{hi} and Emcn^{lo} regions. The frequencies of F4/80^+ cells decrease significantly from day 3 until day 21 post-injury (Figure 3E), confirming the qualitative results from Figure 3C. Next, we analyzed the position of macrophages relative to the endothelium, and found that, a two- to three-fold higher number of objects (F4/80^+ objects or identified nuclei, which serve as a control for all cells) localize in proximity to the endothelium in the Emcn^{hi} region as compared to the Emcn^{lo} region (Figure 3F). Cells are defined as “in proximity” when they are located less than half a nuclear diameter in distance (<3.5 μm) away from the endothelium.

During analysis of immunofluorescence staining in samples of osteotomized, LIMB-implanted bones, we noticed a transient, strongly polarized distribution of newly formed vessels to the distal area of the osteotomy gap (Figure 5A; Supplementary Figure 4A). A similar polarization occurs in samples of the osteotomy-model (Supplementary Figure 4B). In some cases, this phenomenon is accompanied by a variation in cell density in the respective area, as shown by differences in the abundance of the DAPI signal. Scoring according to the criteria described in the methods section for the abundance and intensity of the markers in the gap-adjacent regions reveals that

CD31^+ vessels are significantly brighter and more abundant adjacent distally to the gap, as compared to the proximal site (Figure 5B). This spatial polarization with respect to bright CD31^+ vessels is pronounced at day 4 and decreases quickly afterwards (Figure 5B). A similar trend is observed for F4/80^+ cells in the same regions (Figure 5B). Taken together, these analyses reveal a transient, directional spatial polarization (regarding the localization from the fracture gap) of CD31^{hi} vessels, adjacent to the fracture gap.

CX3CR1⁺ F4/80⁺ Macrophages Precede Vascularization

In order to understand the dynamics of macrophages during bone regeneration, we took advantage of the fractalkine receptor (CX3CR1) reporter mouse strain $\text{CX3CR1}:\text{GFP}$. These mice were implanted with a Gradient Refractive INdex (GRIN) lens, enabling longitudinal imaging of the bone marrow during regeneration (10). At the same time, these mice underwent osteotomy surgery. Since the first wave of vascularization occurs during resolution of the fracture hematoma, bones that had been treated using the procedure described were fixed and analyzed at day 4, 6, and 8 using immunofluorescence histology. In order to be able to exclude monocytes and granulocytes from the macrophage analysis, we stained sections using antibodies against Ly-6C/Ly-6G (Gr-1). We find that almost all F4/80^+ macrophages in the osteotomy gap are also CX3CR1^+ (Figures 5C,D, yellow), confirming that the reporter mice are suitable for tracking macrophage dynamics during bone regeneration. GFP^+ cells are present within the osteotomy gap at early time points and become less abundant over time. They locate in close proximity to CD31^{hi} endothelium, do not express Gr-1 (Figure 5D), excluding the possibility that some of them are granulocytes, which are also described to be CX3CR1^+ . We analyzed the osteotomy gap between the cortices and the bone marrow as described in Figure 5E. At day 6, of all identified cells in the osteotomy gap, the CX3CR1^+ cells display the highest increase in cell number, as compared to homeostasis. A minor increase is detected in F4/80^+ cells and a strong reduction of Gr-1^+ cells is observed compared to homeostasis (Figure 5F). The space is largely occupied by F4/80^+ myeloid cells, which are not monocytes (Gr-1^-). The strongest increase in cell number is observed in the $\text{CX3CR1}^+\text{Gr-1}^-\text{F4/80}^+$ subset, which make up to 12% in ratio to all nuclei at day 6 (Figure 5G). Almost 6% of CX3CR1^+ objects are F4/80^- and only few are Gr-1^+ . Morphologically, the cell phenotype is of non-round shape (Figure 5E, Supplementary Figure 5). We then longitudinally sampled time-lapse videos with two-photon microscopy from individual mice over the course of the early regeneration process. On the first and second day, almost no signal is detected inside

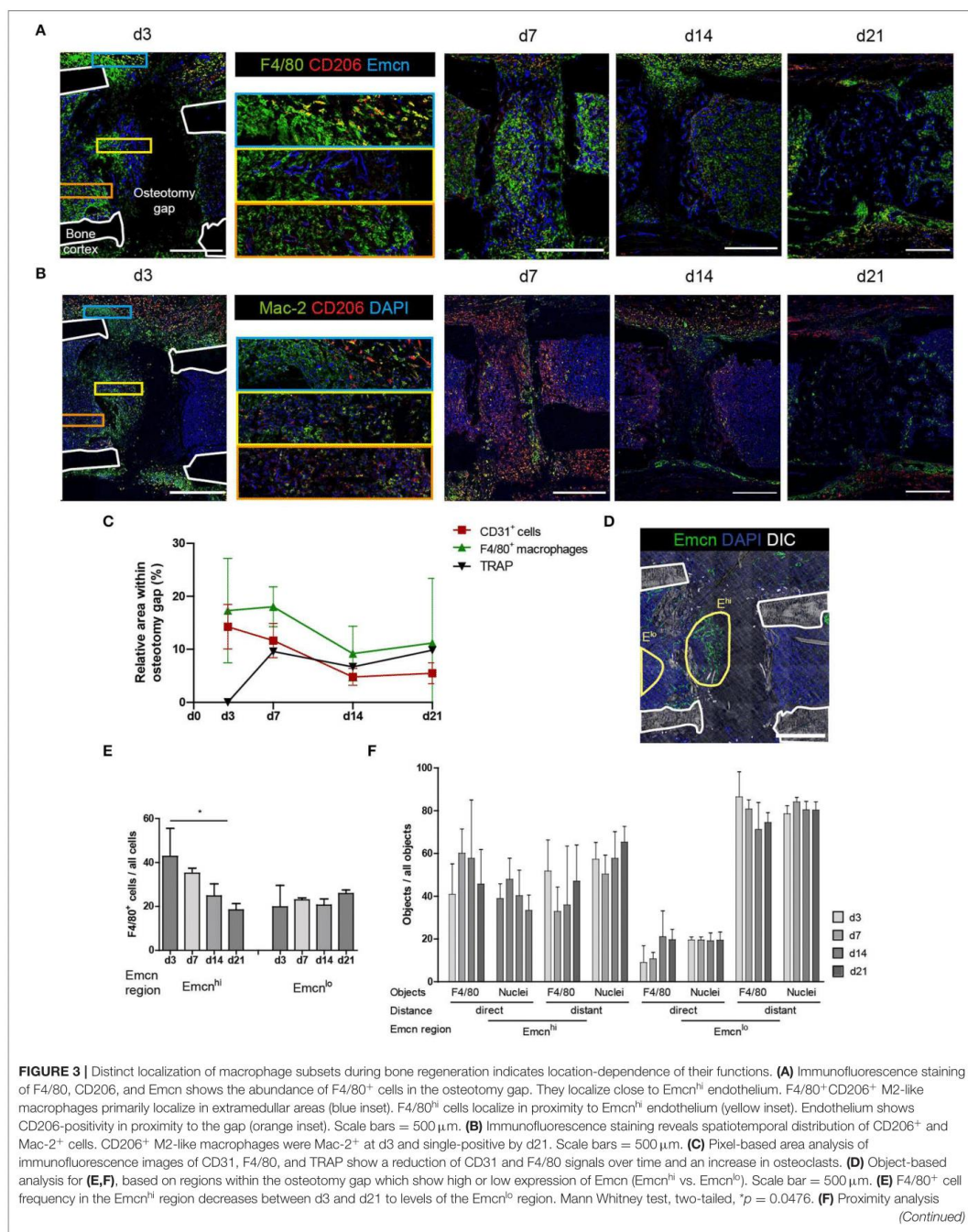


FIGURE 3 | performed by object-based quantification in two distances from the endothelium. Data was normalized to the overall number of the object population in the respective region. Compared to the Emcn^{lo} region, more objects (F4/80⁺ or nuclei) localize in proximity to the endothelium in the Emcn^{hi} region. Cells were considered in proximity to each other when their distance amounted to that equivalent to less than half of a nucleus diameter (<3.5 μm), in order to include cells which are either in contact with or in the direct vicinity of vessels. Cells were considered distant were located further than one cell layer (>7 μm) apart from each other. Data are representative for $n = 3$ (d3/7) and $n = 6$ (d14/21).

the osteotomy gap (data not shown). On day 3, individual CX3CR1⁺ cells enter the hematoma (Figure 5Hd3). Those cells display a non-round, but non-ramified shape and move through the tissue (Supplementary Movie 1). A front of CX3CR1⁺ cells forms at the edge of the field of view at day 4, containing both round and non-round cellular phenotypes, forming a dense, partially resident population which expands into the entire field of view (Figure 5H, Supplementary Movies 2, 3). This invasion is accompanied by the occurrence of perfused vessels that expand, following the CX3CR1⁺ cell front until the field of view appears vascularized (Supplementary Movie 4). Under full vascularization, sessile CX3CR1⁺ cells localize towards the vasculature and motile cells can be observed to move along the endothelium (Supplementary Movie 3). Generally, the abundance of CX3CR1⁺ in the gap increases with progression of the regeneration process (Figure 5F, Supplementary Movies 3, 4).

These results indicate that most cells in the fracture gap are myeloid, non-monocytic, non-granulocytic, non-round CX3CR1⁺ which invade the osteotomy hematoma starting day 2–3, become gradually sessile in the fracture gap at day 3–4, where they precede the vasculature until it becomes fully perfused. After vascularization, CX3CR1⁺F4/80⁺ cells persist until the onset of the remodeling phase.

DISCUSSION

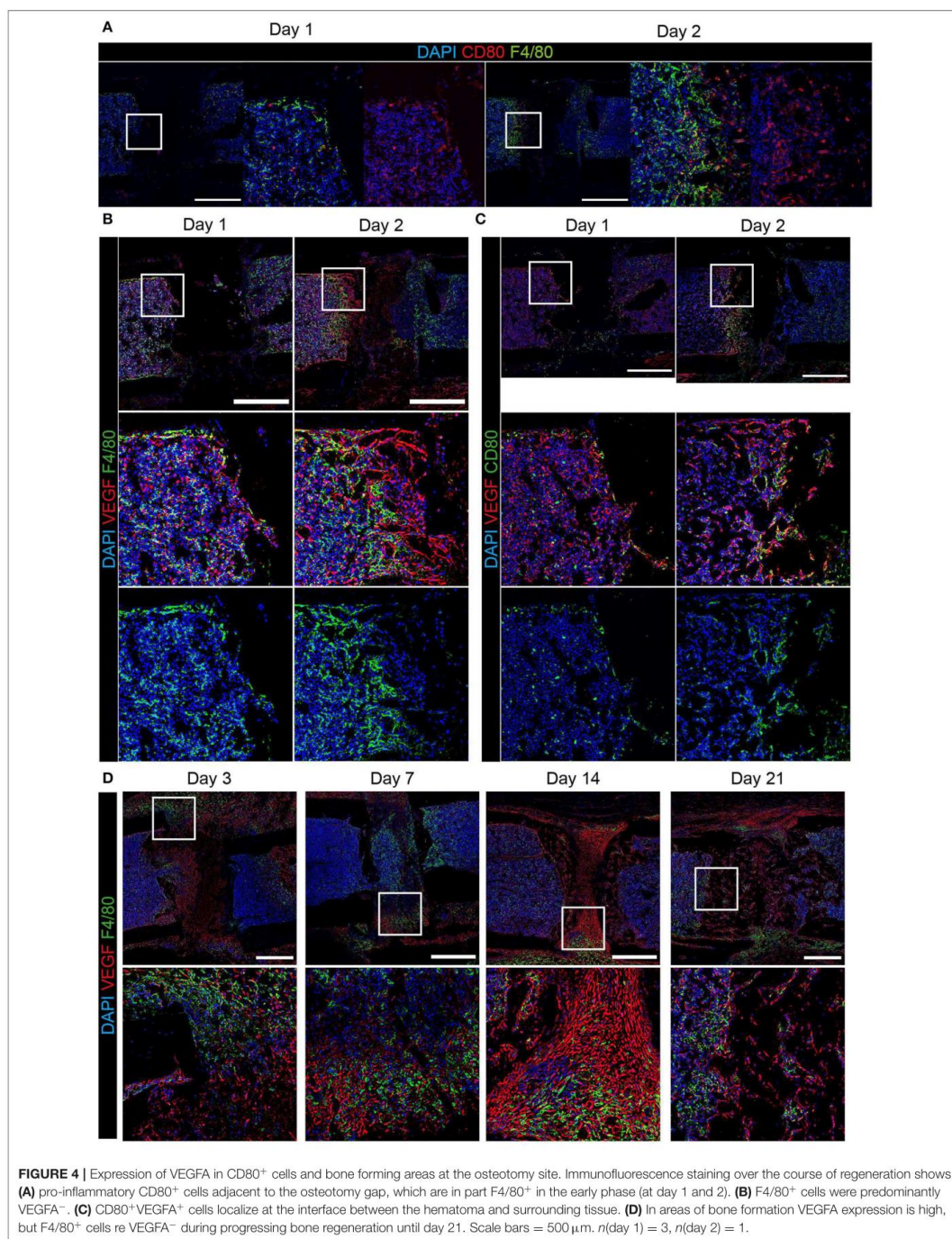
Vascularization is pivotal to the success of complete, scar-free bone regeneration. Here, we show that after bone injury, type H endothelium evolves in the bone formation region and persists throughout the entire bone regeneration process. Our findings show that the phenotype of type H endothelial cell structures described in endochondral long bone growth, is also reflected in bone regeneration. Emcn^{hi}CD31^{hi} endothelium shows association with Osx⁺ osteoblasts and displays typical features that can be observed in the growth plate during longitudinal growth, such as invading vessel buds and arch-like structures described before (7). Other than their counterparts in the growth plate, type H vessels generated during regeneration are not columnar. However, this feature is probably not inherent to type H vessels, but merely the result of the highly ordered structure of chondrocytes in the metaphyseal areas. These chondrocytes are organized into columns that are produced in the growth plate, and probably impose their structure on the type H vessels in these areas. In contrast, the tissue structure surrounding type H vessels in a fracture gap appears more disorganized. We have previously shown that the amount of type H vessels can be used as a measure of fracture healing progression (21). Ramasamy et al. reported the effect of shear stress in the vascular formation during bone development, therefore

it would be interesting to analyze whether interfragmentary, compressional mechanical cues also act on the formation and structure of type H vessels in fracture healing (39).

We found an extensive staining of CD31 in the gap, which dominates the initial hematoma phase (until day 3–4). This staining seems not to be associated with intact cells, since no nuclei are present. It is possible that CD31⁺ cells are present in the early fracture hematoma during the first hours after injury and undergo cell death due the hypoxic microenvironment, including a low pH and high lactate level in the tissue, and that the staining pattern observed represents dead endothelial cells.

Based on our results, and similar to a previously reported model in sheep (6), we propose that two phases of vascularization occur during bone regeneration also in mice. The first wave of vascularization occurs during disintegration of the fracture hematoma, where vascular sprouts from existing endothelial cells enter into a hypoxic environment. It occurs between the initial injury and day 6, until the entire volume is fully vascularized for soft callus formation. We observe this phase histologically and by intravital microscopy. After the first wave, and once the callus becomes calcified, we assume that the vascular network within hard callus and bone is remodeled in a second phase, based on the changes that happen during tissue reorganization. It has been described that most of the progenitor cells that contribute to fracture repair immigrate from the periosteum (40). In addition, these progenitor cells either express Sox9 or Runx2, which are regulated by direct repression of the opposing pathway (via β-catenin expression) and define further differentiation into chondrocytes or osteoblasts, respectively (41). However, several studies show the importance of Sox9 expressing progenitor cells that support mineralization and osteogenesis within the fracture gap (42–44). At day 7, we observe a co-localization of Sox9 and Runx2 (Figure 1B), it can be speculated that co-expression of both transcription factors marks a switch in the genetic program, from uncommitted pre-osteoblasts to chondrocyte differentiation, similar to what has been shown in bone development (45). Alternatively, Sox9 expressing cells might differentiate into osteoblasts, as described previously (42–44). Our results show close proximity between osteoprogenitors (Runx2⁺) or osteoblasts (Osx⁺) and CD31⁺ endothelium (Figures 1C,D). Endothelial cells, which display the phenotype of type H vessels (Emcn^{hi}CD31^{hi}) closely associate with Osx⁺ cells in this osteotomy (= cortical defect) model. Type H endothelia have been previously described to be present in the metaphyseal areas of young animals, where they promote bone growth (7). The results presented here indicate a similar crosstalk to occur in endochondral osteogenesis during regeneration.

The large extent of angiogenesis, which occurs in the fracture gap, raises the question for factors and cell types which trigger this event. In the growth plate, hypertrophic chondrocytes



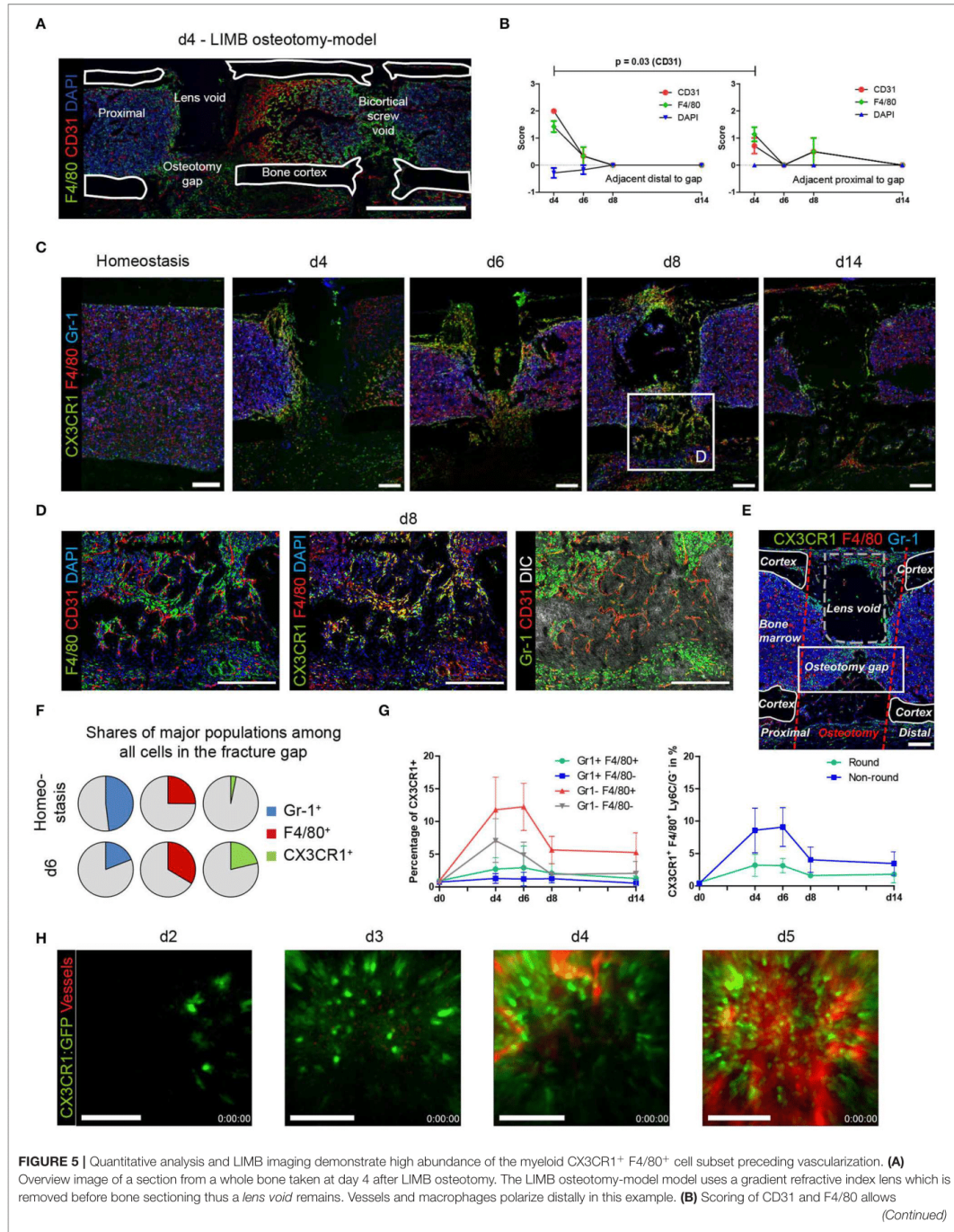


FIGURE 5 | quantification of polarization in proximal or distal orientation with respect to the fracture gap. Scoring of DAPI staining was used as internal control. Wilcoxon matched-pairs signed rank test. Data are representative for $n = 7$ (d4), $n = 6$ (d6), $n = 4$ (d8), and $n = 3$ (d14). **(C)** Immunofluorescence images of sections from bones showing the presence of myeloid subsets at various time points after LIMB osteotomy. CX3CR1:GFP⁺ and F4/80⁺ cells negative for Ly6C/Ly6G (Gr-1), accumulate at and invade into the fracture gap. Scale bars = 200 μm . **(D)** Inset of the area of d8. The majority of myeloid cells are CX3CR1⁺F4/80⁺ and localize in distance from Gr-1⁺ cells. Scale bars = 200 μm . **(E)** Quantitative analysis is performed in the rectangular region of the fracture gap between corticalis, osteotomy cuts, and lens void (osteotomy gap). Scale bar = 100 μm . **(F)** Quantitative, object-based analysis of the osteotomy gap for Gr-1, F4/80, CX3CR1:GFP show a decrease of Gr-1⁺, an increase of F4/80⁺ and massive increase of CX3CR1⁺ cells. Results of 20 pooled samples. **(G)** Object-analysis among the CX3CR1⁺ cells reveals that Gr-1⁻F4/80⁺ account for the majority of cells present in the gap over the whole time course of regeneration (left panel). Of those, the majority were non-round cells (right panel). **(H)** Intravital two-photon LIMB-microscopy of the osteotomy gap in an individual CX3CR1:GFP mouse. CX3CR1:GFP⁺ cells invade the osteotomy gap in the displayed field of view (250 \times 250 μm) at day 2–3 and fully populate the region by day 3–4. Simultaneously, numerous CX3CR1⁺ cells precede the vascularization in space and time. Vasculature was made visible using intravenous injection of Qtracker 655. Scale bars = 100 μm . Data are representative of 5 mice analyzed.

produce high amounts of VEGFA, due to the hypoxic microenvironment in those areas, in which HIF stimulates VEGFA expression (7). In a recent publication, Buettmann et al. deleted VEGFA from early osteolineage (Osx⁺) cells, mature osteoblasts and osteocytes (Dmpl⁺) as well as ubiquitously in models of cortical fractures (full and stress fractures) and a cortical defect model (drilling). Bone regeneration and periosteal angiogenesis after a cortical defect was impaired only when VEGFA was deleted either ubiquitously or from Osx⁺ cells, indicating a predominant role of osteolineage cells. After drill hole injury, however, the deletion did not lead to delayed healing, indicating that another cell type than Osx⁺ is responsible for VEGFA production and the progression of vascularization.

Macrophages have been identified to play a role in bone regeneration, as their deletion either via clodronate (24, 25) or genetically delays healing. Data available in the literature indicate multiple functions for macrophages during bone regeneration. Recently, the supportive function of F4/80⁺ macrophages during bone regeneration via enhanced osteogenesis when transplanted to aged individuals was demonstrated (46). In addition, it is known that F4/80⁺ osteomacs support osteoblast function (47). Osteoblast differentiation and mineralization have also been shown to be modulated by macrophages (48, 49). However, the role of macrophages in the vascularization of the fracture is largely unknown. Here, for the first time, we quantitatively and qualitatively map out the vascular network, relate it to the presence of macrophages at relevant time points during bone regeneration in mice and analyze presence and proximity with different approaches. We find that F4/80⁺ macrophages and type H endothelium localize at the front of damaged tissue in the first phase until soft callus formation, when their presence is reduced. In detail, our proximity analysis reveals that all cells, including F4/80⁺ macrophages in the regenerating tissue, localize much closer to the endothelium than in unaffected areas in both, the first (d3–d7 after injury) and second (d14–d21 after injury) phase of revascularization. We find CX3CR1⁺F4/80⁺ macrophages to be a predominant subset in this process. Phenotypically, these cells are for the most part non-round and ramified. They localize predominantly in a one-cell layer around the endothelium. Future work is needed to study the fate of this subset. It is possible that those cells differentiate or merge with osteoclasts and therefore promote remodeling of the bone.

Using longitudinal intravital microendoscopy of the osteotomized region, we find that CX3CR1⁺ macrophages

precede the occurrence of perfused vessels into the hematoma in the first phase and remain associated to the endothelium. We show the type H endothelium to be closely associated with CX3CR1⁺F4/80⁺ macrophages, suggesting that this myeloid population is responsible for vascularization and progression of bone regeneration.

In the fracture hematoma, no chondrocytes are present, so macrophages may be a source of VEGFA in that situation. Here, we identify two major cell populations, which produce VEGFA over the course of regeneration. In the earliest phase, at day 1 and 2 post injury, CD80⁺ cells are found to be positive for VEGFA by immunofluorescence. From day 3 on, cells inside the area of bone formation and on bone surfaces show a strong VEGFA signal. Based on their localization, the proximity to bone surfaces, we assume that these cells are precursors of, and committed osteoblasts, as well as chondrocytes in cartilage (16; compare **Figures 1A–C**). Until day 3, among the CD80⁺ cells, we find F4/80⁺, which we consider M1-like cells, as well as F4/80⁻, which could either be a subpopulation of mature F4/80⁺ macrophages or precursors of macrophages, such as F4/80^{low} monocytes (50). In addition, other antigen-presenting cells such as B cells and dendritic cells can be CD80⁺ (51, 52). It has been previously described that VEGFA-expression of macrophages depends on the stimulation state (53, 54). Additionally, tissue resident F4/80⁺ macrophages are not known to express VEGFA constantly, but rather they interact with VEGFA-producing cells on promoting vascularization and supporting sprout fusion (29, 55). Our results support previous literature by showing VEGFA-expression from immune cells (56). Here, CD80⁺ cells were expressing VEGFA in the early phase until day 3, while the majority was F4/80⁻. CD80⁺ M1-like macrophages have not been reported to express VEGFA. It can be speculated from our data that CD80⁺ cells contribute to the presence of VEGFA within the fracture gap until bone cells differentiate and become the dominant producers of VEGFA during the bone formation and remodeling phase.

The presence of M1-like macrophages until day 3, the subsequent decrease, and the absence at later time points in our study indicates that the transition from the pro-inflammatory phase to the anti-inflammatory phase in the myeloid compartment has already taken place at day 3 in the osteotomy models analyzed here. It has been described that a switch from M1-like macrophages to an M2-like phenotype is essential for successful healing. Under chronic inflammatory conditions

it is impaired and accompanied by the prolonged presence of M1-like macrophages (57). Consequently, recent research focuses on this switch to improve healing (58, 59). Interestingly, M1- and M2-like macrophages do not localize inside the fracture gap, and rather CX3CR1⁺F4/80⁺ cells participate in the initial and crucial vascularization process. Our spatial analyses reveal that CD206⁺ macrophages localize in extramedullary areas and, moreover, that they remain positive for the pro-inflammatory marker Mac-2 until d14. After that, cells that are positive for either CD206 or Mac-2 remain present until the remodeling phase. The extramedullary localization of CD206⁺ macrophages may indicate that M2-like macrophages serve functions beyond bone regeneration, for example skeletal muscle regeneration (60).

Of note, during the regeneration process, the immunofluorescence signal for Emcn⁺ in the endothelium partially co-localizes with the signal for the mannose receptor CD206. CD206 expression in endothelial cells has been previously reported to be linked to the phagocytic activity of this cell type (61). In addition, Awert et al. describe CD206 as a marker for perivascular macrophages and show that they locate closely to Emcn⁺ cells in tumors (62). CD206⁺ endothelial cells can be found in different tissues such as the liver (63, 64) or placenta (61). Future experiments need to be performed to investigate the cellular origin of the CD206 signal we observe.

In tissue areas adjacent of the fracture gap, an inhomogeneous distribution of macrophages, as well as endothelia toward the distal end of the femur (spatial polarization), is evident. We suspect that the osteotomy, which interrupts all vessels in the tissue, in combination with placement of the neighboring, distal screw (one of four screws) creates damage to the blood supply occurring from both sides of the fracture (Supplementary Figure 6). Large veins and the main sinus exit the bone at few points. However, transcortical vessels are predominantly responsible for the arterial blood supply in long bones, as described recently (65). Since the cortical integrity is disrupted by the osteotomy and the screw placement, the blood supply is disturbed to a high degree in a complete osteotomy model. We assume that this results in extensive tissue damage, which in turn initiates the recruitment of macrophages followed by vascularization, leading to the observed phenomenon of transient distal polarization.

Taken together, we demonstrate here that type H endothelium is present throughout the regeneration in standardized osteotomy models in mice. Osx⁺ osteoblasts as well as macrophages are present in close proximity to the vasculature, indicating an important crosstalk. M2-like macrophages are mainly found in extramedullary regions, with no obvious interconnection to the vasculature. In addition, we describe CX3CR1⁺F4/80⁺ cells to be the predominant macrophage population, which progressively infiltrates the hematoma. These macrophages precede perfused vascularization in the first phase of vascularization and reside there until remodeling takes place.

A strong polarization of type H endothelium as well as of macrophages distally to the fracture gap is found in the fracture models. Our findings underline the importance of the innate immune system within the bone regeneration process by linking myeloid cells present in the fracture gap to local angiogenesis.

DATA AVAILABILITY STATEMENT

The authors declare that all data supporting the findings of this study are available within the paper and its supplementary information file. Further information is made available by the authors upon request.

ETHICS STATEMENT

The animal study was reviewed and approved by the local animal protection authority (LaGeSo; permit numbers: G0039/16, G0111/13, and G0302/17), and were performed in accordance with the German Animal Welfare Act.

AUTHOR CONTRIBUTIONS

JS, AL, TG, RN, and AH: study design. JS, AL, AR, LA, MK, KS-B, and AF: data collection and analysis. JS, AL, and AH: data interpretation and writing of the manuscript. KS-B, FB, RN, TG, and GD: revising manuscript.

FUNDING

This study was supported by funding from the Deutsche Forschungsgemeinschaft, FOR2165 (HA5354/6-2 to AH, NI-1167/4-2 to RN), and TRR130, project C01 (to AH and RN). This study was financially supported by the Berlin Institute of Health Center for Regenerative Therapies and the Berlin-Brandenburg School for Regenerative Therapies (BCRT, BSRT). The work of TG was funded by the Deutsche Forschungsgemeinschaft (353142848). AL, FB, and TG acknowledge the support of this work by a grant from the German Federal Institute for Risk Assessment (grant no. 1328-542). We acknowledge support from the German Research Foundation (DFG) and the Open Access Publication Fund of Charité - Universitätsmedizin Berlin.

ACKNOWLEDGMENTS

The authors would like to thank Robert Günther and Mattea Durst for assistance during osteotomy surgeries. JS and AL are members of the Berlin-Brandenburg School for Regenerative Therapies (BSRT).

SUPPLEMENTARY MATERIAL

The Supplementary Material for this article can be found online at: <https://www.frontiersin.org/articles/10.3389/fimmu.2019.02588/full#supplementary-material>

REFERENCES

- Manjubala I, Liu Y, Epari DR, Roschger P, Schell H, Fratzl P, et al. Spatial and temporal variations of mechanical properties and mineral content of the external callus during bone healing. *Bone*. (2009) 45:185–92. doi: 10.1016/j.bone.2009.04.249
- Borgiani E, Figge C, Kruck B, Willie BM, Duda GN, Checa S. Age-related changes in the mechanical regulation of bone healing are explained by altered cellular mechanoresponse. *J Bone Miner Res*. (2019) 34:1923–37. doi: 10.1002/jbmr.3801
- Schmidt-Bleek K, Petersen A, Dienelt A, Schwarz C, Duda GN. Initiation and early control of tissue regeneration - bone healing as a model system for tissue regeneration. *Expert Opin Biol Ther*. (2014) 14:247–59. doi: 10.1517/14712598.2014.857653
- Winkler T, Sass FA, Duda GN, Schmidt-Bleek K. A review of biomaterials in bone defect healing, remaining shortcomings and future opportunities for bone tissue engineering: the unsolved challenge. *Bone Joint Res*. (2018) 7:232–43. doi: 10.1302/2046-3758.73.BJR-2017-0270.R1
- Waddington RJ, Roberts HC, Sugars RV, Schonherr E. Differential roles for small leucine-rich proteoglycans in bone formation. *Eur Cell Mater*. (2003) 6:12–21. doi: 10.22203/eCM.v006a02
- Lienau J, Schmidt-Bleek K, Peters A, Haschke F, Duda GN, Perka C, et al. Differential regulation of blood vessel formation between standard and delayed bone healing. *J Orthop Res*. (2009) 27:1133–40. doi: 10.1002/jor.20870
- Kusumbe AP, Ramasamy SK, Adams RH. Coupling of angiogenesis and osteogenesis by a specific vessel subtype in bone. *Nature*. (2014) 507:323–8. doi: 10.1038/nature13145
- Ramasamy SK, Kusumbe AP, Wang L, Adams RH. Endothelial Notch activity promotes angiogenesis and osteogenesis in bone. *Nature*. (2014) 507:376–80. doi: 10.1038/nature13146
- Filipowska J, Tomaszewski KA, Niedzwiedzki L, Walocha JA, Niedzwiedzki T. The role of vasculature in bone development, regeneration and proper systemic functioning. *Angiogenesis*. (2017) 20:291–302. doi: 10.1007/s10456-017-9541-1
- Reismann D, Stefanowski J, Gunther R, Rakhymzhan A, Matthys R, Nutzi R, et al. Longitudinal intravital imaging of the femoral bone marrow reveals plasticity within marrow vasculature. *Nat Commun*. (2017) 8:2153. doi: 10.1038/s41467-017-01538-9
- Street J, Winter D, Wang JH, Wakai A, McGuinness A, Redmond HP. Is human fracture hematoma inherently angiogenic? *Clin Orthop Relat Res*. (2000) 378:224–37. doi: 10.1097/00003086-200009000-00033
- Kolar P, Gaber T, Perka C, Duda GN, Buttgerit F. Human early fracture hematoma is characterized by inflammation and hypoxia. *Clin Orthop Relat Res*. (2011) 469:3118–26. doi: 10.1007/s11999-011-1865-3
- Hoff P, Gaber T, Strehl C, Schmidt-Bleek K, Lang A, Huscher D, et al. Immunological characterization of the early human fracture hematoma. *Immunol Res*. (2016) 64:1195–206. doi: 10.1007/s12026-016-8868-9
- Olson S, Hahn D. Surgical treatment of non-unions: a case for internal fixation. *Injury*. (2006) 37:681–90. doi: 10.1016/j.injury.2004.11.039
- Hu K, Olsen BR. The roles of vascular endothelial growth factor in bone repair and regeneration. *Bone*. (2016) 91:30–8. doi: 10.1016/j.bone.2016.06.013
- Buettmann EG, Mckenzie JA, Migotsky N, Sykes DA, Hu P, Yoneda S, et al. VEGFA from early osteoblast lineage cells (Osterix+) is required in mice for fracture healing. *J Bone Miner Res*. (2019) 34:1690–706. doi: 10.1002/jbmr.3755
- Piroso A, Gottardi R, Alexander PG, Tuan RS. Engineering *in-vitro* stem cell-based vascularized bone models for drug screening and predictive toxicology. *Stem Cell Res Ther*. (2018) 9:112. doi: 10.1186/s13287-018-0847-8
- Xie H, Cui Z, Wang L, Xia Z, Hu Y, Xian L, et al. PDGF-BB secreted by preosteoclasts induces angiogenesis during coupling with osteogenesis. *Nat Med*. (2014) 20:1270–8. doi: 10.1038/nm.3668
- Romeo SG, Alawi KM, Rodrigues J, Singh A, Kusumbe AP, Ramasamy SK. Endothelial proteolytic activity and interaction with non-resorbing osteoclasts mediate bone elongation. *Nat Cell Biol*. (2019) 21:430–41. doi: 10.1038/s41556-019-0304-7
- Sivan U, De Angelis J, Kusumbe AP. Role of angiocrine signals in bone development, homeostasis and disease. *Open Biol*. (2019) 9:190144. doi: 10.1098/rsob.190144
- Lang A, Kirchner M, Stefanowski J, Durst M, Weber MC, Pfeiffenberger M, et al. Collagen I-based scaffolds negatively impact fracture healing in a mouse-osteotomy-model although used routinely in research and clinical application. *Acta Biomater*. (2019) 86:171–84. doi: 10.1016/j.actbio.2018.12.043
- Alexander KA, Chang MK, Maylin ER, Kohler T, Muller R, Wu AC, et al. Osteal macrophages promote *in vivo* intramembranous bone healing in a mouse tibial injury model. *J Bone Miner Res*. (2011) 26:1517–32. doi: 10.1002/jbmr.354
- Raggatt LJ, Wulschlegler ME, Alexander KA, Wu AC, Millard SM, Kaur S, et al. Fracture healing via periosteal callus formation requires macrophages for both initiation and progression of early endochondral ossification. *Am J Pathol*. (2014) 184:3192–204. doi: 10.1016/j.ajpath.2014.08.017
- Schlundt C, El Khassawna T, Serra A, Dienelt A, Wendler S, Schell H, et al. Macrophages in bone fracture healing: their essential role in endochondral ossification. *Bone*. (2015) 106:78–89. doi: 10.1016/j.bone.2015.10.019
- Alexander KA, Raggatt LJ, Millard S, Batoon L, Chiu-Ku Wu A, Chang MK, et al. Resting and injury-induced inflamed periosteum contain multiple macrophage subsets that are located at sites of bone growth and regeneration. *Immunol Cell Biol*. (2017) 95:7–16. doi: 10.1038/icb.2016.74
- Batoon L, Millard SM, Raggatt LJ, Pettit AR. Osteomacs and bone regeneration. *Curr Osteoporos Rep*. (2017) 15:385–95. doi: 10.1007/s11914-017-0384-x
- Spinelli FM, Vitale DL, Demarchi G, Cristina C, Alaniz L. The immunological effect of hyaluronan in tumor angiogenesis. *Clin Transl Immunol*. (2015) 4:e52. doi: 10.1038/cti.2015.35
- David Dong ZM, Aplin AC, Nicosia RF. Regulation of angiogenesis by macrophages, dendritic cells, and circulating myelomonocytic cells. *Curr Pharm Des*. (2009) 15:365–79. doi: 10.2174/138161209787315783
- Fantin A, Vieira JM, Gestri G, Denti L, Schwarz Q, Prykhodzij S, et al. Tissue macrophages act as cellular chaperones for vascular anastomosis downstream of VEGF-mediated endothelial tip cell induction. *Blood*. (2010) 116:829–40. doi: 10.1182/blood-2009-12-257832
- Al-Roubaie S, Hughes JH, Filla MB, Lansford R, Lehoux S, Jones EA. Time-lapse microscopy of macrophages during embryonic vascular development. *Dev Dyn*. (2012) 241:1423–31. doi: 10.1002/dvdy.23835
- He H, Mack JJ, Güç E, Warren CM, Squadrito ML, Kilarski WW, et al. Perivascular macrophages limit permeability. *Arterioscler Thromb Vasc Biol*. (2016) 36:2203–12. doi: 10.1161/ATVBAHA.116.307592
- He H, Xu J, Warren CM, Duan D, Li X, Wu L, et al. Endothelial cells provide an instructive niche for the differentiation and functional polarization of M2-like macrophages. *Blood*. (2012) 120:3152–62. doi: 10.1182/blood-2012-04-422758
- Jirkof P, Durst M, Klopfeisch R, Palme R, Thone-Reineke C, Buttgerit F, et al. Administration of Tramadol or Buprenorphine via the drinking water for post-operative analgesia in a mouse-osteotomy model. *Sci Rep*. (2019) 9:10749. doi: 10.1038/s41598-019-47186-5
- Lang A, Schulz A, Ellinghaus A, Schmidt-Bleek K. Osteotomy models - the current status on pain scoring and management in small rodents. *Lab Anim*. (2016) 50:433–41. doi: 10.1177/0023677216675007
- Kawamoto T, Kawamoto K. Preparation of thin frozen sections from nonfixed and undecalcified hard tissues using Kawamoto's film method (2012). *Methods Mol Biol*. (2014) 1130:149–64. doi: 10.1007/978-1-62703-989-5_11
- Carpenter AE, Kamentsky L, Eliceiri KW. A call for bioimaging software usability. *Nat Methods*. (2012) 9:666–70. doi: 10.1038/nmeth.2073
- Caicedo JC, Cooper S, Heigwer F, Warchal S, Qiu P, Molnar C, et al. Data-analysis strategies for image-based cell profiling. *Nat Methods*. (2017) 14:849–63. doi: 10.1038/nmeth.4397
- Einhorn TA, Gerstenfeld LC. Fracture healing: mechanisms and interventions. *Nat Rev Rheumatol*. (2015) 11:45–54. doi: 10.1038/nrrheum.2014.164
- Ramasamy SK, Kusumbe AP, Schiller M, Zeuschner D, Bixel MG, Milia C, et al. Blood flow controls bone vascular function and osteogenesis. *Nat Commun*. (2016) 7:13601. doi: 10.1038/ncomms13601
- Colnot C. Skeletal cell fate decisions within periosteum and bone marrow during bone regeneration. *J Bone Miner Res*. (2009) 24:274–82. doi: 10.1359/jbmr.081003
- Bragdon BC, Bahney CS. Origin of reparative stem cells in fracture healing. *Curr Osteoporos Rep*. (2018) 16:490–503. doi: 10.1007/s11914-018-0458-4

42. Akiyama H, Kim JE, Nakashima K, Balmes G, Iwai N, Deng JM, et al. Osteochondrogenitor cells are derived from Sox9 expressing precursors. *Proc Natl Acad Sci USA*. (2005) 102:14665–70. doi: 10.1073/pnas.0504750102
43. He X, Bougioukli S, Ortega B, Arevalo E, Lieberman JR, McMahon AP. Sox9 positive periosteal cells in fracture repair of the adult mammalian long bone. *Bone*. (2017) 103:12–9. doi: 10.1016/j.bone.2017.06.008
44. Kuwahara ST, Serowky MA, Vakhshori V, Tripuraneni N, Hegde NV, Lieberman JR, et al. Sox9+ messenger cells orchestrate large-scale skeletal regeneration in the mammalian rib. *Elife*. (2019) 8:e40715. doi: 10.7554/eLife.40715
45. Zhou G, Zheng Q, Engin F, Munivez E, Chen Y, Sebald E, et al. Dominance of SOX9 function over RUNX2 during skeletogenesis. *Proc Natl Acad Sci USA*. (2006) 103:19004–9. doi: 10.1073/pnas.0605170103
46. Vi L, Baht GS, Soderblom EJ, Whetstone H, Wei Q, Furman B, et al. Macrophage cells secrete factors including LRP1 that orchestrate the rejuvenation of bone repair in mice. *Nat Commun*. (2018) 9:5191. doi: 10.1038/s41467-018-07666-0
47. Chang MK, Raggatt LJ, Alexander KA, Kuliwaba JS, Fazzalari NL, Schroder K, et al. Osteal tissue macrophages are intercalated throughout human and mouse bone lining tissues and regulate osteoblast function *in vitro* and *in vivo*. *J Immunol*. (2008) 181:1232–44. doi: 10.4049/jimmunol.181.2.1232
48. Vi L, Baht GS, Whetstone H, Ng A, Wei Q, Poon R, et al. Macrophages promote osteoblastic differentiation *in-vivo*: implications in fracture repair and bone homeostasis. *J Bone Miner Res*. (2015) 30:1090–102. doi: 10.1002/jbmr.2422
49. Hoff P, Gaber T, Strehl C, Jakstadt M, Hoff H, Schmidt-Bleek K, et al. A pronounced inflammatory activity characterizes the early fracture healing phase in immunologically restricted patients. *Int J Mol Sci*. (2017) 18:E583. doi: 10.3390/ijms18030583
50. Gordon S, Plüddemann A, Martinez Estrada F. Macrophage heterogeneity in tissues: phenotypic diversity and functions. *Immunol Rev*. (2014) 262:36–55. doi: 10.1111/immr.12223
51. Mclellan AD, Starling GC, Williams LA, Hock BD, Hart DN. Activation of human peripheral blood dendritic cells induces the CD86 co-stimulatory molecule. *Eur J Immunol*. (1995) 25:2064–8. doi: 10.1002/eji.1830250739
52. Subauste CS, De Waal Malefyt R, Fuh F. Role of CD80 (B7.1) and CD86 (B7.2) in the immune response to an intracellular pathogen. *J Immunol*. (1998) 160:1831–40.
53. Wu WK, Llewellyn OP, Bates DO, Nicholson LB, Dick AD. IL-10 regulation of macrophage VEGF production is dependent on macrophage polarisation and hypoxia. *Immunobiology*. (2010) 215:796–803. doi: 10.1016/j.imbio.2010.05.025
54. Gurevich DB, Severn CE, Twomey C, Greenhough A, Cash J, Toye AM, et al. Live imaging of wound angiogenesis reveals macrophage orchestrated vessel sprouting and regression. *EMBO J*. (2018) 37:e97786. doi: 10.15252/embj.201797786
55. Britto DD, Wyroba B, Chen W, Lockwood RA, Tran KB, Shepherd PR, et al. Macrophages enhance Vegfa-driven angiogenesis in an embryonic zebrafish tumour xenograft model. *Dis Model Mech*. (2018) 11:dmm035998. doi: 10.1242/dmm.035998
56. Bahney CS, Zondervan RL, Allison P, Theologis A, Ashley JW, Ahn J, et al. Cellular biology of fracture healing. *J Orthop Res*. (2019) 37:35–50. doi: 10.1002/jor.24170
57. Claes L, Recknagel S, Ignatius A. Fracture healing under healthy and inflammatory conditions. *Nat Rev Rheumatol*. (2012) 8:133–43. doi: 10.1038/nrrheum.2012.1
58. Lin T, Kohno Y, Huang JF, Romero-Lopez M, Pajarinen J, Maruyama M, et al. NFkappaB sensing IL-4 secreting mesenchymal stem cells mitigate the proinflammatory response of macrophages exposed to polyethylene wear particles. *J Biomed Mater Res A*. (2018) 106:2744–52. doi: 10.1002/jbm.a.36504
59. Lin T, Pajarinen J, Kohno Y, Maruyama M, Romero-Lopez M, Huang JF, et al. Transplanted interleukin-4-secreting mesenchymal stromal cells show extended survival and increased bone mineral density in the murine femur. *Cytotherapy*. (2018) 20:1028–36. doi: 10.1016/j.jcyt.2018.06.009
60. Saclier M, Cuvelier S, Magnan M, Mounier R, Chazaud B. Monocyte/macrophage interactions with myogenic precursor cells during skeletal muscle regeneration. *FEBS J*. (2013) 280:4118–30. doi: 10.1111/febs.12166
61. Sheikh H, Yarwood H, Ashworth A, Isacke CM. Endo180, an endocytic recycling glycoprotein related to the macrophage mannose receptor is expressed on fibroblasts, endothelial cells and macrophages and functions as a lectin receptor. *J Cell Sci*. (2000) 113:1021–32.
62. Arwert EN, Harney AS, Entenberg D, Wang Y, Sahai E, Pollard JW, et al. A unidirectional transition from migratory to perivascular macrophage is required for tumor cell intravasation. *Cell Rep*. (2018) 23:1239–48. doi: 10.1016/j.celrep.2018.04.007
63. Azad AK, Rajaram MVS, Schlesinger LS. Exploitation of the macrophage mannose receptor (CD206) in infectious disease diagnostics and therapeutics. *J Cytol Mol Biol*. (2014) 1:1000003. doi: 10.13188/12325-14653.1000003
64. Beljaars L, Schippers M, Reker-Smit C, Martinez FO, Helming L, Poelstra K, et al. Hepatic localization of macrophage phenotypes during fibrogenesis and resolution of fibrosis in mice and humans. *Front Immunol*. (2014) 5:430. doi: 10.3389/fimmu.2014.00430
65. Grüneboom A, Hawwari I, Weidner D, Culemann S, Müller S, Henneberg S, et al. A network of trans-cortical capillaries as mainstay for blood circulation in long bones. *Nat Metab*. (2019) 1:236–50. doi: 10.1038/s42255-018-0016-5

Conflict of Interest: The authors declare that the research was conducted in the absence of any commercial or financial relationships that could be construed as a potential conflict of interest.

Copyright © 2019 Stefanowski, Lang, Rauch, Aulich, Köhler, Fiedler, Buttgerit, Schmidt-Bleek, Duda, Gaber, Niesner and Hauser. This is an open-access article distributed under the terms of the Creative Commons Attribution License (CC BY). The use, distribution or reproduction in other forums is permitted, provided the original author(s) and the copyright owner(s) are credited and that the original publication in this journal is cited, in accordance with accepted academic practice. No use, distribution or reproduction is permitted which does not comply with these terms.

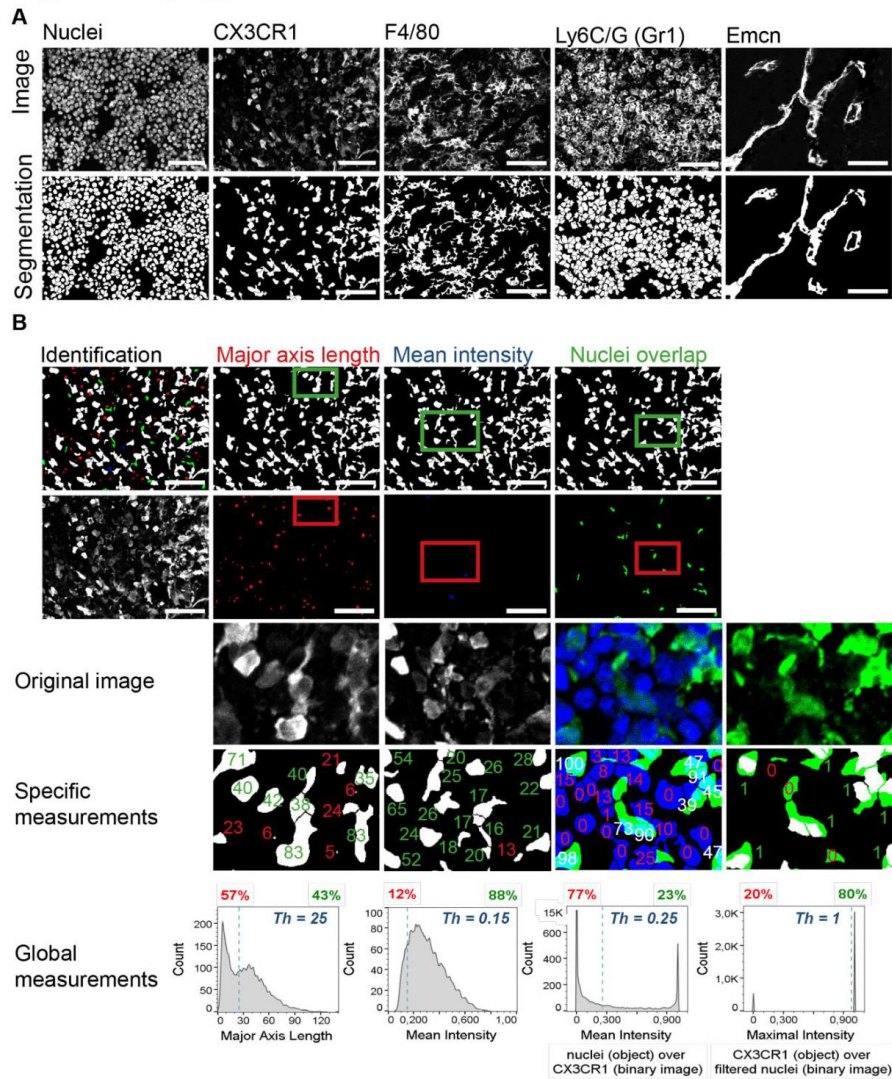
8.4 Stefanowski et al., 2019 – Supporting Material

Supplementary Material

Spatial distribution of macrophages during callus formation and maturation reveals close crosstalk between macrophages and newly forming vessels

Macrophages & vessels during bone healing

Supplementary Figure 1

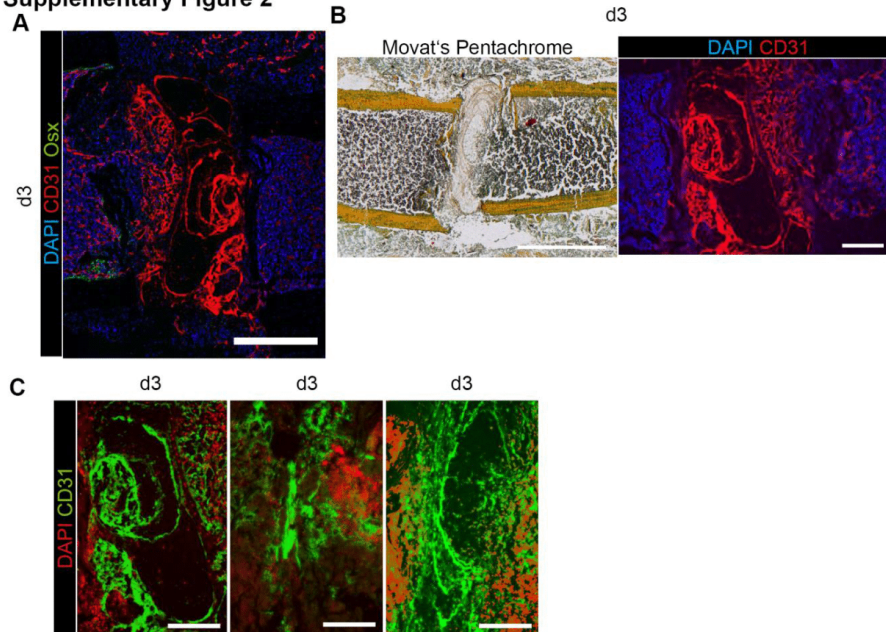


Supplementary Figure 1: Image analysis strategy for object identification. (A) Immunofluorescence images of sections of bone regeneration using the LIMB microendoscope internal fixator with their refined segmentation within CellProfiler. Scale bars = 50 μ m. (B) Refinement of the segmentation of CX3CR1:GFP⁺ cells based on various object features. Identified objects were removed based on their size (major axis length; red) and their signal intensity (mean intensity; blue). Only cells in the focus plane (i.e. with nuclei) were analyzed (nuclei overlap; green).

Macrophages & vessels during bone healing

The thresholding (Th, blue line) was based on one hand on the visual observation of specific measurements of individual objects in relation their identification within the original image (depicted as absolute values for the major axis length and as percentages for the intensity measurements with the measurements associated with removed values in red and the other values in green). Additionally, the global measurement distribution of all objects within the image (depicted in *FlowJo*) was taken into account. The measurements above the histograms depict the portions of removed (red) and correct (green) signals within the example image. Scale bars = 50 μm .

Supplementary Figure 2

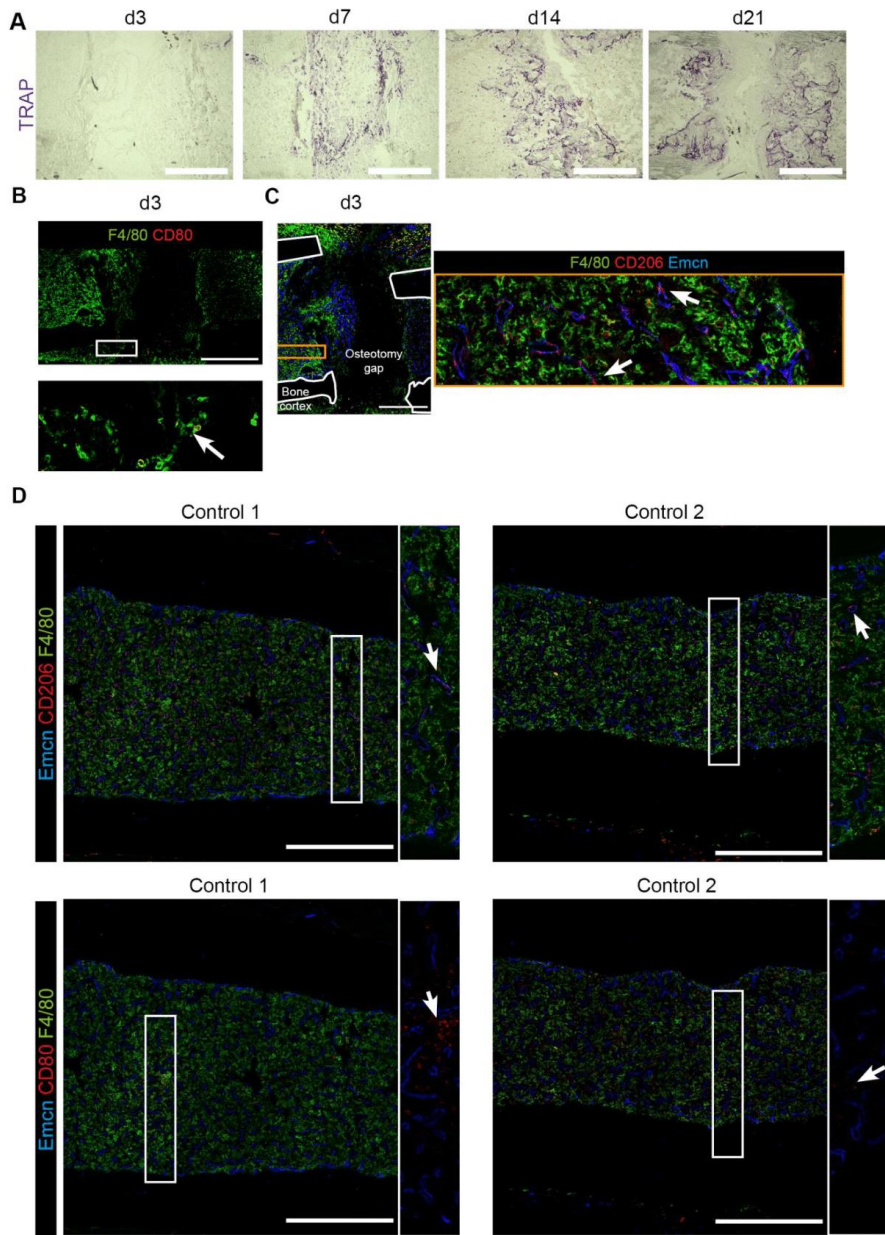


Supplementary Figure 2: Crosstalk between vessel formation and Osx^+ osteoprogenitor cells during bone regeneration and accumulation of CD31 in the fracture hematoma at day 3

(A, B) At day 3 the residuals of the fracture hematoma are still visible in Movat's Pentachrome staining and strongly CD31⁺. Scale bars = 500 μm . (C) Images exemplifies that the residuals of the fracture hematoma are cell-free. Scale bars = 200 μm .

Macrophages & vessels during bone healing

Supplementary Figure 3

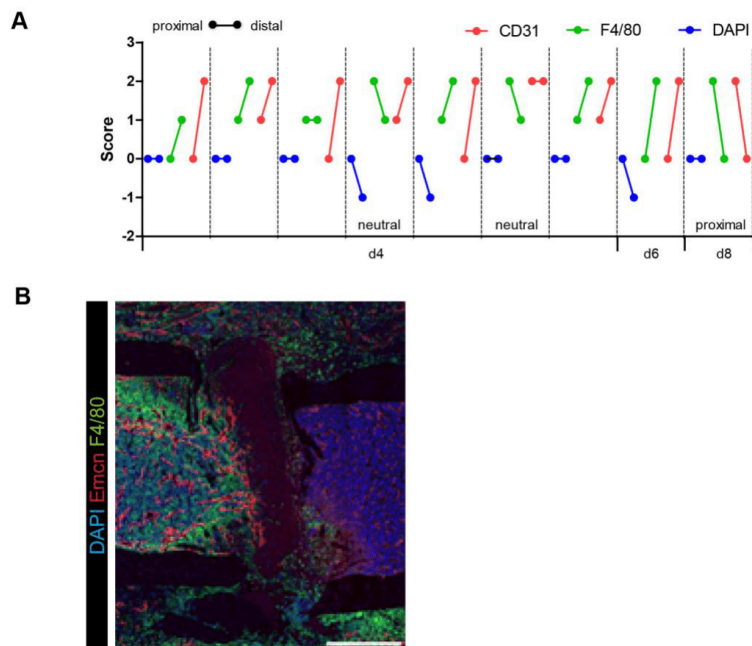


Supplementary Figure 3: Spatial localization of M1-like macrophages, CD206+ cells and scoring of polarization. (A) Exemplary images of TRAP staining within the fracture gap at day 3, 7,

Macrophages & vessels during bone healing

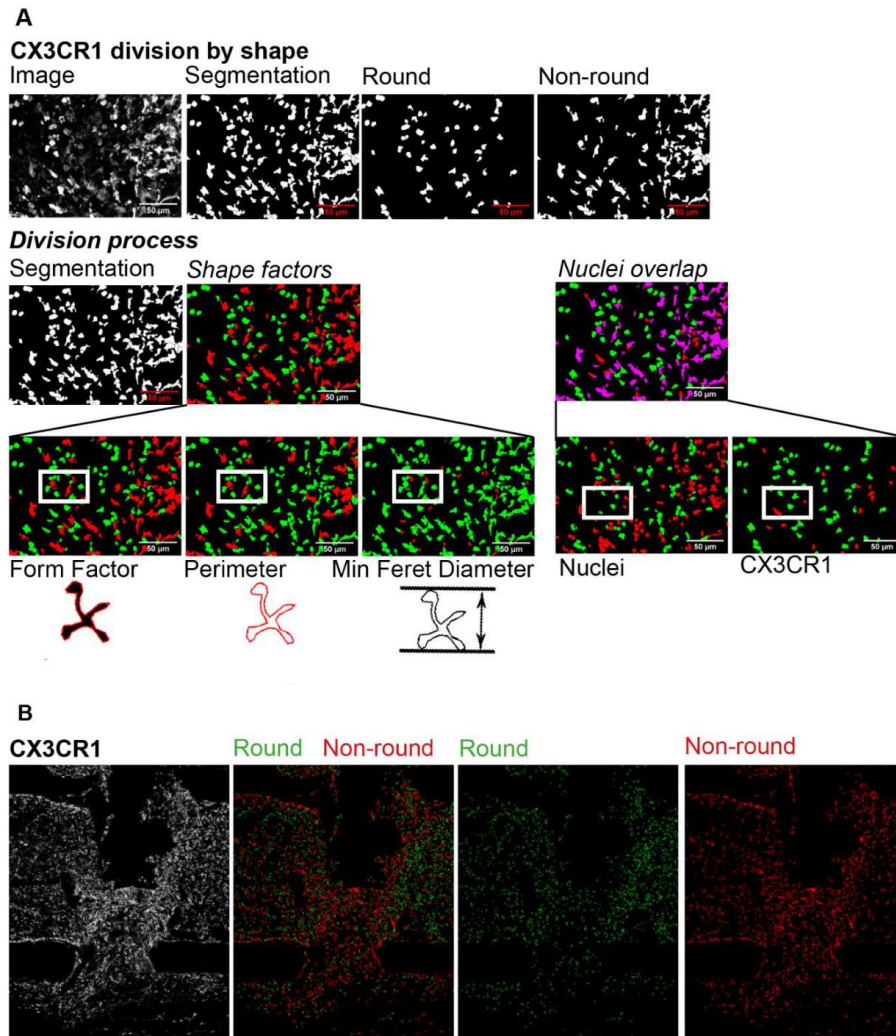
14 and 21 show TRAP⁺ cells in the fracture gap from day 7. (B) Immunofluorescence image of CD80 and F4/80 in an osteotomized bone 3 days post-surgery show few cells extramedullar adjacent to the gap. Scale bar = 500 μ m (C) Immunofluorescence image of CD206 and F4/80 show elongated F4/80⁺ structures right next to endothelium suggesting CD206⁺ endothelium during bone regeneration. (D) In contralateral control samples (n = 2) F4/80⁺ cells are evenly distributed throughout the bone marrow. CD206⁺F4/80⁺ signals are detected along the endothelium of sinusoids. (E) CD80⁺F4/80⁺ cells were rare in control sections. No signal is detected extramedullar. Scale bars = 500 μ m.

Supplementary Figure 4



Supplementary Figure 4: Polarization scoring accumulated and individual scoring for the LIMB osteotomy-model show distal polarization. Polarization scoring for individual samples which were scored as described in the methods section. Samples were considered polarized when the scored values for F4/80 and vessel marker of proximal and distal resulted in a difference > 2 favoring one side (indicated: proximal, distal). Samples which scored a difference of < 2 were neutral (indicated: neutral). In total n = 20 samples were analyzed, 9 samples scored values other than 0 of which 2 are neutral, 1 polarized proximally and 6 polarized distally. (B) Polarization is also observed in the osteotomy-model. Scale bar = 500 μ m.

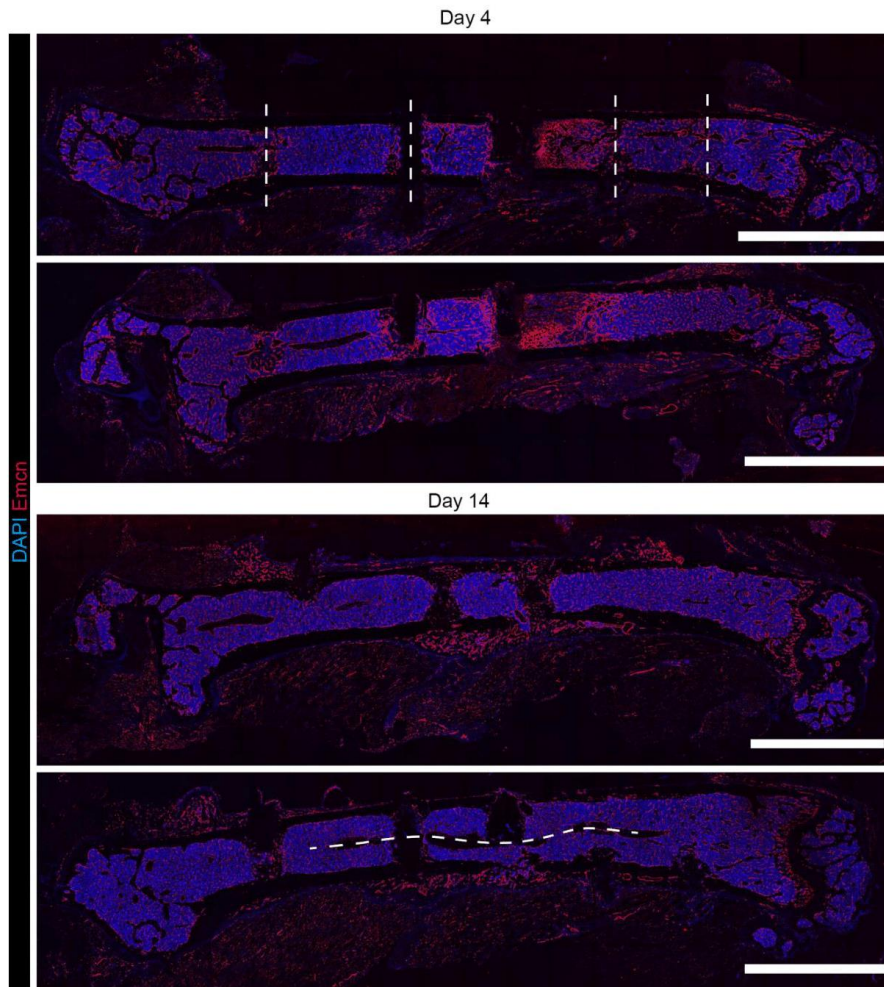
Supplementary Figure 5



Supplementary Figure 5: Segmentation and division in round and non-round objects. (A) Exemplary segmentation process of a CX3CR1 fluorescent image, its segmentation via three shape factors (form factor, perimeter, and min Feret diameter). Objects were considered cells when they overlapped with a nucleus. (B) Exemplary result of the segmentation and division result.

Macrophages & vessels during bone healing

Supplementary Figure 6



Supplementary Figure 6: Disrupted vascularization and polarization is transient. Exemplary immunofluorescence overview images of complete bones stained for Emcn in samples 4 and 14 days post-osteotomy show type H endothelium in damaged tissue and around the four screws (straight dashed lines). The main sinus is regenerated and fully visible at day 14. Scale bars = 2500 μ m. n(day 4) = 3, n(day 14) = 2. Pictures were acquired using a 4x objective in tile scan mode at a Zeiss LSM880.

Macrophages & vessels during bone healing

Supplementary Movie 1-4: Longitudinal intravital microendoscopy of the osteotomy gap using CX3CR1:GFP mice and Qtracker 655 (red). Low numbers of motile GFP⁺ cells (green) enter the osteotomy gap in the field of view 2 days post-surgery and populate the observed volume before endothelium enters the volume, in close proximity to motile and sessile GFP⁺ cells. The vascular network continues to remodel until day 6. Images 250 x 250 μm . Scale bar = 100 μm . (1) Day 2. (2) Day 3. (3) Day 4. (4) Day 5.

8.5 Stefanowski et al., 2020 – Limbostomy: Longitudinal Intravital Microendoscopy in Murine Osteotomies

The following presents the publication

Stefanowski, J.*, Fiedler, A.F.*, Köhler, M., Günther, R., Liublin, W., Tschalkner, M., Rauch, A., Reismann, D., Matthys, R., Nützi, R., Bixel, M.G., Adams, R.H., Niesner, R.A., Duda, G.N., Hauser, A.E., 2020. Limbostomy: Longitudinal Intravital Microendoscopy in Murine Osteotomies. *Cytom. Part A* 97, 483–495. Impact Factor N.A <https://doi.org/10.1002/cyto.a.23997> (*shared first-coauthor)

as a part of this dissertation. For optimal pdf and image quality or the publication's digital supporting information, such as movies access the publisher's website under the digital object identifiers of the selected publication. All information is publicly available.



Limbostomy: Longitudinal Intravital Microendoscopy in Murine Osteotomies

Jonathan Stefanowski,^{1,2†} Alexander F. Fiedler,^{2,5†} Markus Köhler,^{2,5} Robert Günther,² Wjatscheslaw Liublin,² Martin Tschaikner,² Ariana Rauch,² David Reismann,² Romano Matthys,⁶ Reto Nützi,⁶ Maria Gabriele Bixel,⁷ Ralf H. Adams,⁷ Raluca A. Niesner,^{2,5} Georg N. Duda,^{3,4‡} Anja E. Hauser^{1,2‡*}

¹Department of Rheumatology and Clinical Immunology, Charité – Universitätsmedizin Berlin, Corporate Member of Freie Universität Berlin, Humboldt-Universität zu Berlin, and Berlin Institute of Health, Berlin, Germany

²Deutsches Rheuma-Forschungszentrum (DRFZ) Berlin, a Leibniz Institute, Berlin, Germany

³Charité – Universitätsmedizin Berlin, Corporate Member of Freie Universität Berlin, Humboldt-Universität zu Berlin, and Berlin Institute of Health, Berlin Institute of Health Center for Regenerative Therapies, Berlin, Germany

⁴Charité – Universitätsmedizin Berlin, Corporate Member of Freie Universität Berlin, Humboldt-Universität zu Berlin, and Berlin Institute of Health, Julius Wolff Institute, Berlin, Germany

⁵Freie Universität Berlin, Veterinary Medicine, Dynamic and Functional *in vivo* Imaging, Berlin, Germany

⁶RISystem AG, Landquart, Switzerland

⁷Max Planck Institute for Molecular Biomedicine, Münster, Germany

Received 23 October 2019; Revised 20 January 2020; Accepted 24 February 2020

Grant sponsor: Deutsche Forschungsgemeinschaft, Grant numbers: DFG FOR 2165/HA5354/6-2, DFG TRR130 TP C01, SPP1937/HA5354/8-2

Additional Supporting Information may be found in the online version of this article.



• Abstract

Bone healing involves the interplay of immune cells, mesenchymal cells, and vasculature over the time course of regeneration. Approaches to quantify the spatiotemporal aspects of bone healing at cellular resolution during long bone healing do not yet exist. Here, a novel technique termed Limbostomy is presented, which combines intravital microendoscopy with an osteotomy. This design allows a modular combination of an internal fixator plate with a gradient refractive index (GRIN) lens at various depths in the bone marrow and can be combined with a surgical osteotomy procedure. The field of view (FOV) covers a significant area of the fracture gap and allows monitoring cellular processes *in vivo*. The GRIN lens causes intrinsic optical aberrations which have to be corrected. The optical system was characterized and a postprocessing algorithm was developed. It corrects for wave front aberration-induced image plane deformation and for background and noise signals, enabling us to observe subcellular processes. Exemplarily, we quantitatively and qualitatively analyze angiogenesis in bone regeneration. We make use of a transgenic reporter mouse strain with nuclear green fluorescent protein and membrane-bound tdTomato under the Cadherin-5 promoter. We observe two phases of vascularization. First, rapid vessel sprouting pervades the FOV within 3–4 days after osteotomy. Second, the vessel network continues to be dynamically remodeled until the end of our observation time, 14 days after surgery. Limbostomy opens a unique set of opportunities and allows further insight on spatiotemporal aspects of bone marrow biology, for example, hematopoiesis, analysis of cellular niches, immunological memory, and vascularization in the bone marrow during health and disease. © 2020 The Authors. *Cytometry Part A* published by Wiley Periodicals, Inc. on behalf of International Society for Advancement of Cytometry.

• Key terms

intravital microscopy; bone regeneration; osteotomy; bone vascularization; internal fixation; chronic window; multiphoton microscopy; GRIN lens; wave front correction; aberration correction; bone microendoscopy

REGENERATIVE healing of tissues is a highly dynamic process that shows a very distinct spatial distribution of the cells involved, governing self-organization of the forming tissue. Bone healing can serve as a model system for such dynamic healing cascades, specifically since bone has the unique capability of complete restoration without scar formation. To understand the underlying principles of this early self-assembly in healing, however, a better insight into the *in vivo* dynamics of these cellular processes is needed. From *ex vivo* and histological observations, we have learned that fracture healing is a tightly regulated process, which occurs in overlapping but distinct phases and involves the interplay of multiple cell compartments, such as the immune system, the vasculature, and various mesenchymal cells. Directly

*Correspondence to: Anja E. Hauser, Charité – Universitätsmedizin Berlin, Corporate Member of Freie Universität Berlin, Humboldt-Universität zu Berlin, and Berlin Institute of Health, Department of Rheumatology and Clinical Immunology, Berlin, Germany
Email: hauser@drfz.de; anja.hauser-hankeln@charite.de

[†]These authors contributed equally to this study.

[‡]These authors contributed equally to this study.

Published online 20 March 2020 in Wiley Online Library
(wileyonlinelibrary.com)

DOI: 10.1002/cyto.a.23997

© 2020 The Authors. *Cytometry Part A* published by Wiley Periodicals, Inc. on behalf of International Society for Advancement of Cytometry.

This is an open access article under the terms of the Creative Commons Attribution-NonCommercial License, which permits use, distribution and reproduction in any medium, provided the original work is properly cited and is not used for commercial purposes.

after injury, a fracture hematoma forms, accompanied by the release of inflammatory mediators and the recruitment of immune cells. The initial, pro-inflammatory phase transits into an anti-inflammatory phase and as inflammation wanes, soft callus is formed, comprising fibro-cartilaginous tissue, which subsequently becomes mineralized and is therefore termed hard callus. Finally, in the remodeling phase, this newly formed bone is refined in an orchestrated interplay between cells of hematopoietic and mesenchymal origin (including osteoblasts and osteoclasts), which remodel the tissue, until an intact and fully functional bone structure is restored (1–3).

However, certain risk factors like age (4,5) or metabolic disorders (6) can delay or even impede the healing process significantly, reflected in fracture healing disorders which occur in 5–10% of patients (7). In order to further define risk factors and design patient-oriented therapeutic strategies, a detailed understanding of the processes underlying bone regeneration is necessary.

It has become evident that these regenerative cascades involve a dynamic and at least partly directed interaction between single cells of various compartments. However, mainly due to a lack of appropriate tools and technology, the details of this interplay, especially its spatiotemporal aspects, are not fully understood. Histological analyses, which demonstrated a role for the innate (8–10) and adaptive (4,11) arms of the immune system, have been performed. These analyses represent *ex vivo* snapshots of the tissue state taken from individuals at defined time points and have laid the foundation for a comprehensive analysis of the cellular composition at the injury site at various phases of bone regeneration. However, they did not allow conclusions on the dynamic regulation of cellular interaction events and interplay of cells with the surrounding matrix over time and in space. Examples for such events and interplays are endothelial cells sprouting into a site of injury, the recruitment of immune cells to an injury, the dynamic transition from the pro- to the anti-inflammatory phase, the dynamics within the mesenchymal compartment promoting callus formation, and finally, the processes of bone remodeling.

Two-photon intravital imaging of the bone marrow has become an important tool for the characterization and quantification of cellular dynamics in immunology (12). Intravital imaging has significantly contributed to our understanding of the dynamic nature of hematopoiesis (13–16) as well as the

dynamics of mature immune cells in the bone marrow (17,18) and their interactions with mesenchymal compartments (19). In many reports, marrow islands within the calvarial flat bone are visualized through the thin bone layer on the top of the skull (3,14,16,18,20–25). There are also reports of intravital multiphoton imaging being performed in long bones, such as the metatarsal bones in young animals (26) and the explanted femur (27). The femur bone marrow has also been analyzed using an external window (28). Imaging in the tibia has been performed using an approach in which an acute injury is introduced to the skin and the bone surface, in order to achieve thinning of the cortex (15,17,19). A similar approach in the tibia has been used for longitudinal imaging (21). In order to optically access the bone marrow, the cortical layer is thinned to 30–50 μm (15,17,19). Finally, access to the bone marrow has been achieved by generating subcutaneous ossicles from medical-grade polycaprolactone-calcium phosphate (mPCL-CaP) scaffolds and application of bone morphogenetic protein (BMP)-7, embedded in fibrin glue (29).

While all these approaches allowed conclusions on cellular dynamics in the tissue, observation time is limited to relatively short time periods, typically in the scale of hours. Chen et al. reported the insertion of a femoral window, which enables observation over the course of 10 days (28). However, none of these procedures covers the time and tissue location necessary to observe the process of endochondral bone regeneration in one and the same individual.

We have recently developed a microendoscopic implant, which allows us to image in the bone marrow of a femoral mouse bone, at the same tissue location, over the course of several months (30,31). The system is based on a gradient refractive index (GRIN) lens attached to an internal bone fixator (MouseFix system) (32), which results in stable fixation of the optical system in the femur, suitable for two-photon microscopy. Implantation of the microendoscopic lens requires opening the cortex with a drill, so the whole procedure closely resembles the damage induced by drill hole injury models. In fact, it can be used to monitor tissue regeneration after this type of injury. Thus, we have previously been able to demonstrate the changes in tissue composition following a drill hole injury, in particular the high degree of vascular dynamics occurring during the regeneration phase.

While drill hole injuries constitute important tools for studying bone regeneration, they mainly represent a form of

regeneration termed intramembranous ossification, where bone is formed directly from mesenchymal progenitors (33). This does not fully recapitulate all the phases of regeneration, which occur during endochondral ossification following a fracture, where a cartilaginous intermediate is generated, which then becomes mineralized and remodeled. In order to fully understand the orchestrated processes occurring during endochondral bone regeneration at a cellular and tissue level, it is highly desirable to combine longitudinal intravital two-photon imaging in bone (LIMB) with an osteotomy model.

In addition, flat bones and long bones display similarities and differences in cell distribution (34,35), ontogeny, and protein composition (36). It is known that the lack of mechanical load leads to a reduction of matrix protein expression (37,38) and bone regeneration of comparable defects is faster in long bones compared to calvarial flat bone (39). An intravital imaging approach for bone regeneration in long bones will help understanding those functional differences between injury regeneration at different sites, and improve our understanding of this process at tissue sites of high relevance in terms of translation. Here, we present a novel technology for intravital imaging termed Limbostomy, which allows to perform longitudinal intravital imaging directly in osteotomized areas, and to analyze spatiotemporal aspects at a cellular level directly at the site of endochondral bone regeneration, in a field of view (FOV) covering a substantial area of the fracture gap.

The microendoscopic lenses used for this approach show inherent optical aberrations, which cause positional or amplitudinal discrepancies of the light wave fronts at the focal plane, leading to artifacts during image acquisition. These include chromatic aberration and spherical wave front aberrations, and result in lower FOV due to less contrast and sharpness in outer radial areas and reduced spatial resolution (40).

In order to gather reliable spatial information using our technique, we thoroughly characterized the wave front and chromatic aberrations and designed a postprocessing pipeline to correct the imaging results in Limbostomy. In this way, we access a cylindrical volume of 400 μm in diameter and up to a theoretical 200 μm depth at high imaging quality, resulting in a promising tool for applications across multiple disciplines.

MATERIAL AND METHODS

Mice

All animal experiments were approved by the local animal protection authority (LaGeSo Berlin; permission number G0302/17) following the German Animal Welfare Act. Cdh5-GFP-tdT mice express a membrane-tagged tandem tomato fluorescent protein (tdT) and histone 2B linked enhanced green fluorescent protein (GFP) under a transgenic VE-cadherin (Cdh5) promoter (41). Animals were bred in our colony and kept in a conventional specific pathogen-free barrier facility. Prior to surgery, 14-week-old female animals received Buprenorphine (0.03 mg/kg; Temgesic[®], Indivior Deutschland GmbH, Mannheim, Germany) s.c. as analgesic, one injection of 0.04% Enrofloxacin (Baytril[®], 10 mg/kg body weight Bayer AG, Leverkusen, Germany) (42), and

dexpanthenol-containing eye ointment (Bepanthen[®], Bayer AG, Leverkusen, Germany). Pain was inhibited using Tramadol (0.05 mg/ml; Grünenthal, Aachen, Germany) for 3 days after surgery in drinking water ad libitum. For calculation of the gap size, results from other female mice of the same genetic background (C57BL/6) have been included.

Lens Gluing Process

In order to fix the lens in the endoscope, tubing glue was applied. The process was recorded and can be observed in the Supporting Information Movie S1. The tubing was positioned with one hole downward onto an inverted stripe of tape, which sealed the hole and simultaneously held the tubing in position. The lens was inserted into the tubing and two drops of two-component glue (EPO-TEK 301-2, John P. Kummer GmbH, Augsburg, Germany) were transferred into the exposed hole using a syringe needle. The glue was cured at 65°C overnight.

Limbostomy Imaging Procedure

For intravital imaging, anesthesia was induced with 2.0% and maintained with 1.25–1.5% of isoflurane. Mice were positioned on a heating pad at 38°C and dexpanthenol ointment was applied on both eyes to protect them from drying out. Under anesthesia, the set screw was removed, the lens examined for particles, and, if necessary, wiped clean with a dry spear swab. The reference plate was slid into a plastic adapter and secured into the stage at a fixed vertical rotation angle. The stage, including the mouse, was positioned onto the intravital microscope table (LaVision BioTec GmbH, Bielefeld, Germany) under an upright laser-scanning microscope based on a commercial scan head (TriMScope II, LaVision BioTec GmbH, Bielefeld, Germany). Using a 20 \times objective lens (IR-coating, NA 0.45, Olympus, Hamburg, Germany), the imaging plane was focused on the GRIN lens outer surface (length ca. 5.07 mm, diameter = 0.60 mm; NEM-060-10-10-850-S-1.0p, GRINTECH GmbH, Jena, Germany). Using the InspectorPro software (version 208, LaVision BioTec GmbH, Bielefeld, Germany), the focal plane was elevated 200 μm . From there, the focus was gradually moved downward (approximately 50 μm) at low laser power (wavelength = 980 nm; Ti-Sapph Laser, Coherent, Dieburg, Germany) until the surface of the GRIN lens inside the tissue was visible. Fluorophores (tdT, GFP) and Qtracker 655 Vascular Labels (Qtracker655, Q21021MP, Thermo Fisher, Waltham, MA, USA) were excited at 980 nm. 3D time-lapse stacks were acquired with a FOV of 505 \times 505 px (500 \times 500 μm , frequency = 1000, line average = 4, unidirectional) using linear power adaption at a z-step size of 5 μm and up to 19 z-steps at a time interval of 1 min over a total duration of up to 2 h. Qtracker 655 were injected into the tail vein prior to acquisition (2–3 μl per animal). Emitted light was detected with photomultiplier tubes in the ranges of 466 \pm 20, 525 \pm 25, 593 \pm 20, and 655 \pm 20 nm. GFP was detected at 525 \pm 25 nm, tdT at 593 \pm 20 nm, Qtracker 655 at 655 \pm 20 nm, and second harmonic generation second harmonic generation (SHG) signal at 593 \pm 20 nm. After

imaging, the mouse was removed from the stage and the lens was secured using a set screw.

Image Correction

The background was corrected with a white top-hat morphological filter (based on the empirically determined size and shape of the cells) of the MorphoLibJ Plugin in FIJI. This filter homogenizes the uneven background and fluorescence signal intensities in the edge and central FOV regions, through performing a mathematical morphological opening (dilation) of the image (43). Finally, in order to reduce noise, a despeckling algorithm was applied to the images using the despeckle function in FIJI.

Image Analysis

Stack images were loaded with Imaris Software (v9.3.0, Bitplane, Zurich, Switzerland) and signal intensity was corrected over time using the *normalize time points* function. A *reference frame* was placed at the center of the image. Next, surfaces for nuclei were reconstructed based on the GFP signal and the vessels based on the tdTomato signal. Nuclei were filtered by *track displacement* (10 μm) and *track duration* (496 s) for moving nuclei. Based on the *reference frame*, the statistics *track position mean*, *track position start*, *track displacement*, and *track velocity* were exported for moving cells. *Volume* was exported for unfiltered vessel and nuclei surfaces. *Track velocity* is the length of the track path divided by the duration of the track.

Analysis toward the center of the FOV

In order to determine the direction of the moving cells, the length of the vectors in the *reference frame* “center” was calculated for *track position start* (defined by the value of the X, Y track start positions; $\begin{bmatrix} a \\ \end{bmatrix}$) and *track position mean* (defined by the mean value of X, Y track coordinates positions; $\begin{bmatrix} b \\ \end{bmatrix}$) in X, Y. The *difference of vector lengths from center* $\begin{bmatrix} a \\ \end{bmatrix} - \begin{bmatrix} b \\ \end{bmatrix}$ was calculated and normalized to the *track displacement* (or: *displacement*; the object’s track displacement is the distance between the first and last object’s position along the selected-axis) in order to account for the actual distance between start and end position. Positive values indicate a movement toward the center, negative values away from the center.

Analysis of the surface volumes

Imaging volume was based on the theoretical volume of the stack. *Total nuclei volume* was the sum of all nuclei surfaces averaged over time. *Total vessel volume* was the sum of all vessel surfaces averaged over time.

Histology

Femoral bones were explanted, muscles largely removed so that osteotomized bone parts maintained one entity. Tissue was fixed using 4% electron microscopy-grade paraformaldehyde in phosphate-buffered saline (PBS) for 4 h at 4°C, washed in PBS, and run through a sucrose gradient (10%,

20%, 30%; for 12–24 h). Bones were frozen in SCEM medium (Sectionlab, Hiroshima, Japan), cut into slices of 7 μm using Kawamoto’s film method (44), and stored at -80°C . For immunofluorescence, individual sections were thawed, rehydrated in PBS, blocked with 10% donkey serum, and stained with antibodies in PBS/0.1% Tween 20/5% donkey serum containing 4’,6-diamidino-2-phenylindole (DAPI) for 1–2 h. Target proteins were identified using antibodies against Emcn (V.7C7 unconjugated, sc-65495, 1:100, Santa Cruz Biotechnology, Inc, Dallas, TX, USA). Primary antibodies were stained with secondary antibodies (1:500, anti-rat conjugated AF594, A21209, Thermo Fisher, Waltham, MA, USA). Samples were washed between steps and after staining with PBS/0.1% Tween 20 for 3 \times 5 min. Stained samples were kept in PBS for 5 min, embedded using aqueous mounting medium (Fluoromount, Thermo Fisher, Waltham, MA, USA), and analyzed microscopically within 6 days. All images were acquired on a Zeiss LSM880 (Carl Zeiss AG, Oberkochen, Germany) in tile scan mode at a resolution of 2048 \times 2048 px. For display, pictures were background subtracted and contrast was adjusted using ImageJ 1.52i.

RESULTS

Limbostomy: Design and Technical Data

In order to establish longitudinal intravital imaging of regeneration processes in long bones, we adapted the previously published LIMB microendoscopic system (31), based on an established, standardized fixator plate for osteotomies in mice (32). Simultaneously, we aimed to increase the FOV, to allow more flexibility regarding imaging depth, and maximize versatility by using only one multipurpose implant for both, osteotomy and imaging. A comparison of the FOV from the original LIMB system, the Limbostomy raw data, and the corrected images is illustrated in Supporting Information Figure 1 and Table S1. In order to combine an osteotomy model with LIMB, the osteotomy must be performed before the lens is inserted into the tissue. This is required to avoid damaging the lens and ensure free movement of the saw through the entire bone cortex. To achieve this, we chose a modular approach, in which the lens tubing is separated from the fixator plate and can be screwed into the plate using a thread on the lower end of the metal tubing (Fig. 1A). The thread terminates at the fixator plate, and only the lens sticks into the tissue (Fig. 1A, right). In this way, the lens can be attached after the injury is made (see also Fig. 3G). As a result, we were able to increase the diameter of the custom-built GRIN lens to 600 μm and simultaneously reduce the diameter of the tubing-lens-system inside the bone tissue by 50 μm , as compared to the previously published LIMB system. This resulted in less space occupied by the implant within the bone (Fig. 1B). Finally, in order to allow the introduction of an osteotomy gap and simultaneously maintain a stable fixation of the bone fragments, the screw positions lateral to the lens position were located equidistant and their intervening distance was maximized (Fig. 1C). In order to guarantee stable fixation, a minimum distance of one screw

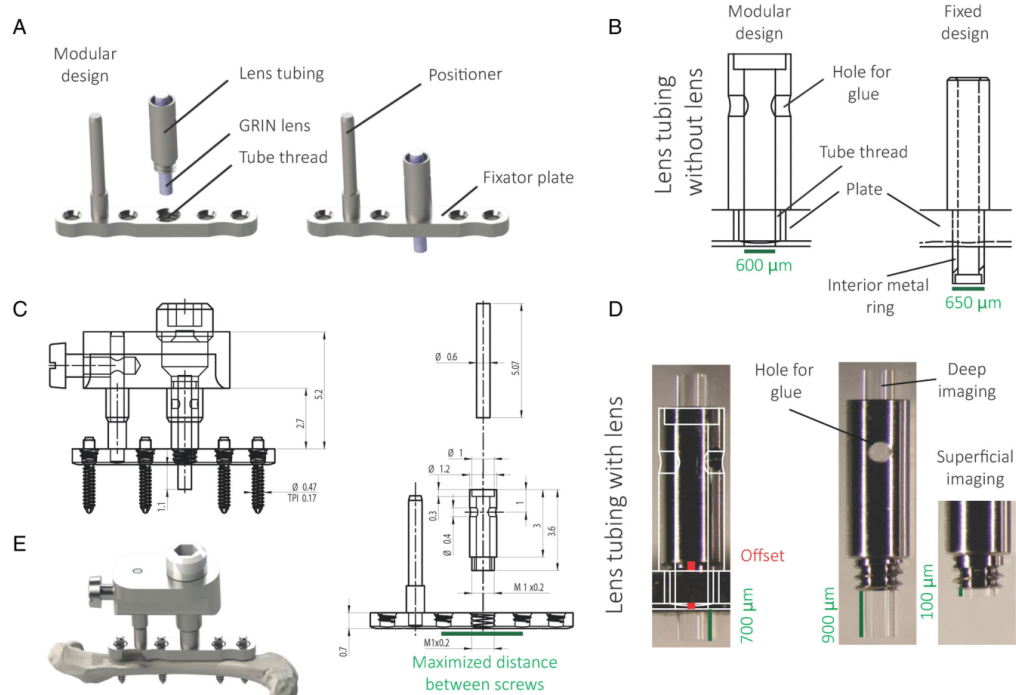


Figure 1. Limbostomy: a modular microendoscope design allows an increased imaging volume, varying depths, and secure fixation for an osteotomy. (A) An internal fixator plate with a rod for mounting the reference plate contains a thread which accepts the lens tubing. (B) In comparison to the fixed LIMB design, the interior metal ring is removed and allows the usage of a lens with a diameter of 600 μm . (C) The fully assembled Limbostomy design with mounted reference plate (left) and an exploded drawing of the fixator-lens design. Distances are in millimeters. The plate contains screw threads which are located in a maximal distance from the lenses. (D) Pictures of glued tubing-lens modules. Offsets are due to production inaccuracy (upper offset, red) and the distance between the end of the tubing and the fixator (lower offset, red). In this example, the lens is glued protruding 900 μm (right), which results in 700 μm penetration depth (left). The lens can be glued protruding for superficial imaging. (E) Fully assembled, all modules are either glued or screwed together to secure the lens and prevent movement in the FOV.

diameter between two screws should be maintained (Romano Mathtys, personal communication). The diameter of one screw is 0.47 mm (Fig. 1C). Consequently, as the distance between the screws amounts to 3.5 mm, the system allows for osteotomy gap sizes of up to 2 mm.

To enable visualization of bone regeneration processes, we aimed to access the center of the femoral long bone in an osteotomy. Based on the average femoral bone diameter of 1,415 μm , calculated from μCT data of 3-month-old mice (as published in Bucher et al.) (4), we glued the lens into the tubing at 900 μm protruding from the bottom of the fixation plate. This includes 700 μm bone and bone marrow as well as 200 μm offset between the plate and the bone surface, before the lens enters the bone. Offsets resulted from the contact-free design of the plate as well as from production inaccuracy, resulting in a variation of 100 μm (Fig. 1D).

The process of fixing the lens is performed manually, as shown in Supporting Information Movie S1. All these features in the Limbostomy system (Fig. 1E) allow the usage of flexible lens-tubing-systems with different penetration depths in the same, standardized fixator system, to achieve any depth up to 700 μm in the femoral bone, for osteotomy gap sizes of up to 2 mm.

Lens Characterization

Like in the LIMB system (31), a GRIN lens (Fig. 2A, Supporting Information Table S2) was used to optically access the bone tissue. In order to determine the relevant parameters for image correction in this two-photon fluorescence microendoscopy approach, we characterized its optical parameters and aberrations. These include chromatic aberration and spherical wave front aberrations.

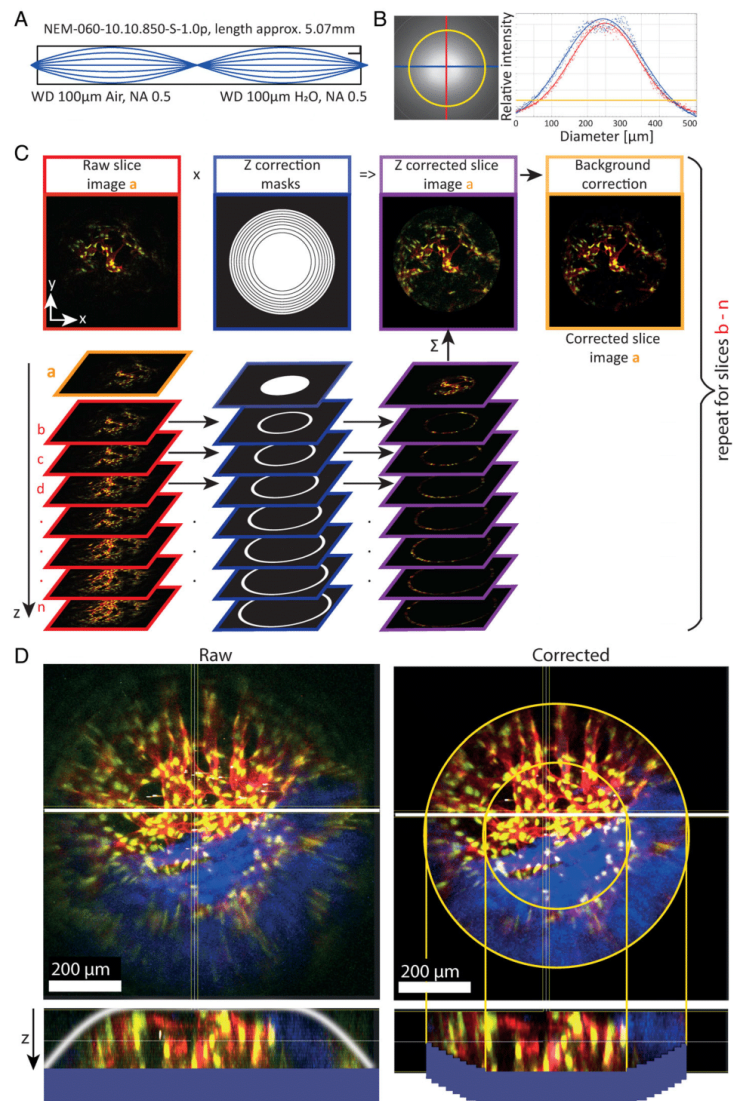


Figure 2. Lens specifications and image correction. (A) Designation of the used GRIN lens and technical drawing of the light path through the GRIN lens. (B) Field of view (yellow) with corresponding Gaussian fitted intensity distributions in x (blue) and y (red). (C) Flowchart visualization of the image correction algorithm. The raw slice image a (orange frame) gets z-corrected by shifting the displaced peripheral areas of lower slices up to their correct z position. This is done by cropping the concentric ring-shaped areas of lower slices (b to n) with binary masks (blue frame) and summing them up (purple frame). This is repeated for slices b to n as the new start points. Afterwards, a background correction is performed (yellow frame). (D) Comparison of the maximum intensity z-projections of raw image (left) and corresponding corrected image (right). The xz-section (of the white line) displays the image plane curvature in the raw and the up-shifted z-slices for the corrected image. Dark blue areas underneath symbolize deeper layers and illustrate how the image correction algorithm shifts deeper slices up to correct for displaced structures.

The FOV was determined based on the $1/e^2$ isoline of the maximum intensity from the lateral center of the illumination distribution through the GRIN lens (Supporting Information Fig. 2A), fitted by a Gaussian function (Fig. 2B). The field curvature and image distortions, which are mainly caused by chromatic and spherical aberrations, were quantified by imaging a reference grid with known dimensions and agarose gel containing fluorescent beads (200 nm diameter), respectively. An overview of all the determined optical parameters is depicted in the Supporting Information Table S2.

The chromatic aberration is defined as axial focal shift when the wavelength is changed. It was determined by sequentially imaging a rigid bead structure at different excitation wavelengths in the range between 800 and 1,030 nm, as we expect the chromatic aberration to scale linearly with the excitation wavelength (Supporting Information Methods Eq. 1, Fig. 2B). Since all analyses presented in this work were performed at the same excitation wavelength, no focal deviation was induced and therefore no correction of chromatic aberration was needed.

The third-order spherical aberration, which contributes significantly to the overall wave front aberration, resulted in a radial parabolic wave front and subsequent image plane deformation. This was quantified by imaging a defined reference grid, in which the radius of the sharpest grid structures, in relation to the focus depth, was measured. The data were fitted by a paraboloid model (Supporting Information Methods) using the least-squares fitting algorithm. Theoretically, in an ideal optical system with no wave front aberrations, the plane reference grid would appear as a sharp structure in one distinct focal plane. In our system, concentric ring-shaped areas appeared as sharp structures at various focal depths, indicating the deformation of peripheral areas of the image plane (Supporting Information Fig. 2C). This paraboloid distortion of the acquired images occurred along the optical axis.

Image Correction

In order to correct for the intrinsic confounding factors of the optical system, an image postprocessing algorithm of two main steps was designed. The first step sequentially corrects the slices of a raw stack (Fig. 2C, red frame) for image plane deformation introduced by the wave front aberrations in the axial dimension (Fig. 2C, purple frame). The second step corrects for system-related inhomogeneous illumination, sample-specific background signals and smoothes the signal in the images (Fig. 2C, yellow frame).

For z-corrections, binary polar masks were generated (Fig. 2C, blue frame) which depend on the z-step size of the raw image stack. The radius of each mask was calculated from the fitted equation (Supporting Information Methods Eq. 2), which best describes the image plane deformation in our experimental data (Supporting Information Fig. 2D). Afterwards, the masks are used to crop the corresponding concentric ring-shaped areas of lower slices in the z-stack, with a similar z-shift as the one caused by the third-order spherical aberration. The cropped image slices are merged at the

corrected z-position. This compensated the curvature of the aberration-induced image plane deformation. The procedure was repeated iteratively with all z-slices as start points.

Image correction resulted in a visual improvement of the peripheral image areas through higher contrast and minimizing positional errors of structures in z (Fig. 2D). We validated the image correction algorithm by calculating and comparing the image plane curvature of raw and corrected images. We found that image quality was increased, and the image plane curvature was minimized (Fig. 2, Supporting Information Methods).

Surgery Procedure for Combined Imaging and Osteotomy

The femoral shaft of the right hind limb of a mouse was approached laterally and exposed under sterile conditions. Anesthesia via a respiratory mask was induced with 2.0% and maintained with 1.5% isoflurane. The mouse was positioned on a heating mat and the shaved and disinfected leg, covered by incision foil, was secured on a custom-made leg platform (Fig. 3A, Supporting Information Fig. 3). An incision of approximately 1.5 cm was made into the skin between the knee and hip joint, parallel to the femur (Fig. 3B, upper picture). The underlying muscles were dissected and retracted along the delimiting fascia (Fig. 3B, lower picture). The fixation plate was fixed onto the exposed bone and stabilized using forceps with a side lock (Fig. 3C, upper picture). A pilot hole was introduced at the distal screw thread position using a 0.31 mm drill bit (Fig. 3C, upper picture) and a 2 mm bicortical screw was inserted manually through the complete shaft and locked into the plate (Fig. 3C, lower picture). The process was repeated for the proximal screw position and the two remaining centered positions; so four screws were placed in total. In order to expose and access the full perimeter of the femur, forceps were placed under the bone (Fig. 3D,E, upper picture) and a Gigli wire saw of approximately 25 cm in length was passed through the gap (Fig. 3D). The two cutting positions were marked by placing small incisions with the saw. Cuts distal (Fig. 3E, lower picture) and proximal (Fig. 3F, upper picture) were made perpendicular to the bone and the bone section was removed (Fig. 3F, lower picture). Subsequently, the lens-tubing was positioned using a hand drill with enlarged drill chuck and screwed into the designated thread over the osteotomy gap (Fig. 3G). The wound was sewed with a surgical thread (Fig. 3H, upper picture). Finally, a reference plate was attached, fixed on the positioner, and closed using a plug screw to protect the lens (Fig. 3H, lower picture). The final result (Fig. 3I) shows the fixed reference plate outside the bone. We measured the gap size based on the distance between the screws and found that we reliably achieve a gap size of $\sim 816 \mu\text{m}$ (confidence interval (CI): 787–844 μm ; SD = 85 μm) (Fig. 3J). As shown previously, the wound heals without impacting the behavior of the mice (Reismann et al., Fig. 3K) (31). Using immunofluorescence histology, we observed normal regeneration and vessel formation at the site of injury indicated by high expression of Endomucin (Emcn) in areas of tissue damage and callus

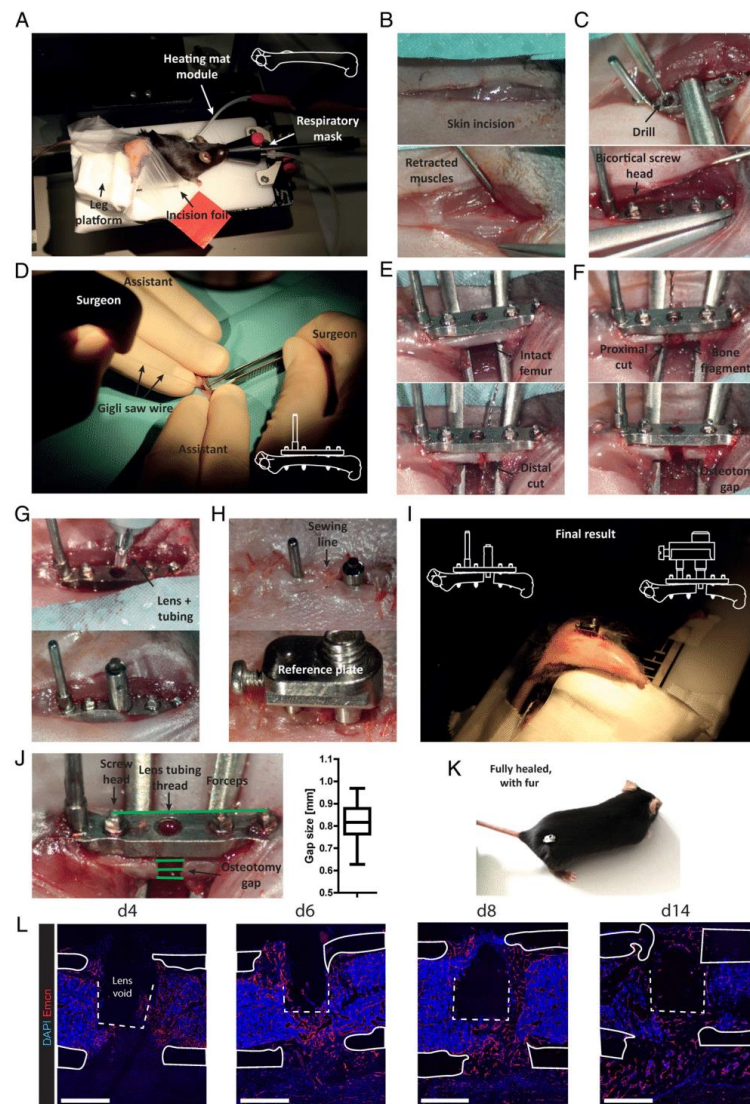


Figure 3. Limbostomy surgical procedure and healing outcome. (A) The mouse's leg is shaved, and the mouse is fixed on a heating mat under isoflurane anesthesia. (B) An incision is made through the incision foil, skin and then muscles are retracted. (C) Guide holes are drilled and screws positioned. (D) Using a Gigli saw wire two cuts (E, F) are made and the bone fragment is removed. (G) The lens tubing is screwed into the fixator and (H) the skin closed before the reference plate is mounted onto the system. (I) The final result shows the reference plate outside of the body. (J) Osteotomy gap size was measured using the distance between screws as reference. Box-plot whiskers max–min (confidence interval, CI: 787–844 μm ; SD = 85 μm ; n = 37). (K) Fully healed, the mouse is not restricted in its movement and fur regrows. (L) Immunofluorescence histology of bone sections shows high expression of the vessel marker Endomucin (Emcn, red) in areas of tissue damage and callus formation over the course of regeneration. Nuclei are stained with DAPI and shown in blue. Images represent $n \geq 4$ for each time point. Scale bars = 500 μm .

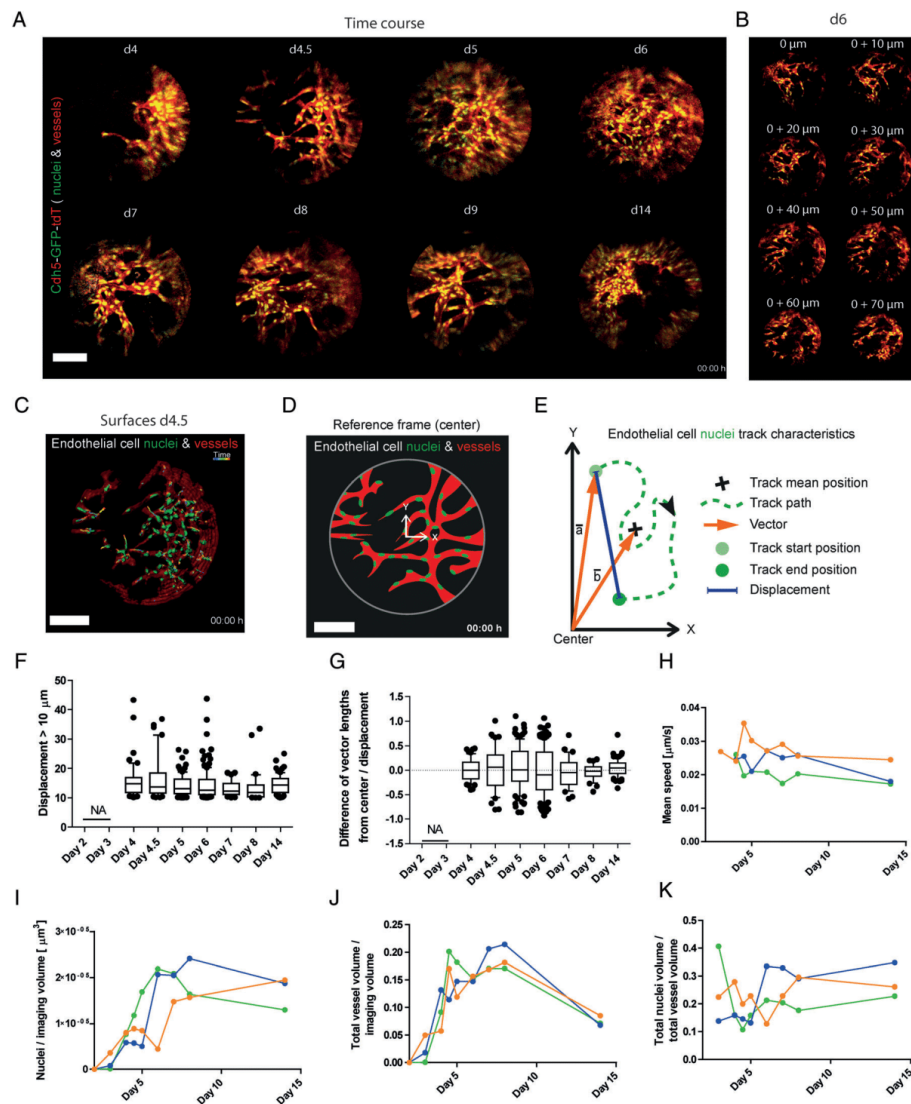


Figure 4. Vasculature after osteotomy is a highly dynamic process shown using Limbostomy. **(A)** Time course of vascularization over 2 weeks in an individual Cdh5-GFP-tdT mouse. Pictures are corrected maximum intensity projections of the FOV. The movies for Day 4 and Day 4.5 can be found in the Supporting Information Movie S4. **(B)** Projections of 10 μm thick slices of the z-stack resolve individual vessels. **(C)** Representative surface reconstructions of endothelial cell vessel volumes and nuclei as well as their tracks over time (rainbow colors). **(D)** Reference frame position in the FOV for direction of endothelial cell nuclei movement. **(E)** Object/endothelial cell nuclei track characteristics used for generating the difference of vector lengths from center ($|\vec{a}| - |\vec{b}|$). **(F)** Displacement and **(G)** normalized difference of vector lengths from center over time in one individual mouse (corresponding to the green curves in **H–K**). **(H)** Mean speed of nuclei, **(I)** nuclei count/imaging volume, **(J)** vessel volume based on tdT signal/imaging volume, and **(K)** the nuclei volume/vessel volume ratio for three individual mice. Scale bars = 100 μm.

formation shown to highly express PECAM-1 (CD31) (Fig. 3L) (45). Emcn expression was lower in contralateral bones, with only few Emcn^{hi} vessels alongside the endosteum (Supporting Information Fig. 4A). Of note, intraindividual bone regeneration progress showed variability of callus formation in front of the lens (Supporting Information Fig. 4B). All necessary utensils for the procedure are listed in the Supporting Information Table S3.

Longitudinal Imaging of Vessel Formation During Regeneration After Osteotomy

During healing, a close interplay of mesenchymal, vascular, and immune cells is required to initiate the regenerative process. Recently, we reported dynamic changes occurring in the vasculature during the tissue regeneration process after bone injury. We also reported vessel plasticity in homeostasis, when analyzed by longitudinal intravital microscopy, using intravenously injected Qtracker 655 Vascular Labels to highlight the vessel lumen (31). These particles are cleared from the blood by the kidney within 30 min. Additionally, a fraction of the label diffuses from the vessel lumen into the bone marrow tissue through the fenestrated sinusoidal endothelium specific to this tissue (Supporting Information Movie S2). In order to analyze the spatial changes of vasculature in the osteotomy model and draw conclusions about both vessel structure and proliferative behavior of the endothelial cells, we implanted the Limbostomy system into Cdh5-GFP-tdT reporter mice. These mice express a membrane-tagged tandem tomato fluorescent protein (tdT) and histone 2B linked enhanced GFP under a transgenic VE-cadherin (Cdh5) promoter. We repeatedly performed imaging in the osteotomy gap over the time course of regeneration, starting at Day 2, up to Day 14 after osteotomy. As shown in Figure 4 and consistent with our observations using immunofluorescence histology (50), vascularization of the fracture hematoma became detectable between Day 3 and Day 4 in the FOV. Vessels developed sprouts into the nonvascularized tissue (Fig. 4A) and rapidly expanded in the FOV. Within 24 h, the entire FOV was pervaded with endothelial cells (Fig. 4A). Using LIMB, we were able to capture a cell division event, which took 30 min from the prophase, in which chromosomal condensation was visible until telophase, when chromosomes decondensate (Supporting Information Movie S3). However, this was the only cell division event we observed. Endothelial cell sprouts were exclusively derived from the existing Cadherin5-expressing vessel network, and not de novo from scattered single cells. Activated tip cells with fine filopodia protruded into the nonvascularized tissue. They preceded the nucleus of the endothelial cell. The nucleus then moved into the tip and was subsequently followed by the cell body (Supporting Information Movie S4). The high density of sprouts made it challenging to discriminate the cell bodies of individual endothelial cells. As many cells showed filopodia, it was not always possible to identify activated tip cells or stalk cells unambiguously. Tip cells from different sprouts contacted each other, suggesting the formation of anastomoses (Supporting Information Movie S4, d4.5). The new vessel network in the FOV was dense by Day

5 and Day 6. Here, individual vessels were best visible in image sections rather than maximum intensity projections of stacks (Fig. 4B). The network rapidly reorganized from day to day until collagen deposition was visible via SHG, in line with the phase of soft callus formation on Day 6 (Supporting Information Fig. 4C). At 14 days postsurgery, the imaging depth is 80 μ m due to collagen deposition and bone mineralization. Immunofluorescence histology observation shows that callus formation within the FOV was dependent on the individual regeneration progress (Supporting Information Fig. 4B,C).

The vessel network is a highly dynamic structure, characterized by motility of endothelial cell nuclei and the endothelial cell structures. We reconstructed three-dimensional surfaces for the nuclei and vasculature and tracked nuclei over time (Fig. 4C). In order to draw conclusions about the direction of movement, a reference frame was positioned in the center of the imaging volume (Fig. 4D) and endothelial cell nuclei tracks were recorded in this coordinate system (Fig. 4E). In order to account for image instability inherent to this type of intravital imaging, only nuclei with a displacement of $>10 \mu$ m were considered moving nuclei. Along the recorded time course, nuclei were motile (Fig. 4F) with no apparent preferred direction of movement (Fig. 4G) or speed (Fig. 4H) even at Day 14 postsurgery. The overall count of nuclei per imaging volume increased over time between Day 3 and Day 7 postsurgery and was stable until Day 14 (Fig. 4I). Simultaneously, total vessel volume increased until Day 8 and decreased until Day 14 (Fig. 4J). We measured the ratio of nuclei volume/vessel volume in order to determine patterns of vessel density, which—somehow unexpected—remained stable over time (Fig. 4K).

DISCUSSION

In this work, we introduce a method for intravital microendoscopy in the bone suitable for established bone regeneration models, as well as for the analysis of the marrow niches in long bones. The new design has a postprocessing FOV of 402 μ m in diameter with a flexible z volume of up to 100 μ m imaging depth inside the tissue. Although this system is not suitable for tile scans, imaging time series are acquired at a resolution comparable with other intravital bone imaging approaches (20,46). Imaging depth is a challenge in intravital bone and bone marrow two-photon imaging approaches, because it is limited to about 150 μ m below the bone surface (34). This is why in most studies, the easily accessible calvarial bone for bone imaging is used (3,14,16,18,20,21,23–25,34,46,47). Ramasamy et al. circumvent this problem by imaging the small, metatarsal bones (26). In another approach, the cortical bone of the tibia was milled down to a small diameter in order to increase imaging depth of the actual marrow tissue (15,17,19). As this method removes the periosteum, it creates an acute injury and inevitably initiates an immune reaction, in addition to likely impacting on blood supply via transcortical vessels (48). Therefore, it is not suitable for longitudinal studies. In order to avoid immune responses and infection, Kim et al. repeatedly close, apply antibiotic ointment, and open the wound in order to perform

longitudinal imaging (49). Using the Limbostomy system or the LIMB system, which both share the same internal fixator plate and screws, imaging can be performed for several months in one individual without losing stability of fixation or image quality (29,31). Although Limbostomy was only tested for a period of several days in this study, and considering the usage of the same internal fixator plate, we expect that Limbostomy and LIMB are equally stable over time.

Here, we show that, after the lens has been placed, depending on its position in the tubing, practically any depth between periosteum and bone marrow center at about 700 μm can be reached and imaged with an extra imaging depth of consistently 100 μm , without further invasive manipulation of the mouse during regeneration. Over the course of regeneration, the maximum imaging depth decreases, most likely dependent on the varying degree of deposition of collagen-containing extra-cellular matrix at different stages. As shown in the Supporting Information Figure 3C, the system allows visualization of vasculature in 80 μm of depth at 14 days postsurgery. It is embedded in collagen-rich structures which produce SHG signals upon two-photon excitation, indicating the formation of a hard callus. This opens up the opportunity to analyze cellular dynamics during the remodeling phase directly at the respective site in the tissue, and will enable insights into the cellular and extracellular dynamics of tissue organization during these late phases of bone regeneration. The flexibility of the system with regard to insertion depth of the lens will allow us to adjust the position of the FOV according to the biological question. As known from histology studies, the callus resolves and becomes replaced by hematopoietic marrow tissue at later phases of regeneration in deeper regions of the bone (50). Limbostomy will us to analyze this important and fascinating process at cellular resolution. Any other method is limited to the 2PM imaging depth starting periostally approximately 150 μm below the bone surface (34), due to the highscattering properties of the bone, which are unique among mammalian tissues.

Compared to our initial LIMB system, Limbostomy has an increased FOV, flexible imaging depth, and occupies less space in the tissue due to a decreased diameter of the lens-tubing. This reduction of spatial limitations is combined with an increase in functionality and reproducibility. The Limbostomy system is the only system, which allows observation of bone regeneration in the long bones by stable fixation. The rigidity of the bone fixation influences the mechanical stability. It will be interesting to compare the impact of various degrees of fixation rigidity with respect to the process of regeneration longitudinally, at a cellular level. Here, we describe for the first time dynamic processes of endochondral bone regeneration in an osteotomy model, longitudinally, *in vivo*. The flexibility of the modular Limbostomy method can be considered an approach for multiple applications, such as the observation of cellular niches under homeostatic conditions (31), regeneration of drill holes injuries using a very short lens, regeneration of osteotomies of up to 2 mm size, over time in one individual, at cellular and subcellular resolution. It is theoretically possible to image endosteal areas

diametrically opposite the lens insertion site, by inserting the lens even deeper than the 700 μm mentioned above. Complementary, the drill hole injury at the insertion site can be investigated by positioning the lens to a penetration depth of 0.

Importantly, bone regeneration is a process with rapid phases such as the onset of vascularization or the distribution of inflammatory cells (50). Vascularization in the fracture gap is completed within 24 h after onset. However, the onset itself is observed to occur at Day 3 or Day 4 and therefore varies up to 24 h in our measurements. Comparing time points in early regeneration of samples from multiple individuals does not resolve these differences and subsequently results in high interindividual variations, which have also been reported by others (44). Using Limbostomy, it is now possible to describe the longitudinal process of regeneration of one individual in detail. This will allow a comparison between individuals in order to determine which stage of regeneration is delayed or accelerated. The increase of data gained from individuals is a good example of how intravital microscopy can also contribute to the Reduce, Refine, & Replace (3R) principle, which aims to improve design of experiments involving animals. Here, the animals undergo one surgery from which they recover quickly. From there, mounting and imaging includes few steps, with minimal impact on the animal or on physiological and inflammatory processes.

For this new microendoscope design, the FOV could be increased by a factor of 1.78 in comparison to the old GRIN lens approach (31) (Supporting Information Table S1) without decreasing resolution or sensitivity. Both the theoretical ($\Delta xy_{\text{theo}} = 0.75 \mu\text{m}$, $\Delta z_{\text{theo}} = 6.38 \mu\text{m}$) and experimental values ($\Delta xy_{\text{exp}} = 0.99 \pm 0.13 \mu\text{m}$, $\Delta z_{\text{exp}} = 6.44 \pm 1.29 \mu\text{m}$) we determined for the resolution showed minimal deviations. Importantly, not only the calculated resolution values, but also the fact that events such as the phases of mitosis could be observed in GFP-labeled nuclei, demonstrated the ability of the optical system to reach subcellular resolution in the context of the bone marrow environment.

GRIN lens technology in combination with a suitable objective in our system lead to optical errors like chromatic and wave-front aberrations. This was corrected using a post-processing algorithm which minimizes the axial image deformation and filters out noise and background signals.

The correction algorithm used here is adequate for the purpose of the performed image analysis, such as the investigation of the volume of nuclei, vessels, and directionality. An improvement of the image quality after image correction was achieved as demonstrated by experimental validation, which showed a decrease of the image plane curvature after correction (Supporting Information Fig. 5A,B), as well as the feature extraction of biological structures, which yielded more reliable and accurate results for the corrected images. In this way, subcellular resolution was achieved even in areas at the edge of the FOV.

Even though an xy-correction was not necessary in our case (Supporting Information Methods, Fig. 5C), it might become necessary when performing imaging at various

wavelengths, simultaneously or sequentially, since the third order spherical aberration is strongly dependent on the excitation wavelength. This holds true also for a correction of the chromatic aberration.

Using Limbostomy, we are for the first time able to observe the de novo formation of the vasculature after osteotomy, over extended time periods, in one and the same animal. Our method reveals that two phases of vascularization exist. The initial vascularization of the hematoma happens around 3–4 days after osteotomy, and by Day 4–5 the whole FOV is entirely pervaded with vessels. The second phase comprises remodeling of the vessel network, which occurs afterward, evident by the change in vessel volume between Day 8 and Day 14. This is in line with previous descriptions (2,51). The first wave of vascularization is rapid, since within 24 h the FOV is pervaded. Interestingly, this is the same time window as described in the much bigger bones of sheep (52). We have shown previously that dynamic changes occur in the vasculature during tissue regeneration, and high vessel plasticity was observed during homeostasis (31). Here, remodeling of the vasculature was observed over the entire process of regeneration, showing that vessel plasticity is also present during regeneration.

Sprouts show activated cells with filopodia, which are visible not only at the tip. The sprouts develop from the existing vessel network and migration into the non-vascularized areas is evident by movement of the nuclei of the stalk. In sprouting during vascularization of the neonatal retina, proliferation occurs in the stalk cells (53). Here, discrimination of tip, stalk, and network, which is a model used for vascularization of the retina (53) was challenging due to vessel density, ambiguous location of sprouts, as well as numerous filopodia at not only tip cells. Proliferation of endothelial cells during regeneration of the osteotomy was not observed, raising the question where those cells derive from. Proliferation of endothelial cells appears to be a rare event in bone tissue regeneration, as shown previously in histological Ki67 analysis after bone injury due to implantation of LIMB (31). In the retina, tip cells do not proliferate, but stalk cells do. It might be possible that proliferation occurs outside the FOV and the endothelial cells migrate into the injury. Another possibility is that the cell division events are so rare that we simply missed them. Here, extensive imaging times could be considered. Not only proliferation, but a complete characterization of the organization of endothelial cells during vascularization and reorganization in the bone regeneration process is of interest. Vascularization is essential for bone regeneration and Limbostomy will shed light on the cellular and subcellular mechanisms in this process. It was previously not possible to analyze tissue dynamics such as directional cell movement, object velocity, cell–cell interactions, anastomosis, sprouting, and collagen deposition during tissue regeneration in the long bones, because those types of analyses were limited to the calvarium.

In order to characterize metabolic conditions in the tissue on a cellular level, related to its perfusion, and analyze their impact on bone regeneration (6), the combination of

Limbostomy with fluorescence lifetime imaging (FLIM) holds great potential. FLIM allows the marker-free investigation of the NAD(P)H-related metabolism of cells (54). To overcome the limitation of decreased imaging depth in mineralized tissue, three-photon microscopy could be an interesting technique that may also be used in combination with Limbostomy. Combining Limbostomy with our recently developed technology for multiplexed intravital microscopy (55) will enable us to come closer to analyzing the complex dynamics of the regeneration process, as it will help to account for the known heterogeneity of bone marrow stromal cells (56,57).

The method of Limbostomy is suitable for applications in health and disease including the proliferation of stem and progenitor cells in their niches during hematopoiesis, mesenchymal cell–cell interactions, endothelial cell functions, or mobilization of cells during infections. It will enable longitudinal monitoring in the context of tumor formation and therapy, and will deliver a better understanding of immunological memory and long-lived cells *in vivo*. Furthermore, the wide range of applications for this method will contribute to standardization of intravital bone marrow imaging experiments and thereby increase comparability among those.

ACKNOWLEDGMENTS

We thank Christian Bucher for providing the measurements of bone thickness based on μ CT data. This study was funded by the Deutsche Forschungsgemeinschaft, Forschergruppe FOR2165 “Regeneration in Aged” (DFG grant 5354/6-2 to AEH), DFG TRR130, TP C01 to AEH and RAN and HA5354/8-1 to AEH. Parts of this work were supported by an “Adding 3R value” grant from the Charité - Universitätsmedizin Berlin. JS is a member of the Berlin-Brandenburg School for Regenerative Therapies (BSRT). AFF is a member of the Dahlem Research School (DRS). AFF is supported by a PhD scholarship of the Beuth Hochschule für Technik Berlin.

CONFLICT OF INTEREST

RM and RN (RISystem AG, Landquart, Switzerland) declare competing financial interests. The implant for longitudinal imaging will be commercialized by RISystem AG, Landquart, Switzerland. The remaining authors declare no competing financial interests.

AUTHOR CONTRIBUTIONS

AEH, RAN, JS, RM, RN, GND, and DR developed the modular implant approach. JS, AFF, MK, WL, MT, RG, and AR performed experiments. JS, AFF, AR, WL, and MT analyzed the data. RHA and MGB provided Cdh5-ttHistone2B-GFP mice. AEH, RAN, JS, and AFF interpreted the results and wrote the manuscript. RM, RN, MK, AR, and GND reviewed the manuscript.

LITERATURE CITED

1. Einhorn TA, Gerstenfeld LC. Fracture healing: Mechanisms and interventions. *Nat Rev Rheumatol* 2014;11:45–54.

2. Schmidt-Bleek K, Petersen A, Dienelt A, Schwarz C, Duda GN. Initiation and early control of tissue regeneration - bone healing as a model system for tissue regeneration. *Expert Opin Biol Ther* 2014;14:247-259.
3. Fujisaki J, Wu J, Carlson AL, Silberstein L, Putheti P, Larocca R, Gao W, Saito TI, Celso CL, Tsuyuzaki H, et al. In vivo imaging of Treg cells providing immune privilege to the haematopoietic stem-cell niche. *Nature* 2011;474:216-219.
4. Bucher CH, Schlundt C, Wulsten D, Sass FA, Wendler S, Ellinghaus A, Thiele T, Seemann R, Willie BM, Volk HD, et al. Experience in the adaptive immunity impacts bone homeostasis, remodeling, and healing. *Front Immunol* 2019;10:797.
5. Reinke S, Geissler S, Taylor WR, Schmidt-Bleek K, Juelke K, Schwachmeyer V, Dahme M, Hartwig T, Akyuz L, Meisel C, et al. Terminally differentiated CD8 + T cells negatively affect bone regeneration in humans. *Sci Transl Med* 2013;5:177ra36.
6. Ambrosi TH, Scialdone A, Graja A, Gohlke S, Jank AM, Bocian C, Woelk L, Fan H, Logan DW, Schürmann A, et al. Adipocyte accumulation in the bone marrow during obesity and aging impairs stem cell-based hematopoietic and bone regeneration. *Cell Stem Cell* 2017;20:771-784.
7. Dimitriou R, Tsiridis E, Giannoudis PV. Current concepts of molecular aspects of bone healing. *Injury* 2005;36(12):1392-1404.
8. Alexander KA, Chang MK, Maylin ER, Kohler T, Müller R, Wu AC, Van Rooijen N, Sweet MJ, Hume DA, Raggatt LJ, et al. Osteal macrophages promote in vivo intramembranous bone healing in a mouse tibial injury model. *J Bone Miner Res* 2012;188:1201-1205.
9. Schlundt C, El Khassawna T, Serra A, Dienelt A, Wendler S, Schell H, van Rooijen N, Radbruch A, Lucius R, Hartmann S, et al. Macrophages in bone fracture healing: Their essential role in endochondral ossification. *Bone* 2015;106:78-89.
10. Wu AC, Raggatt LJ, Alexander KA, Pettit AR. Unraveling macrophage contributions to bone repair. *Bonekey Rep* 2013;2:1-7.
11. Ono T, Okamoto K, Nakashima T, Nitta T, Hori S, Iwakura Y, Takayanagi H. IL-17-producing $\gamma\delta$ T cells enhance bone regeneration. *Nat Commun* 2016;7:10928.
12. Niesner RA, Hauser AE. Recent advances in dynamic intravital multi-photon microscopy. *Cytometry Part A* 2011;79A:789-798.
13. Ding L, Saunders TL, Enikolopov G, Morrison SJ. Endothelial and perivascular cells maintain haematopoietic stem cells. *Nature* 2012;481:457-462.
14. Itkin T, Gur-Cohen S, Spencer JA, Schajnovitz A, Ramasamy SK, Kusumbe AP, Ledergor G, Jung Y, Milo I, Poulos MG, et al. Distinct bone marrow blood vessels differentially regulate haematopoiesis. *Nature* 2016;532:323-328.
15. Köhler A, Schmithorst V, Filippi MD, Ryan MA, Daria D, Gunzer M, Geiger H. Altered cellular dynamics and endosteal location of aged early hematopoietic progenitor cells revealed by time-lapse intravital imaging in long bones. *Blood* 2009;114:290-298.
16. Lassailly F, Foster K, Lopez-Onieva L, Currie E, Bonnet D. Multimodal imaging reveals structural and functional heterogeneity in different bone marrow compartments: Functional implications on hematopoietic stem cells. *Blood* 2013;122:1730-1740.
17. Köhler A, de Filippo K, Hasenberg M, van den Brandt C, Nye E, Hosking MP, Lane TE, Männ L, Ransohoff RM, Hauser AE, et al. G-CSF-mediated thrombopoietin release triggers neutrophil motility and mobilization from bone marrow via induction of Cxcr2 ligands. *Blood* 2011;117:4349-4357.
18. Mazo JB, von Andrian UH. Adhesion and homing of blood-borne cells in bone marrow microvessels. *J Leukoc Biol* 1999;66:25-32.
19. Zehentmeier S, Roth K, Cserenyessy Z, Sercan Ö, Horn K, Niesner RA, Chang HD, Radbruch A, Hauser AE. Static and dynamic components synergize to form a stable survival niche for bone marrow plasma cells. *Eur J Immunol* 2014;44:2306-2317.
20. Bixel MG, Kusumbe AP, Ramasamy SK, Sivaraj KK, Butz S, Vestweber D, Adams RH. Flow dynamics and HSPC homing in bone marrow microvessels. *Cell Rep* 2017;18:1804-1816.
21. V-H L, Lee S, Lee S, Wang T, Jang WH, Yoon Y, Kwon S, Kim H, Lee S-W, Kim KH. In vivo longitudinal visualization of bone marrow engraftment process in mouse calvaria using two-photon microscopy. *Sci Rep* 2017;7:1-10.
22. Lo Celso C, Wu JW, Lin CP. In vivo imaging of hematopoietic stem cells and their microenvironment. *J Biophotonics* 2009;631:619-631.
23. Scott MK, Akinduro O, Lo Celso C. In vivo 4-dimensional tracking of hematopoietic stem and progenitor cells in adult mouse calvarial bone marrow. *J Vis Exp* 2014;91:1-7.
24. Sipkins DA, Wei X, Wu JW, Runnels JM, Côté D, Means TK, Luster AD, Scadden DT, Lin CP. In vivo imaging of specialized bone marrow endothelial microdomains for tumour engraftment. *Nature* 2005;435:969-973.
25. Wang L, Kamocka MM, Zollman A, Carlesso N. Combining intravital fluorescent microscopy (IVFM) with genetic models to study engraftment dynamics of hematopoietic cells to bone marrow niches. *J Vis Exp* 2017;121:54253.
26. Ramasamy SK, Kusumbe AP, Schiller M, Zeuschner D, Bixel MG, Milia C, Gamrekelashvili J, Limbourg A, Medvinsky A, Santoro MM, et al. Blood flow controls bone vascular function and osteogenesis. *Nat Commun* 2016;7:13601.
27. Xie Y, Yin T, Wiegand W, He XC, Miller D, Stark D, Perko K, Alexander R, Schwartz J, Grindley JC, et al. Detection of functional hematopoietic stem cell niche using real-time imaging. *Nature* 2009;457:97-101.
28. Chen Y, Maeda A, Bu J, DaCosta R. Femur window chamber model for in vivo cell tracking in the murine bone marrow. *J Vis Exp* 2016;113:1-9.
29. Dondossola E, Alexander S, Holzapfel BM, Filippini S, Starbuck MW, Hoffman RM, Navone N, de-Juan-Pardo EM, Logothetis CJ, Hutmacher DW, et al. Intravital microscopy of osteolytic progression and therapy response of cancer lesions in the bone. *Sci Transl Med* 2018;10:eaao5726.
30. Lindquist RL, Niesner RA, Hauser AE. In the right place, at the right time: Spatio-temporal conditions determining plasma cell survival and function. *Front Immunol* 2019;10:788.
31. Reismann D, Stefanowski J, Günther R, Rakhymzhan A, Matthys R, Nützi R, Zehentmeier S, Schmidt-Bleek K, Petkau G, Chang HD, et al. Longitudinal intravital imaging of the femoral bone marrow reveals plasticity within marrow vasculature. *Nat Commun* 2017;8:2153.
32. Matthys R, Perren SM. Internal fixator for use in the mouse. *Injury* 2009;40(Suppl 4):S103-S109.
33. Raggatt LJ, Alexander KA, Kaur S, Wu AC, MacDonald KPA, Pettit AR. Absence of B cells does not compromise intramembranous bone formation during healing in a tibial injury model. *Am J Pathol* 2013;182:1501-1508.
34. Lo Celso C, Fleming HE, Wu JW, Zhao CX, Miake-Lye S, Fujisaki J, Côté D, Rowe DW, Lin CP, Scadden DT. Live-animal tracking of individual hematopoietic stem/progenitor cells in their niche. *Nature* 2009;457:92-96.
35. Pinho S, Frenette PS. Hematopoietic stem cell activity and interactions with the niche. *Nat Rev Mol Cell Biol* 2019;20:303-320.
36. van den Bos T, Speijer D, Bank RA, Brömme D, Everts V. Differences in matrix composition between calvaria and long bone in mice suggest differences in biomechanical properties and resorption. Special emphasis on collagen. *Bone* 2008;43:459-468.
37. Huiskes R, Rulmerman R, Van Lenthe GH, Janssen JD. Effects of mechanical forces on maintenance and adaptation of form in trabecular bone. *Nature* 2000;405:704-706.
38. Umemura Y, Nagasawa S, Honda A, Singh R. High-impact exercise frequency per week or day for osteogenic response in rats. *J Bone Miner Metab* 2008;26:456-460.
39. Lim J, Lee J, Yun HS, Shin HI, Park EK. Comparison of bone regeneration rate in flat and long bone defects: Calvarial and tibial bone. *Tissue Eng Regen Med* 2013;10:336-340.
40. Meng G, Liang Y, Sarsfield S, Jiang W-c, Lu R, Dudman JT, Aponte Y, Ji N. High-throughput synapse-resolving two-photon fluorescence microendoscopy for deep-brain volumetric imaging in vivo. *Elife* 2019;8:1-24.
41. Jeong HW, Hernández-Rodríguez B, Kim JM, Kim KP, Enriquez-Gasca R, Yoon J, Adams S, Schöler HR, Vaquerizas JM, Adams RH. Transcriptional regulation of endothelial cell behavior during sprouting angiogenesis. *Nat Commun* 2017;8:726.
42. Lang A, Schulz A, Ellinghaus A, Schmidt-Bleek K. Osteotomy models - The current status on pain scoring and management in small rodents. *Lab Anim* 2016;50:433-441.
43. Legland D, Arganda-Carreras I, Andrey P. MorphoLibJ: Integrated library and plugins for mathematical morphology with ImageJ. *Bioinformatics* 2016;32:3532-3534.
44. Kawamoto T, Kawamoto K. Preparation of thin frozen sections from nonfixed and undecalcified hard tissues using Kawamoto's film method (2012). *Methods Mol Biol* 2014;1130:149-164.
45. Lang A, Kirchner M, Stefanowski J, Durst M, Weber MC, Pfeiffenberger M, Damerau A, Hauser AE, Hoff P, Duda GN, et al. Collagen I-based scaffolds negatively impact fracture healing in a mouse-osteotomy-model although used routinely in research and clinical application. *Acta Biomater* 2019;86:171-184.
46. Hawkins ED, Duarte D, Akinduro O, Khorshed RA, Passaro D, Nowicka M, Straszewski L, Scott MK, Rothery S, Ruivo N, et al. T-cell acute leukaemia exhibits dynamic interactions with bone marrow microenvironments. *Nature* 2016;538:518-522.
47. Lo Celso C, Lin CP, Scadden DT, Celso CL. In vivo imaging of transplanted hematopoietic stem and progenitor cells in mouse calvarium bone marrow. *Nat Protoc* 2011;6:1-14.
48. Grüneboom A, Hawwari I, Weidner D, Culemann S, Müller S, Henneberg S, Brenzel A, Merz S, Bornemann L, Zec K, et al. A network of trans-cortical capillaries as mainstay for blood circulation in long bones. *Nat Metab* 2019;1:236-250.
49. Kim S, Lin L, Brown GAJ, Hosaka K, Scott EW. Extended time-lapse in vivo imaging of tibia bone marrow to visualize dynamic hematopoietic stem cell engraftment. *Leukemia* 2016;31:1-11.
50. Stefanowski J, Lang A, Rauch A, Aulich L, Köhler M, Fiedler AF, Buttgerit F, Schmidt-Bleek K, Duda GN, Gaber T, et al. Spatial distribution of macrophages during callus formation and maturation reveals close crosstalk between macrophages and newly forming vessels. *Front Immunol* 2019;10:2588.
51. Schmidt-Bleek K, Schell H, Lienau J, Schulz N, Hoff P, Pfaff M, Schmidt G, Martin C, Perka C, Buttgerit F, et al. Initial immune reaction and angiogenesis in bone healing. *J Tissue Eng Regen Med* 2012;8:120-130.
52. Lienau J, Schmidt-Bleek K, Peters A, Haschke F, Duda GN, Perka C, Bail HJ, Schütze N, Jakob F, Schell H. Differential regulation of blood vessel formation between standard and delayed bone healing. *J Orthop Res* 2009;27:1133-1140.
53. Gerhardt H, Golding M, Fruttiger M, Ruhrberg C, Lundkvist A, Abramsson A, Jeltsch M, Mitchell C, Alitalo K, Shima D, et al. VEGF guides angiogenic sprouting utilizing endothelial tip cell filopodia. *J Cell Biol* 2003;161:1163-1177.
54. Leben R, Köhler M, Radbruch H, Hauser AE, Niesner RA. Systematic enzyme mapping of cellular metabolism by phasor-analyzed label-free NAD (P) H fluorescence lifetime imaging. *Int J Mol Sci* 2019;20:5565.
55. Rakhymzhan A, Leben R, Zimmermann H, Günther R, Mex P, Reismann D, Ulbricht C, Acs A, Brandt AU, Lindquist RL, et al. Synergistic strategy for multi-color two-photon microscopy: Application to the analysis of germinal center reactions in vivo. *Sci Rep* 2017;7:7101.
56. Addo RK, Heinrich F, Heinz GA, Schulz D, Sercan-Alp Ö, Lehmann K, Tran CL, Bardua M, Matz M, Löhning M, et al. Single-cell transcriptomes of murine bone marrow stromal cells reveal niche-associated heterogeneity. *Eur J Immunol* 2019;49:1372-1379.
57. Holzwarth K, Köhler R, Philippen L, Tokoyoda K, Ladyhina V, Wahlby C, Niesner RA, Hauser AE. Multiplexed fluorescence microscopy reveals heterogeneity among stromal cells in mouse bone marrow sections. *Cytometry Part A* 2018;93A:876-888.

8.6 Stefanowski et al., 2020 – Supporting Material

Supporting Tables

Supporting Table 1 – Field of view

System	Lens in diameter	FOV in diameter	FOV in circular area ($\pi \cdot r^2$)
LIMB	350 μm	~280 μm	61575 μm^2
Limbostomy	600 μm	~500 μm	196350 μm^2
Limbostomy, post-processing	600 μm	402 μm	126923 μm^2

Supporting Table 2 – Optical parameters of the GRIN lens (NEM-060-10.10.850-S-1.0p; Needle microendoscope, 600 μm diameter, 100 μm WD image side air NA~0.5, 100 μm WD object side water NA~0.5, at 850 nm, singlet, pitch 1.0)

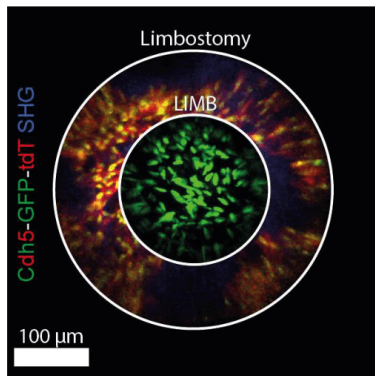
Parameter	Value
Overall transmission of the system @ 850nm	15 \pm 2 %
Transmission of the GRIN lens @ 850nm	69 \pm 7 %
Angular aperture	(38.78 \pm 1.22) $^\circ$
Numerical aperture in air	0.33 \pm 0.01
Numerical aperture in water	0.44 \pm 0.01
Field of view for $1/e^2$ criterion	(380 \pm 15) μm
Magnification	1.0 \pm 0.03
Theoretical lateral resolution (Abbe) @ 850nm	0,75 μm
Theoretical axial resolution (Abbe) @ 850nm	6,38 μm
Lateral resolution (for rayleigh criterion) @ 850nm	(0.99 \pm 0.13) μm
Axial Resolution (for rayleigh criterion) @ 850nm	(6.44 \pm 1.29) μm
Spherical aberration	$\Delta z(r) = (1.08 \pm 0.06) \cdot 10^{-3} \cdot r^2 \mu\text{m}$
Chromatic aberration	$\Delta z(\Delta\lambda) = (95 \pm 8) \cdot \Delta\lambda \mu\text{m}$

Supporting Table 3 – Utensils for surgical procedure

Utensil	Supplier
Forceps with side lock	#11062-10, F.S.T.
Bicortical screw, 2 mm	RIS.401.100, RISystem, Davos, Switzerland
Drill bit, 0.31 mm	RIS.590.202, RISystem, Davos, Switzerland
Forceps for positioning during osteotomy	
Forceps angled 45°, tip width 0.4 mm	#11063-07, F.S.T
Forceps Dumont #5 /45, 45°	#11251-35, F.S.T
Gigly wire saw, 0.22 mm	RIS.590.100, RISystem, Davos, Switzerland
Hand drill	RIS.309.130, RISystem, Davos, Switzerland
Surgical thread	Surgicryl rapid, USP 6/0 12mm, #14071512, SMI, Netherlands

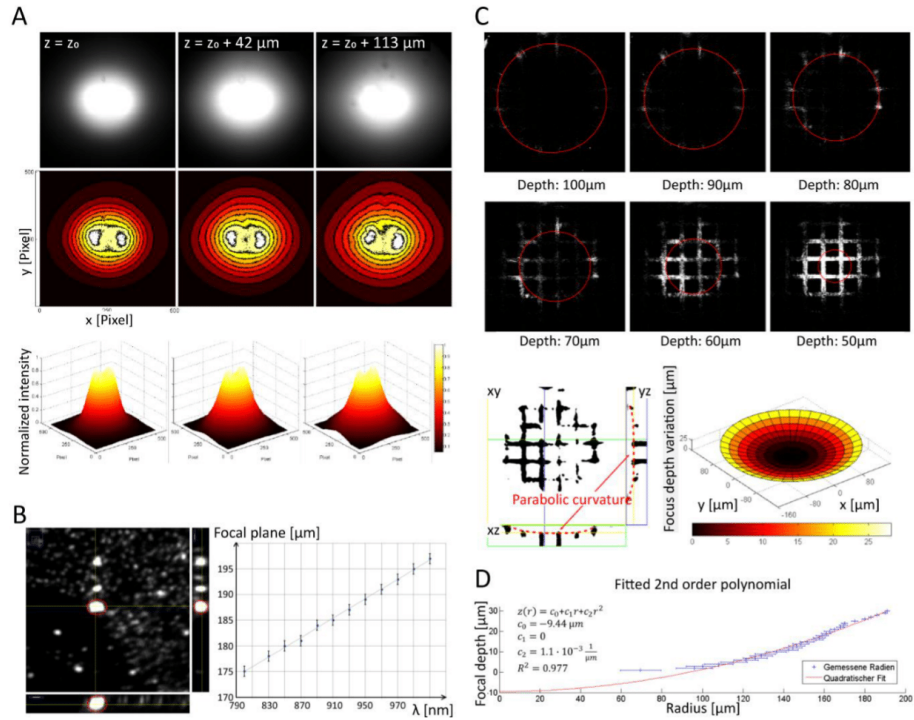
Supporting Figures

Supporting Figure 1



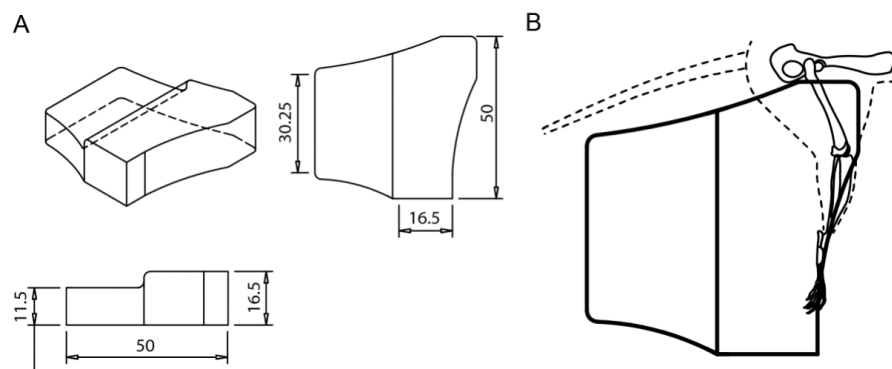
Supporting Figure 1: Comparison of LIMB and Limbostomy FOV. The increase in diameter of the GRIN lens applied maximizes the FOV in Limbostomy making it comparable to other IVM methods of the bone.

Supporting Figure 2



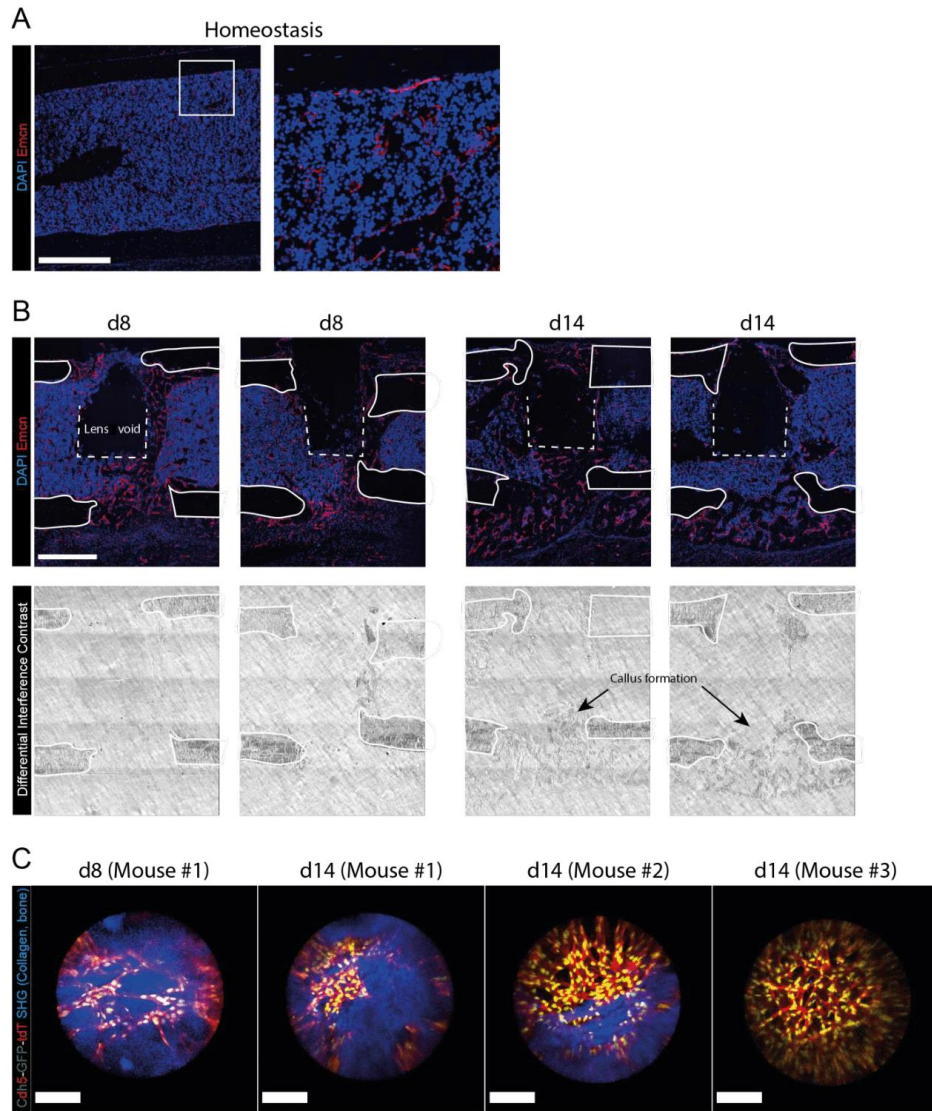
Supporting Figure 2: Quantification of the optical specifications of the GRIN lens. (A) Intensity distributions through the GRIN lens as raw images (top), isoline depiction (middle) and 3D model (bottom). (B) Fluorescent bead cluster used for determining the chromatic aberration (left) and the linear correlation for the chromatic aberration (right). (C) The sharpest structures of the reference grid, imaged at different focal depths, appear as concentric ring-shaped areas of varying radius. This demonstrates the image plane curvature due to spherical aberration. The xz- and yz-sections of the grid image underneath show the parabolic image plane curvature (left) and the corresponding 3D model (right). (D) Graph of the fitted 2nd order polynomial which best described the image plane curvature.

Supporting Figure 3



Supporting Figure 3: Technical drawing of the leg stage for surgery. (A) Custom made mouse leg stage. Distances are in mm. (B) The mouse is positioned on the left body side and the right leg secured using tape at the edge of the stage.

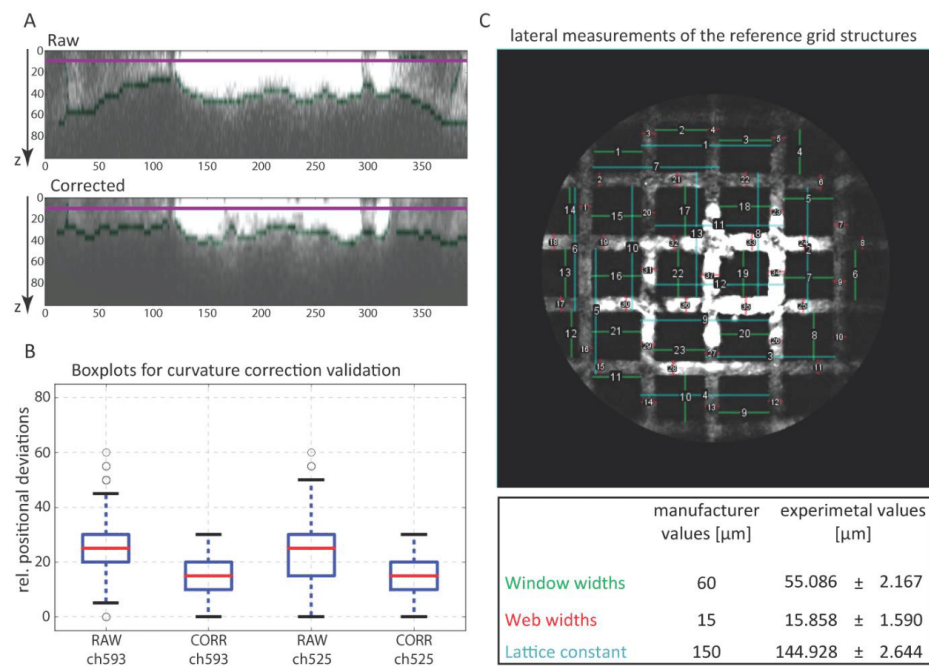
Supporting Figure 4



Supporting Figure 4: Inter-individual variability in normal bone regeneration. (A) Immunofluorescence histology in bone section of a contra-lateral bone post-surgery shows $Emcn^{hi}$ expressing endothelium in endosteal regions of the diaphysis. (B) The course of regeneration shows inter-individual variability in location and extent of vascularization and callus formation. Scale bars = 500 μm . (C) Inter-individual variability is also evident in

Limbostomy maximum intensity projections of z-stacks from three individual mice. Collagen deposition, indicated by the second harmonic generation (SHG) signal is visible as early as 8 day post-surgery in mouse #1 in the entire FOV until day 14. Approximately half of the FOV is occupied by SHG in mouse #2 and only small dots are visible in mouse #3 14 days post-surgery. Imaging depth 14 days post-surgery = 80 μm . Scale bars = 100 μm .

Supporting Figure 5



Supporting Figure 5: Validation of the image correction. (A) Raw image (top) and corrected image (bottom) of the xz-section of a transverse web of the reference grid with their detected edges (dark green) and the reference line (violet) used for the calculation of the positional deviations as a measure of the curvature of the image. (B) Boxplots of positional deviations show that the positional deviation to the reference line and therefore the image curvature of the corrected image (in both channels ch593 and ch525) is lower with respect to the raw image. (C) Lateral measurements of the widths of reference grid windows

(green), webs (red) and lattice constant (cyan) by hand-drawn lines. The table underneath the image lists a comparison of the values of the measurement and the manufacturer's values.

Supporting Movies

Supporting Movie 1: Lens gluing process. The movie shows how a lens is positioned inside the lens tubing and glued to a desired penetration depth using two-component glue, a syringe needle, tape, and a scale under a biocular microscope.

Supporting Movie 2: Vascular label leakage. In a Limbostomy control mouse experiment 5 weeks post-implantation, without osteotomy, tissue regeneration is completed and the bone marrow under homeostatic conditions. Video z-stacks are not corrected for aberration. Qtracker 655 vascular label (red) is injected and imaged for 30 min. The label fluorescence intensity decreases over the observed time until almost no signal is detected. Note the shadows of intra-vascular cells, which are migrating along the endothelium. The movie also shows the typical sinusoidal structure of the bone marrow vasculature and vessels small in diameter in the FOV. Scale bar = 100 μm .

Supporting Movie 3: Cell division event. Using LIMB containing a 350 μm lens a cell division event was observed two weeks post-implantation, without osteotomy. Video z-stacks are not corrected for aberrations but smoothed using a median filter 3 x 3 x 3 px. The movie shows the phases of mitosis: The condensation of DNA (prophase), the metaphase (chromosomes lie up along metaphase plate), the anaphase (chromatids move to opposite ends of the cell), and finally the decondensation of the chromosomes. Scale bar = 50 μm .

Supporting Movie 4: Sprouting vasculature 4 days post-surgery. Using Limbostomy in a Cdh5-GFP-tdT mouse (endothelial cell nuclei – green, endothelial cell membrane – red) shows sprouting and invasion of tip cells into unvascularized tissue. (First part) 4 days post-surgery a tip cell develops sprouts which grow into the tissue. A nucleus moves along the vessel structure toward the tip. At the upper left rim of the imaging FOV, cells are entering the FOV. In all areas, where endothelial cells are visible nuclei are motile. (Second part) 12 h later vasculature spread significantly and tip cells touch each other at some locations, indicating anastomosis events. Sprouting and vessel growth as well as motility of nuclei is present. Scale bar = 100 μm .

Supporting Methods

Quantification of the optical properties of the GRIN lens

The overall transmission of the imaging system was measured multiple times with and without the microendoscopic GRIN lens using a thermopile power meter (NewPort, Glasgow, UK) placed at the focal plane. That way the overall transmission of the whole system and the transmission solely of the GRIN lens could be determined (Supporting Table 2).

Intensity distribution (Supporting Fig. 2A) was determined by imaging a homogeneous fluorescent reference slide through the GRIN lens via water immersion. From that, the FOV was determined as the area enclosed by the isoline at which the intensity drops to 13.5% of the maximum intensity (following the $1/e^2$ criterion). Note that the intensity distribution and therefore the FOV, are not symmetrical. This is because of slight changes of the beam shape which occur along the beam path and the laser source itself, which does not produce perfectly Gaussian distributed TEM_{00} mode. This leads to a FOV difference in x and y of approx. 4% and is not significant in the context of our image analysis.

The corresponding numerical apertures (NA) in air and water were determined from the solid angle defined by the nominal working distance and the FOV.

An expected magnification of the GRIN lenses of approx. 1 was proven by imaging a reference grid, determining the web width, window width and lattice constant and comparing it to the known data provided by the manufacturing company (analogous to Supporting Fig. 5C).

The theoretical lateral resolution was calculated as the Abbe limit under two-photon-excitation conditions $\Delta_{xy} = \sqrt{\frac{1,22}{2}} \cdot \frac{\lambda}{NA}$ and $\Delta_z = \sqrt{2} \cdot \frac{\lambda \cdot \eta_{sample}}{NA^2}$ with a theoretical NA = 0.5.

In addition the optimal axial and lateral resolutions were determined as the axial and lateral dimensions of the Point Spread Functions (PSF), following the Rayleigh criterion for a circular aperture $\Theta_R = 1,22 \frac{\lambda}{D}$ (translating to 80% of maximum) measured using fluorescing beads (200 nm diameter). The spatial resolution is similar to the theoretical resolution calculated using the paraxial approximation, only slightly degraded by scattering.

For the quantification of the chromatic aberration a distinct rigid bead structure was imaged for several excitation wavelengths in the range of 800 to 1030 nm. The focal shift was then calculated as the differences of the determined focal depths for every wavelength with respect to the highest possible sharpness of the defined bead structure. The experimental data showed a linear correlation of wavelength and focal drift, and were fitted accordingly by the linear function (Supporting Fig. 2B):

$$\Delta z = (95 \pm 8) \text{ nm} \cdot \Delta \lambda \quad (1)$$

The spherical aberration, which causes a parabolically deformed image plane, was quantified by examining the sharpest structures of the images of a reference grid with known properties for several focal depths (Supporting Fig. 2C). Based on the experimental data, for the concentric sharpest structures of the grid, a rotation paraboloid model was fitted by a least squares algorithm. The fitting, which was done for the non-planar peripheral regions of the radial interval $r = [100,200]$, yielded the formula which best describes the focal plane deformation (Supporting Fig. 1D) :

$$z(r) = -9.44 \mu\text{m} + 1.1 \cdot 10^{-3} \frac{1}{\mu\text{m}} \cdot r^2 \quad (2)$$

Image correction validation

To evaluate the compensation of the image plane curvature done by the image correction algorithm raw images and corrected images of the reference grid were compared. Before the correction a clear image plane deformation is visible in the raw images (Supporting Fig. 5A). After z correction the curvature of the image of the grid is compensated.

The lower edges of the raw and corrected images were segmented (using the canny algorithm of the scikit-image library in python) and the distances of each point with respect to the reference line were calculated, individually. This was done for horizontal and vertical z-sections in multiple grid images. The resulting boxplots (Supporting Fig. 5B) showed that in any case the positional deviations to the reference line are significantly lower in the corrected images. Moving the reference line adds an offset to the positional deviations, so that the boxplots differ depending on the positional choice of the reference line. This does

not change the result of the corrected image having lower positional deviations (as the measure for reduced image curvature), provided that the reference line lies spatially above the detected edges in both raw and corrected images.

Image correction procedure

z-correction:

The radius of each mask was calculated from the fitted equation (Supporting Methods, Eq 2) which best described the image plane deformation in our experimental data. Since lower z-slices are required to correct the respective superjacent image slice, a full correction could only be performed for the n_{th} image slice at $n \leq n_{max} - N^e$ of masks, because the fluorescence signal of deeper layers would be necessary but has not been acquired. The inner central areas of the FOV were not z-corrected, since the image plane curvature shows significant z shifts ($\geq 1 \mu\text{m}$) only on outer peripheral areas ($r \geq 100 \mu\text{m}$).

xy-correction:

The experimental data from the quantification of the optical parameters and intravital measurements showed minimal positional errors in x and y, so that the presence of lateral image distortions is neglectable. To verify this, the dimensions and orientation of the reference grid structure was measured manually multiple additional times in FIJI. The results (Supporting Fig. 5C) show, that the dimensions of the web widths, window widths, and lattice constant show minimal deviations ($\leq 8\%$) to the values provided by the manufacturing company. These deviations are neglectable, excluding the subjective error induced by the manual drawing of the measured lines.

9 Curriculum Vitae

Mein Lebenslauf wird aus datenschutzrechtlichen Gründen in der elektronischen Version meiner Arbeit nicht veröffentlicht

10 Complete List of Publications

- Riedel, R., Addo, R., Ferreira-Gomes, M., Heinz, G.A., Heinrich, F., Kummer, J., Greiff, V., Schulz, D., Klaeden, C., Cornelis, R., Menzel, U., Kröger, S., Stervbo, U., Köhler, R., Haftmann, C., Kühnel, S., Lehmann, K., Maschmeyer, P., McGrath, M., Naundorf, S., Hahne, S., Sercan-Alp, Ö., Siracusa, F., **Stefanowski, J.**, Weber, M., Westendorf, K., Zimmermann, J., Hauser, A.E., Reddy, S.T., Durek, P., Chang, H., Mashreghi, M., Radbruch, A., 2020. Discrete populations of isotype-switched memory B lymphocytes are maintained in murine spleen and bone marrow. *Nat. Commun.* 11, 2570. Impact Factor N.A <https://doi.org/10.1038/s41467-020-16464-6>
- Stefanowski, J.**, Fiedler, A.F., Köhler, M., Günther, R., Liublin, W., Tschakner, M., Rauch, A., Reismann, D., Matthys, R., Nützi, R., Bixel, M.G., Adams, R.H., Niesner, R.A., Duda, G.N., Hauser, A.E., 2020. Limbostomy: Longitudinal Intravital Microendoscopy in Murine Osteotomies. *Cytom. Part A* 97, 483–495. Impact Factor N.A <https://doi.org/10.1002/cyto.a.23997>
- Stefanowski, J.**, Lang, A., Rauch, A., Aulich, L., Köhler, M., Fiedler, A.F., Buttgerit, F., Schmidt-Bleek, K., Duda, G.N., Gaber, T., Niesner, R.A., Hauser, A.E., 2019. Spatial Distribution of Macrophages During Callus Formation and Maturation Reveals Close Crosstalk Between Macrophages and Newly Forming Vessels. *Front. Immunol.* 10. Impact Factor 3.124 <https://doi.org/10.3389/fimmu.2019.02588>
- Lang, A., Kirchner, M., **Stefanowski, J.**, Durst, M., Weber, M.-C., Pfeiffenberger, M., Damerau, A., Hauser, A.E., Hoff, P., Duda, G.N., Buttgerit, F., Schmidt-Bleek, K., Gaber, T., 2019. Collagen I-based scaffolds negatively impact fracture healing in a mouse-osteotomy-model although used routinely in research and clinical application. *Acta Biomater.* 86, 171–184. Impact Factor 6.690 <https://doi.org/10.1016/j.actbio.2018.12.043>
- Reismann, D., **Stefanowski, J.**, Günther, R., Rakhymzhan, A., Matthys, R., Nützi, R., Zehentmeier, S., Schmidt-Bleek, K., Petkau, G., Chang, H.-D., Naundorf, S., Winter, Y., Melchers, F., Duda, G., Hauser, A.E., Niesner, R.A., 2017. Longitudinal intravital imaging of the femoral bone marrow reveals plasticity within marrow vasculature. *Nat. Commun.* 8, 2153. Impact Factor 12.353 <https://doi.org/10.1038/s41467-017-01538-9>
- Herrtwich, L., Nanda, I., Evangelou, K., Nikolova, T., Horn, V., Sagar, Erny, D., **Stefanowski, J.**, Rogell, L., Klein, C., Gharun, K., Follo, M., Seidl, M., Kremer, B., Münke, N., Senges, J., Fliegau, M., Aschman, T., Pfeifer, D., Sarrazin, S., Sieweke, M.H., Wagner, D., Dierks, C., Haaf, T., Ness, T., Zaiss, M.M., Voll, R.E., Deshmukh, S.D., Prinz, M., Goldmann, T., Hölscher, C., Hauser, A.E., Lopez-Contreras, A.J., Grün, D., Gorgoulis, V., Diefenbach, A., Henneke, P., Triantafyllopoulou, A., 2016. DNA Damage Signaling Instructs Polyploid Macrophage Fate in Granulomas. *Cell* 167, 1264-1280.e18. Impact Factor 30.410 <https://doi.org/10.1016/j.cell.2016.09.054>
- Palm, N.W., de Zoete, M.R., Cullen, T.W., Barry, N.A., **Stefanowski, J.**, Hao, L., Degnan, P.H., Hu, J., Peter, I., Zhang, W., Ruggiero, E., Cho, J.H., Goodman, A.L., Flavell, R.A., 2014. Immunoglobulin A Coating Identifies Colitogenic Bacteria in Inflammatory Bowel Disease. *Cell* 158, 1000–1010. Impact Factor 28.710 <https://doi.org/10.1016/j.cell.2014.08.006>

11 Acknowledgements

Clarity lets light shine into the depths of the unknown but the hidden within is only seen through understanding.

I thank Prof. Anja Hauser for the unique opportunity to work independently in excellently equipped laboratories of the DRFZ and Charité on my multidimensional topic regarding bone regeneration between immunology and physics. Many thanks especially for the confidence in my scientific work and the honest supervision of my dissertation, as well as the support towards my honorary activities.

In the synergistic collaboration of the research groups of Prof. Raluca Niesner and Prof. Anja Hauser I found myself in a communicative, motivating, and productive working atmosphere. Here, the space for ideas, discussions, and personal responsibility is valued. I would like to thank Anja and Raluca for this lasting experience.

For the mentoring within the Berlin-Brandenburg School for Regenerative Therapies (BSRT) I would like to thank Prof. Anja Hauser, Prof. Georg Duda, and Prof. Raluca Niesner. The BSRT offered valuable opportunities for my further education and displayed perspectives outside the academic landscape.

My science would be lifeless without the wonderful people I met during my doctoral studies. In particular, I would like to thank David Reismann for the productive collaboration at the LIMB endoscope and the good friendship. I am grateful to Robert Günther for the precise operative and technical support, as well as the honest discussions. For the intensive work on bone regeneration and helpful discussions I thank Annemarie Lang. For the physical perspective and the reliable work on the Limbostomy method I thank Alexander Fiedler. I would like to thank Sandra, Randy, Ralf, and Vero for the inspiring scientific discussions. Always at my side were Ronja, Ruth and Markus. I would like to thank the team of the working groups Niesner / Hauser for their cooperation over the past years.

I would like to thank Ariana Rauch for her excellent work as a master student. I am grateful to Linus Aulich for his great work during his bachelor thesis.

Science is changing due to doctoral researchers that participate in their representation such as in the Leibniz PhD Network. I would like to thank Katharina Willenbücher for successful committee work in that regard. I am grateful to Marie and Meike for their active exchange on scientific- and socio-political topics.

Understanding the unknown requires freedom. I thank my parents for encouraging my curiosity. Especially, I thank my partner Andra for the security to be free.